ISSN 0044-4510

Volume 165, Issue 6

June 2024

JOURNAL OF EXPERIMENTAL and THEORETICAL PHYSICS

NAUKA
1727

RUSSIAN ACADEMY OF SCIENCES

JOURNAL OF EXPERIMENTAL AND THEORETICAL PHYSICS

FOUNDED IN MARCH 1873
PUBLISHED 12 TIMES A YEAR
MOSCOW

VOLUME 165, ISSUE 6
JUNE 2024
RAS

THE JOURNAL IS PUBLISHED UNDER THE SUPERVISION
OF THE PHYSICAL SCIENCES DEPARTMENT OF THE RUSSIAN ACADEMY OF SCIENCES

CONTENTS

ATOMS, MOLECULES, OPTICS

NUCLEI, PARTICLES, FIELDS, GRAVITATION, AND ASTROPHYSICS

SOLIDS AND LIQUIDS

ORDER, DISORDER, AND PHASE TRANSITION IN CONDENSED MEDIA

ELECTRONIC PROPERTIES OF SOLID

STATISTICAL, NONLINEAR, AND SOFT MATTER PHYSICS

JOURNAL OF EXPERIMENTAL AND THEORETICAL PHYSICS, 2024, Vol. 165, No. 6, pp. 766–774

ATOMS, MOLECULES, OPTICS

ROLE OF NEPHELAUXETIC EFFECT FOR Fe^{2+} ION IN ZINC SELENIDE AND CADMIUM TELLURIDE MATRICES

© 2024 **V. S. Krivobok**[a, b*], **D. F. Aminev**[a], **D. A. Zazymkina**[a], **V. V. Ushakov**[a], **A. A. Narych**[a], **V. I. Kozlovsky**[a], **Yu. V. Korostelin**[a]

[a] *Lebedev Physical Institute of Russian Academy of Sciences 119991, Moscow, Russia*
[b] *National Research University MPTI 141701, Dolgoprudny, Moscow region, Russia*
**e-mail: larionov.nickolay@gmail.com*

Received September 12, 2023
Revised January 23, 2024
Accepted January 29, 2024

Abstract. For the electronic subsystem of transition metal ions embedded in a crystal lattice or formed a complex with ligands, an effective decrease in interelectron repulsion is observed compared to free ions, which in modern literature is referred to as the nephelauxetic effect. In this work, we study the role of the nephelauxetic effect in the Fe^{2+} ions electronic spectrum formation in CdTe and ZnSe matrices. Experimental assessment of the corresponding corrections was carried out based on the analysis of two transitions – the well-known $^5T_2(^5D) \rightarrow {}^5E(^5D)$, enabling us to record the magnitude of the crystal field, and the less studied $^3T_1(^3H) \rightarrow {}^5E(^5D)$. The discovery of the zero-phonon line of this transition in CdTe:Fe enabled us to compare the two luminescent systems properties and demonstrate that for the Fe^{2+} ion in CdTe the nephelauxetic effect role increases noticeably. Based on the experimental data obtained in combination with calculations within crystal field theory, we have refined the values of the Racah parameters for Fe^{2+} ions in CdTe and ZnSe matrices. The role of the nephelauxetic effect for Fe^{2+} ions in two matrices similar in structure is important both for practical problems related to IR laser systems improvement, and for resolving some fundamental questions of quantum chemistry.

Keywords: *transition metal ions, crystal lattice, crystal field, nephelauxetic effect, CdTe, ZnSe*

DOI: 10.31857/S004445102406e014

1. INTRODUCTION

Group II-VI semiconductors with cubic structure, doped with transition elements, are widely used in the development of tunable [1] and pulsed [2] lasers in the mid-IR range. Further progress in laser technologies aimed at improving existing laser systems [3, 4] or developing new approaches for laser generation [5] requires a more detailed understanding of the mechanisms of electronic spectrum formation of transition element ions in crystalline matrices. Among them, the greatest attention is paid to iron and chromium [6–8]. A consistent solution to this problem could rely on modern *ab-initio* calculations, which allow determining not only the structure and electronic spectrum of luminescent centers but also studying possible scenarios of their formation [9]. Nevertheless, at present, the capabilities of this approach are often quite limited due to the fact that for embedded transition element ions, both the correlation of interelectron motion and the existence of a large number of alternative electronic configurations contributing to the total electron density have a significant influence [10]. In this context, much attention is paid to discussing many-electron corrections within the crystal field theory, in particular, the role of the so-called nephelauxetic effect is discussed [11,12].

From the crystal field theory perspective, the nephelauxetic effect manifests as an effective reduction in Racah parameters (B, C), determined by the structure of electron shells, during the transition from a free ion to an ion embedded in the crystal lattice [12]. This tendency can be interpreted as an effective reduction in electron repulsion. In other words, in the presence of surroundings, a correction arises due to many-electron effects, whose physical meaning can be qualitatively described as delocalization of single-electron orbitals and interaction of center electrons with the surroundings. Accordingly, experimental study of the nephelauxetic effect allows not only to refine the parameters of the electronic spectrum of the radiative center but also to provide some quantitative assessment of the role of many-electron motion correlation arising due to the presence of ligands. The latter circumstance is of considerable interest, particularly for establishing the accuracy of actively developing theoretical approaches [13], combining the convenience of formulation inherent in ligand field theory [14] with high-precision quantum chemistry methods [15,16], allowing for a self-consistent description of correlation effects and contributions from spin-orbital and spin-spin interactions.

Despite active study of the nephelauxetic effect for a number of chemical compounds [11, 17], its role remains poorly understood for transition element ions in crystal matrices, including the practically important case of II-VI group semiconductors with cubic structure. Experimental studies of materials in this group are complicated by the fact that spectroscopic information about several (at least two) transitions involving different electron shells becomes necessary. This feature is determined by the fact that to fix the nephelauxetic effect within crystal field theory, it is necessary to determine both the crystal field magnitude (Dq) and the exact values of Racah parameters (*B, C*). The difference of these parameters from values characteristic of the free ion will determine the role of the nephelauxetic effect.

Recently, for the quantitative description of the nephelauxetic effect, the parameter [11] has been used

$$\beta_1 = \sqrt{\left(\frac{B}{B_0}\right)^2 + \left(\frac{C}{C_0}\right)^2}, \qquad (1)$$

where *B, C* are the Racah parameters for the ion in the crystal lattice, and B_0, C_0 are the Racah parameters for the free ion. It is considered that at $\beta_1 \sim 1$ the role of the nephelauxetic effect is secondary and becomes significant if β_1 is notably less than unity [12]. In the case of cubic II-VI semiconductors, one of the promising systems for investigating the nephelauxetic effect is iron ions in zinc selenide [18, 19]. This is due to the fact that for the optically active ion Fe^{2+} in ZnSe, at least two different transitions with well-studied fine structure are known: $^5T_2(^5D) \rightarrow {}^5E\ (^5D)$ [19. 20] and $^3T_1(^3H) \rightarrow {}^5T_2(^5D$ [21]. The first transition allows determining the role of the crystal field, while the second one helps determine the range of permissible Racah parameters and evaluate the role of the nephelauxetic effect.

Along with the well-known ZnSe:Fe, interest is drawn to a system with similar properties CdTe:Fe, which also has a cubic lattice but is characterized by a larger lattice constant, smaller value of parameter *Dq* and, apparently, more significant role of many-electron effects. The latter is determined by the fact that the matrix components Cd and Te are significantly heavier than Zn and Se [22]. For CdTe:Fe the fine structure of the transition $^5T_2(^5D) \rightarrow {}^5E\ (^5D)$ was studied in [23]; the transition $^3T_1(^3H) \rightarrow {}^5E(^5D)$ in this system has not been previously studied.

In this work, based on low-temperature photoluminescence measurements, we identified the transition $^3T_1(^3H) \rightarrow {}^5E(^5D)$ for the CdTe:Fe system. The obtained data allowed us to experimentally determine the value of parameter for this system and experimentally demonstrate the different roles of many-electron corrections, which determine the nephelauxetic effect for the inner shells of the ion Fe^{2-}, in CdTe and ZnSe matrices. The evaluation of the nephelauxetic effect obtained in this work can help not only in the development of IR laser systems but also in resolving some general issues related to many-electron effects in quantum mechanical calculations.

2. MATERIALS AND EXPERIMENTAL METHODOLOGY

For the research, polycrystalline ZnSe samples were selected, doped by Fe^{2+} thermal diffusion method, which demonstrated laser generation parameters close to record values [24]. These samples in the form of parallelepipeds were cut from a polycrystalline druse with uniform microstructure. Then, an iron film was deposited on the sample surface, and the samples were annealed in Ar atmosphere at temperature 1000–1100°C for 240 hours. For luminescence measurements, the faces of parallelepipeds located perpendicular to the surface on which the iron film was deposited were used. Along these faces, a notable gradient of dopant iron concentration was observed [25]. Structural and optical characterization of selected samples ZnSe:Fe are described in work [26].

The laser-quality CdTe crystal doped with iron was grown at LPI using an original method [27]. The methodology is based on vapor phase transport of impurities in He atmosphere during free crystal growth. The main features of the technology are the use of two separate sources – polycrystalline II-IV material and impurity, as well as individual control of the flow rate of II-IV materials and doping impurity. The studied crystal was cut from a boule grown in He atmosphere at 1250 K. During furnace cooling, the boule was annealed for 24 hours at 1080 K. The concentration of iron ions was $4 \cdot 10^{18}\,\text{cm}^{-3}$.

Low-temperature photoluminescence (PL) measurements of the samples were conducted in a wide spectral range from 0.9 to 5.5 μm (1.4–0.22 eV). For measuring spectra in the near-IR range up to 1.1 μm, a setup based on an Acton monochromator (Princeton Instruments) with a cooled silicon array was used. For operation at longer wavelengths, a setup based on a modernized IKS-31 monochromator with interchangeable diffraction gratings was used. The detection scheme employed various detectors, providing maximum sensitivity in their respective ranges. In the spectral region of 1–1.7 μm, a Hamamatsu H10330B-75 photomultiplier tube operating in photon counting mode was used for signal detection. In the 1.1–2.4 μm range, a cooled InGaAs photodiode with a transimpedance preamplifier (with cooled resistance) was used. In the mid-infrared range, a cooled MCT D313 detector was employed. For detecting the photoresponse of the InGaAs photodiode and MCT detector, we used synchronous detection implemented with a Princeton Instruments SR 830 lock-in amplifier.

To excite PL transitions from level $^3T_1(^3H)$ in ZnSe:Fe, the second harmonic of a solid-state Nd:YAG laser with a wavelength of 532 nm was used. Such excitation effectively populates level $^3T_1(^3H)$ [21]. Also, with such excitation, the population of level $^5T_2(^5D)$ will be determined $^3T_1(^3H) \to {}^5T_2(^5D)$ by transition $^5T_2(^5D) \to {}^5E(^5D)$, and the $^5T_2(^5D) \to {}^5E(^5D)$ intensity of PL line will be relatively low. Therefore, for exciting the PL transition $^3T_1(^3H) \to {}^5E(^5D)$, it is more effective to use a laser with photon energy lower than the transition energy. We used a semiconductor InGaAs laser with an excitation wavelength of 995 nm and power of 200 mW. The same laser was used to excite the main PL transition in the CdTe:Fe sample. To excite luminescence from higher-lying states, a semiconductor InGaAl laser with a radiation wavelength of 660 nm was used. This laser implements the possibility of controlling radiation using an external signal. This allows, using a pulse generator, to implement pulsed excitation of the sample and thus measure the luminescence kinetics. To control the 660 nm semiconductor laser, we used a G5-72 pulse generator. In the vast majority of cases, a pulse duration of 200 μs and a pulse repetition rate of 480 Hz were selected. This mode was chosen to register relatively long-term PL decays characteristic of intracenter transitions. The pulse front width did not exceed 100 ns, which is quite sufficient for measuring relatively slow luminescence kinetics Fe^{2-} at helium temperatures.

3. LOW-TEMPERATURE LUMINESCENCE Fe^{2+} IN CdTe AND ZnSe

Fragments of low-temperature photoluminescence spectra of the studied samples, demonstrating intracenter transitions Fe^{2+} in CdTe and ZnSe, are presented in Fig. 1. Free iron ion Fe^{2+} has configuration d^6 with the ground state being ^5D, and the first excited state – ^3H. In this work, the spectrum of ions Fe^{2+}, substituting Zn(Cd) in the lattice ZnSe(CdTe) is discussed. In this case, the impurity is in a tetrahedral field, which causes splitting of the initial levels, see Fig. 2. From crystal field theory, confirmed by experimental studies of the electronic spectrum, see, for example, [19], it follows that when considering only the electric field, the ground state ^5D splits into two terms, ^5E and $^5T_2$, while the excited term splits into three levels, $^3H \to {}^3T_1, {}^3E, {}^3T_2$. The transition between the lower levels $^5T_2(^5D) \to {}^5E(^5D)$, is well studied. Both for CdTe:Fe [23] and for ZnSe [19], a series of phonon-free lines is resolved, which allows quite accurate determination of the energy shift between levels ^5E and $^5T_2$.

From early works for ZnSe:Fe a broad emission band with a maximum around 980 nm is known [18]. Experiments with optical detection of magnetic resonance unambiguously indicate the connection of this band with the transition of $^3T_1(^3H) \to {}^5E(^5D)$ ion Fe^{2+} [18]. Recently, the use of low temperatures combined with high-quality ZnSe:Fe crystals made it possible to register six phononless components of

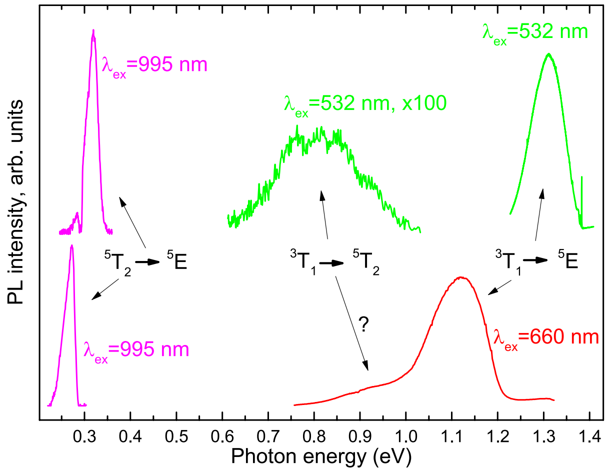

Fig. 1. Overview spectra of low-temperature photoluminescence for ions Fe^{2+} in ZnSe crystals (top) and CdTe (bottom) at a temperature of 7 K. The excitation wavelengths used are shown in the figure

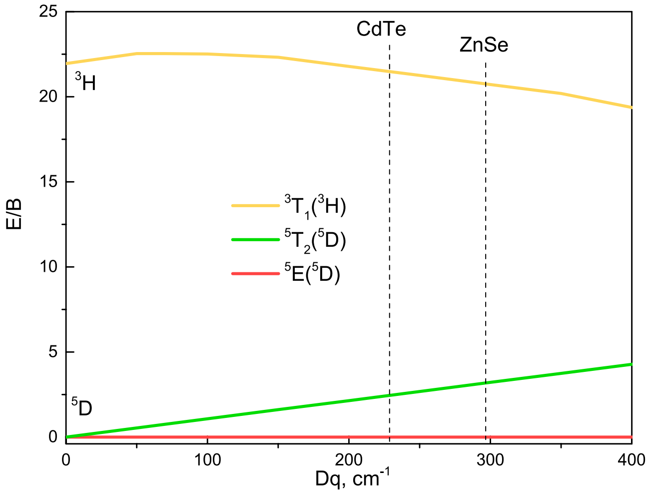

Fig. 2. Energy splitting scheme of ^{3}H- and ^{5}D- levels Fe^{2+} in a tetrahedral field (Tanabe-Sugano diagram). Vertical dashed lines correspond to the parameter values *Dq* for CdTe and ZnSe

the fine structure for the transition $^3T_1(^3H) \rightarrow {}^5E(^5D)$, each with a width not exceeding 0.3 meV [28]. The very presence of these components excludes a significant role of non-adiabatic effects, their number indicates tetrahedral coordination of the ion Fe^{2+}, and the energy position provides the possibility of more or less correct restoration of the Racah parameters in the ZnSe matrix. In turn, the transition $^3T_1(^3H) \rightarrow {}^5T_2(^5D)$ to the first excited sublevel was discussed in works [21,28]. The position of the blue boundary for the corresponding emission line agrees with the electronic spectrum structure derived from the spectroscopy of transitions $^3T_1(^3H) \rightarrow {}^5E(^5D)$ and $^5T_2(^5D) \rightarrow {}^5E(^5D)$. Characteristic luminescence signal decay times for transitions $^3T_1(^3H) \rightarrow {}^5E(^5D)$ and $^3T_1(^3H) \rightarrow {}^5T_2(^5D)$, determined by relaxation from state $^3T_1$ (^{3}H), are on the order of hundreds of microseconds [29].

For ZnSe crystals studied in this work, the luminescence spectrum corresponding to the transition $^3T_1(^3H) \rightarrow {}^5T_2(^5D)$ is shown in the center of the upper part of Fig. 1. The fine structure of the spectrum in the region corresponding to the phononless components of the transition $^3T_1(^3H) \rightarrow {}^5E(^5D)$ is shown separately in Fig. 3. The presence of several phononless peaks in the 1.379–1.387 eV region is determined by the splitting of states $^3T_1$ (^{3}H) and $^5E(^5D)$ due to first- and second-order spin-orbit interaction [28]. The spectral positions of the phononless lines are systematized in Table 1.

Unlike ZnSe, only the transition $^5T_2(^5D) \rightarrow {}^5E(^5D)$ was previously confidently registered for cadmium telluride. The fine structure of this transition indicates that, as in ZnSe, the coordination of the ion is close to tetrahedral. Consequently, the long-wavelength shift of the transition $^5T_2(^5D) \rightarrow {}^5E(^5D)$ [23] in CdTe compared to ZnSe is determined by the decrease in crystal field splitting (parameter D_q). For the studied CdTe:Fe crystals, the emission line corresponding to the transition $^5T_2(^5D) \rightarrow {}^5E(^5D)$ is shown in Fig. 1 bottom left.

In work [30], the emergence of new emission bands with emission maxima of 1.13 and 1.03 eV after iron implantation into CdTe and subsequent annealing is mentioned. This work also provides an estimate of emission decay time of 30 μs, which allows concluding that these bands are related to intracenter transitions of iron ions. However, no assumptions about the nature of the corresponding center were made in [30].

As seen in Fig. 1, in the studied crystals CdTe:Fe the emission band 1.2–0.75 eV has a complex shape, and it can be assumed that it is formed by the superposition of two bands – a more intense one with a maximum at 1.1 eV and a less intense one with a maximum around 0.9 eV. This assumption is based on the analogy with the emission spectrum Fe^{2+} in ZnSe, see the upper part of Fig. 1. However, this

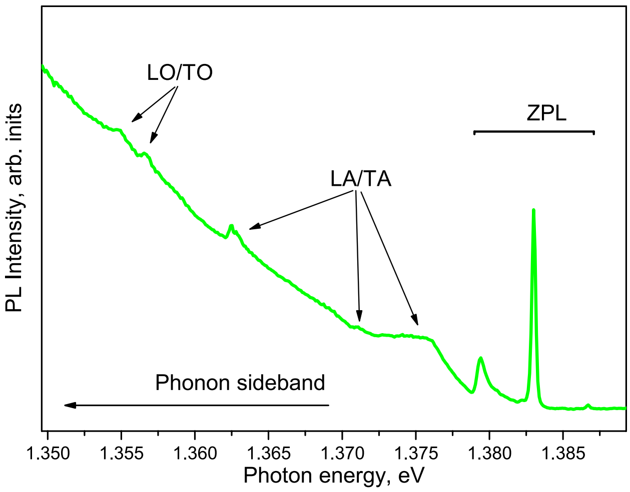

Fig. 3. Fine structure of the emission spectrum for crystal ZnSe:Fe in the zero-phonon line (ZPL) transition region $^3T_1(^3H) \to {}^5E(^5D)$ at a temperature of 5K. For PL excitation, radiation with a wavelength of 532 nm is used. LO/TO and LA/TA denote phonon replicas involving optical and acoustic phonons, respectively

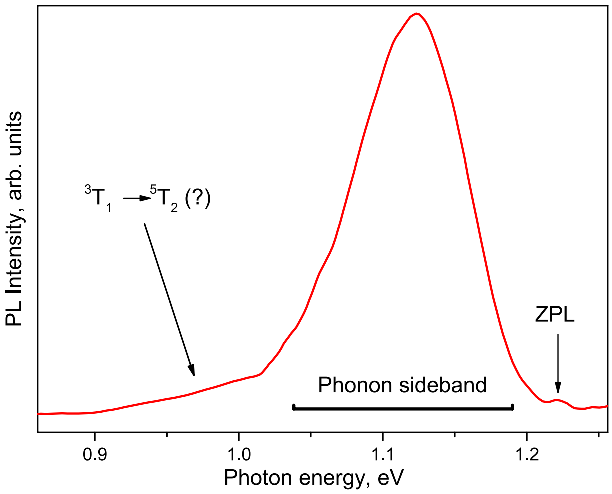

Fig. 4. Photoluminescence spectrum CdTe:Fe, recorded under pulsed excitation conditions at a temperature of 7 K. The delay relative to the end of the exciting laser pulse is 1.4 ms. The zero-phonon transition (ZPL) is located around 1.22 eV

spectral range may be overlapped by the emission of CdTe structural defects, see, for example, [31]; besides that, a contribution to the emission from iron ions in a different charge state is possible.

Unlike intra-center luminescence, conventional impurity-defect emission in semiconductors with a direct fundamental absorption edge is characterized by nano- or microsecond decay times. Therefore, to separate the luminescent background, we conducted time-resolved PL measurements. An example of an emission spectrum obtained at relatively long delay times of about 1.4 ms is shown in Fig. 4. It can be seen that this spectrum shows the main band with a maximum at 1.1 eV, a long-wavelength feature around 0.9 eV, and a weak short-wavelength component with a maximum at 1.22 eV. Based on the relatively long decay times, it can be stated that all these components represent intra-center PL.

To evaluate the nephelauxetic effect, as in the case of ZnSe:Fe, the spectral position of the zero-phonon transition (transitions) is of greatest interest. In the case of the PL spectrum in Fig. 4, the narrow component around 1.22 eV is obviously the main candidate for the zero- phonon transition. As in the case of ZnSe (Fig. 3), this line may have a fine structure that is not resolved in our experiments. To confirm this interpretation, we measured the luminescence kinetics of the 1.1 eV band and the narrow component at 7 K. The measurement results are illustrated in Fig. 5 (upper panel) (PL rise) and Fig. 5 (lower panel) (PL quenching). As can be seen in these figures, similar characteristics of signal rise and quenching are observed, which confirms that the narrow line at 1.22 eV and the broad band at 1.1 eV belong to the same luminescent system. Thus, it can be stated that the 1.22 eV peak is indeed a zero-phonon transition, and the 1.1 eV band arises from interaction with the phonon subsystem.

In CdTe crystals studied in this work, the presence of optically active iron ions Fe^{2+} is confirmed by intense luminescence corresponding to the transition $^5T_2(^5D) \to {}^5E(^5D)$, see Fig. 1. Nevertheless, Fe^{3+} ions could be a possible alternative candidate for the discussed luminescent system in CdTe. As estimates show (see Appendix), the first excited state for the ion is located around 2 eV. This is significantly higher than the spectral position of the bands in Fig. 4 (about 1.1-1.2 eV). Furthermore, in the experiments described above, we used optical excitation with quantum energy exceeding the fundamental absorption edge of CdTe. In this case, the exciting radiation is absorbed in a thin near-surface layer, and direct (intracenter) excitation of Fe^{3+} is unlikely due to the small cross-section value for the corresponding process. The most efficient excitation mechanism apparently consists of capturing a photoexcited electron by the Fe^{3+} ion and then relaxation into one of the excited states of

Table 1. Energy values of transitions observed in the experiment for ZnSe:Fe and CdTe:Fe (values given in cm^{-1})

	$^5T_2(^5D)\to{}^5E\ (^5D)$	$^3T_1(^3H)\to{}^5T_2(^5D)$	$^3T_1(^3H)\to{}^5E(^5D)$
ZnSe:Fe	2700-2950	7140	11155
CdTe:Fe	2197	6250	8695

the Fe^{2+} ion [21]. The Fe^{3+} ion in the CdTe lattice forms a Coulomb potential similar to a hydrogen-like donor in CdTe (properties of hydrogen-like donors in CdTe are described, in particular, in work [32]). Therefore, at helium temperatures, efficient electron capture should be expected with subsequent formation of weakly bound (hydrogen-like) states. At the same time, the Fe^{2+} ion does not form a long-range attractive potential for holes, so the process where a hole is captured by the Fe^{2+} ion with subsequent formation of the Fe^{3+} ion in anexcited state seems unlikely.

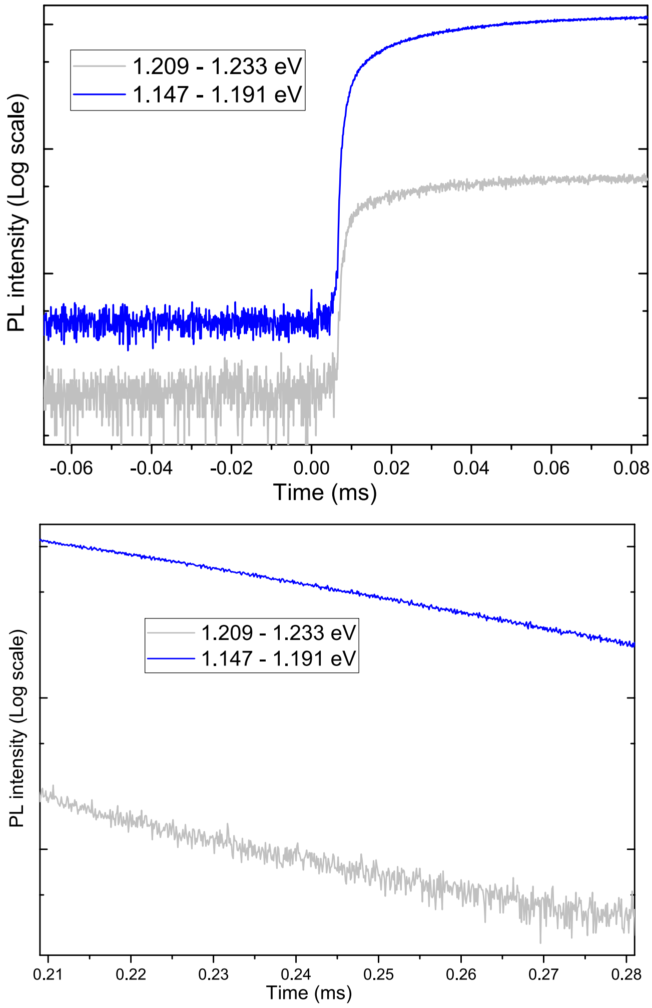

Fig. 5. The kinetics of rise (upper panel) and decay (lower panel) of the photoluminescence signal, recorded in two different spectral regions under excitation of the CdTe:Fe crystal with rectangular pulses. The first region (gray curves) corresponds to the zero-phonon (ZPL) transition in Fig. 4, the second region to a fragment of the broad band around 1.1 eV. Temperature 5 K, laser excitation wavelength 660 nm

The paper [30] mentions the emergence of new emission bands with maxima 1.13 and 1.03 eV, after implantation of iron in CdTe and subsequent annealing. iron in CdTe and subsequent annealing. In this work, an estimate of the of the radiation attenuation time of 30 μs, which allows us to conclude that these bands are related with intra-centre transitions of iron ions. However, no assumptions were made in [30] on the nature of the corresponding centre.

Thus, under experimental conditions, when excited above the fundamental absorption edge, one should expect intracentral luminescence specifically from ions Fe^{2+}. In this case, qualitative analysis based on Tanabe-Sugano diagrams allows unambiguous identification of the zero-phonon component at 1.22 eV and the 1.1 eV band with the transition $^3T_1(^3H) \to {}^5E(^5D)$. Therefore, from the spectroscopic data presented above, it follows that the transition $^3T_1(^3H) \to {}^5E(^5D)$ between the inner shells of the ion Fe^{2+} in ZnSe and CdTe forms similarly structured emission spectra, consisting of zero-phonon peak(s) and a broad band arising from interaction with the phonon subsystem. The spectral position of the zero-phonon peak (or center of gravity of the peak series) agrees with qualitative analysis within the framework of Tanabe-Sugano diagrams. Spectroscopic data on zero-phonon transitions involving states $^5T_2$ (^5D), ^5E (^5D), $^3T_1$ (^3H), obtained in this work and taken from works [28,31], are systematized in Table 1.

4. ROLE OF THE NEPHELAUXETIC EFFECT FE^{2+} IN CDTE AND CDTE

As follows from Fig. 2*a* and Table 1, in contrast to qualitative reasoning, quantitative analysis of spectroscopic data based on Tanabe-Sugano

Table 2. Energy values of transitions observed in the experiment for ZnSe:Fe and CdTe:Fe

	B, cm^{-1}	C, cm^{-1}	Dq, cm^{-1}	B_0, cm^{-1}	C_0, cm^{-1}	β_1
ZnSe:Fe	600(±15)	2733(±18)	300 [28]	917 [34]	4040 [34]	0.941
CdTe:Fe	500(±15)	2242(±29)	228 [28]	917 [34]	4040 [34]	0.778

diagrams for free ions Fe^{2+} encounters certain contradictions. The spectral position of zero-phonon lines for the transition corresponds to ^{5}T$_2$ (^{5}D) → ^{5}E (^{5}D) and thus characterizes the crystal field magnitude. As seen from Table 1, the crystal field magnitude in ZnSe is 20–25 % higher than in CdTe. From the Tanabe-Sugano diagram in Fig. 2*a*, it immediately follows that in CdTe the transition ^{3}T1(^{3}H) → ^{5}E(^{5}D) should shift to the short-wavelength region compared to ZnSe. At the same time, experimental data shows the opposite trend – the corresponding line demonstrates a pronounced long-wavelength shift. We assume that this discrepancy illustrates an increase in the nephelauxetic effect during the transition from ZnSe to CdTe. Note that if we accept the decrease in energy of the state ^{3}T$_1$ (^{3}H) relative to ^{5}E(^{5}D) and ^{5}T$_2$ (^{5}D) due to the nephelauxetic effect, then the observed band for CdTe in the region of 0.9 eV falls exactly in the area where the emission of transition ^{3}T$_1$(^{3}H) → ^{5}T$_2$(^{5}D) should be registered.

According to crystal field theory, calculations of energy level splitting values can be performed with the crystal field splitting parameter *Dq* (ligand field splitting) for the matrix material and parameters determining electron-electron interaction [33]. In calculations, Slater integrals are used F_i, which, due to the complexity of performing initio calculations for ions in a crystal matrix that give results with spectroscopic accuracy, usually remain theoretical parameters and are determined experimentally [33]. Racah introduced new notations for Slater integrals, which are convenient to use as semi-empirical parameters when solving the problem [33],

$$B = \frac{9F^2 - 5F^4}{441}, \tag{2}$$

$$C = \frac{5F^4}{63}. \tag{3}$$

As noted above, the parameter *Dq* determines the distance between the lower levels ^{5}E and ^{5}T$_2$ and therefore is unambiguously determined from experimental data. Parameters *B* and *C* for the free ion Fe^{2+} are given in reference books: $B_0 = 917$ cm^{-1}, $C_0 = 4040$ cm^{-1} [34]. When interpreting experimental data, phenomenological accounting for nephelauxetic effects can be accomplished by using Racah parameters *B* and *C*, whose values differ from those for free ions. In fact, this corresponds to an effective reduction in electron-electron repulsion. For an ion in the lattice, these parameters can also be calculated *ab initio* and are therefore convenient in developing and adapting rather complex modern theories.

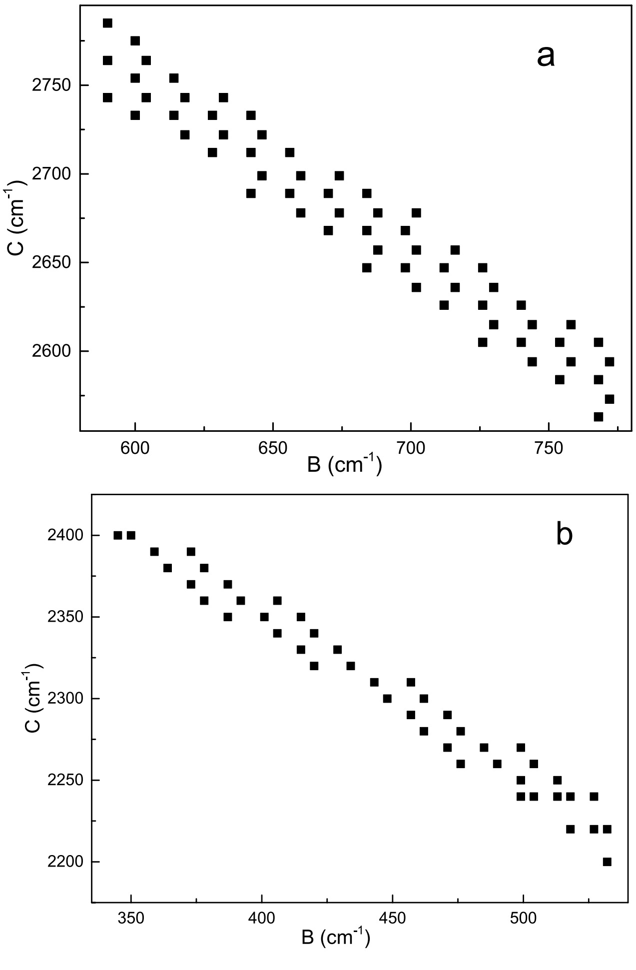

Fig. 6. Range of parameter values *B* and *C* , at which the desired value of 1.383 eV for level ^{3}T$_1$ ZnSe:Fe (*a*) and 1.078 eV for level ^{3}T$_1$ CdTe:Fe (*b*)

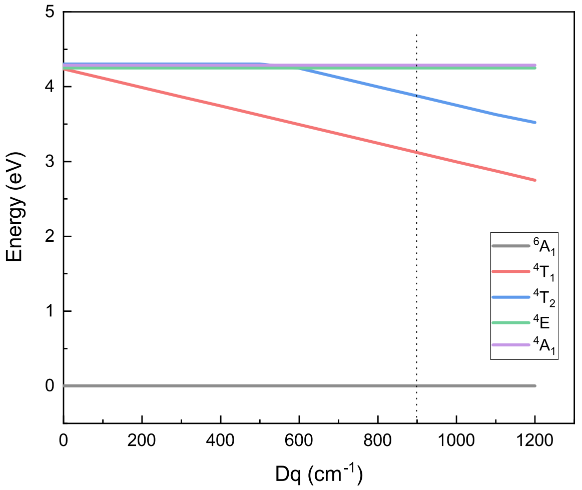

Fig. 7. Calculated dependence of energy splitting values in a tetrahedral crystal field on the field magnitude for ions Fe^{3+} (d^5). The dashed line shows the approximate position of the crystal field for the CdTe matrix

Our experimental data allowed us to refine the parameter values B and C for the ion Fe^{2+}, embedded in ZnSe and CdTe lattices. Fig. 6 shows the spread of acceptable parameter values B and C for our task, which give an energy shift between $^5E(^5D)$ and $^3T_1(^3H)$ of approximately 1.383 eV in ZnSe (Fig. 3) and approximately 1.078 eV in CdTe. As can be seen, the range of suitable value pairs in the case of ZnSe: $C = 2550 - 2800$ cm^{-1}, $B = 590 - 783$ cm^{-1}. These values were chosen according to the rule (pattern) of ratio $C/B = 4 - 4.5$ [26].

Furthermore, for iron group ions, a more significant decrease in parameter B than parameter C is expected, relative to free ion values. Consequently, as optimal parameters, one can choose $B = 600$ cm^{-1} (±15) and $C = 2733$ cm^{-1} (±18). The crystal field splitting magnitude $Dq = 228$ cm^{-1} cm in CdTe is somewhat lower than in ZnSe (see Table 1), due to differences in lattice parameters determining the crystal field magnitude, such as the ionic bond fraction. The range of suitable value pairs for Fe^{2+} in CdTe also differs from the free ion: $C = 2220 - 2280$ cm^{-1}, $B = 476 - 518$ cm^{-1} (Fig. 2*b*). We chose the average suitable Racah parameters and for the ion in CdTe: $B = 500$ (±18) cm^{-1}, $C = 2242$ (±29) cm^{-1}.

The determined Racah parameters (B, C) allowed us to further calculate the nephelauxetic effect magnitude, describing the degree of bond rigidity weakening in the ion (transition from ionic to covalent bonds). This effect (cloud expansion effect), most significant for *d*-transition elements, was very consistently considered by Jorgensen [8]. For these ions, there is an increase in *d*-orbital size due to their screening by lone electron pairs of ligands. The increase in nephelauxetic effect approximately corresponds to the growth of ligand-metal bond covalency.

As noted in the Introduction, several modified approaches to evaluating the nephelauxetic effect have recently emerged β_1 [7]. From relation (1), it follows that in ZnSe β_1(ZnSe)=0.941 (±0.04). A similar calculation for CdTe:Fe gives significantly lower values, indicating some weakening of the covalent bond: β_1(CdTe)= 0.778 (±0.08). All obtained parameters are shown in Table 2.

It should be noted that the increased role of the nephelauxetic effect in the case of the CdTe matrix is generally expected, as the higher value of Dq places ZnSe further right in the spectrochemical series of ligands [35], and the nephelauxetic effect typically manifests more strongly for weaker ligands [12]. However, this relationship is rather crude and often breaks down (see, for example, [36] and references therein), which is one manifestation of crystal field theory violations. A correct description of the nephelauxetic effect requires consideration of several factors, such as the influence of a specific ion's electron shell on the ligand electron shell, the dependence of the effect on the distance from the center to the ligand, as well as the role of dynamic and static correlation of electronic motion. To solve this problem, initio ligand field theory (*ab initio* ligand field theory, AILFT) [13] has been actively developed in recent years, combining ligand field theory methodology [14] and high-precision quantum chemistry methods that account for the multi-reference nature of electron wave functions involved in ion-ligand bonding, as well as dynamic correlation of ion and ligand electron motion. To the authors' knowledge, due to the complexity of the studied systems, such calculations for them are currently absent in the literature. Thus, the results obtained in this work can also serve to determine the accuracy and further development of modern theoretical approaches in the physics and chemistry of transition metal ions embedded in crystal matrices.

5. CONCLUSION

Thus, at helium temperatures, emission lines corresponding to transitions and $^3T_1$ (^5D) → ^5E (^5D) and $^3T_1$ (^5D) → $^5T_2$ (^5D) of the ion Fe^{2+} in the CdTe matrix were recorded. Taking into account the availability of comprehensive experimental data on the fine structure of the transition $^5T_2$ (^5D) → ^5E (^5D), this made it possible to conduct a comparative analysis of the nephelauxetic effect in the formation of the electronic spectrum of ions Fe^{2+} in CdTe and ZnSe matrices. These matrices have the same lattice type but differ in lattice constant value, crystal field magnitude, and the role of multi-electron corrections.

Calculations within the crystal field theory, based on the obtained experimental data and recent results from work [28], allowed to refine the semi-empirical Racah parameters for ions Fe^{2+} both in ZnSe — $B = 600\ \text{cm}^{-1}$, $C = 2733\ \text{cm}^{-1}$, and in CdTe — $B = 500\ \text{cm}^{-1}$, $C = 2242\ \text{cm}^{-1}$, as well as the magnitude of the nephelauxetic effect $\beta_1 = 0.941$ for ions Fe^{2+} in ZnSe and $\beta_1 = 0.778$ for Fe^{2+} in CdTe. We attribute the observed significant increase in the nephelauxetic effect in CdTe to the fact that in the case of ZnSe, the bond is more ionic in nature, which is expressed in a larger value of Dq. The tendency of the cubic CdTe matrix to form covalent bonds indicates that for ions placed in this matrix, one can expect more pronounced spectral effects related to the influence of multi-electron correlations. The obtained data, besides the possibility of direct use for quantitative description of the spectral properties of the studied centers, can serve to evaluate the accuracy of currently developing high- precision methods for describing the electronic properties of transition metal ions embedded in crystalline matrices.

FUNDING

This work was supported by the Russian Science Foundation under project No. 19- 79-30086.

APPENDIX. TANABE–SUGANO DIAGRAM FOR Fe^{3+} ION

In calculations, we used the values $B = 1015\ \text{cm}^{-1}$ and $C = 4800\ \text{cm}^{-1}$. The crystal field splitting parameter for CdTe varies in the range 800–900 cm^{-1}. The calculation results are shown in Fig. 7. As follows from the diagram, the possible levels $^4T_1$ and $^4T_2$ lie significantly higher in energy ($^4T_1$ ~ 3.1 eV and $^4T_2$ ~ 4 eV), than the experimental values obtained and the results of similar calculations for Fe^{2+} ions presented in the main text of the work. Thus, we exclude the possibility of intracenter radiative transitions in Fe^{3+} in the luminescence spectra of the studied samples.

REFERENCES

1. A. E. Dormidonov, K. N. Firsov, E. M. Gavrishchuk et al., Appl. Phys. B 122, 211 (2016).
2. Y. Wang, T. T. Fernandez, N. Coluccelli et al., Opt. Express, 25, 25193 (2017).
3. S. Mirov, V. Fedorov, I. Moskalev et al., Journal of Luminescence, 133, 268 (2013).
4. J. Cook, M. Chazot, A. Kostogiannes et al., Opt. Mater. Express 12, 1555 (2022).
5. Y. Luo, M. Yin, L. Chen et al., Opt. Mater. Express 11, 2744 (2021).
6. A. I.Belogorokhov, M. I. Kulakov, V. A. Kremerman et al., Sov. Phys. JETP 67, 1184 (1988).
7. M. N. Sarychev, I. V. Zhevstovskikh, Yu. V. Korostelin, et al., JETP 163, 96 (2023).
8. A. M. Vorotynov, A. I. Pankrats, M. I. Kolkov, JETP 160, 670 (2021).
9. S. B. Mirov, I. S. Moskalev, S. Vasilyev et al., IEEE Journal of Selected Topics in Quantum Electronics 24, 1 (2018).
10. J. Shee, M. Loipersberger, D. Hait et al., J. Chem. Phys. 154, 194109 (2021).
11. K. Li, H. Lian, R. Van Deun et al., Dyes and Pigments 162, 214 (2019).
12. Chr. K. Jurgensen, Progress in Inorganic Chemistry 4, 73 (1962).
13. Molecular Electronic Structures of Transition Metal Complexes II. Structure and Bonding, ed. by D. Mingos, P. Day and J. Dahl, Springer, Berlin (2011).
14. B. N. Figgis and M. A. Hitchman, Ligand field theory and its applications, Wiley–VCH, New York (2000).
15. L. Lang, M. Atanasov and F. Neese, J. Phys. Chem. A 124, 1025 (2020).
16. E.-L. Andreici Etimie, N. M. Avram, and M. G. Brik, Opt. Mater.: X 16, 100188 (2022).
17. A. Suchocki, S. W. Biernacki, A. Kaminska et al., J. Lumin. 102-103, 571(2003).
18. K. P. O’Donnell, K. M. Lee, and G. D. Watkins, J.Phys.C: Solid State Phys. 16, 723 (1983).
19. J. W. Evans, T. R. Harris, B. R. Reddy et al., J. Lumin. 188, 541 (2017).

20. G. Roussos, H.-J. Schulz, M. Thiede, J. Lumin. 31-32, 409 (1984).

21. V. V. Fedorov, S. B. Mirov, A. Gallian et al., IEEE J. Quant. Electr. 42, 907 (2006).

22. A. Salem, E. Saion, N. Al-Hada et al., Appl. Sci. 6, 278 (2016).

23. E. E. Vogel, O. Mualin, M. A. de Orue et al., Physical Review B 50, 5231 (1994).

24. S. B. Mirov, V. V. Fedorov, D. Martyshkin et al., IEEE J. Selected Topics in Quan. Electron. 21, 1601719 (2015).

25. R. I. Avetisov, S. S. Balabanov, K. N. Firsov et al., J. Crystal Growth 491, 36 (2018).

26. A. Gladilin, S. Chentsov, O. Uvarov et al., J. Appl. Phys. 126, 015702 (2019).

27. M. P. Frolov, Yu. V. Korostelin, V. I. Kozlovsky, Ya. K. Skasyrsky, Opt. Lett. 44, 5453 (2019).

28. V. S. Krivobok, D. F. Aminev, E. E. Onishchenko et al., JETP Lett. 117, 344 (2023).

29. J. Peppers, V. V. Fedorov, and S.B. Mirov, Opt. Express 23, 4406 (2015).

30. R. Kernocker, K. Lischka, L. Palmetshofer et al., J. Crystal Growth 86, 625 (1988).

31. D. F. Aminev, A. A. Pruchkina, V. S. Krivobok et al., Opt. Mat. Express 11, 210 (2021).

32. V. S. Bagaev, V. S. Krivobok, E. E. Onishchenko et al., JETP 140, 929 (2011).

33. S. Sugano, Y. Tanabe, and H. Kamimura, Multiplets of Transition-Metal Ions in Crystals, Academic Press, New York (1970).

34. Y. Tanabe, S. Sugano, Journal of the Physical Society of Japan 9, 753 (1954).

35. C. E. Housecroft, A. G. Sharpe, Inorganic Chemistry (4th ed.), Prentice Hall, Hoboken (2012).

36. A. L. Tchougreff and R. Dronskowski, International Journal of Quantum Chemistry 109, 2606 (2009).

JOURNAL OF EXPERIMENTAL AND THEORETICAL PHYSICS, 2024, Vol. 165, No. 6, pp. 776–784

ATOMS, MOLECULES, OPTICS

COMPARISON OF ELECTRON EMISSION IN LINEARLY AND CIRCULARLY POLARIZED GAUSSIAN FIELDS

© 2024 **A. V. Borovskiy**[a], **A. L. Galkin**[b*]
[a] *Baikal State University 664003, Irkutsk, Russia*
[b] *Prokhorov General Physics Institute, Russian Academy of Sciences, 119991, Moscow, Russia*
**e-mail: galkin@kapella.gpi.ru*

Received September 11, 2023
Revised January 23, 2024
Accepted January 23, 2024

Abstract. A comparative analysis of electromagnetic emission by an electron in Gaussian fields of linear and circular polarization was carried out. For a short laser pulse, local (power in solid angle and power) and integral (energy emitted from the trajectory) characteristics of emission are determined. It is shown that the previously discovered law of growth of the emitted peak angular power in a linearly polarized field also extends to the case of a circularly polarized field with a decrease in the numerical coefficient by a factor of 2 due to a decrease in the field amplitude by a factor of √2. During backscattering in both considered cases of linear and circular polarization, the emission characteristics have a power-law increase with indices 6 (peak power per solid angle) and 4 (power, radiated energy) in terms of the initial electron energy and significantly exceed the values of the radiation characteristics from symmetric trajectories.

An estimate of the radiated angular power in the direction of the motion speed is obtained.

Keywords: *UV and soft-X-ray generation, emitted electromagnetic field, radiation reaction force, residual electron oscillation energy, integral emission energy*

DOI: 10.31857/S004445102406e026

1. INTRODUCTION

A charged particle experiences maximum impact from the electromagnetic field in the vicinity of the laser pulse focus. As a result, the electron radiation spectrum can reach X-ray and gamma ranges [1]. The study of radiation generation has both applied and fundamental significance. Radiation sources with prediction of peak intensity values and radiation power distribution are of interest in biomedicine and atomic physics [2,3]. Applied task formulations are based on the initial position of a "stationary" electron directly in the laser pulse focus, which leads to radiation in the form of classical Thomson scattering with "forward-backward" symmetry. The radiation of an electron that acquires kinetic energy due to interaction with the field is interpreted as nonlinear Thomson scattering. In the case of electron counter-propagation relative to the laser pulse, electron radiation also fits into the scheme of nonlinear Thomson scattering.

From a fundamental perspective, obtaining maximum radiation characteristics is of interest, as well as establishing radiation features in connection with the possibility of radiation-dominant regime emergence [4–5]. A notable contribution of radiation friction is noted in works [6–8].

Various aspects of nonlinear Thomson scattering are considered in works [9–11]. The development of methods for calculating radiation power, alternative to the relativistic Larmor formula [12], is relevant. Thus, in work [13], a methodology for constructing electron radiation diagrams is proposed, which also allows determining the directionally integrated radiation power. A power-law growth with an exponent of 6 for the angular power of backscattering in a linearly polarized laser field with respect to the initial electron kinetic energy was discovered [14].

The aim of this work is a comparative analysis of electron radiation in laser fields of linear and circular polarization.

2. MODELS OF FOCUSED LASER FIELD

When choosing a focused laser field model, one is usually guided by the criterion of accuracy in correspondence with Maxwell's equations. The second important criterion is the consistency of theory with experiment. The complexity of model implementation should also be considered. Let's evaluate the models according to these criteria.

The model of transverse fields with a flat phase front and inhomogeneous transverse distribution does not satisfy Maxwell's equations [15]. It was used, for example, in works [6–8]. In general, it does not describe the axially symmetric ejection of ionization electrons from the interaction region with a linearly polarized laser field observed in experiments. It describes ejection along the polarization direction, which according to existing understanding is not important for the problems solved in works [6–8].

The model of Gaussian beams with transverse-longitudinal field components, due to accounting for the phase front tilt, is a solution to the parabolic equation — an approximation of the wave equation — a direct consequence of Maxwell's equations in vacuum, i.e., it is an approximate solution to Maxwell's equations [18]. There are many solutions in the form of Gauss–Laguerre fields. The fundamental Gauss–Laguerre mode has an exponentially decreasing transverse inhomogeneity from the axis. This field distribution satisfies the criterion of axial symmetry for electron ejection from the interaction region. The applicability conditions for this approximation are as follows:

$$\varepsilon = \frac{1}{kp_0}, \quad d = \frac{1}{kL}, \ \varepsilon^2 \ll 1, \delta \ll 1.$$

Here ρ_0 is the transverse waist size of the laser pulse at half-height in the focal plane, L is the longitudinal size of the laser pulse, k is the wave number of laser radiation. The coefficient ε^2 appears in the wave equation for the complex amplitude of the vector potential. Note that both conditions are obtained when applying the method of variable separation to the wave equation and are less burdensome than in other works. The first condition limits the focal spot size from below. The second condition limits the envelope application since $L = c\tau$, τ is the pulse duration, c is the speed of light.

2.1. Field Models Based on Exact Solution of Maxwell's Equations

Maxwell's equations in vacuum reduce to the wave equation for vector potential, which should be solved with boundary conditions on the focusing lens surface. The solution of the linear wave equation with boundary conditions can be obtained through variable separation methods, reduction to Kirchhoff's integral, and Fourier–Laplace transformation. The paper [19] presents some exact solutions of Maxwell's equations describing time-stationary focused laser pulses. In particular, the electric-type laser pulse with transverse electric field and transverse-longitudinal magnetic field differs from the fundamental Gauss–Laguerre mode. As it approaches the diffraction limit, the solution transitions into a Gaussian beam-type field distribution, representing a complex combination of Gauss–Laguerre modes. The model was applied [20] to interpret experiments with asymmetric electron acceleration [21]. We should also note the construction of sharply focused fields using the generalized Kirchhoff integral [18].

Thus, when considering laser fields with focusing not reaching the diffraction limit, the most suitable are the fields of the fundamental Gauss–Laguerre mode — Gaussian beam. In this article $k\rho_0 = 26.7, kL = 10$. Therefore, the Gaussian beam approximation is adequate. In terms of model implementation complexity, the computation volume in this work exceeds that of [14] by an order of magnitude. Increasing the pulse duration would lead to an inefficient increase in computation volume at distances far from the focus.

The vector potential of a Gaussian beam laser field propagating along the axis in the vicinity of the focus can be represented as

$$A = A_0 \cos\sigma \exp\left(-\frac{1}{2}\rho^2\cos^2\sigma\right) \times$$
$$\times\left(e_x\sqrt{\frac{1+\alpha}{2}}\cos\varphi_{ph} + e_y\sqrt{\frac{1-\alpha}{2}}\sin\varphi_{ph}\right), \quad (1)$$

where A_0 and φ_{ph} — are amplitude and phase,

$$\varphi_{ph} = \omega t - kz + \sigma - \frac{1}{4}\rho^2 \sin 2\sigma,$$

$$\cos^2\sigma = \frac{1}{1+(z/z_R)^2}, \qquad (2)$$

$$z_R = k\rho_0^2, \quad \rho = r/\rho_0,$$

r is the transverse coordinate, e_x, e_y are unit vectors. Linear polarization along x and y corresponds to values $\alpha = 1$ and $\alpha = -1$, circular — $\alpha = 0$, for other values in the interval $(-1,1)$ the polarization is elliptical. The peak intensity (time-averaged Poynting vector magnitude) is identical and is defined through the relativistic intensity

$$I_0 = \frac{c}{8\pi}(A_0k)^2 = \mu I_R,$$

$$I_R = \frac{m^2c^5\pi}{2e^2\lambda^2},$$

where m and e are the electron rest mass and charge. If μ, is given, then A_0 is determined. Fields in the general case of elliptical polarization are determined by components $(E_x, E_y, \delta E_z, H_x, H_y, \delta H_z)$, longitudinal components $\delta E_z, \delta H_z \approx \varepsilon = 1/k\rho_0$, (paper [22] considers expressions for fields with higher orders ε, but the advantage of such expansion is not discussed). As follows from expression (1), the amplitude of the main (transverse) field in the case of circular polarization ($\alpha = 0$) is $\sqrt{2}$ times smaller than the amplitude of linear polarization ($\alpha = \pm 1$), and the maximum amplitude of elliptical polarization has an intermediate value, so that for the numerical factors of these amplitudes, the inequalities

$$\frac{1}{\sqrt{2}} \le \sqrt{\frac{1}{2} + \frac{|\alpha|}{2}} \le 1.$$

hold. When transitioning from a Gaussian beam to a pulse also with a Gaussian time distribution, the field description should include a temporal envelope as a multiplier

$$\exp\left(-\left(\frac{t-(z-z_d)/c}{2\tau}\right)^2\right),$$

where τ is the pulse duration at half intensity, z_d is the initial distance from the temporal envelope maximum to the focal plane.

3. ELECTRON MOTION TRAJECTORIES IN GAUSSIAN FIELDS OF DIFFERENT POLARIZATION

Solutions of the Lorentz equation with initial conditions and the complete set of field components $(E_x, E_y, \delta E_z, H_x, H_y, \delta H_z)$,

$$m\frac{d}{dt}\left(\frac{\frac{dr}{dt}}{\sqrt{1-\left(\frac{v}{c}\right)^2}}\right) = -eE - \frac{e}{c}\frac{dr}{dt} \times H, \qquad (3)$$

$$r(0) = r_0, \quad v(0) = v_0,$$

allow determining the electron motion trajectory, as well as instantaneous values of velocity components v and acceleration v'.

The standard problem (3) of three nonlinear second-order differential equations is numerically solved using Wolfram Mathematica package, but requires decomposition of relativistic nonlinearity (it is necessary to expand all derivatives component-wise and reduce to normal form with isolation of higher derivatives, which explains the notation (3)). Testing is performed by constructing symmetric trajectories: the electron initially rests on the pulse axis before the focus and after interaction with the pulse stops at the same distance beyond the focus. Selection of initial conditions ensures compensation of the dynamic impact when the field is turned on. Calculation of the motion of an initially resting electron, displaced from the axis, in the field of a Gaussian pulse of the fundamental mode leads to symmetric ejection from the interaction region.

A short pulse $\tau c/\lambda = 1.5$, corresponding to a duration of 3.5 fs is considered. Figure 1 shows symmetric trajectories of electron motion in fields with parameters $\rho_0 = 26.7, \tau c/\lambda = 1.5, \mu = 5$ (waist size, temporal envelope length in oscillation periods, and peak intensity μ relative to relativistic) of different polarization $\alpha = 0(a), 1(b), -1(c)$. Initial data for problem (3):

$$x_0/\lambda = 0, y_0/\lambda = 0, z_0/\lambda = -1.2,$$

$$v_{0x}/c = 10^{-18}, v_{0y}/c = 5\cdot 10^{-10}, v_{0z}/c = 10^{-18}.$$

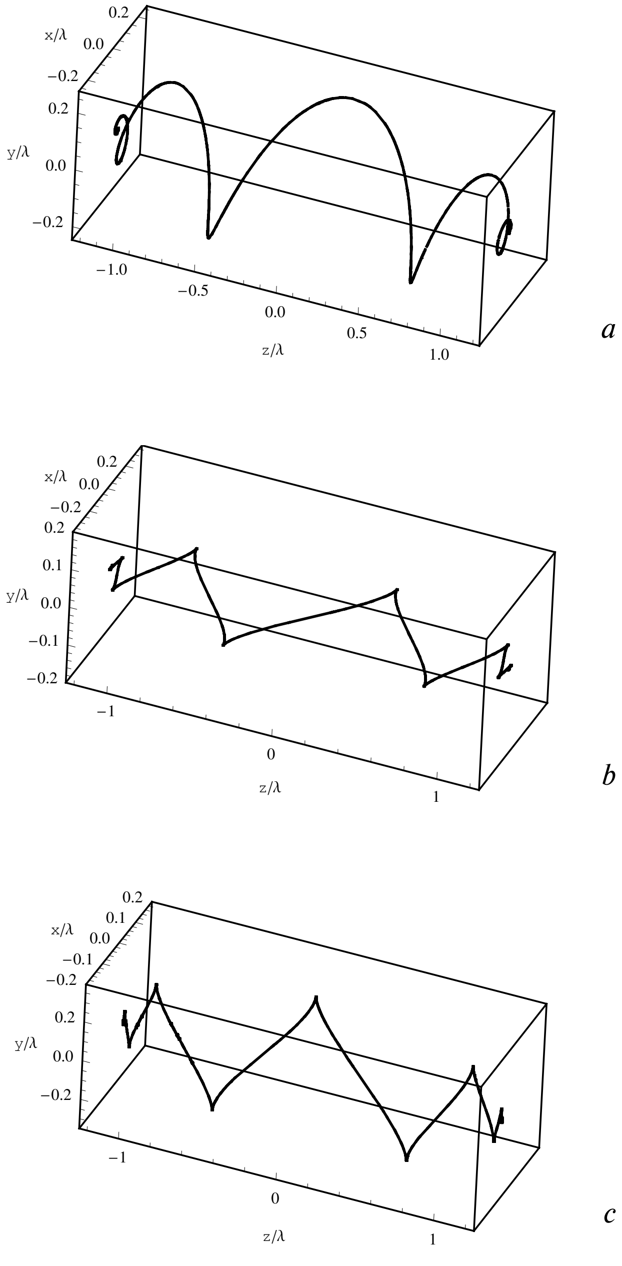

Fig. 1. Symmetric electron trajectories at μ = 5, τ*c* / λ = 1.5, α = 0 (*a*), 1 (*b*), −1 (*c*)

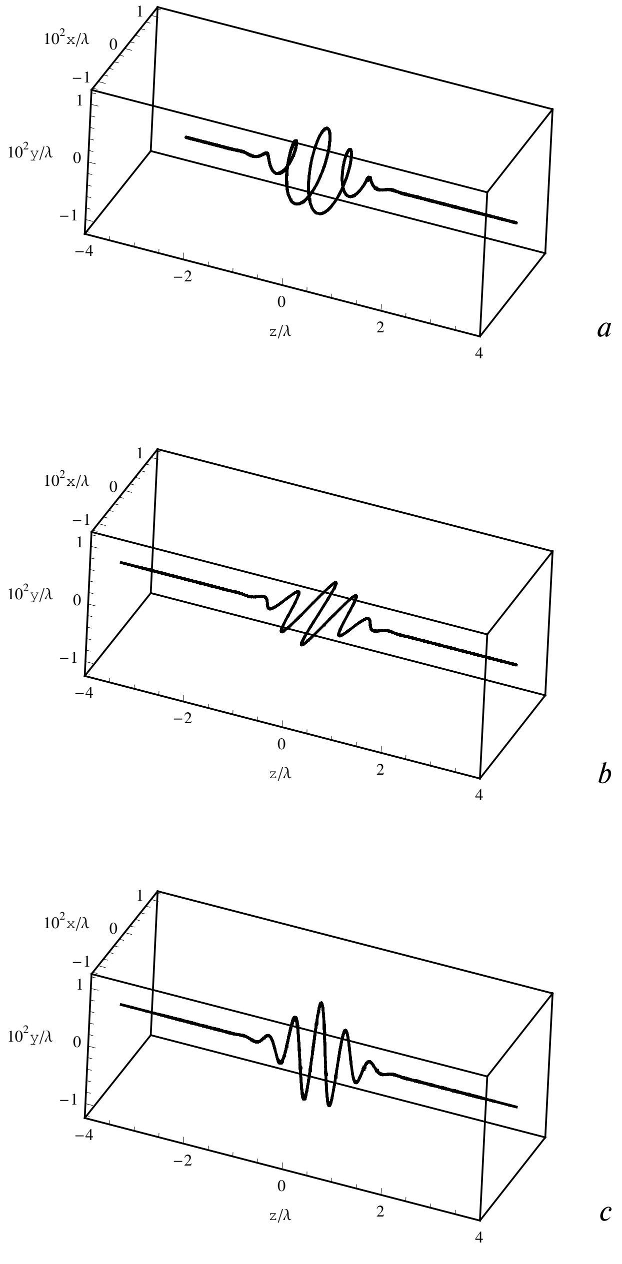

Fig. 2. Trajectories of electron motion with initial kinetic energy $p = 20$ towards the laser pulse with parameters $k_{\rho 0} = 26.7$, τ*c* / λ = 1.5, μ = 5 of different polarization α = 0 (*a*), 1 (*b*), −1 (*c*)

Trajectories α = 1 (Fig. 1*b*), α = −1 (Fig. 1*c*) do not coincide when rotated around axis *z* by angle π / 2 , as the acting fields (1) are phase-shifted. For an electron moving towards the laser pulse, the initial velocity is related to the initial kinetic energy

$$\frac{W_{k_0}}{mc^2} = \frac{1}{\sqrt{1-(v_{0z}/c)^2}} - 1 = p.$$

Since symmetric trajectories, besides the test value, describe the maximum radiation energy compared to all trajectories of an initially resting electron (not only on the axis) at fixed laser pulse parameters, we will further assume that motion along symmetric trajectories corresponds to the case $p = 0$. For $p > 0$ we assume that the electron passes near the focus at the moment of the temporal envelope maximum. This corresponds to a change in

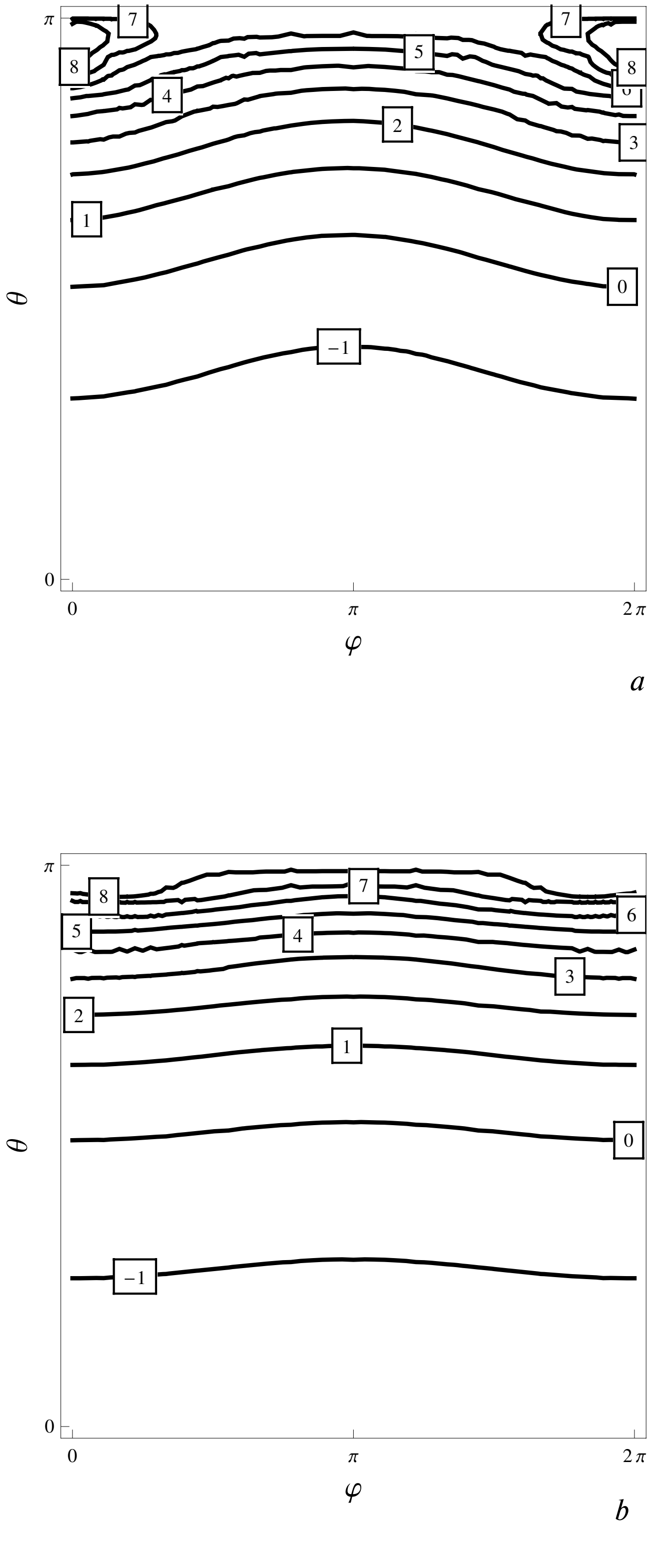

Fig. 3. Level lines $\lg\left[I_1^{-1}dI / d\Omega(\varphi,\theta)\right]$ of electron radiation with initial kinetic energy $p = 10$ towards the laser pulse with parameters $k_{\rho 0} = 26.7$, $\tau c / \lambda = 1.5$, $\mu = 5$ of different polarization $\alpha = 0$ (*a*), 1 (*b*)

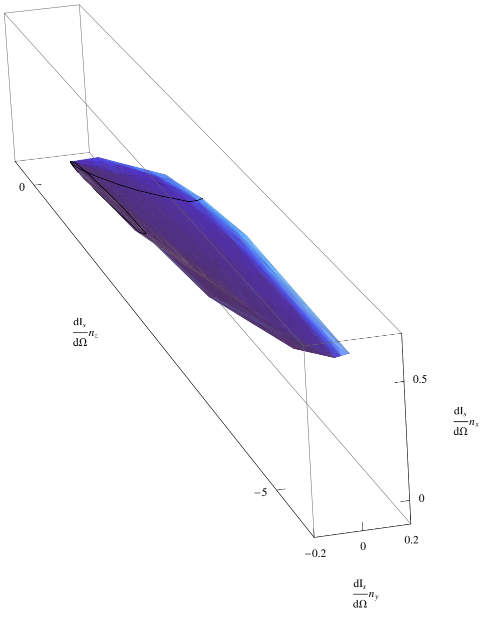

Fig. 4. Radiation pattern of the electron, built according to the distribution in Fig Figure 3*a* ($p = 10$, $\alpha = 0$)

initial conditions $z_0 = v_{0z}(p)z_d / c, v_{0z} = v_{0z}(p)$ — the magnitude of the counter velocity determined by p. Fig. 2 shows electron motion trajectories in fields with parameters $k\rho_0 = 26.7, \tau c / \lambda = 1.5, \mu = 5$ of different polarization $\alpha = 0,1,-1$ and with initial kinetic energy $p = 20$ (electron moves in the direction of decreasing coordinate z). Since $z_\text{d} = 6\lambda$, and $v_{0z}(20) / c = 0.998866$, initial conditions $z_0 / \lambda = 6, v_{0z} / c = -0.998866$, others as for symmetric trajectories.

4. ELECTRON RADIATION IN GAUSSIAN FIELDS

Electron motion occurs under the action of the Lorentz force, while the electron emits electromagnetic pulses. In the radiation model based on Lienard-Wiechert potentials, the electron emits field

$$\mathbf{E}_{rad} = e\frac{1 - v^2 / c^2}{(R - \mathbf{R}\cdot\mathbf{v} / c)^3}\left(\mathbf{R} - \frac{\mathbf{v}}{c}R\right) + \\ + \frac{e}{c^2(R - \mathbf{R}\cdot\mathbf{v} / c)^3}\left[\mathbf{R} \times \left[\left(\mathbf{R} - \frac{\mathbf{v}}{c}R\right) \times \mathbf{v}'\right]\right], \quad (4)$$

$$t_r + \frac{R(t_r)}{\mathbf{c}} = t.$$

For $\mathbf{R} = R\mathbf{n}$, $R \sim 10^4\,\lambda$ we have

$$\mathbf{E}_{rad} = e\frac{1 - v^2 / c^2}{R^2(1 - \mathbf{n}\cdot\mathbf{v} / c)^3}\left(\mathbf{n} - \frac{\mathbf{v}}{c}\right) +$$

$$+\frac{e}{c^2R(1 - \mathbf{n}\cdot\mathbf{v} / c)^3}[\mathbf{n}\times\left[\left(\mathbf{n} - \frac{\mathbf{v}}{c}\right)\times\mathbf{v}'\right]]. \quad (5)$$

The distribution of radiation power over the solid angle Ω in the direction *n* (hereinafter briefly referred to as intensity),

$$\mathbf{n} = (\sin\theta\cos\varphi, \sin\theta\sin\varphi, \cos\varphi),$$

focus has coordinates (0,0,0), θ — azimuthal angle from the focus relative to the axis *z*, φ — polar angle in the focal plane *xy*, is determined by the second (radiative) term in (4):

$$\frac{dI}{d\Omega} = \frac{\mathbf{1}}{4\pi}\frac{e^2}{c^3(1 - \mathbf{n}\cdot\mathbf{v} / c)^6}\,|\,\mathbf{n}\times\left[\left(\mathbf{n} - \frac{\mathbf{v}}{\tilde{n}}\right)\times\mathbf{v}'\right]|^{\mathbf{2}}. \quad (6)$$

To construct the radiation directivity pattern in the Lienard–Wiechert model, it is necessary to calculate the distribution $dI / d\Omega(\varphi,\theta)$ and construct the surface $ndI / d\Omega$. Integration of expression (6) over the solid angle gives the power radiated by the electron at a given moment of time. Normalization of radiation patterns $\mathbf{n}dI / d\Omega$ in the Lienard–Wiechert model is performed by the value

$$I_1 = \frac{\mathbf{2}}{3}\frac{e^2}{\lambda}\frac{\mathbf{1}}{\lambda / c}.$$

Determination of the maximum value of radiated power into the solid angle, $dI / d\Omega$, consists in conducting optimization calculations. A methodology has been developed [23]; the task is non-standard; the program is implemented in Fortran. Fig. 3 shows the level lines of distributions $\lg\left[I_1^{-1}dI / d\Omega(\varphi,\theta)\right]$ of maximum-in-time radiation of the counter electron ($p = 10$) in the field of a laser pulse with parameters $k\rho_0 = 26.7, \tau c / \lambda = 1.5, \mu = 5$ for circular ($\alpha = 0$) and linear ($\alpha = 1$) polarizations. As follows from Fig. 3, in the case of linearly polarized field, backscattering occurs into a narrow cone in the vicinity of $\theta = \pi$ and is well described by expression

$$\frac{\mathbf{1}}{I_1}\frac{dI}{d\Omega}\Big|_{\theta=\pi} \cong$$

$$\cong 6\pi\mu(p + 1)^6\left[1 + \sqrt{1 - \frac{\mathbf{1}}{(p + 1)^2}}\right]^4. \quad (7)$$

In the case of circular polarization, the radiation solid angle is inclined due to electron motion in a circle in the focal plane and is concentrated in the vicinity of $\theta = 0.95\pi$. The electron radiation directivity pattern for this case $10^{-8} / I_1\,(\mathbf{n}dI / d\Omega)$ is shown in Fig. 4. Maximum angular power is the maximum longitudinal size of the pattern; main radiation goes into a cone; the cone is inclined.

To estimate the maximum radiation intensity without optimization, the following approach is proposed. The denominators of expression (4) are maximum at $\mathbf{n} \parallel \mathbf{v}$, i.e., we can set $\mathbf{n} = \mathbf{v} / v$, then

$$[\mathbf{n}\times\left[\left(\mathbf{n} - \frac{\mathbf{v}}{c}\right)\times\mathbf{v}'\right]] =$$

$$= (\left(\mathbf{n} - \frac{\mathbf{v}}{c}\right)(\mathbf{n}\cdot\mathbf{v}') - \mathbf{v}'\left(1 - \frac{\mathbf{n}\cdot\mathbf{v}}{c}\right)) \cong$$

$$\cong (\left(\frac{\mathbf{v}}{v} - \frac{\mathbf{v}}{c}\right)\left(\frac{\mathbf{v}}{v}\cdot\mathbf{v}'\right) - \mathbf{v}'\left(1 - \frac{v}{c}\right)) =$$

$$= \left(1 - \frac{v}{c}\right)\left(\frac{\mathbf{v}}{v^2}(\mathbf{v}\cdot\mathbf{v}') - \mathbf{v}'\right),$$

$$[\mathbf{n}\times\left[\left(\mathbf{n} - \frac{\mathbf{v}}{c}\right)\times\mathbf{v}'\right]]^2 \cong$$

$$\cong \left(1 - \frac{v}{c}\right)^2\left(\frac{(\mathbf{v}\cdot\mathbf{v}')^2}{v^2} + (\mathbf{v}')^2 - 2\frac{(\mathbf{v}\cdot\mathbf{v}')^2}{v^2}\right) =$$

$$= \left(1 - \frac{v}{c}\right)^2\left((\mathbf{v}')^2 - \frac{(\mathbf{v}\cdot\mathbf{v}')^2}{v^2}\right),$$

$$\max\left[\frac{dI}{d\Omega}\right] = \frac{cE_{rad}^2}{4\pi}R_0^2 =$$

$$= \frac{\boldsymbol{c}}{4\pi}R_0^2\frac{e^2}{c^4R_0^2(1 - v / c)^6}\left(1 - \frac{v}{c}\right)^2(\mathbf{v}')^2\sin^2(\underset{\wedge}{\mathbf{v}'\,\mathbf{v}}) =$$

$$= \frac{e^2(\mathbf{v}')^2\sin^2(\underset{\wedge}{\mathbf{v}'\,\mathbf{v}})}{4\pi c^3(1 - v / c)^4}. \quad (8)$$

To characterize the velocity of motion, we use kinetic energy W_k / mc^2. The time course of kinetic energy and acceleration modulus over time is shown in Fig. 5.

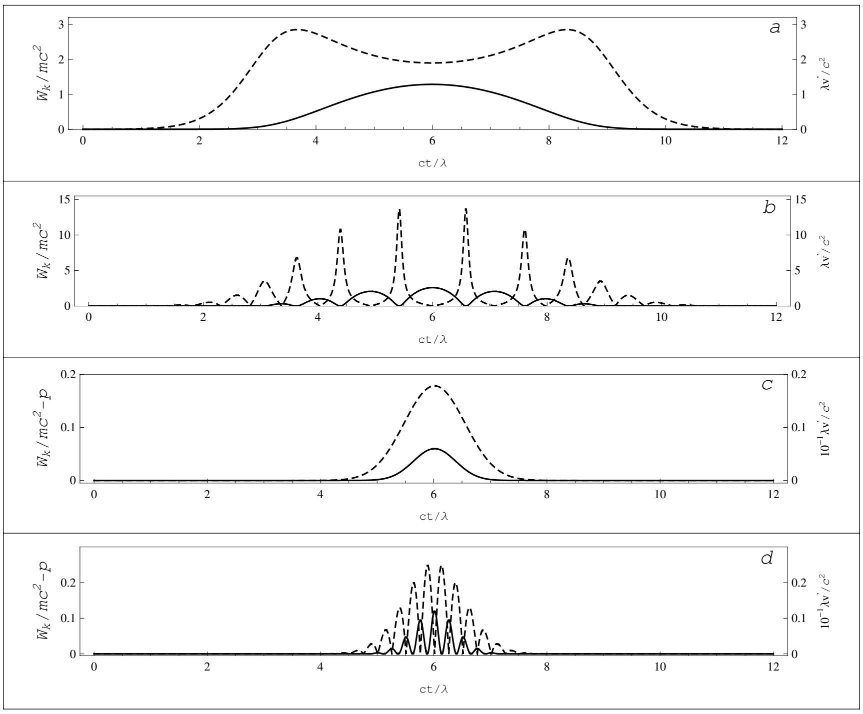

Fig. 5. Time course of kinetic energy W_k / mc^2 (solid curve) and acceleration modulus $|\mathbf{v}'|\lambda/c^2$ (dashed curve) of the electron moving along trajectories: $\alpha = 0, p = 0$ (*a*); $\alpha = 1, p = 0$ (*b*); $\alpha = 0, p = 10$ (*c*); $\alpha = 1, p = 10$ (*d*)

5. CALCULATION OF ELECTRON RADIATION CHARACTERISTICS IN GAUSSIAN FIELDS

The following characteristics are of interest.

1. Maximum power per solid angle, $\max[dI/d\Omega]$ normalized to I_1.

2. Radiation power

$$I = \int \frac{dI}{d\Omega} d\Omega$$

also normalized to I_1.

3. Radiated energy from the trajectory of motion

$$E = \int I dt$$

normalized to

$$E_1 = \frac{2}{3}\frac{e^2}{\lambda},$$

where for $\lambda = 800$ nm

$$E_1 \frac{1}{mc^2} = \frac{2}{3}\frac{e^2}{\lambda}\frac{1}{mc^2} \approx 2.35 \cdot 10^{-9}.$$

Figure 6*a* shows the temporal progression of electron radiation power during motion along symmetric trajectories in Fig. 1 for $\alpha = 0, 1, -1$. Radiation bursts with linear polarization sometimes exceed radiation power values with circular polarization, which is associated with higher acceleration values. The energy radiated from trajectories (integral of power over time) at $p = 0$, equals $E/E_1 = 1.83 \cdot 10^3$ ($\alpha = 0$); $1.01 \cdot 10^3$ ($\alpha = 1$); $1.02 \cdot 10^3$ ($\alpha = -1$).

In Fig. 6*b* shows the temporal progression of electron radiation power with initial kinetic energy $p = 20$ during motion along trajectories in Fig. 2 for ($\alpha = 0, 1, -1$). The energy radiated from trajectories at $p = 20$ increases by orders of magnitude and equalizes across polarizations: $E/E_1 = 1.03 \cdot 10^8$ ($\alpha = 0$); $1.08 \cdot 10^8$ ($\alpha = 1$); $1.10 \cdot 10^8$ ($\alpha = -1$).

Summary information on the dependence of radiation characteristics on initial kinetic energy is presented in Fig. 7. Calculated values are shown as points in black ($\alpha = 0$), blue ($\alpha = 1$) and red ($\alpha = -1$) colors. The upper curve 1 (a straight line in logarithmic scale) is the dependence (7); according to work [14], this curve contains the values of maximum angular radiation power in a linear polarization field, $\alpha = \pm 1$. Curve 2 is a dependence of type (7) with half the coefficient; this curve contains the values of maximum angular radiation power in a circular polarization field, $\alpha = 0$. On the approximation curve 3

$$\frac{I_{\max}}{I_1} \cong 64\pi\mu(p+1)^4$$

lie the values of maximum radiation power in a linear polarization field, $\alpha = \pm 1$. On the approximation curve 4

$$\frac{I_{\max}}{I_1} \cong 32\pi\mu(p+1)^4$$

lie the values of maximum radiation power in a circular polarization field, $\alpha = 0$.

The energy dependencies E/E_1, radiated from trajectories both in linear and circular polarization, $\alpha = 0, \pm 1$, in the considered logarithmic scale and with the used non- dimensionalization, coincide with high accuracy with the dependence $I_{\max}/I_1$ for $\alpha = 0$ and lie on the approximating curve 4.

6. DISCUSSION OF RESULTS

According to estimation (8), the intensity maximum can be achieved at the maximum of velocity and acceleration moduli, while $\sin^2(\mathbf{v}', \mathbf{v}) \approx 1$. The time coincidence of maxima occurs for $\alpha = 0$, $p > 0$ (Fig. 4*c*), in this case, approximation (8) works well. In the case of $\alpha = \pm 1$, $p = 0$ (Fig. 4*b*), there is a time separation of velocity and acceleration moduli maxima [14]. In the case of $\alpha = \pm 1$, $p > 0$ (Fig. 4*d*), backscattering occurs in the direction opposite to the z ($\theta = \pi$), axis, at the moment when the maximum of the modulus $v_{y'}$ and $v_z = v_{0z}$; is reached; under these assumptions, estimation (7) was obtained [14]. The agreement of calculations for circular polarization $\alpha = 0$, p > 0 with the approximating curve (with a coefficient reduced by 2 due to field amplitude reduction by √2 times) extends the limits of analytical applicability. At the direction of maximum intensity radiation has an inclination due to electron motion in a circle in the focal plane (see Fig. 3*a* and Fig. 4). Also, the dependencies of radiation power maxima differ by a factor of two for linear and circular polarization (dependencies *3*, *4* in Fig. 7).

Overall, the scattering process responds to instantaneous values of field intensity (Poynting vector modulus) without averaging over the wave period, therefore, the generalization of expression (7) for elliptically polarized field consists in adding the factor $1/2 + |\alpha|/2$. Thus, for an elliptically polarized field, an intermediate position should be expected between dependencies *1*, *2* for maximum power into solid angle and *3*, *4* for maximum radiation power with a change relative to characteristics at linear polarization by $1/2 + |\alpha|/2$ times.

In the field of linear polarization, $\alpha = \pm 1$, $p = 0$, radiation with sharp piecewise-linear symmetric trajectory (Fig. 1*b*, *c*) transforms into a smoothed temporal profile of radiation power (Fig. 3*a*) and, conversely, radiation from a smoothed trajectory $\alpha = \pm 1$, $p > 0$ at high values p (Fig, 2*b*, *c*) transforms into a sharp temporal profile of radiation power (Fig. 3*b*). On symmetric trajectories at $\alpha = 0$, $p = 0$ longitudinal and transverse velocity components are comparable, and at the moment of reaching the maximum velocity modulus lead to higher values of radiation power and energy emitted from the trajectory compared to the case $\alpha = 1$, $p = 0$, where there is temporal separation of velocity and acceleration moduli maxima. At large values, the difference in field amplitudes for $\alpha = \pm 1$, $p > 0$ and $\alpha = 0$, $p > 0$ leads to a twofold difference in maximum power values. Due to quasi-linear change in radiation power for $\alpha = \pm 1$, $p > 0$ during the wave period, the radiation energy from trajectories coincides with the emitted energy in the circular polarization field, $\alpha = 0$, $p > 0$, and normalization to E_1 leads to the coincidence of dependencies 4 in Fig. 7. This coincidence is accidental, since only the energy emitted from the trajectory increases with the laser pulse duration. The energy emitted from the trajectory increases as a power law, as $(p + 1)^4$, with increasing initial electron kinetic energy, reaching values of 0.132 MeV for $\lambda = 800$ nm in the considered range p and for the given pulse duration. Significantly higher values of emitted energy from the symmetric trajectory ($p = 0$) in the circular polarization field compared to radiation in the linear polarization field and the equalization of emitted energy by polarization at $p = 20$ can be explained by the decrease in electron orbit radius with increasing p. The question of

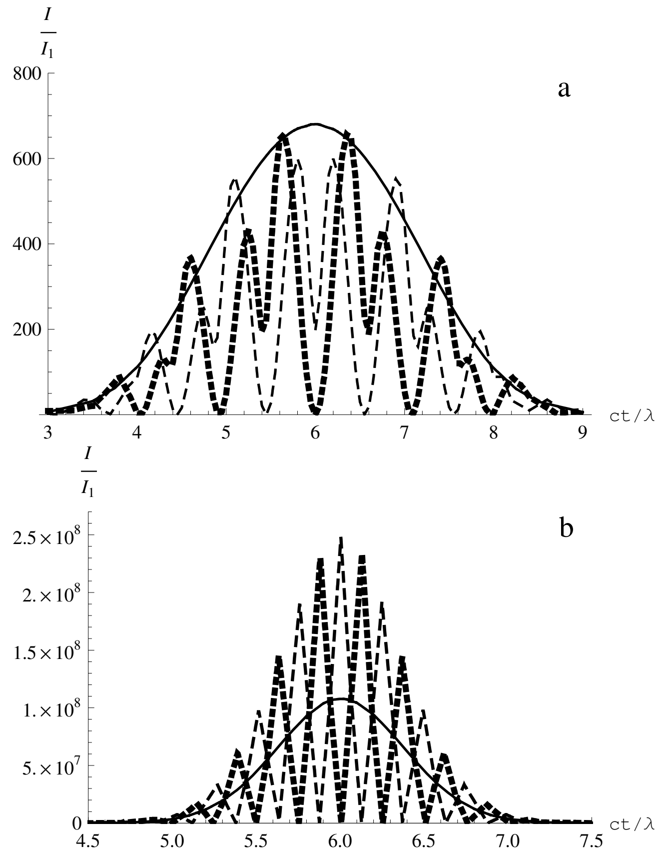

Fig. 6. Time evolution of electron radiation power during motion: *a* – along symmetric trajectories Fig. 1; *b* – with initial kinetic energy $p = 20$ along trajectories Fig. 2; $\alpha = 0$ (solid curves), $\alpha = 1$ (dashed curves), $\alpha = -1$ (dotted curves)

studying the dependence of electron orbit radius in the focal plane on gaussian pulse parameters of circular polarization and on electron energy is interesting for separate consideration.

7. CONCLUSIONS

A comparative analysis of electron radiation in Gaussian fields of linear and circular polarizations has been conducted. An estimate of the radiated power into the solid angle in the direction of motion velocity was obtained. Local (power into solid angle and power) and integral (energy radiated from trajectory) radiation characteristics were determined. During backscattering in a circularly polarized field, the direction of maximum intensity radiation is inclined due to electron motion in a circle in the focal plane, but due to the small radius, this does not lead to a difference in energy radiated from the trajectory compared to the case of linearly polarized field, as for symmetric trajectories. It is shown that the peak intensity growth law discovered in work [14] for linear polarization field extends to the case of circular polarization field. The numerical coefficient decreases by 2 times due to the decrease in field amplitude by $\sqrt{2}$ times. During backscattering in both considered cases of linear and circular polarizations, the radiation power and radiated energy grow as $(p + 1)^4$ with respect to the initial electron energy and significantly exceed the values of radiation characteristics from symmetric trajectories.

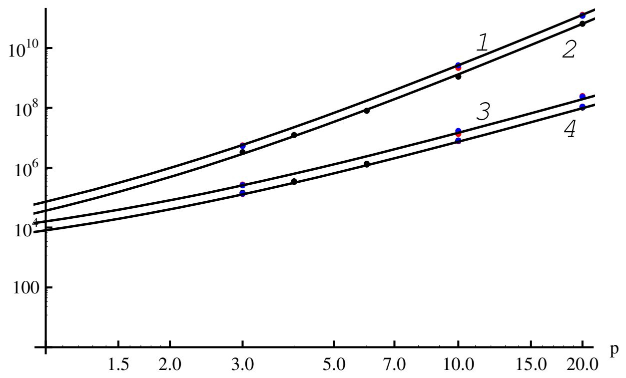

Fig. 7. Dependencies of radiation characteristics on initial kinetic energy *p*: maximum angular radiation power in linear polarization field $\alpha = \pm 1$ (curve 1); maximum angular radiation power in circular polarization field $\alpha = 0$ (curve 2); radiation power in linear polarization field $\alpha = \pm 1$ (curve 3); radiation power in circular polarization field $\alpha = 0$ and energy radiated from trajectories under linear and circular polarizations $\alpha = 0, \pm 1$ (curve 4)

ACKNOWLEDGMENTS

The authors thank M. V. Fedorov for pointing out the possibility of interpreting the results for elliptical polarization.

REFERENCES

1. A.L. Galkin, V.V. Korobkin, M. Yu.Romanovsky et al., Proc. of SPIE , 799319-1(2011).
2. A.Baltuška, Th.Udem, M.Uiberacker et al., Nature 421, 611 (2003).
3. K.Lee, Y.H.Cha, M.S.Shinet al.,Phys. Rev. E 6, 7 026502 (2003).
4. S.V.Bulanov, T. Zh.Esirkepov, J.Koga et al., Plasma Physics Reports 30, 3, 196 (2004).
5. A.V. Bashinov, A.A. Gonoskov, A.V. Kim et al., Quantum Electronics. 43, No. 4, 291 (2013).
6. A. Di Piazza, K. Z. Hatsagortsyan, C.H. Keitel, Phys. Rev. Lett.102, 254802 (2009).
7. A.L. Galkin JETP. 115, 2 ,201 (2012).
8. C.N. Harvey, Phys.Rev.Accel.Beams 21, 114001 (2018).

9. Ju Gao, Phys. Rev. Lett. 93, 243001 (2004).

10. P.A. Golovinskii, E.A. Mikhin, JETP 113,545 (2011).

11. Yifan Chang, Zishuai Cai, Yuting Shen et al., Laser Physics 32, 035302(2022).

12. V.V. Lidskii, Bull. Lebedev Phys. Inst. 36,2, 31 (2009).

13. A.V. Borovskiy, A.L.Galkin, Laser Phys. 32, 084008 (2022).

14. A.V. Borovskiy, A.L. Galkin, Laser Phys. Lett. 20, 036002 (2023).

15. B. Quesnel, P. Mora, Phys. Rev. E 58, 3719 (1998).

16. S. Banerjee, S. Sepke, R. Shah et al., Phys. Rev. Lett. 95, 035004 (2005).

17. A.V. Borovskiy, A.L. Galkin, M.P. Kalashnikov. Phys. of Plasmas. 22, 043107 (2015).

18. A.V. Borovskiy, A.L. Galkin, Selected Problems of Laser Physics. Vacuum Electron Acceleration. Focusing by a Parabolic Mirror. Diffraction on an Edge as a Problem of Subwavelength Physics. Palmarium Academic Publishing, Saarbrucken, Deutschland (2016) 267p (in Russian).

19. V.S. Popov, V.D. Moore, N. B. Narozhny et al., JETP 122, 3, 539 (2016).

20. N.B. Narozhny, M.S. Fofanov, Phys. Letters A 295, 87 (2002).

21. G. Malka, E. Lefebvre, J.L. Miquel, Phys. Rev. Lett. 78, 3314 (1997).

22. Qingyu Yang, Yubo Wang, Yifei Cao et al., Laser Physics Lett.,20, No. 4, 045301(2023).

23. A.V.Borovskiy, A.L. Galkin, System Analysis & Mathematical Modeling 6, in print (2024).

JOURNAL OF EXPERIMENTAL AND THEORETICAL PHYSICS, 2024, Vol. 165, No. 6, pp. 786–792

ATOMS, MOLECULES, OPTICS

EELECTROMECHANICAL SELF-OSCILLATING SYSTEMS WITH FLEXIBLE FIELD ELECTRON EMITTERS

© 2024 **V. I. Kleshch**[a*], **A. N. Obraztsov**[a]

[a] Department of Physics, Lomonosov Moscow State University 119991, Moscow, Russia

**e-mail: klesch@polly.phys.msu.ru*

Received January 18, 2024

Revised January 18, 2024

Accepted February 06, 2024

Abstract. The paper presents the results of an experimental and theoretical study of electromechanical self-oscillations in systems consisting of a vacuum diode with a flexible field emission cathode, depending on its elastic properties and ability to deform. Self-oscillation regime experimentally demonstrated for field electron emitters based on carbon nanotubes and diamond microneedles. A mathematical model is developed to describe the electromechanical processes in the self-oscillating systems under consideration. Based on the analysis of the experimental data and simulation results, it is shown that the excitation of self-oscillations in a system with a flexible field emission cathode is determined by a combination of system parameters that result in a negative effective damping coefficient. The potential practical applications of self-oscillations of field emission cathodes in various micro- and nano-electromechanical systems are explored.

Keywords: *self-oscillations, field electron emission, microelectromechanical systems, carbon nanotubes, diamond*

DOI: 10.31857/S004445102406e038

1. INTRODUCTION

Over the past two decades, considerable experimental evidence has been obtained for a phenomenon involving the emergence of stable undamped mechanical oscillations in field emission cathodes possessing certain mechanical flexibility and elasticity during electron emission under constant applied voltage [1–9]. This phenomenon was initially observed while studying field electron emission from individual carbon nanotubes (CNTs) and their yarns in an electron microscope chamber (see, for example, [1, 2]). However, in these first studies, the mechanism of such oscillations was not established. Later, mechanical oscillations occurring during electron emission were thoroughly investigated for silicon carbide nanowires [3, 4], individual multi-walled CNTs [5], microscale yarns twisted from CNTs [6], and field emission cathodes of macroscopic dimensions made from thin CNT membranes [7, 8]. These works demonstrated that this phenomenon represents electromechanical self-oscillations arising due to the fact that electric field that causes field emission current also leads to mechanical deformation of the elastic emitter.

Recently, it has been demonstrated that under certain conditions, self-oscillations can be observed not only for sufficiently flexible CNT-based cathodes or nanowires but also for diamond microscale emitters possessing high elastic modulus and relatively high rigidity [9]. Evidence has also been obtained that the self-oscillation effect can be one of the causes of degradation in CNT-based field emission cathodes [10, 11]. It was shown that during field electron emission from an array of aligned CNTs grown on a flat substrate, self-oscillations of individual nanotubes can occur, with amplitudes that can become sufficiently high and lead to partial or complete destruction of the nanotube.

In this work, based on characteristic experimental dependencies, we analyze the general properties of such systems and patterns determining the process of self-oscillation excitation, and discuss the prospects for practical application of this effect.

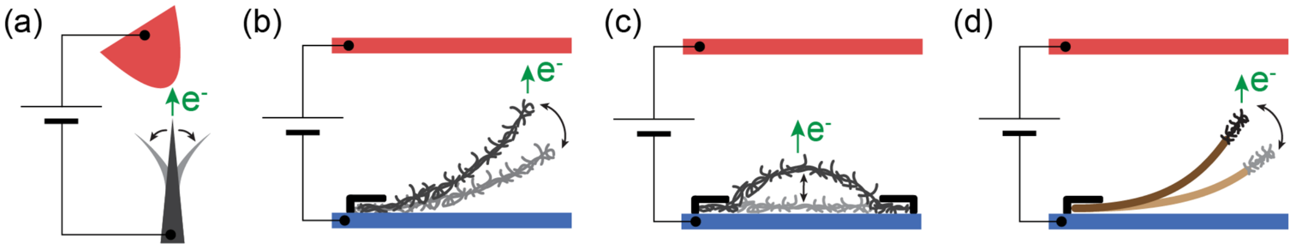

Fig. 1. Experimental setups in which electromechanical self-oscillations of various types of field electron emitters were observed. *a* - Individual nanoscale emitter. *b* - Emitter in the form of a CNT strip fixed at one end. *c* - Emitter in the form of a CNT yarn fixed at both ends. *d* - emitter based on metal elastic wire with CNT at the end

2. EXPERIMENTAL CONDITIONS AND RESULTS

2.1. Experimental Samples of Self-Oscillating Systems

As mentioned in the Introduction, electromechanical self-oscillations were experimentally observed for field electron emitters of various types. Moreover, the experimental geometry and measurement conditions could also differ significantly. Figure 1 shows diagrams of self-oscillating systems that were studied in works [3–9]. In the most general form, such systems represent a vacuum diode with a field electron emitter mounted on the cathode, possessing certain flexibility and elasticity. In the experiment, a constant voltage sufficient for observing field electron emission is applied between the cathode and anode of the diode.

Figure 1a shows the measurement setup used to study nanoscale emitters, for example, in the form of a single CNT [5], CNT yarn [2], or silicon carbide nanowire [3]. In this case, a metal tip anode was used, positioned in close proximity to the emitter apex, at a distance not exceeding several micrometers.

For macroscopic emitters, such as narrow strips made from thin membranes or yarns twisted from a large number of CNTs, self-oscillations were studied in a flat vacuum diode configuration, as shown in Fig. 1 *b*, *c*. Moreover, self-oscillations were observed with point attachment of such flexible emitters on a flat base both at one end [7] (Fig. 1*b*) and at both ends [6] (Fig. 1*c*). The self-oscillating mode was also implemented for an emitter in the form of a metal wire segment with a CNT membrane fragment attached to its end [8] (Fig. 1*d*). The oscillation parameters and excitation conditions were determined in this case by a combination of the wire's elastic properties and field emission characteristics of CNTs.

This paper examines the results of experiments conducted on emitters made from two types of materials with significantly different mechanical properties. One of the studied emitters was a needle-like diamond crystallite (microneedle) with a single-crystal structure, 100 μm in length, approximately 1 μm thick near the base, and with a tip radius of about 10 nm (Fig. 2*a*). A detailed description of the manufacturing technique for diamond microneedles and their structural properties is presented in works [12,13]. The elastic modulus value of such microneedles corresponds to that characteristic of bulk single-crystal diamond, and the typical quality factor of oscillations for a microneedle fixed at its base is around 1000 [9]. The second type of emitters studied in this work was a strip 5 mm long and 0.5 mm wide, cut from a thin membrane, which consisted of intertwined single-walled CNTs (SWCNTs) and had a thickness of about 0.1 mm (Fig. 3*a*). The manufacturing technique and structure of such SWCNT membranes are described in detail in works [7, 14]. The SWCNT strip emitters had a much lower elastic modulus compared to diamond microneedles, and the quality factor of the oscillatory system made from such strips, fixed at one end, typically did not exceed 10.

2.2 Diamond-based emitters

The results of experiments with the diamond microneedle are presented in Fig. 2. In this case, the experiment was conducted according to the scheme shown in Fig. 1*a*, inside a scanning electron microscope chamber (SEM, model FEI Versa 3D) at a vacuum level of about Torr. A sharpened tungsten wire was used as the anode, with its tip positioned several micrometers away from the diamond microneedle apex.

When a constant voltage was applied to the diode, field electron emission was observed from the tip of

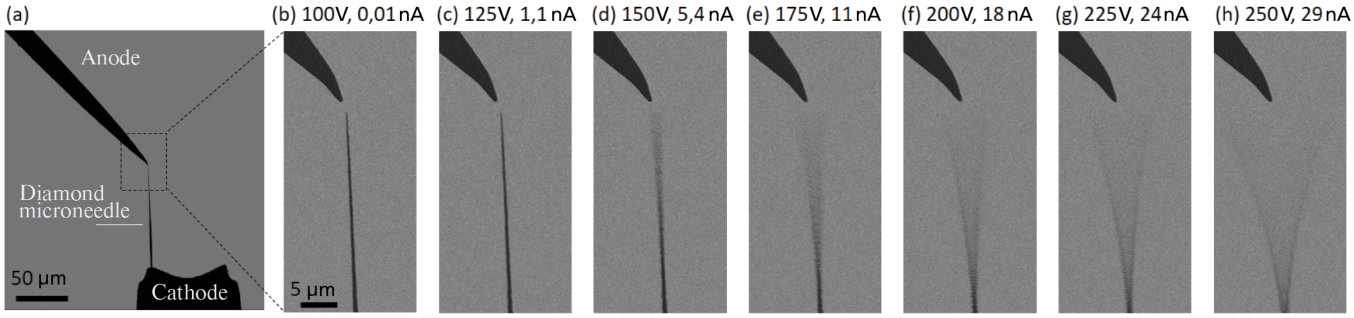

Fig. 2. a — SEM image showing the arrangement of elements during the field emission experiment with a diamond microneedle. b—h — SEM images of the diamond microneedle tip (cathode) and tungsten anode at various applied voltages and field emission currents

the diamond microneedle, with the current value measured using a picoammeter (Keithley 6487 model). When exceeding a certain threshold voltage value, stable undamped mechanical oscillations of the needle tip were observed with a frequency of about 1.4 MHz, close to the natural frequency of the microneedle. The oscillation amplitude increased with increasing voltage, which also led to an increase in field emission current, as shown in Fig. 2*b—h*. The threshold voltage for self-oscillations in the presented case was 150 V. At a voltage of 250 V, the maximum deviation of the needle tip from its axis was about 20°, which is close to the limit deformation at which there is a high probability of needle breaking at the point of maximum mechanical stress. It is important to note that the measured field emission current values did not change when the microscope electron beam was turned off. This means that the oscillations are not related to the electron beam action, as, for example, was observed in work [15]. Therefore, in the system under consideration, there are self-oscillations maintained by the applied constant voltage.

2.3. SWCNT-based emitters

The measurement results with an emitter in the form of a thin SWCNT strip are presented in Fig. 3. The experiments were conducted according to the scheme shown in Fig. 1*b*. The SWCNT strip was fixed on a flat metal base at one of its ends using conductive graphite tape. The base with the membrane strip was mounted on the cathode holder in the measuring vacuum cell parallel to the flat metal anode at a distance of 10 mm. The studies were conducted at a vacuum level in the cell of 10^{-6} Torr.

When a constant voltage was applied between the cathode and anode, the free end of the strip deflected towards the anode under the influence of electrostatic forces (Fig. 3 d). As the voltage increased, the membrane bending increased, and at 3000 V, field electron emission occurred from the CNTs located at the end of the strip. At 3300 V, the field emission current reached 25 μA, and the end of the strip began to oscillate, as shown in Fig. 3*c*. The time dependence of the field emission current, recorded using an oscilloscope, showed non-harmonic periodic oscillations (Fig. 3*c*, *b*). The oscillation frequency in this case was 140 Hz. The oscillation amplitude increased with increasing voltage; however, when exceeding a certain threshold voltage of about 3900 V, oscillations were

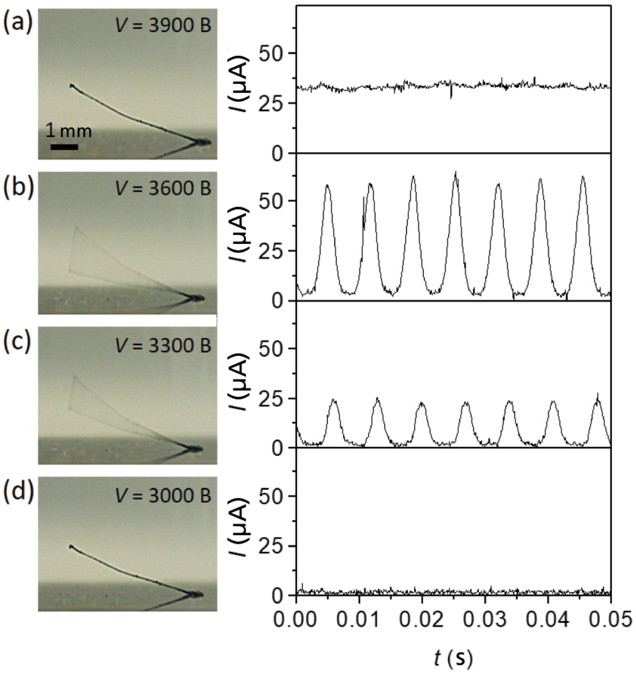

Fig. 3. *a-d* — Photographs of the emitter in the form of a CNT strip and corresponding dependencies of field emission current on time at various values of applied constant voltage. At the bottom of the photographs, the reflection of the CNT strip from the mirror surface of the metal base is visible (*a*)

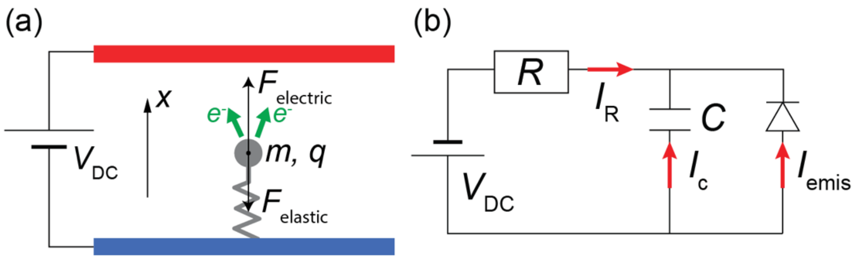

Fig. 4. *a* — Empirical representation of the system with a flexible field electron emitter. *b* — Equivalent electrical circuit of the system

not observed (Fig. 3*a*). Thus, in this case, self-oscillations in the system occurred only within a specific voltage range.

3. MODEL OF SELF-OSCILLATING SYSTEM

An empirical model describing electromechanical processes in a system with a flexible field electron emitter was previously proposed in works [4, 7]. In the present work, this model is used to analyze experimental data and determine the necessary general conditions for implementing the self-oscillating regime.

To describe the general patterns in the studied self-oscillating systems, let us consider a one-dimensional case of a material point motion under the influence of an electric field (Fig.4*a*). The equation of motion for a particle with effective mass and coordinate can be written in general form

$$mx = F_{electric} + F_{elastic} + F_{friction}.$$

Here

$$F_{elastic} = m\omega_0^2 x$$

is the elastic force determined by the natural frequency $f_0 = \omega_0 / 2\pi$;

$$F_{friction} = m(\omega_0 / Q)x$$

is the velocity-proportional internal friction force determined by the quality factor Q;

$$F_{electric} = dW / dx$$

is the electrostatic force (Coulomb force), which is related to the electrostatic energy $W = C(x)V^2/2$, determined by the voltage on the emitter V and its effective capacitance $C(x)$, depending on the coordinate x. The voltage on the emitter V is related to the voltage V_{DC}, which is applied to the capacitor plates, by Kirchhoff's equation

$$I_{emis} + I_C = I_R$$

for the equivalent electrical circuit of the system shown in Fig. 4*b*. Here I_{emis} is the field emission current

$$I_C = \frac{d(C(x)V)}{dt}$$

is the capacitive current,

$$I_R = \frac{V_{DC} - V}{R}$$

is the current through the emitter body with resistance R. Analysis of the equation of motion when substituting small harmonic oscillations of the coordinate

$$x(t) = X_0 + X\cos(\omega_0 t)$$

and voltage near the equilibrium position

$$V(t) = V_0 + V\cos(\omega_0 t + \phi_0)$$

shows that the effective damping coefficient in the system can be written as

$$\gamma = \gamma_0 - \Delta\gamma(V) = \frac{\omega_0}{Q} - const\frac{\partial I / \partial x}{1 + (\omega_0 \tau)^{-2}}V. \quad (1)$$

The following notations are introduced in this formula γ_0 is the damping coefficient of natural mechanical oscillations, $\Delta\gamma(V)$ is the change in damping coefficient due to the presence of field emission current. The constant

$$const = C'(m\omega_0^2 C)^{-1},$$

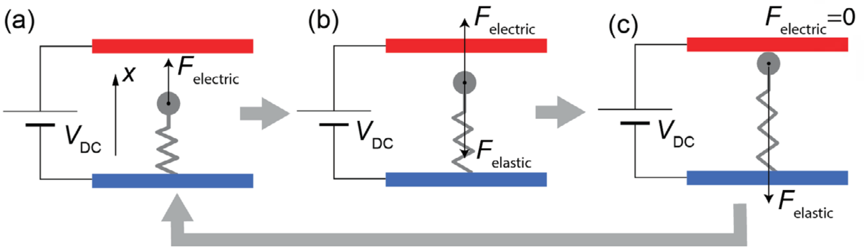

Fig. 5. *a-c* — Diagram of particle motion under the influence of electrostatic and elastic forces.

included in the expression for Δγ, includes parameters independent of voltage. The time constant

$$\tau = R_\Sigma C = \left(\frac{\partial I}{\partial V} + \frac{1}{R}\right)^{-1} C$$

is determined by both the emitter resistance R, and the differential resistance $(\partial I / \partial V)^{-1}$, i.e., the slope of the current-voltage characteristic of field emission.

From formula (1), it can be seen that at certain values of system parameters, the friction coefficient can take negative values. In this case, self-excitation of the system occurs and the oscillations become increasing in amplitude. Due to the presence of nonlinear terms in the original equation of motion, amplitude stabilization can occur, and as a result, self-oscillations will be observed, i.e., stable oscillations in a system with dissipation, maintained by an external energy source (DC voltage source) [16].

The role of field emission current can be clearly demonstrated using a model system shown in Fig. 5, where during the motion of a material point under electrostatic and elastic forces, its direct contact with the anode is possible. Fig. 5 a-c shows diagrams corresponding to the material point's movement towards the anode. At the moment of contact, the electrostatic force becomes zero, as all the charge of the material point instantly "flows" to the anode. After contact, the material point will move in the opposite direction under the force arising from elastic deformation until its charge is restored, after which the process repeats again. The return motion time and, consequently, the oscillation period in such a system will be determined by the time constant RC, i.e., the characteristic charging time of the system's capacitance.

In a system with a field emission cathode, when instead of anode contact, field electron emission occurs at a certain voltage value, the emitter charge also begins to "flow" to the anode, but not instantly, rather according to the emission current value determined by the current-voltage characteristic $I(V)$. The charge drainage due to field emission current, by reducing the voltage on the emitter and, consequently, the electrostatic force magnitude, effectively "pushes" the material point away from the anode, thereby implementing positive feedback in the system. Thus, the field emission current plays the role of a nonlinear element, which is an integral part of any self-oscillating system [16]. Moreover, as will be shown in the next section, the determining factor for the emergence of self-oscillations is the relationship between the time constant $\tau = R_\Sigma C$ and the natural oscillation period of the flexible cathode $2\pi\omega_0^{-1}$.

4. CONDITIONS FOR SELF-OSCILLATION EXCITATION

As discussed above, self-oscillations occur when the effective damping coefficient becomes negative. The obtained formula (1) allows formulating the physical causes of self-oscillations, i.e., the conditions under which the change in the damping coefficient Δγ, arising due to the presence of field emission current, exceeds the damping coefficient of mechanical oscillations of the emitter $\gamma_0 = \omega_0/Q$. A typical form of the function $\Delta\gamma\ (V_{DC})$ is shown in Fig. 6 for parameters corresponding to experiments with CNT strips.

At the quality factor value $Q = 10$, obtained in the experiment, the curve Δγ intersects the level γ_0 at points V_{min} and V_{max}, which are the boundaries of the range where self-oscillations occur. The quality factor characterizes internal friction in the system, and at lower values of Q (for example, at $Q = 5$ in Fig. 6*a*) the damping coefficient is positive everywhere and self-oscillations do not occur. At the same time, in the case of low friction (for example, at $Q = 50$ in Fig. 6*a*) self-oscillations are observed in the entire voltage range exceeding the threshold voltage. The latter case corresponds to the experiment with a diamond microneedle, where the quality factor was significantly higher than for the SWCNT strip, and self-oscillations did not disappear with increasing voltage up to the limiting values of field emission current and oscillation amplitude.

Fig. 6*b* shows the dependence of $\omega_0\tau$ on the applied voltage. It can be seen that self-oscillations occur under the condition $\omega_0\tau \approx\sim 1$, i.e., when the characteristic charging time of the system capacity is of the same order as the natural oscillation period of the flexible field emission cathode. In the low voltage region, the value of τ is constant, since $R_\Sigma \approx R$, and takes the maximum value $\tau = RC$. With increasing voltage, field emission current appears and decreases, as the system capacity recharging process accelerates due to the decrease in the differential resistance value $(\partial I / \partial V)^{-1}$. In the limit at high voltages $R_\Sigma = (\partial I / \partial V)^{-1}$, so tends R_Σ to zero. Therefore, the condition $\omega_0\tau \sim 1$ is met when the emitter resistance R and differential resistance $(\partial I / \partial V)^{-1}$ are of the same order of magnitude.

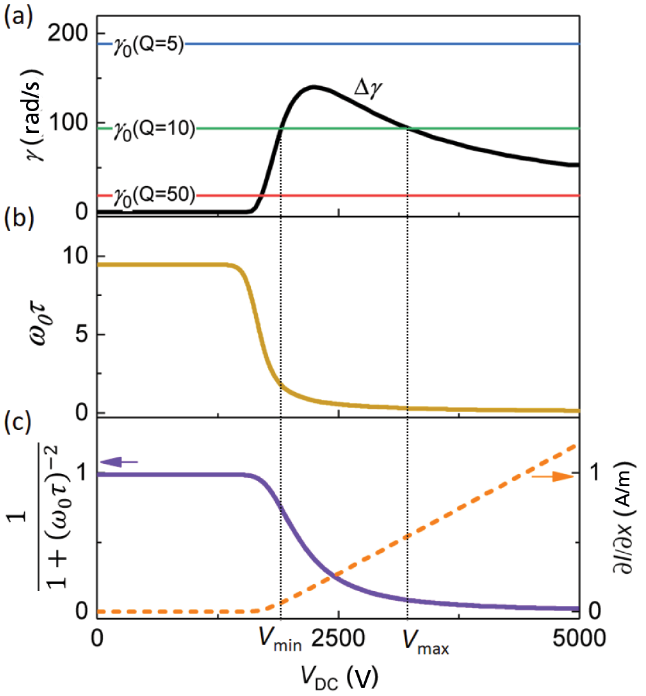

Fig. 6. *a-c* — Dependencies of various terms included in formula (1) on the applied voltage at model parameter values corresponding to the experiment with CNT strip.

The value $\Delta\gamma$ in formula (1) is determined by the product of functions $1/[1 + (\omega_0\tau)^{-2}]$ and $\partial I/\partial x$, typical graphs of which are shown in Fig. 6 c. It can be seen that that expression $1/[1 + (\omega_0\tau)^{-2}]$, like $\omega_0\tau$, tends to zero with increasing voltage. The current derivative $\partial I/\partial x$, on the contrary, increases with increasing voltage. Therefore, the product of these two functions reaches its maximum in a certain voltage range, where self-oscillations become possible.

It is important to note that the large value of the derivative $\partial I/\partial x$, which characterizes the degree of field emission current change when the emitter deviates from the equilibrium position, can enable the observation of self-oscillations for samples with relatively high rigidity, as is the case with the diamond microneedle (Fig. 2). Indeed, due to the chosen geometry of the anode, made in the form of a tip, a relatively small deviation of the diamond microneedle from the equilibrium position leads to a significant change in the field emission current due to the change in distance between its end and the anode. Also, the large value of $\partial I/\partial x$ provides higher efficiency in converting the applied DC voltage into AC voltage, which may be important for practical applications of the considered self-oscillating systems.

Thus, the analysis of formula (1) shows that to achieve a negative value of the effective damping coefficient, it is preferable to meet the condition $(\partial I/\partial V)^{-1} \sim R$ and $\omega_0\tau \sim 1$, while the parameters $\partial I/\partial x$, Q, C' should have the maximum possible value, and the values of parameters ω_0, m, C should be minimal. With a negative damping coefficient, the oscillation amplitude increases with time, so the oscillations cease to be small, and further system behavior can be determined by solving the original nonlinear equation of motion. Over time, due to the presence of nonlinear terms, the oscillation amplitude stabilizes. The characteristics of the established self-oscillations are determined by the specific form of the system parameters' dependencies (capacitance, field strength, etc.) on coordinate and voltage. In general, the frequency of self-oscillations turns out to be slightly higher than the natural frequency of the flexible field emission cathode due to additional mechanical stress created as a result of its deformation under electrostatic force. Both the amplitude and frequency of self-oscillations increase with increasing electrical voltage and are largely determined by the dependence of the field emission current on coordinate.

The presented model adequately describes the experimentally observed dependencies for both macroscopic emitters based on membranes and CNT yarns, as well as micro- and nanoscale emitters in the form of a single diamond needle, carbon nanotube, or semiconductor nanowire. Thus, the phenomenon of electromechanical self-oscillations in systems with flexible field emission cathodes is of a general nature and can be observed for field emission cathodes of any type and size, provided certain conditions and system parameters ensure a negative value of the effective damping coefficient.

5. PROSPECTS FOR PRACTICAL APPLICATION OF SELF-OSCILLATING SYSTEMS

The practical use of self-oscillations of flexible field emitters in various micro- and nanoelectromechanical systems may be of significant interest. Such devices will not require an external AC source and can be used similarly to active microelectronic elements. First of all, this interest is related to the potential possibility of creating generator devices directly at the micro level. Furthermore, examples of electromechanical devices based on the considered effect can be DC to AC voltage converters, clock pulse generators, etc. Moreover, when using nanoscale emitters, the frequencies of electromechanical oscillations can reach values corresponding to the microwave range of electromagnetic radiation. Indeed, in experiments with diamond microneedles with characteristic transverse dimensions of about 1 μm, oscillation frequencies ranged from 100 kHz to several MHz. The oscillation frequency is inversely proportional to the characteristic size of the system in the first approximation, so for a single emitter with a diameter of 1 nm (for example, for a single carbon nanotube), the self-oscillation frequency will be in the range from 100 MHz to several GHz. This estimate coincides with the resonant frequencies values for individual nanotubes that are typically registered experimentally when excited by an external alternating electric field [17]. In the case of self-oscillations excitation during field electron emission from a single nanotube, the charge at its end will generate a high-frequency electromagnetic field in the surrounding space. The electron motion creating the electromagnetic wave in this case will be mainly due to the mechanical movement of the emitter tip, rather than electric current, as occurs in a standard transmitting antenna. Thus, when using self-oscillating electromechanical systems, it is potentially possible to create nanoscale electromagnetic wave sources and transmitting antennas based on them, which can be fully integrated into various microelectronic devices. Additionally, the availability of such sources also allows the integration of various nanoelectromechanical devices based on individual carbon nanotubes that use external macroscopic high-frequency oscillation generators in their operation. Such devices include, for example, ultra-sensitive mass or force sensors created based on individual oscillating carbon nanotubes or graphene films [18,19], devices for transmitting and receiving radio signals at the nanoscale [20,21], clock generators [22], electronic logic elements [23], and others.

6. CONCLUSION

The paper investigates the effect of electromechanical self-oscillations occurring in systems with flexible field electron emitters. The main types of systems exhibiting this effect are considered, and experimental results are presented for two representative types of emitters based on CNTs and diamond microtips, which had significant differences in mechanical properties. Using the developed mathematical model of the considered self-oscillating systems, requirements for mechanical (quality factor, natural frequency) and electronic (capacitance, resistance, current-voltage characteristic) system parameters necessary for the emergence of negative effective damping coefficient, at which the self-oscillating regime is realized, are determined. In particular, it is shown that the time constant, which determines the characteristic charging time of the system capacitance and is related to the electrical resistance of the emitter and the steepness of the current-voltage characteristic, should be of the same order of magnitude as the period of natural oscillations of the elastic field emission cathode. From a practical perspective, the self-oscillation effect may be of considerable interest due to the possibility of creating microelectromechanical generator devices based on it, such as DC-to-AC voltage converters, clock pulse generators, transmitting antennas, etc.

FUNDING

This work was supported by the Russian Science Foundation (project No. 19-72-10067).

REFERENCES

1. Z. L. Wang, R. P. Gao, W. A. de Heer, P. Poncharal, In situ imaging of field emission from individual carbon nanotubes and their structural damage, Applied Physics Letters 80, 856 (2002).

2. Y. Saito, K. Seko, J.-i. Kinoshita, Dynamic behavior of carbon nanotube field emitters observed by in situ transmission electron microscopy, Diamond and Related Materials 14, 1843 (2005).

3. A. Ayari, P. Vincent, S. Perisanu, M. Choueib, V. Gouttenoire, M. Bechelany, D. Cornu, S. T. Purcell, Self-oscillations in field emission nanowire mechanical resonators: A nanometric dc– ac conversion, Nano Letters 7, 2252 (2007).

4. T. Barois, S. Perisanu, P. Vincent, S. T. Purcell, A. Ayari, Role of fluctuations and nonlinearities on field emission nanomechanical self-oscillators, Physical Review B 88, 195428 (2013).

5. J. A. Weldon, B. Aleman, A. Sussman, W. Gannett, A. K. Zettl, Sustained mechanical self-oscillations in carbon nanotubes, Nano Letters 10, 1728 (2010).

6. V. I. Kleshch, A. A. Zakhidov, A. N. Obraztsov, E. D. Obraztsova, R. H. Baughman, Self-oscillations of carbon nanotube twist-yarn during field emission, Physica Status Solidi B-Basic Solid State Physics 246, 2658 (2009).

7. V. I. Kleshch, A. N. Obraztsov, E. D. Obraztsova, Self-oscillations in an electromechanical system with a field emitter, JETP Letters 90, 464 (2009).

8. V. I. Kleshch, A. N. Obraztsov, E. D. Obraztsova, Electromechanical self-oscillations of carbon nanotube field emitter, Carbon 48, 3895 (2010).

9. V. I. Kleshch, R. R. Ismagilov, V. V. Mukhin, A. S. Orekhov, P. Poncharal, S. T. Purcell, A. N. Obraztsov, Electromechanical resonances and field-emission-induced self-oscillations of single crystal diamond needles, Applied Physics Letters 122, 144101 (2023).

10. P. Vincent, F. Panciera, I. Florea, N. Blanchard, C. S. Cojocaru, M. Ezzedine, H. Taoum, S. Perisanu, P. De Laharpe, A. Ayari, J. Chaste, K. Saidov, U. Mirsaidov, S. T. Purcell, P. Legagneux, Observations of the synthesis of straight single wall carbon nanotubes directed by electric fields in an Environmental Transmission Electron Microscope, Carbon 213, 118272 (2023).

11. P. Vincent, F. Panciera, I. Florea, M. Ezzedine, M.-R. Zamfir, S. Perisanu, C. S. Cojocaru, N. Blanchard, D. Pribat, S. Purcell, P. Legagneux, in 2021 34th International Vacuum Nanoelectronics Conference (IVNC) (IEEE, 2021), pp. 1.

12. A. N. Obraztsov, P. G. Kopylov, B. A. Loginov, M. A. Dolganov, R. R. Ismagilov, N. V. Savenko, Single crystal diamond tips for scanning probe microscopy, Review of Scientific Instruments 81, 013703 (2010).

13. A. N. Obraztsov, P. G. Kopylov, A. L. Chuvilin, N. V. Savenko, Production of single crystal diamond needles by a combination of CVD growth and thermal oxidation, Diamond and Related Materials 18, 1289 (2009).

14. A. Lobach, N. Spitsina, S. Terekhov, E. Obraztsova, Comparative analysis of various methods of purification of single-walled carbon nanotubes, Physics of the Solid State 44, 475 (2002).

15. P. Vincent, S. Perisanu, A. Ayari, M. Choueib, V. Gouttenoire, M. Bechelany, A. Brioude, D. Cornu, S. Purcell, Driving self-sustained vibrations of nanowires with a constant electron beam, Physical Review B 76, 085435 (2007).

16. G. S. Gorelik, Oscillations and Waves (Fizmatgiz, Moscow, 1959) [in Russian].

17. T. Natsuki, Carbon nanotube-based nanomechanical sensor: Theoretical analysis of mechanical and vibrational properties, Electronics 6, 56 (2017).

18. K. Jensen, K. Kim, A. Zettl, An atomic-resolution nanomechanical mass sensor, Nature Nanotechnology 3, 533 (2008).

19. J.-X. Shi, X.-W. Lei, T. Natsuki, Review on carbon nanomaterials-based nano-mass and nano-force sensors by theoretical analysis of vibration behavior, Sensors 21, 1907 (2021).

20. K. Jensen, J. Weldon, H. Garcia, A. Zettl, Nanotube radio, Nano Letters 7, 3508 (2007).

21. P. Vincent, P. Poncharal, T. Barois, S. Perisanu, V. Gouttenoire, H. Frachon, A. Lazarus, E. de Langre, E. Minoux, M. Charles, Performance of field-emitting resonating carbon nanotubes as radio-frequency demodulators, Physical Review B 83, 155446 (2011).

22. Y. Saito, Nanostructured Carbon Electron Emitters and Their Applications (CRC Press, 2022).

23. Y. V. Pershin, S. Shevchenko, Computing with volatile memristors: an application of non-pinched hysteresis, Nanotechnology 28, 075204 (2017).

JOURNAL OF EXPERIMENTAL AND THEORETICAL PHYSICS, 2024, Vol. 165, No. 6, pp. 794–796

MOLECULES OF REPELLING ATOMS ADSORBED ON SURFACES AND THREADS

© 2024 A. V. Maksimychev[a*], L. I. Menshikov[a, b**], P. L. Menshikov[a, b***]

[a]National Research University MPTI 141701, Dolgoprudny, Moscow region, Russia
[b] National Research Centre Kurchatov institute 123182, Moscow, Russia
*e-mail: maksimychev.av@mipt.ru
** e-mail: mleonid1954@mail.ru
*** e-mail: menshikov2005@mail.ru

Received February 02, 2024
Revised February 02, 2024
Accepted February 08, 2024

Abstract. The interaction of two slow atoms adsorbed on a surface or thread is considered. It is shown that, for any sign of the scattering length, this system has a bound state. In particular, such a state exists for two atoms with interaction in the form of a spherical potential with an infinitely high wall.

Keywords: *zero radius potential, bound states of atoms, quasimolecule, adsorption, scattering length, Efimov effect*

DOI: 10.31857/S004445102406e04X

1. INTRODUCTION

One of the unexpected results of quantum mechanics is the Efimov effect — the presence of bound states in a system of three repulsive particles [1] (see also works [2–5]). In this article, which is a further development of work [6], a similar phenomenon is indicated: the possibility of the existence of a bound state (van der Waals molecule) of repulsive atoms adsorbed on a surface or filament, acting as a third body.

In work [6], a pair of such atoms with mass m, interacting with the surface through an oscillator potential

$$u(z) = m\omega^2 z^2 / 2$$

was considered (z-axis is directed perpendicular to the surface).

It is known [7] that the scattering length a is the only parameter that determines the interaction of two atoms at low energy. Based on this, to describe the motion of atoms, the authors applied in [6] the method of zero radius potentials [8], i.e., imposed a boundary condition on the wave function (WF) of the atom pair

$$\lim_{r\to 0}\left(\frac{1}{\varphi}\frac{\partial\varphi}{\partial r}\right) = \gamma. \tag{1}$$

Here

$$\varphi = r\psi, \quad \gamma = -1/a,$$

$$r = |\mathbf{r}|, \quad \mathbf{r} = \mathbf{r_1} - \mathbf{r_2} = (z, \rho),$$

$z = z_1 - z_2, \rho = (x_1 - x_2, y_1 - y_2)$ is a two-dimensional vector characterizing the relative motion of atoms along the surface. According to [6], the dissociation energy of the adsorbed molecule equals

$$D = \kappa^2,$$

where κ is determined from the equation

$$f(\kappa) = \gamma. \tag{2}$$

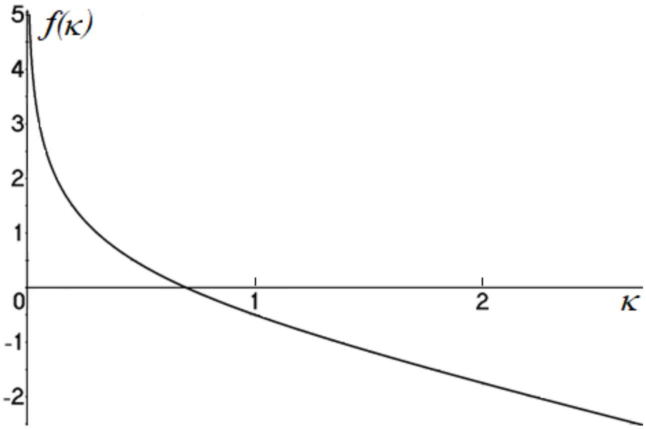

Fig. 1. Graph of function $f(\kappa)$ from (2)

The graph of function $f(\kappa)$ is shown in Fig. 1 (here and further we use units $\hbar = m = \omega = 1$).

From formula (2) and Fig. 1, it is evident that the bound state exists for any sign of γ, despite the fact that for $\gamma > 0$ (in paper [6] this case is called repulsion) such states do not exist for a pair of atoms in free space. Paper [9] considers attractive interaction between atoms in the form of a spherical well

$$V(r) = -u_0\theta(r_0 - r),$$

where $u_0 > 0$, θ – is the Heaviside function. It is indicated that depending on the parameter values u_0 and r_0, both cases $\gamma > 0$, and $\gamma < 0$. are possible. Hence, it is clear that the case $\gamma > 0$ does not always correspond to repulsion. It is clear, however, that $\gamma > 0$ can also correspond to explicit repulsion of atoms. Let's demonstrate this using an example of a definitely repulsive interaction

$$V(r) = +u_0\theta(r_0 - r). \tag{3}$$

2. HARD SPHERE APPROXIMATION FOR ADSORPTION ON A PLANE

For a pair of free slow atoms, it is sufficient to consider s-wave. In their center of mass system

$$\varphi(r) = \mathrm{Ash}(qr), \quad r < r_0,$$

$$\varphi(r) = \sin[k(r - r_0) + \eta], \quad r > r_0.$$

Here k^2 is the kinetic energy of relative motion of atoms, $q = \sqrt{u_0 - k^2}$. Wave function matching at the boundary gives

$$\eta = \frac{q}{k}\mathrm{cth}(qr_0). \tag{4}$$

At $r > r_0$ we get

$$\frac{\varphi'}{\varphi} = k[k(r - r_0) + \eta].$$

Condition $r \to 0$ in (1) should now be understood as $r \ll 1/k$. From (1) and (4) we obtain

$$\lim_{r\to 0}\frac{\varphi'}{\varphi} = k\cdot(-kr_0 + \eta). \tag{5}$$

Statements [6] are valid if

$$\gamma(\kappa) = \mathrm{const}. \tag{6}$$

This is satisfied at

$$kr_0 \ll 1, k \ll q_0, \tag{7}$$

where $q_0 = \sqrt{u_0}$. In this case

$$\gamma = q_0\,\mathrm{cth}(q_0 r_0). \tag{8}$$

Thus, if (6) is satisfied, which is true under conditions (7), then according to the conclusions of paper [6], even in case (3) there exists a bound state of the adsorbed quasi-molecule.

The value k corresponds to distances between atoms $r \sim 1/k$. For motion along the axis x $r \sim 1$, therefore from (7) we obtain the conditions for validity of this work's conclusions:

$$r_0 \ll 1, q_0 \gg 1, \tag{9}$$

or, in conventional units,

$$r_0 \ll \sqrt{\frac{\hbar}{m\omega}}, u_0 \gg \hbar\omega \tag{10}$$

From (8) and (9) we conclude

$$\gamma > q_0 \gg 1. \tag{11}$$

According to [6], in this limiting case

$$\mathrm{k} \sim \exp\left(-\gamma\sqrt{\frac{\pi}{2}}\right), \tag{12}$$

therefore, considering (11), we come to the conclusion that the quasi-molecule size, determining the characteristic distance for longitudinal motion, is large and equals

$$r \sim \frac{1}{k} \sim \exp\left(\gamma\sqrt{\frac{\pi}{2}}\right) \gg 1.$$

Thus, for longitudinal motion, the conditions for satisfying (7) are less stringent compared to (10):

$$r_0 \ll \sqrt{\frac{\hbar}{m\omega}} \cdot \exp\left(\gamma\sqrt{\frac{\pi\hbar}{2m\omega}}\right),$$

$$u_0 \gg \hbar\omega \ \exp\left(\gamma\sqrt{\frac{\pi\hbar}{2m\omega}}\right),$$

The second condition (10) is typically satisfied under typical conditions, and the first one is the most stringent. Based on the known stability of bound states in two-dimensional and one-dimensional systems, it can be stated that such states can exist in case (3).

3. ADSORPTION ON A FILAMENT

Now let's direct the axis z along the filament, and for the adsorption potential, we'll again adopt the oscillator approximation

$$u(\rho) = \rho^2 / 2, \quad \rho^2 = x^2 + y^2.$$

According to formula (8) from work [6], the WF of relative motion of atoms is given by the expression

$$\psi(\mathbf{r}) \propto G(\mathbf{r}),$$

where $G(\mathbf{r})$ is found from the equation

$$\left(-\Delta_r + \frac{1}{4}\rho^2 - 1 + \kappa^2\right)G(r) = \delta(x)\delta(y).$$

Now we need to perform a Fourier transform over z, after which, similar to [6], we obtain, omitting constant factors

$$\psi = \int_0^\infty \frac{d\tau}{\sqrt{\tau}(1 - e^{-2\tau})}\exp\left(-\kappa^2\tau - \frac{1}{4}\rho^2 cth\tau - \frac{z^2}{4\tau}\right).$$

When substituting into (1) here we can set $\rho = 0$, so that $r = |z|$, and also apply the identity

$$\frac{1}{1 - e^{-2\tau}} = \frac{1}{2\tau} + \left(\frac{1}{1 - e^{-2\tau}} - \frac{1}{2\tau}\right).$$

The integral of the first term is solved analytically and equals

$$\frac{\sqrt{\pi}}{r}e^{-kr} \approx \sqrt{\pi}\left(\frac{1}{r} - \kappa\right).$$

The second term is non-singular, and we can set $z = 0$. in it. This gives for the filament equation (2), in which

$$f(\kappa) = -\kappa + \frac{1}{\sqrt{\pi}}\int_0^\infty \frac{d\tau}{\sqrt{\tau}}e^{-k^2\tau}\left(\frac{1}{1 - e^{-2\tau}} - \frac{1}{2\tau}\right).$$

The graph of this function is similar to that shown in Fig. 1, i.e., again the solution (2) exists for any sign of γ. For large γ instead of exponential smallness (12), characteristic for the two-dimensional case, we obtain power-law smallness of binding energy $\kappa \approx 1/\gamma$.

4. CONCLUSIONS

From the above, we conclude that restricting the motion of atoms in one or two directions can lead to the appearance of a bound state absent in a pair of free atoms or to an increase in the binding energy of the quasi-molecule they already form.

Let's apply our model to describe experiments [10–12] with a two-dimensional gas of spin-polarized hydrogen atoms adsorbed on the surface of liquid helium.

For the applicability of the zero-radius potential approximation (1), it is required that the characteristic size of r_0 pair interaction $u(r)$ between hydrogen atoms in the triplet state should be small compared to both the amplitude of z_{ads} atomic oscillations in the adsorption potential ($r_0 / z_{ads} = 1$), and the characteristic de Broglie wave length of hydrogen atoms under experimental conditions [10–12], that is $kr_0 \ll 1$, where $k \sim \sqrt{2mT} / \hbar$ is the characteristic wave vector of hydrogen atoms with mass m. The experiments were conducted at temperature $T \sim 0.15$ K, therefore k ~ $6 \cdot 10^6$ cm^{-1}. According to [13], at

$$r_0 = 7.85a_0, \tag{13}$$

where a_0 is the Bohr radius, the potential energy $u(r)$ has a minimum $u(r_0) = -u_0$, where $u_0 = 6.2$ K. In this adsorption potential, hydrogen atoms have only one bound state with binding energy $E_q = 1.14$K [14]. From this, we conclude that

$$z_{ads} \sim z_{in} + z_{out} \sim 20a_0,$$

where $z_{\text{in}} \sim 10a_0$ is the characteristic oscillation amplitude in the classically accessible region of hydrogen atoms motion in the adsorption state and $z_{out} \sim \hbar / \sqrt{2mE_a} \sim 10a_0$ is the characteristic depth of their penetration under the potential barrier in the classically inaccessible region of motion. Thus,

$$r_0 / z_{ads} \sim 0.3 \qquad (14)$$

Taking (13) as the characteristic size of pair interaction between hydrogen atoms in the triplet state, we obtain

$$kr_0 \sim 0.2 \qquad (15)$$

We should add that condition (15) also allows us to neglect the correction terms ~ kr_0 to formula (1) (see [15], as well as formulas 133.9, 133.10, and 133.14 from work [16]).

Within our adopted oscillator approximation for the adsorption potential, the distance from the adsorption level to the bottom of the well should be equal to $\hbar\omega/2$. According to the data provided above, it amounts to $u_0 - E_a \approx 5$ K, which corresponds to $\omega \approx 1.3 \cdot 10^{12}\ \text{s}^{-1}$. From this, we find the unit of length used in calculations:

$$L = \sqrt{\frac{h}{m\omega}} \approx 4a_0.$$

The scattering length of hydrogen atoms in the state with total spin $S = 1$ equals $a \approx 1.2a_0$ [17]. In our units, this equals $a \approx 0.3$, which corresponds to

$$\gamma = -\frac{1}{a} \approx -3.3.$$

From Fig. 1, we conclude that $k \approx 2.5$, therefore the binding energy of the adsorbed quasi- molecule equals

$$D = \hbar\omega \cdot \text{k}^2 \approx 60\text{K}$$

As noted in work [6], this conclusion may indicate the instability of Bogoliubov two-dimensional Bose-condensates obtained in experiments [10–12], formed by hydrogen atoms adsorbed on the surface of liquid helium

FUNDING

The work was carried out within the framework of the scientific assignment of the National Research Center “Kurchatov Institute”.

REFERENCES

1. V. I. Efimov, Physics of Atomic Nuclei 12, 1080 (1970).
2. S. P. Merkuryev, L. D. Faddeev, Quantum scattering theory for systems of several particles (Moscow.: Nauka, 1985).
3. V. B. Belyaev, Lectures on the theory of small-particle systems (Moscow: Energoatomizdat, 1986).
4. F. M. Penkov, JETP 106, 1046 (1994.)
5. E. A. Kolganova, A. K. Motovilov, and W. Sandhas, Few-Body Systems 51, 249 (2011).
6. A. V. Maksimychev, L. I. Menshikov, P. L. Menshikov, JETP Lett. 113, 523 (2021).
7. P. V. Elyutin, V. D. Krivchenkov, Quantum mechanics (Moscow: Nauka, 1976).
8. Yu N. Demkov, V. N. Ostrovsky, Method of zero-radius potentials in atomic physics (Leningrad: Leningrad University Publishing House, 1975).
9. A. S. Ioselevich, JETP Letters 113, 854 (2021).
10. A. I. Safonov, S. A. Vasiliev, I. S. Yasnikov, I. I. Lukashevich, S. Yaakkola, JETP Lett. 61, 998 (1995).
11. A. I. Safonov, S. A. Vasiliev, I. S. Yasnikov, E. Tjukanov, I. I. Lukashevich, S. Yaakkola, Czech. J. Phys. 46 539 (1996)
12. A. I. Safonov, S. A. Vasiliev, I. S. Yasnikov, I. I. Lukashevich, S. Yaakkola, Phys. Rev. Lett. 81, 4545 (1998)
13. W. Kolos and L. Wolniewicz, J. Chem. Phys. 43, 2429 (1965).
14. A.I. Safonov, S.A. Vasilyev, A.A. Kharitonov, S.T. Boldarev, I.I. Lukashevich, and S. Jaakkola, Phys. Rev. Lett. 86, 3356 (2001).
15. L.D. Landau, Ya.A. Smorodinsky, JETP 14, 269 (1944).
16. L.D. Landau, E.M. Lifshitz, Quantum Mechanics, Nauka, Moscow (1974).
17. E. Tiesinga, Phys. Rev. A 48, 4801 (1993).

JOURNAL OF EXPERIMENTAL AND THEORETICAL PHYSICS, 2024, Vol. 165, No. 6, pp. 798–809

POLARIZATION PROPERTIES OF BLACK HOLES AND WORMHOLES

© 2024 S. V. Chernov
Astro Space Center, Lebedev Physical Institute of the Russian Academy of Sciences 117997, Moscow, Russia
e-mail: chernov@lpi.ru

Received December 29, 2023
Revised December 29, 2023
Accepted January 23, 2024

Abstract. In this paper, using the example of the Lamy metric, the polarization properties of black holes and wormholes are investigated. Maps of linear polarization and the position of the angle of the electric vector are constructed for the toroidal and radial distribution of the magnetic field in thin disks. Using these results from future RSDB observations on the next-generation Event Horizon telescope and the Millimetron spacemission, it will be possible to determine whether the source is a black hole or a wormhole.

Keywords: *black hole, wormhole, linear polarization, lamy's metric*

DOI: 10.31857/S004445102406e051

1. INTRODUCTION

The Event Horizon Telescope (EHT) obtained an image of hot magnetized plasma emitting synchrotron radiation around supermassive black holes in the elliptical galaxy M87 [1] and in our Milky Way galaxy [2]. The images form a ring-like morphology and were obtained in the millimeter range at 230 GHz. However, intensity maps carry significantly less information than polarization maps. Because of this, it is not possible to constrain numerical models and determine plasma and black hole parameters from observations [3]. In 2021, based on EHT data, a linear polarization map of the supermassive black hole in M87* was published, revealing a spiral structure of the electric vector position angle in hot magnetized plasma [4]. The polarization map of M87* strongly constrained numerical models; in particular, it was found that the accretion flow structure is better described by the magnetically arrested disk (MAD) regime than by the standard and normal evolution (SANE) disk [5]. Therefore, polarimetric observations are a critically important step towards understanding physical processes in strong gravitational fields.

Another question that arises here is whether the image obtained in the EHT observations is actually an image of a black hole or an image of another object, such as a wormhole? To answer this question, a criterion for distinguishing between a black hole and a wormhole is needed. In this work, it is assumed that a black hole can be distinguished from a wormhole by linear polarization of radiation.

To construct polarization maps, it is necessary to calculate the polarization change along the photon trajectory. As known, radiation polarization can change for two reasons. The first is due to the rotation of the electric vector along the geodesic in strongly curved spacetime. The second is due to photon propagation in magnetized plasma. Here we will investigate the first reason. The strongly curved spacetime will be created either by a black hole or a wormhole.

In this article, using the Lamy metric as an example, the change in the linear polarization vector during photon motion in a strong gravitational field is calculated for both a black hole and a wormhole. For this purpose, a metric is chosen that describes both black holes and wormholes and in the limiting case coincides with the Kerr rotating black hole metric. Maps of linear polarization and electric vector angle position depending on the magnetic field direction in a thin disk are constructed. Toroidal and radial magnetic field distributions in thin disks are considered. The decomposition coefficient β_2 of linear polarization depending on metric parameters is calculated and a criterion for distinguishing a black hole from a wormhole is given.

The paper uses a system of units in which the speed of light and gravitational constant are equal to unity, $c = G = 1$. The dimension of length is Gm/c^2, the dimension of time is Gm/c^3, where m is the mass parameter.

2. PHOTON EQUATIONS OF MOTION

In this section, we briefly describe the basic equations for light ray propagation in curved spacetime using the Lamy metric as an example.

The Lamy metric in Boyer-Lindquist coordinates (t, r, θ, φ) has the form [6]

$$ds^2 = -\left(1 - \frac{2rM(r)}{\Sigma}\right)dt^2 + \frac{\Sigma}{\Delta}dr^2 +$$
$$+\Sigma d\theta^2 + \frac{\sin^2\theta}{\Sigma}\Big((r^2 + a^2)^2 - \Delta a^2\sin^2\theta\Big)d\phi^2 -$$
$$-\frac{4raM(r)\sin^2\theta}{\Sigma}dtd\phi, \quad (1)$$

where standard notations are introduced

$$\Sigma = r^2 + a^2\cos^2\theta,$$

$$\Delta = r^2 - 2rM(r) + a^2,$$

a — rotation parameter, spin. This metric differs from the Kerr rotating black hole metric in that the mass parameter M is not a constant value but is a function of the radial coordinate of the form [6]

$$M(r) = m\frac{|r|^3}{|r|^3 + 2mb^2}. \quad (2)$$

In this case, the parameter m is a constant value and we will call it the mass parameter, and the parameter b, as shown in work [7], is the magnetic charge. In the case when the magnetic charge is zero, $b = 0$, this metric coincides with the Kerr rotating black hole metric. Without loss of generality, we will assume that the mass parameter equals one, one, $m = 1$. Also in this work, we will consider the case when the magnetic charge takes values from zero to two, $0 \leqslant b \leqslant 2$. As shown in work [6], this manifold is geodesically complete and non-singular in all spacetime $-\infty < r < \infty$. This means that two asymptotically flat spacetimes are connected at the point $r = 0$. From expression (2), one can see that the value $M(r) \geqslant 0$ is always greater than or equal to zero for any radius, $-\infty < r < \infty$.

The Lamy metric has coordinate singularities that correspond to event horizons in the case of the Kerr metric. These conditions are determined by the expression of the form

$$\Delta = r^2 - 2rM(r) + a^2 = 0.$$

In the case when both parameters a and b are not equal to zero, equation $\Delta = 0$ is solved numerically. Figure 4 of article [6] shows cases when this equation either has no roots, or has one (extreme case) or two roots. These roots of equation $\Delta = 0$ will be called event horizons by analogy with the roots of the equation in the Kerr metric. If the Lamy metric has two or one event horizon, then this metric corresponds to a black hole metric, otherwise it corresponds to a wormhole.

Photons propagate in the Lamy metric, moving along geodesics described by equations of the form

$$\begin{aligned} \frac{dx^\alpha}{d\tau} &= p^\alpha, \\ \frac{dp^\alpha}{d\tau} &= -\Gamma^\alpha_{\beta\gamma}x^\beta x^\gamma, \end{aligned} \quad (3)$$

where $\Gamma^\alpha_{\beta\gamma}$ are Christoffel symbols, p^α is the photon momentum, τ is the affine parameter. Paper [8] presents metric coefficients and Christoffel symbols for the Lamy metric (1) with function form (2). Below we will show images of black holes and wormholes obtained through numerical solution of eight equations (3). Qualitatively, photon propagation in the Lamy metric, by analogy with the Kerr metric, can be described using radial and angular potentials of the form [3]

$$R(r) = (r^2 + a^2 - aL)^2 - \Delta\Big(Q + (L - a)^2\Big), \quad (4)$$

$$\Theta(\theta) = Q + \cos^2\theta\left(a^2 - \frac{L^2}{\sin^2\theta}\right), \quad (5)$$

where L is the angular momentum of the photon, Q is Carter's constant. In the Kerr metric ($b = 0$) dial potential is a fourth-order polynomial with respect to the radial coordinate. In the Lamy metric, this potential is a seventh-order polynomial [6] and, as shown in work [6], some photon trajectories can have more than one radial turning point.

To determine the position of the image on the observer's screen, Cartesian coordinates (α, β) are introduced, first presented in work [9]. These coordinates connect the conserved photon parameters (L, Q) with the position on the observer's screen:

$$\alpha = -\frac{L}{\sin\theta_o}, \quad \beta = \pm\sqrt{\Theta(\theta_o)}, \quad (6)$$

where θ_0 is the observer's inclination angle to the rotation axis of the black hole or wormhole. Thus, knowing the photon's position on the observer's screen, one can determine the photon parameters (L, Q), and consequently, the position of the photon source in the disk.

To construct polarization maps, we will primarily be interested in photon polarization. To calculate the polarization change of a photon moving in a strong gravitational field, we will use the Walker-Penrose constants [10]. For this, we need to show that the Lami metric belongs to type D according to Petrov classification [10]. To demonstrate this, we will use the Newman-Penrose formalism. This formalism is a tetrad formalism in an isotropic basis consisting of four isotropic vectors (l, n, m, m*) [10]. The Appendix defines a quartet of isotropic vectors satisfying orthogonality conditions, isotropy, and normalization condition. The Ricci rotation coefficients in the Lami metric, which in this formalism are called spin coefficients [10], are also written out. Since the spin coefficients in the Lami metric

$$\kappa = \sigma = \lambda = \nu = \varepsilon = 0 \quad (7)$$

are equal to zero (see Appendix), from the corollary of the Goldberg-Sachs theorem, it follows that the Lami metric belongs to type D according to Petrov classification [10]. The Appendix also lists the non-zero Weyl scalar Ψ_2. All these quantities will be needed to calculate the Walker-Penrose constants.

We proceed to calculate the change in the photon polarization vector when moving in curved spacetime [10]. Let f^μ — 4-vector be the photon polarization, which is orthogonal to the photon 4-momentum p^μ, i.e.,

$$f^\mu p_\mu = 0,$$

and is parallel transported along the photon trajectory, i.e.,

$$p^\mu \nabla_\mu f^\nu = 0.$$

Then the quantity

$$K_s = -p^i f^j (l_i n_j - l_j n_i - m_i m_j^* + m_i^* m_j)\Psi_2^{-1/3} \quad (8)$$

remains constant along the geodesic [10]. The quantity

$$K_s = K_2 + iK_1$$

is a constant complex value called the Walker-Penrose constant. The existence of this constant allows us to calculate the change in the 4-vector of polarization along the photon trajectory and compare polarization values for black hole and wormhole metric cases. For this, we need to relate the quantities f and p near the observer and the source. We introduce the notations

$$A = p^t f^r - p^r f^t + a\sin^2\theta(p^r f^\phi - p^\phi f^r), \quad (9)$$

$$B = \sin\theta[(p^\phi f^\theta - p^\theta f^\phi)(r^2 + a^2) - \\ -a(p^t f^\theta - p^\theta f^t)]. \quad (10)$$

Then expression (8) can be rewritten as

$$K_2 + iK_1 = -(A - iB)\Psi_2^{-1/3}. \quad (11)$$

The values of 4-momentum at any point in spacetime are given in the Appendix by formulas (38). By setting the initial magnetic field at the emission point and calculating the constants K_1 and K_2, one can determine the values of the polarization 4-vector at the observation point, and consequently, the Stokes parameters (see (53) and (54)).

Another important quantity is the linear polarization decomposition coefficient β_{m}, introduced in [11]:

$$\beta_m = \frac{1}{I_{ann}} \int\limits_{\rho_{\min}}^{\rho_{\max}} \int\limits_{0}^{2\pi} P(\rho,\phi) P_m^*(\phi) \rho d\rho d\phi =$$

$$= \frac{1}{I_{ann}} \int\limits_{\rho_{\min}}^{\rho_{\max}} \int\limits_{0}^{2\pi} P(\rho,\phi) e^{-im\phi} \rho d\rho d\phi, \qquad (12)$$

where

$$I_{ann} = \int\limits_{\rho_{\min}}^{\rho_{\max}} \int\limits_{0}^{2\pi} I(\rho,\phi) \rho d\rho d\phi, \qquad (13)$$

$$P(\rho,\phi) = Q(\rho,\phi) + iU(\rho,\phi). \qquad (14)$$

Here Q and U are the Stokes parameters of linear polarization, (ρ,ϕ) are polar coordinates on the observer's screen, the asterisk "*" denotes complex conjugation, is the radiation intensity. Without loss of generality, we set the value I_{ann} equal to one, $I_{ann} = 1$. Let us denote the total linear polarization as

$$LP = \sqrt{Q^2 + U^2},$$

and the electric vector angle positions as

$$EVPA = \frac{1}{2} arctg \frac{U}{Q}. \qquad (15)$$

In the next section, we will present maps of total linear polarization and electric vector angle positions for radial and toroidal magnetic fields in a thin disk located in the equatorial plane of a black hole or wormhole, and compare the obtained results.

3. RESULTS

In this section, we will discuss the difference in maps of linear polarization and electric vector angle positions for a black hole and wormhole using the Lamy metric as an example.

We will assume that the source of photon radiation is a thin disk located in the equatorial plane of the black hole (wormhole), which radiates isotropically in all directions. The thin disk is penetrated by a radial or toroidal magnetic field. The inner radius of the disk was set to $r_{in} = 8.$. The rotation parameter in the Lamy metric was set to $a = 0.9$, and the magnetic charge to $b = 0, 0.3, 0.5, 0.7, 0.9, 2.0$. The case when $b \lessapprox 0.245$ corresponds to a black hole, and the case when $b \gtrapprox 0.245$ to a wormhole (see Fig. 4 from [6]). The value 0.245 is determined numerically from the equation $\Delta = 0$ for spin $a = 0.9$. The observer is located at a distance from the black hole (wormhole) $r_o = 50$ at an angle $i = 17^\circ, 45^\circ, 80^\circ$ to the rotation axis of the black hole (wormhole). To construct polarization maps, the ray-tracing method was used. The geodesic equations (3) were solved numerically using the fourth-order Runge-Kutta method. All polarization maps are shown on a scale from −10 to 10 in units of Gm / c^2 and with a resolution of 2500×2500 pixels. The intensity images for the same metric parameters are shown in Fig. 3 of paper [8].

Figure 1 and 2 show linear polarization maps for the initial distribution of radial and toroidal magnetic fields, respectively. The color indicates the magnitude of linear polarization, LP value. Green arrows show the direction of the electric vector of linear polarization. The arrow length is proportional to the magnitude of linear polarization. The top three figures correspond to a black hole, the rest to a wormhole. The figures from left to right are for different inclination angles of the observer relative to the rotation axis of the black hole (wormhole), $i = 17^\circ, 45^\circ, 80^\circ$. The figures from top to bottom are for different magnetic charge values, $b = 0, 0.3, 0.5, 0.7, 0.9, 2.0$.

Comparing linear polarization for black holes and wormholes, the following conclusions can be drawn. Linear polarization in photon rings for wormholes has higher values than in the disk. This is because for some photons, circular orbits are located closer to the center and, consequently, the gravitational field will much more strongly curve the trajectory of motion, and hence the magnitude of linear polarization. This statement is true for both radial and toroidal distributions of the magnetic field in the disk. The directions of linear polarization (shown by green arrows in the figures) in photon rings will be approximately perpendicular to each other for radial and toroidal magnetic fields when the observer is

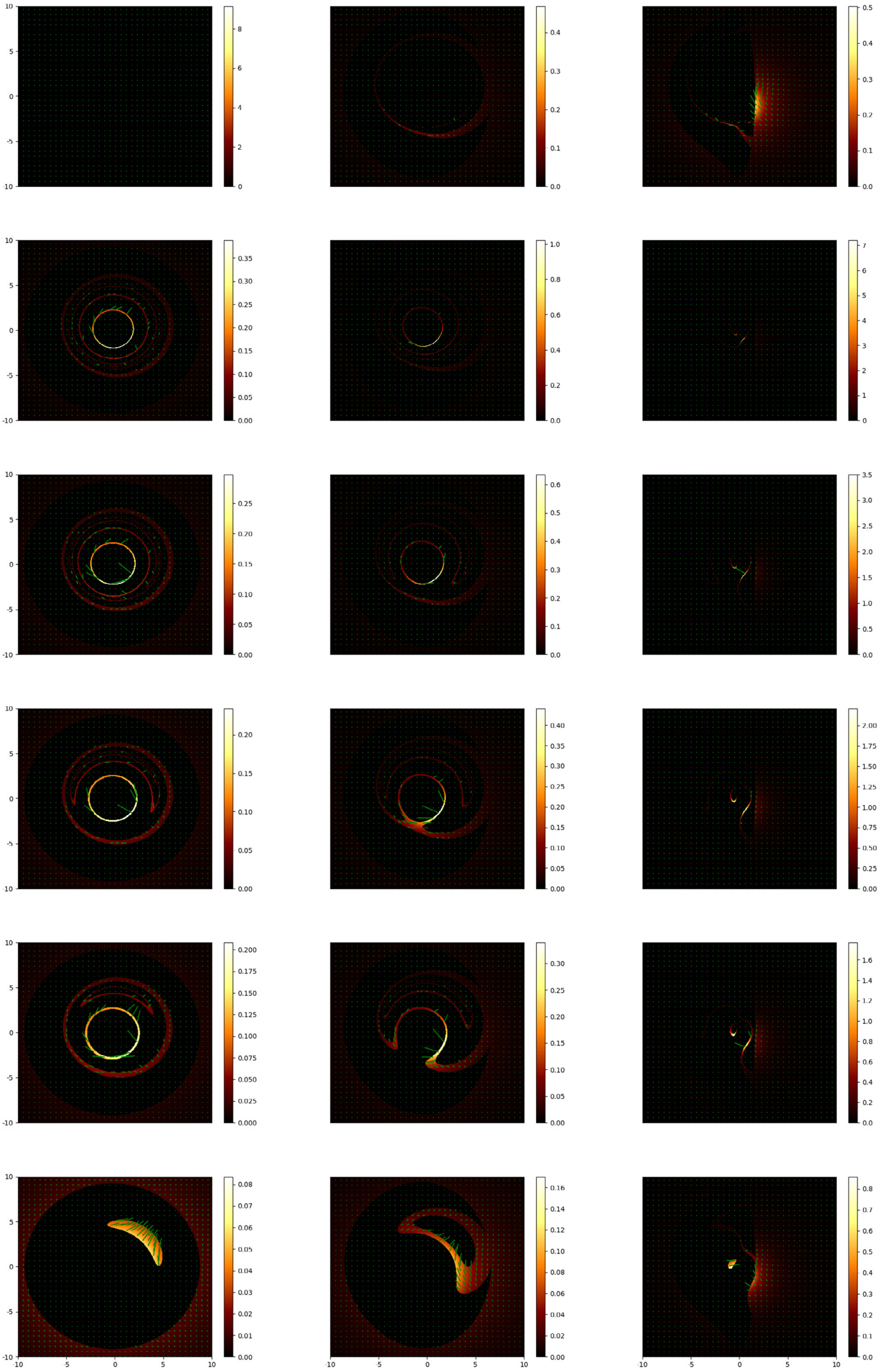

Fig. 1. Map of total linear polarization (shown in color) LP for the initial radial distribution of magnetic field around a black hole and wormhole. From left to right, inclination angles are $i = 17^{\circ}, 45^{\circ}, 80^{\circ}$. From top to bottom, magnetic charge is $b = 0, 0.3, 0.5, 0.7, 0.9, 2.0$. Map scale to $-10\mathrm{Gm}/c^3$ to $10\mathrm{Gm}/c^3$

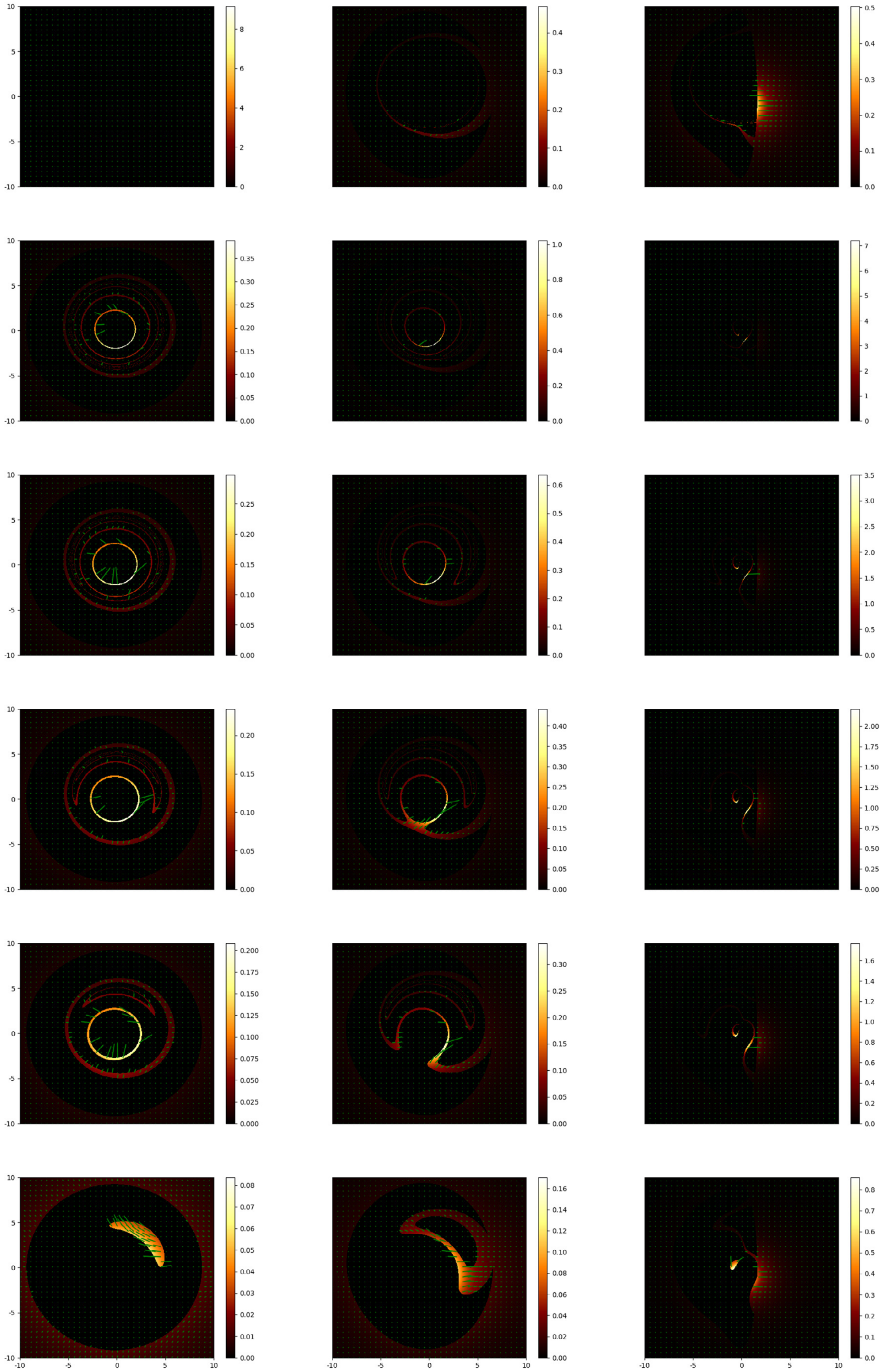

Fig. 2. Map of total linear polarization (shown in color) LP for the initial toroidal distribution of magnetic field around a black hole and wormhole. From left to right, inclination angles are $i = 17^\circ, 45^\circ, 80^\circ$. From top to bottom, magnetic charge is $b = 0, 0.3, 0.5, 0.7, 0.9, 2.0$. Map scale to $-10Gm/c^3$ to $10Gm/c^3$

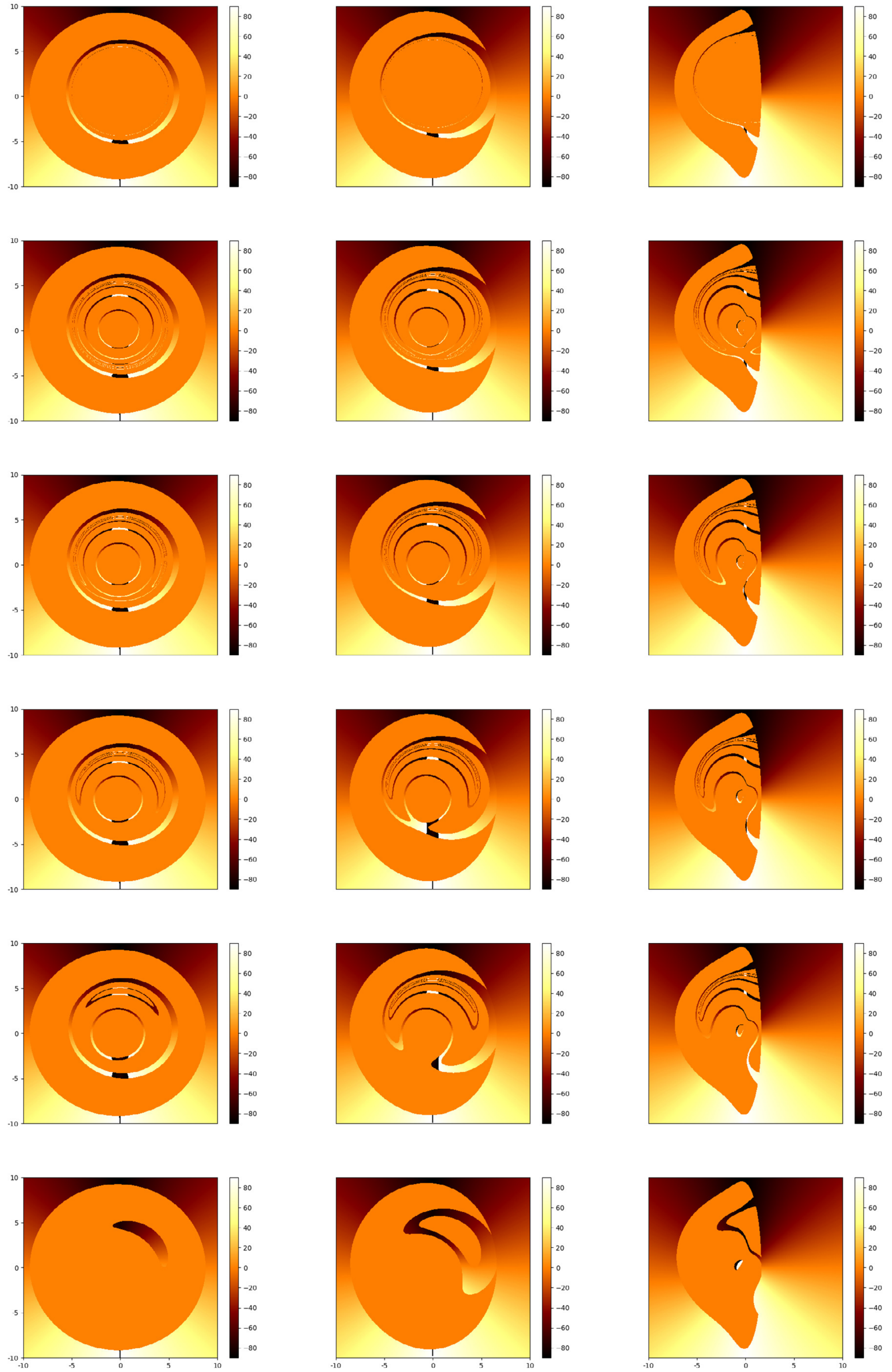

Fig. 3. Map of electric vector position angle (shown in color) for the initial radial distribution of magnetic field around a black hole or wormhole. From left to right, inclination angles are $i = 17^\circ, 45^\circ, 80^\circ$. From top to bottom, magnetic charge is $b = 0, 0.3, 0.5, 0.7, 0.9, 2.0$. Map scale to $-10\mathrm{G}m/c^3$ to $10\mathrm{G}m/c^3$

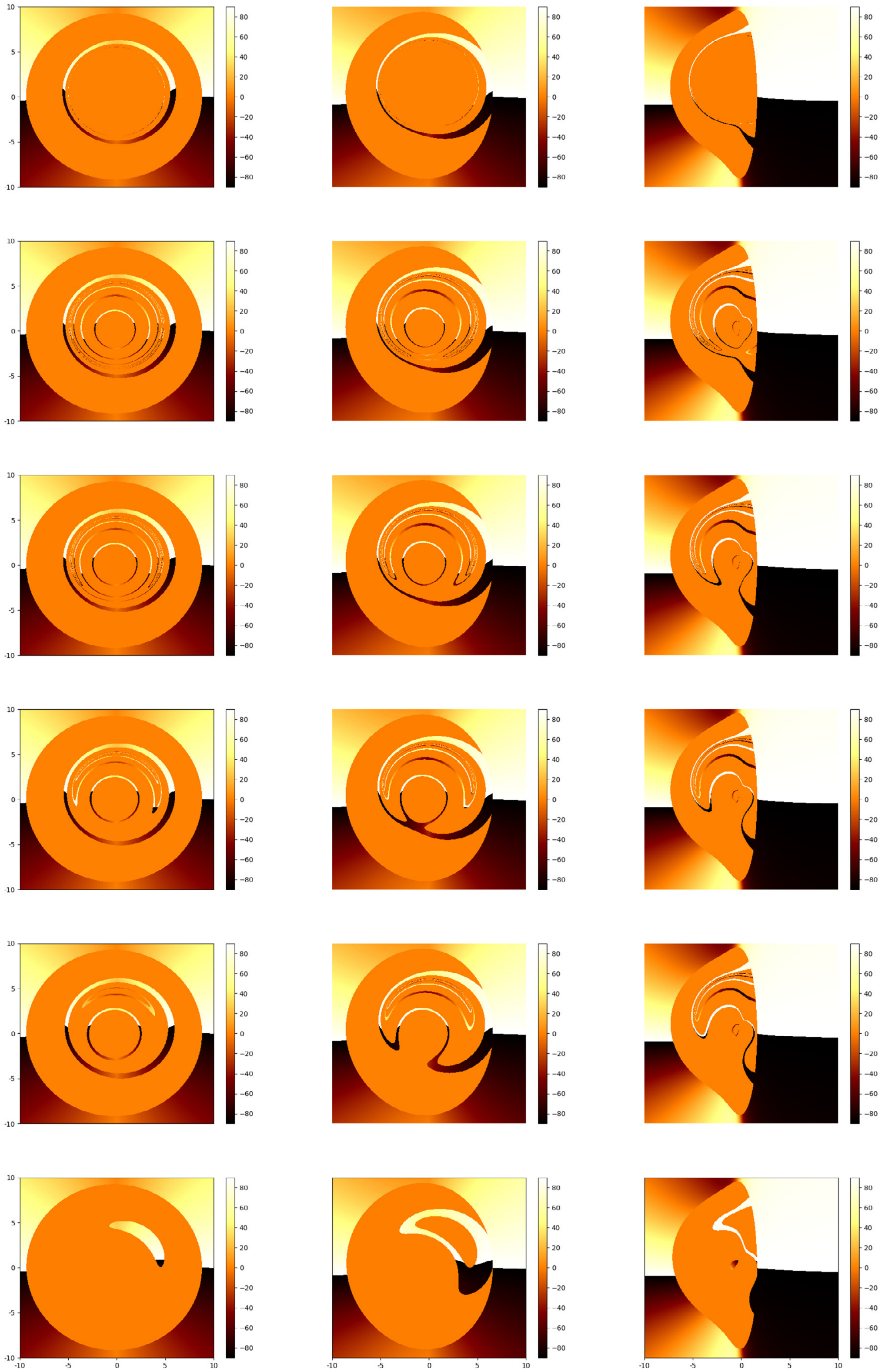

Fig. 4. Map of electric vector position angle (shown in color) for the initial toroidal distribution of magnetic field around a black hole or wormhole. From left to right, inclination angles are $i = 17^\circ, 45^\circ, 80^\circ$. From top to bottom, magnetic charge is $b = 0, 0.3, 0.5, 0.7, 0.9, 2.0$. Map scale to $-10Gm/c^3$ to $10Gm/c^3$

positioned at an angle $i = 17^\circ$ to the rotation axis of the black hole or wormhole. When the observer is positioned at an angle $i = 45^\circ$ or $i = 80^\circ$, the angle between the directions of linear polarization for the initial radial and toroidal magnetic fields will increase.

Figures 3 and 4 show maps of the electric vector position angle for the initial distribution of radial and toroidal magnetic fields, respectively. The color indicates the magnitude of the electric vector position angle. The angle varies from −90° to 90°. Comparing the maps of the electric vector position angle, the following conclusions can be drawn. The magnitude of the electric vector position angle for the radial magnetic field in the disk differs by approximately 90° from the corresponding magnitude for the toroidal magnetic field in the disk. Thus, using the maps of electric vector position angle, one can determine the directions of magnetic field in the disk, i.e., reconstruct the magnetic field topology.

Figures 5 and 6 show the dependencies of the absolute value of parameter on the magnetic charge value at different observer inclination angles to the rotation axis of the black hole or wormhole for cases of radial (Fig. 5) and toroidal (Fig. 6) magnetic fields in the disk. The black solid curve corresponds to the case when the observer is positioned at an angle $i = 17^\circ$ to the rotation axis of the black hole or wormhole, the blue dash-dotted curve corresponds to the case when $i = 45^\circ$, and the green dashed curve corresponds to the case when $i = 80^\circ$. The red vertical line defines the boundary between the black hole (left) and wormhole (right). Figures 5 and 6 show that β_2 remains constant for black holes and changes abruptly at the boundary between the black hole and wormhole. For the radial magnetic field in the disk, the absolute value of $|\beta_2|$ for the black hole will be less than for the wormhole. For the toroidal distribution of the magnetic field in the disk, the situation depends on the observer's inclination to the rotation axis of the black hole (wormhole). For inclinations $i = 17^\circ$ and $i = 45^\circ$, the absolute value of $|\beta_2|$ for the black hole will be less than for the wormhole, while for inclination $i = 80^\circ$ – the situation is reversed. Knowing the observer's inclination angle to the source's rotation axis (black hole or wormhole), the magnetic field distribution in the disk, and measuring the absolute value of $|\beta_2|$ linear polarization, one can conclude whether the source is a black hole or a wormhole.

4. CONCLUSION

This work numerically investigated the polarization properties of black holes and wormholes using the Lamy metric as an example. This metric accurately reproduces the Kerr rotating black hole metric for small magnetic charges and a rotating wormhole otherwise. Using the ray-tracing method, maps of linear polarization and electric vector position angle were constructed for both black hole and wormhole cases.

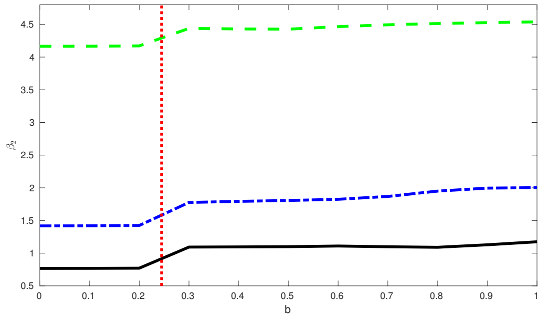

Fig. 5. Dependencies of the absolute value of parameter $|\beta2|$ on magnetic charge for radial magnetic field in the disk. The solid black curve corresponds to the case when the observer is located at an angle $i = 17^\circ$ to the rotation axis of the black hole or wormhole, the blue dash-dotted curve corresponds to the case $i = 45^\circ$, and the green dashed curve corresponds to the case $i = 80^\circ$. The red vertical dotted line corresponds to the boundary between the black hole (left) and wormhole (right)

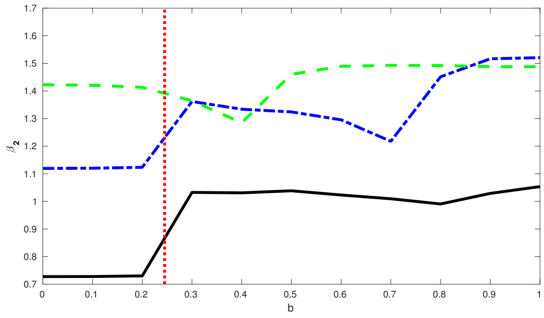

Fig. 6. Dependencies of the absolute value of parameter $|\beta2|$ on magnetic charge for toroidal magnetic field in the disk. The solid black curve corresponds to the case when the observer is located at an angle $i = 17^\circ$ to the rotation axis of the black hole or wormhole, the blue dash- dotted curve corresponds to the case $i = 45^\circ$, and the green dashed curve corresponds to the case $i = 80^\circ$. The red vertical dotted line corresponds to the boundary between the black hole (left) and wormhole (right)

The photon emission source was set as a thin disk with toroidal or radial magnetic field. Maps of linear polarization and electric vector position angle were constructed. The dependence of the decomposition coefficient $|\beta_2|$ of linear polarization on the magnetic charge magnitude was constructed for different values of observer inclination angles to the rotation axis of the black hole (wormhole) and initial magnetic field distribution. A criterion for distinguishing between a black hole and a wormhole using linear polarization was proposed. By measuring linear polarization, one can reconstruct the magnetic field topology, calculate the decomposition coefficient $|\beta_2|$ and, knowing the inclination, determine whether the source is a black hole or a wormhole.

The study of alternative space-time geometries different from Kerr rotating black hole proves to be particularly timely in connection with the recent results of the Event Horizon Telescope group. The obtained images of galactic centers in M87* and SGR A* have opened new tests of general relativity in strong gravitational fields. The similarity of images of black holes, boson stars, wormholes, and other objects encourages researchers to study alternative geometries in more detail.

APPENDIX

In the Newman-Penrose formalism, four null vectors are introduced ***l, n, m, m****, which satisfy the following conditions [10]: orthogonality condition

$$l \cdot m = l \cdot m^* = n \cdot m = n \cdot m^* = 0, \qquad (16)$$

isotropy condition

$$l \cdot l = n \cdot n = m \cdot m = m^* \cdot m^* = 0 \qquad (17)$$

and normalization condition

$$l \cdot n = 1, \quad m \cdot m^* = -1, \qquad (18)$$

where the asterisk denotes complex conjugation. By analogy with the Kerr black hole, it can be shown that in the Lamy metric, the following tetrad of vectors satisfies the above relations:

$$l^\alpha = \frac{1}{\Delta}(r^2 + a^2, \Delta, 0, a), \qquad (19)$$

$$n^\alpha = \frac{1}{2\Sigma}(r^2 + a^2, -\Delta, 0, a), \qquad (20)$$

$$m^\alpha = \frac{1}{\sqrt{2}\bar{\rho}}\left(ia\sin\theta, 0, 1, \frac{i}{\sin\theta}\right), \qquad (21)$$

$$m^{\alpha*} = \frac{1}{\sqrt{2}\bar{\rho}^*}\left(-ia\sin\theta, 0, 1, \frac{-i}{\sin\theta}\right). \qquad (22)$$

For the chosen tetrad of null vectors, the non-zero λ-symbols (see definition of λ-symbols in [10]) are determined by the following relations:

$$\lambda_{(1)(2)(2)} = -\left(\frac{r - M - rM'}{\Sigma} - \frac{r\Delta}{\Sigma^2}\right), \qquad (23)$$

$$\lambda_{(1)(3)(2)} = \frac{\sqrt{2}ira\sin\theta}{\bar{\rho}\Sigma}, \quad \lambda_{(1)(3)(4)} = \frac{1}{\bar{\rho}^*}, \qquad (24)$$

$$\lambda_{(1)(4)(2)} = -\frac{\sqrt{2}ira\sin\theta}{\bar{\rho}^*\Sigma}, \quad \lambda_{(1)(4)(3)} = \frac{1}{\bar{\rho}}, \qquad (25)$$

$$\lambda_{(2)(1)(3)} = -\frac{\sqrt{2}a^2\sin\theta\cos\theta}{\bar{\rho}\Sigma}, \qquad (26)$$

$$\lambda_{(2)(1)(4)} = -\frac{\sqrt{2}a^2\sin\theta\cos\theta}{\bar{\rho}^*\Sigma}, \qquad (27)$$

$$\lambda_{(2)(3)(4)} = -\frac{\Delta}{2\Sigma\bar{\rho}^*}, \quad \lambda_{(2)(4)(3)} = -\frac{\Delta}{2\Sigma\bar{\rho}}, \qquad (28)$$

$$\lambda_{(3)(1)(4)} = -\frac{2ia\cos\theta}{\Sigma}, \qquad (29)$$

$$\lambda_{(3)(2)(4)} = -\frac{ia\Delta\cos\theta}{\Sigma^2}, \lambda_{(3)(3)(4)} = \frac{r\cos\theta + ia}{\sqrt{2}\sin\theta\bar{\rho}^2}, \qquad (30)$$

$$\lambda_{(3)(4)(4)} = \frac{ia - r\cos\theta}{\sqrt{2}\sin\theta\bar{\rho}^{*2}}. \tag{31}$$

The spin coefficients (see definition of spin coefficients in [10]) in the Lamy metric are equal to

$$\kappa = \sigma = \nu = \lambda = \varepsilon = 0, \tag{32}$$

$$\mu = -\frac{\Delta}{2\Sigma\bar{\rho}^{*}}, \quad \pi = \frac{ia\sin\theta}{\sqrt{2}\bar{\rho}^{*2}}, \tag{33}$$

$$\tau = -\frac{ia\sin\theta}{\sqrt{2}\Sigma}, \quad \rho = -\frac{1}{\bar{\rho}^{*}}, \tag{34}$$

$$\beta = \frac{\cos\theta}{2\sqrt{2}\sin\theta\bar{\rho}}, \quad \alpha = \pi - \beta^{*}, \tag{35}$$

$$\gamma = \mu + \frac{r - M - rM'}{2\Sigma}. \tag{36}$$

It can be noted that only the spin coefficient Υ in the Lamy metric differs from the spin coefficient Υ in the Kerr metric.

The Weyl scalar ψ_2 in the Lamy metric is non-zero and equals

$$\Psi_2 = -\frac{M}{(r - ia\cos\theta)^3} + rM'\frac{r + ia\cos\theta}{\Sigma^2}. \tag{37}$$

In the case when $b = 0$, this expression transitions into the Weyl scalar Ψ_2 in the Kerr metric.

The equations of photon motion in the spacetime of Lamy metric in Boyer-Lindquist coordinates have the same form as in the Kerr metric:

$$\begin{aligned}
\Sigma p^t &= \frac{r^2 + a^2}{\Delta}(r^2 + a^2 - aL) - a^2\sin^2\theta + aL, \\
\Sigma p^r &= \sqrt{(r^2 + a^2 - aL)^2 - \Delta(Q + (a - L)^2)}, \\
\Sigma p^\theta &= \sqrt{Q + a^2\cos^2\theta - L^2\frac{\cos^2\theta}{\sin^2\theta}}, \\
\Sigma p^\phi &= \frac{a}{\Delta}(r^2 + a^2 - aL) + \frac{L}{\sin^2\theta} - a.
\end{aligned} \tag{38}$$

Let us recall that the quantity Δ includes parameter (2).

Physical quantities are defined by introducing an orthonormal tetrad. Let us specify an orthonormal tetrad of the form (see [10])

$$\begin{aligned}
e^{\alpha}_{(t)} &= (e^{-\nu}, \omega e^{-\nu}, 0, 0), \\
e^{\alpha}_{(r)} &= (0, e^{-\mu_2}, 0, 0), \\
e^{\alpha}_{(\theta)} &= (0, 0, e^{-\mu_3}, 0), \\
e^{\alpha}_{(f)} &= (0, 0, 0, e^{-\Psi}),
\end{aligned} \tag{39}$$

where the metric coefficients $e^{\nu}, e^{\Psi}, e^{\mu_2}, e^{\mu_3}, \omega$ are given in the Appendix of paper [8]. The index in parentheses denotes the tetrad index.

We relate quantities in the tetrad basis with quantities in Boyer-Lindquist coordinates through the relations

$$f^{\alpha} = e^{\alpha}_{(a)} f^{(a)}, \quad p^{(a)} = e^{(a)}_{\alpha} p^{\alpha}.$$

In expanded form we have

$$f^t = e^{-\nu} f^{(t)}, \quad p^{(t)} = e^{\nu} p^t, \tag{40}$$

$$f^r = e^{-\mu_2} f^{(r)}, \quad p^{(r)} = e^{\mu_2} p^r, \tag{41}$$

$$f^\theta = e^{-\mu_3} f^{(\theta)}, \quad p^{(\theta)} = e^{\mu_3} p^\theta, \tag{42}$$

$$f^\phi = e^{-\Psi} f^{(\phi)} + \omega e^{-\nu} f^{(t)}, \quad p^{(\phi)} = e^{\Psi} p^\phi - \omega e^{\Psi} p^t. \tag{43}$$

4-vector of polarization is expressed through the magnetic field in tetrad basis by the formulas

$$f^{(t)} = 0, \tag{44}$$

$$f^{(r)} \propto p^{(\phi)} B^{(\theta)} - p^{(\theta)} B^{(\phi)}, \tag{45}$$

$$f^{(\theta)} \propto p^{(r)} B^{(\phi)} - p^{(\phi)} B^{(r)}, \tag{46}$$

$$f^{(\phi)} \propto p^{(\theta)} B^{(r)} - p^{(r)} B^{(\theta)}. \tag{47}$$

Radial field corresponds to the case

$$B^{(r)} = 1, \quad B^{(\theta)} = B^{(\phi)} = 0,$$

toroidal field corresponds to the case

$$B^{(\phi)} = 1, \quad B^{(r)} = B^{(\theta)} = 0.$$

Without loss of generality, we assumed that $f^{(t)} = 0$. By specifying the magnetic field, we can determine the 4-vector of polarization in the radiation source $f^{(a)}$ and using Walker—Penrose constants find the polarization at the observation point. At infinity $r \to \infty$ the values of photon 4-momentum are equal to

$$p^t \to 1, \quad p^r \to 1, \quad p^\phi \to \frac{\lambda}{r^2 \sin^2\theta}, \tag{48}$$

$$p^\theta \to \frac{\sqrt{\eta + a^2\cos^2\theta - \lambda^2\dfrac{\cos^2\theta}{\sin^2\theta}}}{r^2}, \tag{49}$$

and 4-vectors of polarization are expressed through Walker—Penrose constants as follows:

$$\sin\theta_0 f^\phi = -\frac{1}{r}\frac{K_1D_1 + K_2D_2}{\eta + (a-\lambda)^2}, \tag{50}$$

$$f^\theta = \frac{1}{r}\frac{K_1D_2 - K_2D_1}{\eta + (a-\lambda)^2}, \tag{51}$$

where

$$\begin{aligned} D_1 &= \sqrt{\eta + a^2\cos^2\theta_0 - \lambda^2\frac{\cos^2\theta_0}{\sin^2\theta_0}}, \\ D_2 &= \frac{\lambda}{\sin\theta_0} - a\sin\theta_0. \end{aligned} \tag{52}$$

Electric field is expressed through polarization 4-vectors as follows:

$$E^f = -r\sin\theta_0 f^f, \quad E^\theta = -rf^\theta. \tag{53}$$

Stokes parameters of linear polarization are defined as

$$Q = E^{\phi 2} - E^{\theta 2}, \quad U = -2E^\phi E^\theta. \tag{54}$$

To calculate the decomposition coefficient β_m, in the integral

$$\beta_m = \int_0^{\rho_{max}}\int_0^{2\pi} P(\rho,\phi)e^{-im\phi}\rho d\rho d\phi \tag{55}$$

we make a change of variables from polar coordinates to Cartesian:

$$x = \rho\cos\phi, \quad y = \rho\sin\phi,$$

$$\rho^2 = x^2 + y^2, \quad \phi = \frac{y}{x}.$$

The Jacobian of transformation equals

$$J = \frac{1}{\sqrt{x^2 + y^2}}.$$

As a result, we obtain

$$\beta_m = \int_{-10}^{10}\int_{-10}^{10} P(x,y)e^{-im\frac{y}{x}}dxdy =$$

$$= \int_{-10}^{10}\int_{-10}^{10} [Q\cos m\phi + U\sin m\phi +$$

$$+i(U\cos m\phi - Q\sin m\phi)]dxdy, \tag{56}$$

where integration limits are determined by the sizes of polarization maps (see Fig. 1—4). Coefficient β_2 equals

$$\beta_2 = \int_{-10}^{10}\int_{-10}^{10} [Q\cos 2\phi + U\sin 2\phi +$$

$$+i(U\cos 2\phi - Q\sin 2\phi)]dxdy, \tag{57}$$

from which we easily obtain

$$\cos 2\phi = \frac{1 -^2 \phi}{1 +^2 \phi} = \frac{x^2 - y^2}{x^2 + y^2}, \tag{58}$$

$$\sin 2\phi = \frac{2\phi}{1 +^2 \phi} = \frac{2xy}{x^2 + y^2}. \tag{59}$$

REFERENCES

1. The Event Horizon Telescope Collaboration et. al. Ap.J.L., 875, L1 (2019).

2. The Event Horizon Telescope Collaboration et. al. Ap.J.L., 930, L12 (2022)

3. S.V. Chernov, Astronomy Reports, 65, 110 (2021).

4. The Event Horizon Telescope Collaboration et. al. Ap.J.L., 910, L12 (2021).

5. The Event Horizon Telescope Collaboration, Astrophys. J. Lett. 910, L13 (2021).

6. F. Lamy, et.al., Classical and Quantum Gravity, 35, 115009 (2018).

7. Z.-Y. Fan, X. Wang, Phys.Rev.D, 94, 124027 (2016).

8. S.V. Chernov, Astronomy Reports, 67, 798 (2023).

9. C.T. Cunningham, J.M. Bardeen, Ap.J. 173, L137 (1972).

10. S. Chandrasekhar, The Mathematical Theory of Black Holes, Moscow, Nauka (1986).

11. D.C.M. Palumbo, G.N. Wong, B.S. Prather, Ap.J. 894, 156 (2020).

JOURNAL OF EXPERIMENTAL AND THEORETICAL PHYSICS, 2024, Vol. 165, No. 6, pp. 811–816

NUCLEI, PARTICLES, FIELDS, GRAVITY AND ASTROPHYSICS

GENERALIZED EINSTEIN–ROSEN BRIDGE INSIDE BLACK HOLES

© 2024 V. I. Dokuchaev *, K. E. Prokopev **
Institute for Nuclear Research of the Russian Academy of Sciences 117312 Moscow, Russia
** e-mail: dokuchaev@inr.ac.ru*
*** e-mail: d1vais@yandex.ru*

Received January 19, 2024
Revised February 09, 2024
Accepted February 10, 2024

Abstract. We generalize the notion of Einstein–Rosen bridge by defining it as a space-ilke connection between two universes with regions of asymptotically minkowskian space-time infinities. The corresponding symmetry and asymmetry properties of the generalized Einstein–Rosen bridge are considered at the cases of Reissner–Nordström and Kerr metrics. We elucidate the versatility of intriguing symmetry and asymmetry phenomena outside and inside black holes. For description of the test particle (planet and photon) motion it is used the Kerr–Newman metric of the rotating and electrically charged black hole. It is demonstrated the symmetry and asymmetry of the one-way Einstein–Rosen bridge inside black hole space-time toward and through the plethora of endless and infinite universes.

DOI: 10.31857/S004445102406e063

1. INTRODUCTION

In this paper, we generalize the notion of Einstein–Rosen bridge by defining it as a space-like connection between two universes with regions of asymptotically minkowskian space-time infinities. The corresponding symmetry and asymmetry properties of the generalized Einstein–Rosen bridge are considered at the cases of Reissner–Nordström and Kerr metrics. We elucidate the versatility of intriguing symmetry and asymmetry phenomena outside and inside black holes. For description of the test particle (planet and photon) motion it is used the Kerr–Newman metric of the rotating and electrically charged black hole. It is demonstrated the symmetry and asymmetry of the one-way Einstein–Rosen bridge inside black hole toward and through the plethora of endless and infinite universes.It seems that the original idea of an infinite series of bridges between universes in the Kerr metric belongs to Boyer and Lindquist [1]. The Reissner–Nordström and Kerr one-way bridge is discussed in Chapter 6.5 of Carroll's textbook [2] and also in Chapters 3.5 and 4.4 of Ullmann's textbook [3]. The last book also points to the physical obstacles to the existence of such a bridge between universes, which can be associated with various types of instabilities (including quantum ones), which are discussed for example in [4,5] and more modern attempts [6]. However, the problem still remains open. Recently symmetrical geodesic motion, bound and unbound orbits and the possibility of passing through the Reissner –Nordström and Kerr bridge are also analyzed in [7] and [8] respectively.

2. BASICS OF THE KERR–NEWMAN METRIC

The famous Kerr–Newman metric or geometry (see e. g., [9–13]), which is the exact solution of Einstein's equations [14–20] for a rotating and electrically black hole, is

$$ds^2 = -\frac{\Delta}{\Sigma}\Big[dt - a\sin^2\theta d\varphi\Big]^2 +$$

$$+\frac{\sin^2\theta}{\Sigma}\Big[\Big(\mathrm{r}^2+\alpha^2\Big)d\varphi - \alpha dt\Big]^2 + \frac{\Sigma}{\Delta}dr^2 + \Sigma d\theta^2, \quad (1)$$

where (r, q, φ) are spherical coordinates and t is the time of static distant observer at the asymptotically radial infinity. In this metric

$$\Delta = r^2 - 2\mathrm{Mr} + a^2 + q^2, \quad (2)$$

$$\Sigma = r^2 + a^2\cos^2\theta, \quad (3)$$

M — black hole mass, q — black hole electric charge, $a = J/M$ — specific black hole angular momentum (spin). The two roots of equation $\Delta = 0$ are

$$r_+ = M + \sqrt{M^2 - a^2 - q^2}\ , \tag{4}$$

the event horizon of the black hole and

$$r_- = M + \sqrt{M^2 - a^2 - q^2}\ , \tag{5}$$

the internal Cauchy horizon of the black hole. In this paper we consider Kerr metric with the black hole event horizon, corresponding to

For simplification of equation and presentation of Figures we will often use units $G = 1$, $c = 1$, $M = 1$, and corresponding dimensionless parameters: radius $r \Rightarrow r/M$, time $t \Rightarrow t/M$, black hole spin $a \Rightarrow a/M$ and black hole charge $q \Rightarrow q/M$.

In the Kerr – Newman metric there the following in-tegrals of motion for test particles [10]: μ — particle mass, E — particle total energy, L — particle azimuthal angular moment and Q — the so-called Carter constant, related with the non-equatorial particle motion.

The corresponding equations of test particle motion in the Kerr–Newman metric in the differential form are [10–13]

$$\Sigma\frac{dr}{d\tau} = \sqrt{R}\ , \tag{6}$$

$$\Sigma\frac{d\theta}{d\tau} = \sqrt{\Theta}\ , \tag{7}$$

$$\Sigma\frac{d\varphi}{d\tau} = -\left(aE - \frac{L}{\sin^2\theta}\right) + \frac{a}{\Delta}P, \tag{8}$$

$$\Sigma\frac{dt}{d\tau} = -a(aE\sin^2\theta - L) + (r^2 + a^2)\frac{P}{\Delta}, \tag{9}$$

Here

$$P = E(r^2 + a^2) - aL + \varepsilon qr, \tag{10}$$

τ — the proper time of a test massive particle or an affine parameter along the trajectory of a massless particle ($\mu = 0$) like photon, ε — the electric charge of test particle. Respectively, the effective radial potential $R(r)$ is

$$R(r) = P^2 - \Delta\,[\mu^2 r^2 + (L - aE)^2 + Q], \tag{11}$$

and the effective polar potential $\Theta(\theta)$ is

$$\Theta(\theta) = Q - \cos^2\theta\,[a^2(\mu^2 - E^2) + L^2\sin^{-2}\mathrm{\theta}]. \tag{12}$$

Trajectories of massive particles ($\mu \neq 0$) depend on three parameters: $\Upsilon = E/\mu$, $\lambda = L/\mu$ and Q/μ^2.

Meantime, trajectories of massless particles like photons (the null geodesics) depend only on two parameters: λ and Q.

The nontrivial specific feature of the rotating Kerr black hole ($a \neq 0$) is the existence of so-called ergosphere [12, 13, 17, 19, 20] with the outer boundary

$$r_{\mathrm{ES}}(\theta) = 1 + \sqrt{1 - q^2 - a^2\cos^2\theta}\ , \tag{13}$$

Inside the ergosphere any test object is dragged into insuperable rotation around black hole with infinite azimuthal winding by approaching the black hole event horizon. Note that the winding effect was discussed also in [8, 21].

In the following Sections we will describe the symmetry and asymmetry of test object motion in the gravitational field of the Kerr–Newman black hole. We use equations of motion in the Kerr–Newman metric (6)–(9) in our analytic and numerical calculations of test particle geodesic trajectories [22–32].

3. ONE-WAY EINSTEIN–ROSEN BRIDGE INSIDE BLACK HOLE

We start to elucidate the versatility of intriguing symmetry and asymmetry phenomena outside and inside black holes by using the Carter–Penrose diagrams (for details see, i. e., [12, 13, 17, 18]), describing in particular the global space-time structure of black holes. The evident manifestation of *symmetry* of this global structure is infinite space volumes as outside and inside the black hole event horizon. See in Fig. 1 the corresponding Carter–Penrose diagram for the Reissner–Nordström black hole, which is a special spherically symmetric case of Kerr–Newman black hole without rotation, i. e., $a = 0$ but $q \neq 0$. From the pure geometric point of view this diagram is both left-right and up-down symmetric. On the contrary, from the physical or space-time point view this diagram is absolutely asymmetric due to the inexorable upward flow of time not only at this diagram but throughout the

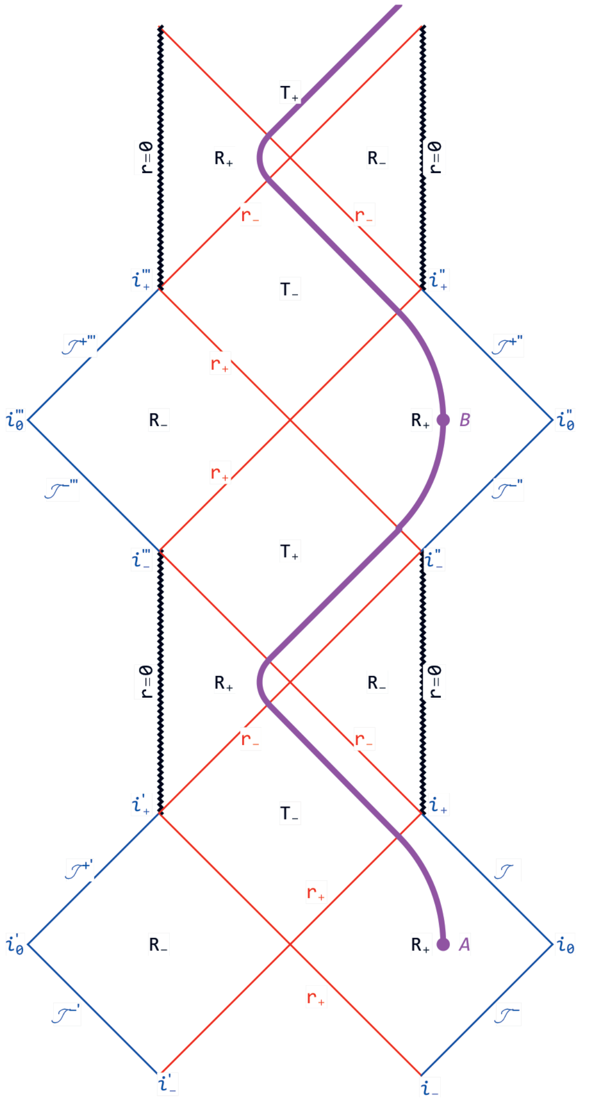

Fig. 1. Carter–Penrose diagram for the spherically symmetric Reissner–Nordström black hole with electric charge q = 0.99. The spaceship starts from the point A at R_+-region toward its multi-planetary future inside the black hole. The astronauts are planning to use the Einstein–Rosen bridge (magenta curve) and intersect both the black hole event horizon r_+ and Cauchy horizon r_- – at finite their proper time. After appearing near the black hole singularity at $r = 0$, the spaceship uses its powerful engines to change the direction of motion and escape the tidal destruction at small radii. In result, the voyage is happily finishing at point B (may be at the Earth-like planet) in another infinite universe. The symmetry is in possibility to repeat the complete route of this voyage staring from the point B but only in the forward direction in time to-ward another multi-planetary future. It is impossible to return the native Earth due to impossibility of any motion beyond the light cone. This is the motion *asymmetry* on the one-way Einstein – Rosen bridge inside black hole

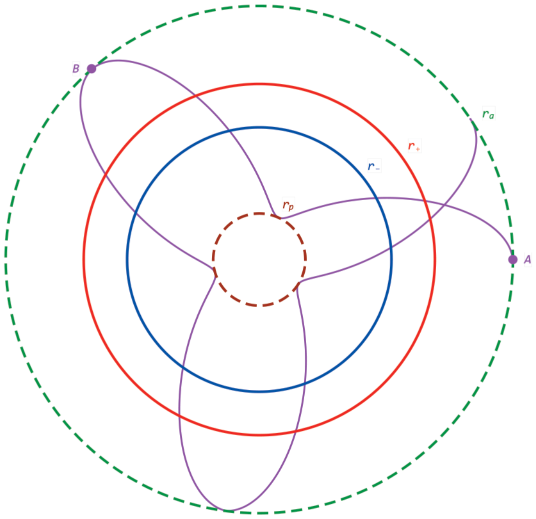

Fig. 2. $2D$ presentation of the voyage through the Reissner–Nordström black hole interiors by using the Einstein–Rosen bridge. This picture is geometrically absolutely *symmetric* or, in other words, it is nicely *symmetric*. At the same time, this picture is misleading and physically controversial: Indeed. the voyage is starting at apogee r_a from the position at point$A$, then reach the perigee r_p and return the apogee r_a at the point B for a finite proper time, demonstrating the absolute geometric *symmetry*. Meanwhile, there is a crucial hitch: this apogee r_a at the point B is not in the native universe, but in the other quite distant universe, as it is clearly viewed at the Carter – Penrose diagram in Fig. 1. The apogee r_a and perigee r_p radii are shown by dashed circles. Respectively, the event radii of event horizon r_+ and Cauchy horizon r_- are shown by solid circles. The magenta curve here and in the Fig. 4 is numerically calculated geodesic trajectory with using equations of motion (6)–(9) for massive test particles

whole universe. More precisely it means that in the General Relativity all objects are allowed to move only inside the upward directed light cones (at ±45° with respect to the upward direction. The upward directed light cone is the inexorable *asymmetry* of the world.

$2D$ presentation of the voyage through the interiors of Reissner–Nordström black hole with interiors by using the Einstein–Rosen bridge is shown in Fig. 2. The electric charge of the black hole is e = 0.99. A test planet (or spaceship) with the electric charge $\varepsilon = -1.5$ is periodically orbiting around black holes with orbital parameters $\Upsilon = 0.5$, $\lambda = 0.5$, corresponding to the maximal radius (apogee) $r_{\max} = 1.65$ and minimal radius (perigee) $r_{\min} = 0.29$, respectively, in dimensional units.

The periodic planet geodesic trajectories (magenta curves, both at Fig. 2 and Fig. 4), were calculated

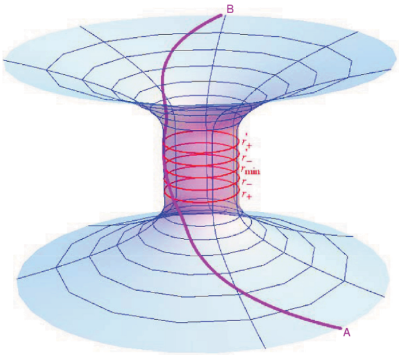

Fig. 3. Embedding diagram for the voyage through black hole interiors by using the Einstein–Rosen bridge. This bridge connects two asymptotically flat universes like wormhole tunnel, but with the only one-way motion from the initial point *A* to the final point *B*. The geometrical *symmetry* of this embedding diagram is deceptive. In fact, this embedding diagram demonstrate the asymmetric space-time origin of the one-way Einstein–Rosen bridge (remember about loss-cone)

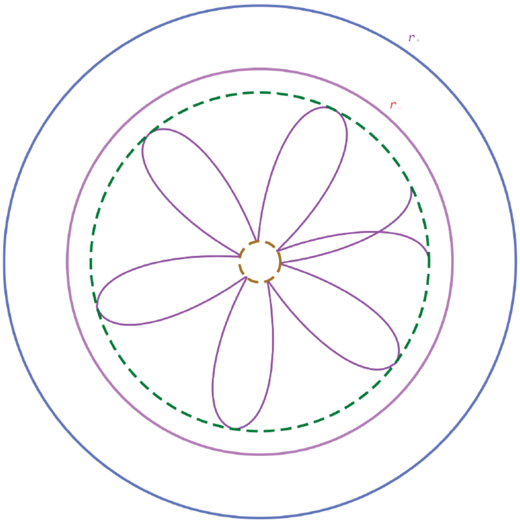

Fig. 4. Both the geometrical and physical completely symmetric picture of the periodic orbital motion of the test planet or spaceship around the central singularity of the Reissner–Nordström black hole inside the Cauchy horizon r_-. The asymmetric Reissner–Nordström bridge is only needed for penetration into this very exotic region at $0 < r < r_-$, where exist the nearly stable periodic orbits for test particles, which are very similar to the periodic orbits outside the black hole event horizon r_+. The apogee r_a and perigee r_p radii are shown by dashed circles. Respectively, the event radii of event horizon r_+ and Cauchy horizon r_- are shown by solid circles

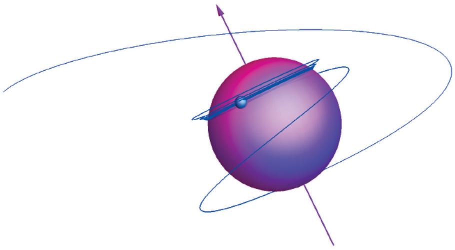

Fig. 5. Trajectory of the test planet ($\mu \neq 0$) with orbital parameters $\Upsilon = 0.85$, $\lambda = 1.7$ and $Q = 1$ plunging into the fast-rotating Kerr black hole with spin $a = 0.9982$. This test planet starts from the upper hemisphere very far from the black hole. Inside the ergosphere (13) this planet is winding up on the black hole event horizon higher the black hole equatorial plane. Blue curve here is the numerically calculated geodesic trajectory with using equations of motion (6)–(9) for test particles

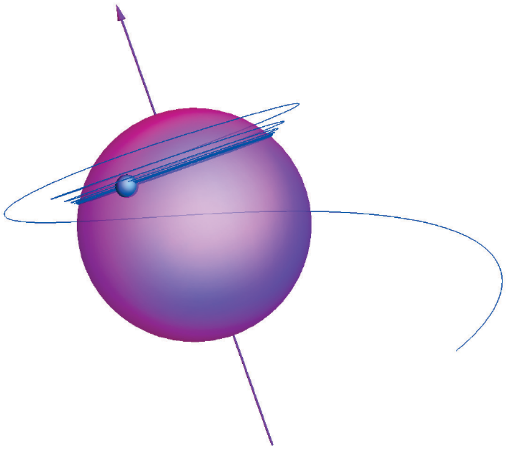

Fig. 6. Trajectory of the test planet ($\mu \neq 0$) with orbital parameters $\Upsilon = 0.85$, $\lambda = 1.7$ and $Q = 1$ plunging into the fast-rotating Kerr black hole with spin $a = 0.9982$. This test planet starts from the lower hemisphere very far from the black hole. Inside the ergosphere this planet is winding up on the black hole event horizon higher the black hole equatorial plane. Blue curve here is the numerically calculated geodesic trajectory with using equations of motion (6)–(9) for test particles

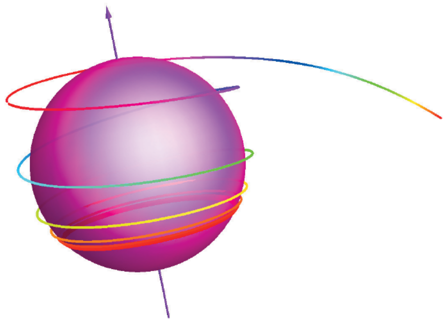

Fig. 7. Photon trajectory with orbital parameters $\lambda = 2$ and $Q = 1$. This photon is plunging into the fast-rotating Kerr black hole with $a = 0.9982$ and is winding up on the black hole event horizon below the equatorial plane. Multi-colored curve is the numerically calculated geodesic trajectory with using equations of motion (6)–(9) for massless test particles like photons ($\mu = 0$)

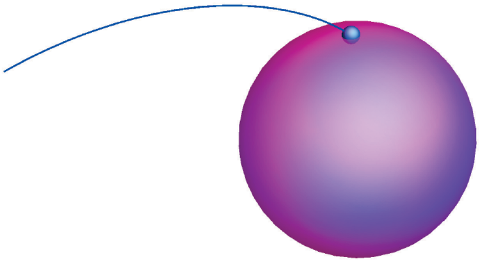

Fig. 9. A trivial but though very expressive trajectory of a test planet ($\mu \neq 0$) with parameters $\Upsilon = 1$, $\lambda = 1$ and $Q = 0.5$, which is plunging into the spherically *symmetric* and nonrotating Schwarzschild black hole (with both the spin $a = 0$ and electric charge $q = 0$). The starting point for this numerically calculated crazy voyage is at the radial distance $r = 6$

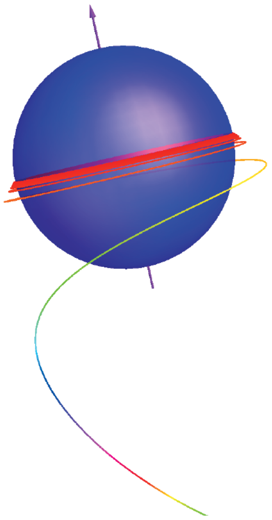

Fig. 8. Numerically calculated photon ($\mu = 0$) trajectory with orbital parameters $\lambda = -1.493$ and $Q = 12.99$, which is plunging into the fast-rotating Kerr black hole with spin $a = 0.9982$. It must be stressed that at large distances from black hole the test particle with negative azimuthal angular momentum ($\lambda = -2.811$) rotates in opposite direction with respect to the black hole. Meanwhile, by approaching the black hole (*inside the ergosphere*) test particle is forced to rotate in the same direction as black hole

numerically by using equations of motion (6)–(9) for massive test particles ($\mu \neq 0$). Note, that the periodical motion of the test planet is limited in time due to energy losses in inevitable emission of the gravitational waves.

The picture in Fig. 2 is geometrically absolutely symmetric or, in other words, it is completely or nicely symmetric. The geodesic trajectories of test planet ($\mu \neq 0$) in this Fig. 2 and in Fig. 3 (the red curves), are numerically calculated [22–32], by using the corresponding equations of motion in the Kerr–Newman metric (6)–(9).

At the same time, this picture is misleading and physically controversial: Indeed, the voyage is starting at apogee r_a from the position at point A, then reach the perigee r_p and return the apogee r_a at the point B for a finite proper time, demonstrating the absolute geometric *symmetry*. Meanwhile, there is a crucial hitch: this apogee r_a at the point B is not in the native universe, but in the other quite distant universe, as it is clearly viewed at the Carter–Penrose diagram in Fig. 1. This hitch again destroys the Einstein–Rosen bridge *symmetry*.

Figure 3 shows the embedding diagram for the voy-age through black hole interiors by using the Einstein–Rosen bridge. The embedding diagram is very useful for the training of intuitive understanding of the peculiarities of the enigmatic black holes. In this embedding diagram the Einstein–Rosen bridge connects two asymptotically flat universes like wormhole tunnel [33, 34], but with the only one-way motion from the initial point A to the final point B. The geometrical *symmetry* of this embedding diagram is deceptive. In fact, this embedding diagram demonstrate the *asymmetric* space-time origin of the one-way Einstein–Rosen bridge (remember about loss-cone).

The completely *symmetric* picture of the periodic orbital motion of the test planet or spaceship around the central singularity of the Reissner–Nordström black hole inside the Cauchy horizon r_- is shown in Fig. 4. The electric charge of the black hole is $e = 0.99$ and test planet (or spaceship) with the electric charge $\varepsilon = -1.5$ is periodically orbiting around black holes with orbital parameters $\Upsilon = 1.7$, $\lambda = 0.1$, corresponding to the maximal radius (apogee) $r_{\max} = 0.75$ and minimal radius (perigee) $r_{\min} = 0.09$, respectively. The *asymmetric* Reissner–Nordström bridge is only needed for penetration into this very exotic region at $0 < r < r_-$, where exist the nearly stable periodic orbits for test particles [35–41], which are very similar to the periodic orbits outside the black hole event horizon r_+.

4. SYMMETRY AND ASYMMETRY OF TEST PARTICLE TRAJECTORIES NEAR ROTATING BLACK HOLE

Figures 5–7 demonstrate both symmetry and asymmetry features of massive and massless particle trajectories plunging into rotating Kerr black hole with spin $a = 0.9982$. Magenta arrows shows the direction of the black hole rotation in accordance with the gimlet rule. The multi-colored curves at Figs. 7 and 8 are the geodesic trajectories for massless test particles like photons ($\mu = 0$) numerically calculated with using equations of motion (6)–(9). By approaching the black hole, the trajectories of all particles, both massive and massless ones, are infinitely winding up on the black hole event horizon in the direction of the black hole rotation and at the fixed latitudes. This winding up is a manifestation of *symmetry* of behavior of all trajectories, plunging into rotating black hole. At the same the direction of the black hole rotation is a corresponding manifestation of *asymmetry* of the gravitational field of the Kerr metric.

At last, for completeness of black hole *symmetric* and *asymmetric* properties, at Fig. 9 is shown the trajectory of the test planet ($\mu \neq 0$) with parameters $\Upsilon = 1$, $\lambda = 1$ and $Q = 0.5$. This test planet is plunging into the spherically symmetric and nonrotating Schwarzschild black hole (with both the spin $a = 0$ and electric charge $q = 0$), starting from the radial distance $r = 6$. It must be especially checked that the traversable (though only one-way in time and direction) Einstein–Rosen bridge is absent at all

5. CONCLUSION AND DISCUSSION

It is demonstrated the symmetry and asymmetry of the voyage on one-way Einstein–Rosen bridge inside black hole toward the endless multiplanetary future. The apparent symmetry of both the Carter–Penrose and embedding diagrams is mainly related with a pure geometrical vision of this phenomenon. Quite the contrary, the physical (space-time) vision elucidates the absolute asymmetry of the Einstein – Rosen bridge due to existence of the light-cone limitation for possible motions.

Note, that the traversable (though only one-way in time and direction) Einstein–Rosen bridge exist only in the case of both rotating Kerr $a \neq 0$ and electrically charged Reissner–Nordström $q \neq 0$ black holes. It is absent at all inside the Schwarzschild black hole (see for details, e. g., [12, 14]) inside the Schwarzschild black hole (see for details, e. g., [12, 14]).The infinite winding up of trajectories of all particles on the black hole event horizon is a manifestation of symmetry behavior of all trajectories, plunging into rotating black hole. At the same time, the fixed direction in space of the black hole rotation axis is a strict manifestation of the Kerr metric both symmetry and asymmetry.

ACKNOWLEDGMENTS

We are grateful to E. O. Babichev, V. A. Berezin, Yu. N. Eroshenko, N. O. Nazarova and A. L. Smirnov for stimulating discussions. Authors also are very indebted to anonymous reviewer for suitable references and historical remarks which improve the presentation of paper.

REFERENCES

1. R. H. Boyer and R. W. Lindquist, J. Math. Phys. 8,265 (1967).
2. S. Carroll, An Introduction to General Relativity, new international edition, Pearson (2014), p. 257.
3. V. Ullmann, Gravity, Black Holes and the Physics of Time-Space; Czechoslovak Astronomic Society, CSAV, Ostrava, (Online version in English: https://astronuclphysics.info/GravitCerneDiry.htm) (1986).
4. Y. Giirsel, V. D. Sandberg, I. D. Novikov, andA.A. Starobinskij, Phys. Rev. D 19, 413 (1979).
5. M. Simpson and R. Penrose, Int. J. Theor. Phys. 7,183 (1973).

6. R. DeMott, S. DeMott, and A. DeMott, Class. Quant. Grav. 39, 195015 (2022).

7. D. Abramson, Thai J. of Phys. 38, 69 (2021).

8. C. Dyson and M. van de Meent, Class. Quant. Grav.40, 195026 (2023).

9. R. P. Kerr, Phys. Rev. Lett. 11, 237 (1963).

10. B. Carter, Phys. Rev. 174, 1559 (1968).

11. I. D. Novikov, and K. S. Thorne, in Black Holes, ed. by C. DeWitt and B. S. DeWitt, Gordon and Breach, New York (1973), p. 343.

12. C. W. Misner, K. S. Thorne, and J. A. Wheeler, Gravitation, W. H. Freeman, San Francisco, CA, USA (1973).

13. S. Chandrasekhar, The Mathematical Theory of Black Holes, in The International Series of Monograph on Physics, Clarendon Press, Oxford (1983), Vol. 69, Chap. 7.

14. R. Penrose, Structure of Space-Time. Battelle Rencontres 1967. Lectures in Mathematical Physics, Chap. VII, ed. by C. M. Dewitt and J. A. Wheeler, W. A.Benjamin, Inc., New York–Amsterdam (1968), Chap. 2.

15. J. M. Bardeen, in Black Holes, ed. by C. DeWitt and B. S. DeWitt, Gordon and Breach Science Publishers, New York (1973), p. 215.

16. Y. Choquet-Bruhat, C. DeWitt-Morette, and M. Dillard-Bleick, Analysis, Manifolds and Physics, Part 1, Basics, Elsevier Science, Amsterdam (1977), Chap. V.

17. R. M. Wald, General Relativity, The Univ. of Chicago Press, Chicago (1984).

18. S. W. Hawking, and G. F. R. Ellis, The Large–Scale Structure of Space–Time, Cambridge Monographs on Mathematical Physics, Cambridge University Press, Cambridge (2011).

19. J. M. Bardeen, W. H. Press, and S. A. Teukolsky, Rotating Black Holes: Locally Nonrotating Frames, Energy Extraction, and Scalar Synchrotron Radiation, Astrophys. J. 178, 347 (1972).

20. J. M. Bardeen, B. Carter, and S. W. Hawking, Commun. Math. Phys. 31, 161 (1973).

21. T. P. Kling, E. Grotzke, K. Roebuck, and H.Roebuck,Gen. Rel. Grav. 51, 32 (2019).

22. E. O. Babichev, V. I. Dokuchaev, and Yu. N. Eroshenko, Uspekhi Fiz. Nauk 183 1257 (2013) [Phys. Usp. 56, 1155 (2013)].

23. V. I. Dokuchaev, GRG 46, 1832 (2014).

24. V. I. Dokuchaev and Yu. N. Eroshenko, Uspekhi Fiz. Nauk 185 829 (2015) [Phys. Usp. 58, 772 (2015)].

25. V. I. Dokuchaev and Yu. N. Eroshenko, Pisma JETP101, 875 (2015) [JETP Lett. 101, 777 (2015)].

26. V. I. Dokuchaev and N. O. Nazarova, J. High EnergyPhys. Lett. 106, 637 (2017).

27. V. I. Dokuchaev and N. O. Nazarova, https://youtu.be/P6DneV0vk7U (2017).

28. V. I. Dokuchaev and N. O. Nazarova, ZhETF 155, 677 (2019) [JETP 128, 578 (2019)].

29. V. I. Dokuchaev, N. O. Nazarova, and V. P. Smirnov, GRG 51, 81 (2019).

30. V. I. Dokuchaev, and N. O. Nazarova, Universe 5, 183 (2019).

31. V. I. Dokuchaev, IJMPD 28, 1941005 (2019).

32. V. I. Dokuchaev, and N. O. Nazarova, https://youtu.be/fps-3frL0AM (2019).

33. J. A. Wheeler, Geometrodynamics, Academic Press, New York (1962).

34. M. S. Morris and K. S. Thorne, Am. J. Phys. 56, 395 (1988).

35. J. Bičák, Z. Stuchlík, and V. Balek, Bull. Astron. Inst. Czech. 40, 65 (1989).

36. V. Balek, J. Bičák, and Z. Stuchlík, Bull. Astron. Inst. Czech. 40, 133 (1989).

37. S. Grunau and S. Kagramanova, Phys. Rev. D 83, 044009 (2011).

38. M. Olivares, J. Saavedra, C. Leiva, and J. R. Villanueva, Mod. Phys. Lett. A 26, 2923 (2011).

39. E. Hackmann, V. Kagramanova, J. Kunz, and C. Lam ¨merzahl, Phys. Rev. D 81, 044020 (2010).

40. D. Pugliese, H. Quevedo, and R. Ruffini, Phys. Rev. D 83, 024021, 23pp. (2011).

41. V. I. Dokuchaev, CQG 28, 235015 (2008).

JOURNAL OF EXPERIMENTAL AND THEORETICAL PHYSICS, 2024, Vol. 165, No. 6, pp. 818–827

SOLIDS AND LIQUIDS

MECHANISMS OF IRON DIFFUSION IN α-Ti

© 2024 N. D. Gorev[a, b], A. V. Bakulin[a*], S. E. Kulkova[a, b]

[a] *Institute of Strength Physics and Materials Science, Siberian Branch, Russian Academy of Sciences, 634055, Tomsk, Russia*

[b] *National Research Tomsk State University 634050, Tomsk, Russia*

**e-mail: bakulin@ispms.ru*

Received January 31, 2024
Revised February 13, 2024
Accepted February 17, 2024

Abstract. Within the transition state theory and the projector augmented-wave method, the mechanisms of iron diffusion in α-Ti were studied. The formation energies of interstitial and substitution defects, as well as the barriers of iron migration in α-Ti along possible paths through both interstitial and vacancy mechanisms were calculated. It was confirmed that the most preferred position for an iron interstitial atom is a crowdion, which formation energy is only 0.17 eV higher than that of iron defect on titanium site. Analytical expressions for the temperature-dependent diffusion coefficients of iron in two crystallographic directions for the interstitial mechanism were obtained by the Landman method. In general, the coefficients of iron diffusion in α-Ti and its anisotropy are consistent with experimental data, while the corresponding diffusion coefficients for the vacancy mechanism are several orders of magnitude lower. The obtained results allow us to conclude that the anomalously fast diffusion of iron in α-Ti is due to the interstitial mechanism.

Keywords: *titanium, impurity diffusion, diffusion mechanism, density functional method, transition state theory*

DOI: 10.31857/S004445102406e075

1. INTRODUCTION

Titanium and its alloys possess a complex of unique mechanical properties, making them promising materials for application in aerospace, automotive, shipbuilding, and other industries. The development of materials based on them with improved functional characteristics and mechanical properties remains a relevant task for many decades [1]. It is known that technically pure titanium has high corrosion resistance, including in aggressive environments containing chlorine and its derivatives, organic compounds with oxygen, and others. However, the addition of alloying impurities can significantly change its corrosion behavior. Furthermore, one of titanium's advantages is the possibility of its strengthening by oxygen, nitrogen, and small additions of other elements (for example, iron and palladium) to obtain different grades of metal suitable for numerous technological applications. The main difference between titanium grades lies in the content of oxygen and iron. Iron, along with elements such as chromium, manganese, cobalt, nickel, and others, belongs to β-eutectoid elements that stabilize the β-phase, lowering the β–α phase transformation temperature, equal to 1556 K. [2] Unlike β-isomorphous elements (Mo, V, and Ta), the solubility of iron in α-Ti is small, about 0.05 at.% [3]. Impurity diffusion can lead to local changes in their concentration and negatively affect titanium properties.

Many processes in materials and their mechanical properties are related to atomic mobility. Knowledge of diffusion coefficients and anisotropy is very important for understanding deformation processes in alloys, thermal stability of protective coatings, creep resistance, and other characteristics. Information about migration barriers and diffusion mechanisms is necessary for a deeper understanding of oxidation and hydrogenation processes in materials, as well as the influence of impurities on these processes [6,7]. In this regard, the study of microscopic mechanisms of diffusion of various elements in titanium and its alloys appears important from both theoretical and practical perspectives. Establishing factors affecting the diffusion of impurities that negatively impact material properties allows expanding their application scope.

Despite intensive experimental studies of atomic diffusion in metals and alloys, theoretical calculations of diffusion properties remain rare. In most works, authors calculate migration barriers of impurities between individual interstitial positions, often considering only a limited set of these positions. Conclusions about the preferential diffusion of impurities in certain crystallographic directions are typically made based on the analysis of obtained migration barrier values. At the same time, the fact that atomic diffusion can occur not only along selected directions but also along paths where an atom shifts in both directions simultaneously is not taken into account. Density Functional Theory (DFT) [8] together with transition state theory [9] allows understanding the mechanisms of diffusion and self-diffusion in materials with various crystal structures. With the emergence of algorithms enabling the calculation of barriers along minimum energy paths within several modern software codes, the number of publications on this topic has increased significantly. Most works are devoted to studying the diffusion of light interstitial impurities such as hydrogen or oxygen (see [10–17] and references therein). However, estimating the temperature-dependent diffusion coefficient, even using simplified models, also requires the development of appropriate programs, so such calculations remain rare.

In work [18], self-diffusion of metals with HCP structure (Mg, Zn, Ti, Zr and Hf) was studied. An analysis was carried out on the influence of several factors on migration barrier values: plane wave cutoff energy, *k*-point grid, supercell size, and structural optimization scheme. It was shown that the supercell size strongly affects migration barriers in *d*-metals (Ti, Zr and Hf), but they remain practically unchanged in the case of Mg. It was established that the difference in migration barriers in the basal plane and between them decreases with increasing supercell size. The optimization of supercell shape and volume also affects migration barriers more significantly when they are calculated in a small-sized supercell. Overall, the calculated self-diffusion coefficients [18] show good agreement with experiment.

It should be noted that substitutional impurity diffusion has been studied much less by *ab initio* methods than interstitial one. For example, in a recent work [19], diffusion coefficients were calculated for impurities of ten elements (Si, Ti, V, Ta, Ru, Cr, Te, Tc, Ir and Y) in Nb. Migration barriers were obtained for these elements along possible diffusion paths. The results of this work are in good agreement with available experimental and earlier theoretical data for individual impurities. The difference in activation energy from experimental values for several impurities is 0.3–0.6 eV, and a slightly smaller deviation from earlier theoretical results was obtained for Ti and Ru impurities [20].

The dependence of the coefficient on the atomic diffusion mechanism (vacancy or interstitial) was also studied in α-Ti. It is believed that rapid diffusion of Fe, Co, Cr and Ni atoms in α-Ti may be related to the interstitial mechanism [21] and relatively weak atomic bonding between impurity and matrix atoms. The diffusion coefficient of Fe and Co is 7–8 orders of magnitude higher than the self-diffusion coefficient of titanium [22]. In the case of Al, Ga, Ge, Nb, Ta, Si, Sn and other elements, the vacancy mechanism was proposed as dominant [23, 24], with calculated coefficients showing good agreement with experiment. Works [25, 26] showed that for Fe and Co in α-Zr, the formation of an interstitial defect is more favorable than a substitutional defect, while in α-Ti the situation is reversed [25, 26]. Impurity diffusion in α-Ti was studied most thoroughly in [27]. The authors considered lattice thermal expansion and showed that the difference between the formation energy of substitutional and interstitial impurities decreases with temperature. They also estimated the exponential part of the diffusion coefficient for a number of impurities in both interstitial and vacancy mechanisms, with the difference reaching 9–10 orders of magnitude for Fe and Co. However, direct calculation of the temperature-dependent diffusion coefficient for Fe and other impurities and its comparison with available experimental data [28–30] was not performed. Furthermore, the authors [27] confirmed that the mechanism involving impurity-vacancy complex formation is not responsible for fast diffusion of several impurities in α-Ti. Thus, currently many phenomena related to impurity diffusion are far from being fully understood even in titanium and its alloys.

The purpose of this work is a theoretical study of iron diffusion in α-Ti within the interstitial and vacancy mechanisms, as well as direct evaluation of the temperature-dependent diffusion coefficient using modern methods.

2. COMPUTATIONAL DETAILS

Calculations of atomic and electronic structure α-Ti were performed using the projector augmented wave (PAW) method [31,32] in a plane-wave basis with the generalized gradient approximation (GGA) [33] for the exchange-correlation functional. A supercell 4 × 4 × 3 containing 96 atoms was used. For atomic structure relaxation, a complete optimization scheme was applied, which allowed changes in both atomic positions and supercell volume. The maximum energy of plane waves from the basis set was 400 eV. Integration over the Brillouin zone was performed using a k-point grid 3×3×3. Convergence was considered achieved if the difference in total energies between two consecutive iterations did not exceed 10^{-6} eV. Relaxation of atomic positions was carried out until the forces on atoms reached 10^{-4} eV/Å. The calculated lattice parameters were a = 2.921 eV and c = 4.634 Å and differed from experimental values (a = 2.951 Å and c = 4.684 Å [34]) by no more than 1%.

The defect formation energy in titanium was calculated using the following formula:

$$E^f = E(\mathrm{Fe} + \mathrm{Ti}) - NE(\mathrm{Ti}) - E(\mathrm{Fe}), \qquad (1)$$

where $E(\mathrm{Fe} + \mathrm{Ti})$ is the total energy of the titanium supercell with an Fe atom, E(Ti) and E(Fe) are the total energies of titanium and iron in their ground states, i.e., Ti in HCP structure and Fe in ferromagnetic BCC structure, parameter N equals 96 in the case of an interstitial defect and 95 when forming a substitutional defect.

Migration barriers were calculated using the climbing image nudged elastic band method CI-NEB [35]. Five images were used to estimate the barriers. The initial position of these images along the minimum energy path was found using linear interpolation between the initial and final positions of the diffusing atom. During the relaxation of all five images, each atom was considered elastically bound to the same atom in neighboring images. This approach allows determining the path with the lowest energy, as well as the saddle point. Migration energy barriers of the iron impurity atom were determined as the difference between the total energies of the system at the saddle and initial points.

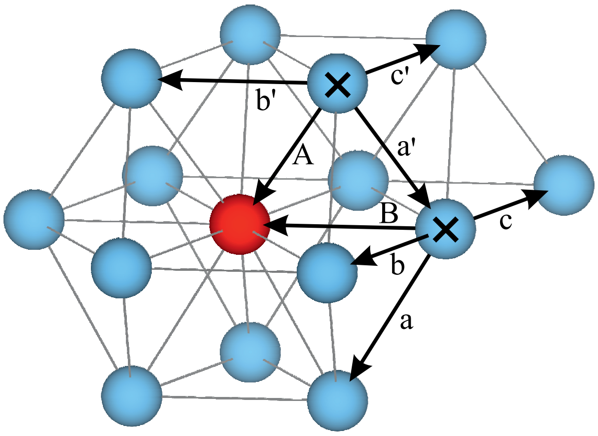

Fig. 1. Schematic representation of atomic jumps within the eight-frequency model. The impurity atom is shown in red, possible initial positions of the vacancy are marked with crosses.

To estimate the temperature-dependent diffusion coefficient of diffusion within the interstitial mechanism, the Landman method [36, 37] was used, which allows obtaining analytical expressions for this characteristic. Based on the Fourier transform of the displacement matrix $\tilde{p}(\mathrm{k})$ and the Laplace transform of the waiting time density matrix $\tilde{\psi}(\mathrm{u})$, this method assumes to construct a propagator matrix $R(\mathrm{k}, u)$, through which the diffusion coefficient is expressed. A detailed description of this approach is given in our earlier works [38, 39].

To estimate the diffusion coefficient within the vacancy mechanism, as in works [23, 24, 40], the eight-frequency model [41] was used. Within this model, the influence of the impurity is considered only for six jumps, whose initial position is located in the first coordination sphere of the impurity atom, and two more jumps are associated with the exchange of vacancy and impurity positions (Fig. 1). Since two initial configurations of the impurity-vacancy complex are possible, four migration energies need to be calculated for each.

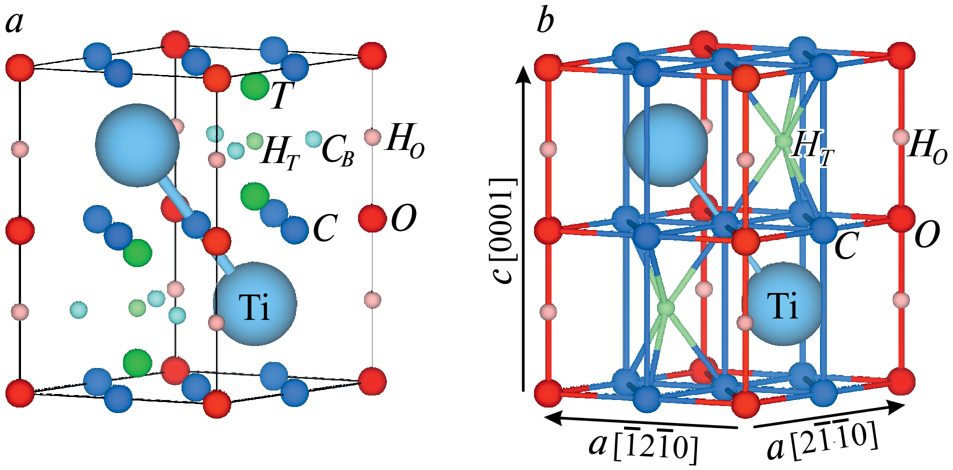

Fig 2. Elementary cell of α-Ti with absorption positions (a), network of possible diffusion paths of Fe atom (b). Large spheres represent titanium atoms, medium red, blue and green spheres represent positions *O*, *C* and *T*, small pink, light blue and light green spheres represent H_O, C_B and H_T

Both methods mentioned above for numerical estimation of the diffusion coefficient require knowledge of jump rates or frequencies, which were calculated using the formula given in [4]:

$$\Gamma = \sqrt{\frac{E^m}{2ml^2}} \exp\left(-\frac{E^m + E^f}{k_B T}\right), \tag{2}$$

where E^m is the migration energy of the defect atom, m is the mass of the diffusing atom, l is the jump length, k_B is the Boltzmann constant, T is temperature.

3. RESULTS AND DISCUSSION

3.1. Defect Formation Energies

Titanium in the low-temperature α-phase has a hexagonal close-packed structure with space group No. 194 ($P6_3/mmc$). Titanium atoms occupy 2c-positions according to Wyckoff classification. The following standard interstitial positions were considered as insertion positions (Fig. 2a): octahedral (O, in Wyckoff notation positions 2a), tetrahedral (*T*, 4*f*), two hexahedral positions (H_O, 2*b* and H_T, 2*d)* and two crowdions and (*C*, 6_g and C_B, 6*h*). Note that a crowdion is understood as a position, located on the bond between the nearest matrix atoms. In the case of HCP crystal, there are two crowdion positions: when the impurity atom is located between titanium atoms in the (0001) plane, such position will be denoted as C_B; and when this atom is located between two nearest titanium atoms which are in adjacent basal planes (*C*-position). Additionally, the substitution position of titanium atom with iron was considered (*S*, 2*c*). The coordinates of these positions, as well as a number of their structural and energetic characteristics are given in Table 1. During structure optimization with the inserted Fe atom, it turned out that the basal crowdion position (C_B) is not stable, as Fe shifts from it to the *O*-position. Phonon frequency calculations showed that Fe in tetrahedral and both hexahedral positions is characterized by imaginary frequencies, with the latter can be considered as first-order transition states, as Fe has only one imaginary frequency. Thus, in α-Ti for the Fe atom, only positions *O* and *C* will be considered as interstitial positions hereafter, and Fe diffusion can occur through network shown in Fig. 2b.

According to definition (1), a positive value E^f indicates the endothermic nature of defect formation, therefore the lower formation energy corresponds to the more preferable defect. From Table 1, it follows that the crowdion (*C*) is the most preferable interstitial position, and the difference in E_f with *O*-position is 0.26 eV, which satisfactorily agrees with the value of 0.16 eV obtained in work [27], and a slightly lower value of 0.14 eV was obtained in work [26]. To explain the preference of crowdion compared to the octahedral position, mechanical (*MC*) and chemical (*CC*) contributions to the defect formation energy were calculated using the standard procedure, which has been repeatedly applied in earlier works [42,43]for various energy characteristics.

Table 1. Formation energy (*Ef*) of Fe defects in α-Ti(4×4×3), mechanical (*MC*) and chemical (*CC*) contributions, relative change in supercell volume (Δ*V*), bond length d(Fe -Ti), orbital overlap population (θ)

Position	Coordinates	E^f, eV	*MC*, eV	*CC*, eV	Δ*V*, %	*d*(Fe–Ti), Å	*θ*(Fe–Ti), el.
O, 2a	(0, 0, 0), (0, 0, 1/2)	1.02, 1.17 [27]	1.47, 1.42 [27]	−0.45, −0.25 [27]	0.75	2.31	0.59
C, 6g	(1/2, 0, 0), (0, 1/2, 0), (1/2, 1/2, 0), (1/2, 0, 1/2), (0, 1/2, 1/2), (1/2, 1/2, 1/2),	0.76, 1.01 [27]	1.63, 1.74 [27]	−0.87, −0.74 [27]	0.74	2.08	0.80
H_O, 2b	(0, 0, 1/4), (0, 0, 3/4)	1.19, 1.38 [27]	1.60, 1.70 [27]	−0.41, −0.33 [27]	0.80	2.10	0.80
H_T, 2d	(1/3, 2/3, 3/4), (2/3, 1/3, 1/4)	2.08	1.82	0.26	0.94	2.22	0.67
T, 4f	(1/3, 2/3, 0.581), (2/3, 1/3, 0.081), (2/3, 1/3, 0.419), (1/3, 2/3, 0.919)	1.35	2.18	−0.83	0.75	1.98, 2.33	0.92, 0.57
S, 2c	(1/3, 2/3, 1/4), (2/3, 1/3, 3/4)	0.59, 0.41 [27]	0.26	0.33	−0.53	in 2.73, out 2.90	in 0.23, out 0.31

It is known that these contributions have opposite signs and their competition determines the preferential positions of incorporation. Although the mechanical contribution in the case of *C*-position exceeds that for *O*-position by 0.16 eV, the chemical contribution in the first case is significantly higher in absolute value by 0.42 eV (0.49 eV [27]). Thus, stronger interatomic interaction Fe–Ti in *C*-position determines its preference compared to *O*-position. When incorporating into the crowdion position, Fe atom causes displacement of nearest Ti atoms by away from it, while the bond length 0.65 Å is 2.08 Å (Table 1). At the same time, Fe incorporation into *O*-position causes significantly smaller displacement of titanium atoms (0.26 Å) and the equilibrium interatomic bond length is considerably larger (2.31 Å) than in the previous case. As shown in Table 1, the supercell volume change for both positions is practically identical (0.74–0.75%). Note that the shorter Fe–Ti bond length also correlates with the higher orbital overlap population value (Table 1), calculated using DDEC6 method [44, 45]. As shown by the calculation of crystal orbital Hamilton population curves (COHP) [46,47], at the Fe–Ti interaction in the considered incorporation positions, no antibonding states are induced (Fig. 3*a*), which can form in case of impurities with more than half-filled *d*-shell. Note that in *O*-position, the Fe valence band is substantially narrower than in *C*-position, which may also indicate relatively weak Fe–Ti interaction in (Fig. 3b).

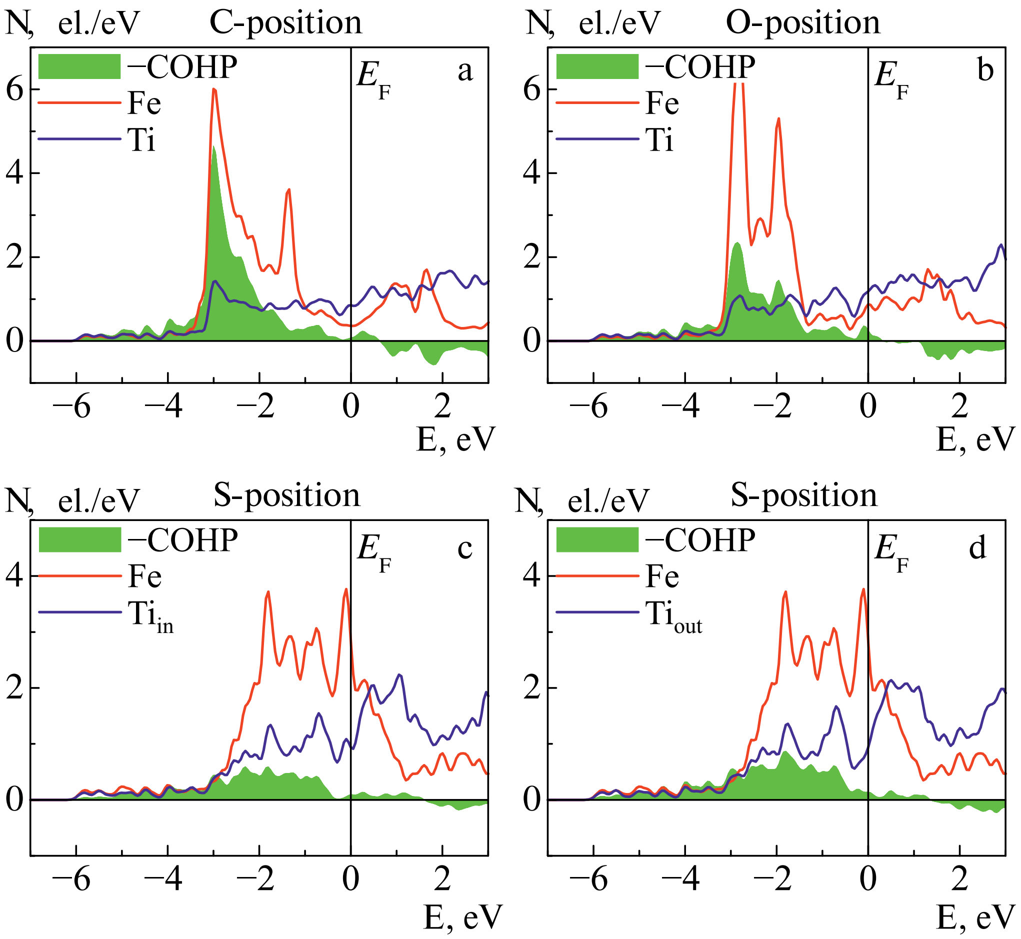

Fig. 3. Local densities of electronic states for Fe atoms (red line) in *C*- (*a*), O-(*b*) and *S*-position (*c*, *d*) and nearest Ti atoms (blue line), as well as COHP curves for Fe–Ti-bonds, shown by filling.

The formation of titanium substitution defect by iron requires only about 0.59 eV, which is 0.17 eV less than the insertion into the crowdion position, while titanium substitution leads to a decrease in the supercell volume (Table 1), as the atomic radius of Fe is smaller than that of the matrix atom. It should be noted that the difference in values E^f of these two defects is significantly lower than the value of 0.60 eV obtained in work [27]. This difference may be related to both different optimization schemes for structures with defects and pseudopotentials. For example, in work [26], where this difference reaches 0.71 eV, the authors used a fixed volume scheme. Information about the used lattice parameters is absent in both works [26,27]. In work [27], the electronic configuration for Fe and Ti included *p*-electrons, while 3*d*- and 4*s*-states were considered in present calculations, as in work [26].

Despite the fact that when titanium is substituted by iron, there is a decrease in the length of Fe–Ti_{in} bonds, oriented in the basal plane (0001), by 0.19 Å compared to ideal titanium and, conversely, an increase in the length of bonds between atoms in adjacent planes Fe–Ti_{out} by 0.04 Å, the orbital overlap population of in-bonds remains less than out-bonds. The latter agrees with the lower height of the COHP curve in the case of Ti_{in}, than for Ti_{out} (Fig. 3 c,d).Note that the electronic structure of atoms Ti_{in} and Ti_{ou} differs insignificantly. The energy difference ΔE^f between defects in *O*- and H_o-positions has a value of 0.17 eV, while values of 0.12 and 0.21 eV were obtained in works [26].

3.2. Interstitial diffusion mechanism

The calculated migration barriers of Fe atom between interstitial positions are shown in Table 2. It can be seen that direct transition between *C*-positions along the *c*-axis (Fig. 2b) requires 0.13 eV more energy than in the perpendicular direction. The migration energy of Fe from *O*-position is small and insignificantly depends on its direction (Table 2). At the same time, the energy

Table 2. Migration energies (E^m in eV) of Fe in α-Ti along two crystallographic directions

Direction	Path	E^m, eV
a	$C \to C$	0.42
	$C \to O$	0.41, 0.33 [27]
	$O \to C$	0.16, 0.17 [27]
c	$O \to (HO) \to O$	0.17, 0.21 [27]
	$C \to (\mathrm{HT}) \to C$	1.31
	$C \to C$	0.55

of indirect jump of Fe between crowdions through the saddle H_T-position ($C \to H_T \to C$) along the *c*-axis is 1.31 eV, which is significantly higher than for direct jump ($C \to C$) along both axes (Table 2). The latter allows excluding this indirect transition from further consideration. Comparison of the calculated energy barriers with available data [27] shows satisfactory agreement.

Since within the Landman method [36, 37] as interstitial positions were used $C(6g)$ and $O(2a)$ and positions, all matrices had the size of 8 × 8. The obtained expressions for Fe diffusion coefficients along two nonequivalent directions have the following form:

$$D_a = \frac{a^2\Gamma_{OC,a}\left(8\Gamma^2_{CC,a} + 6\Gamma_{CC,a}\Gamma_{CO,a} + \Gamma^2_{CO,a}\right)}{\left(\Gamma_{CO,a} + 3\Gamma_{OC,a}\right)\left(\Gamma_{CO,a} + 3\Gamma_{CC,a}\right)} \quad (3)$$

and

$$D_c = \frac{c^2\left(3\Gamma_{CC,\tilde{n}}\Gamma_{OC,a} + \Gamma_{CO,a}\Gamma_{OO,c}\right)}{4\left(\Gamma_{CO,a} + 3\Gamma_{OC,a}\right)}, \quad (4)$$

where *a*, *c* are lattice parameters, $\Gamma_{ij,k}$ is jump rate $i \to j$ along axis *k*, which coincides with crystallographic axes.

In Fig. 4, it can be seen that Γ rates differ from each other by several orders of magnitude, particularly $\Gamma_{CO,a}/\Gamma_{OC,a} \approx 0.06$ in the temperature range 500–1150 K, therefore expressions (3) and (4) can be simplified:

$$D_a = \frac{a^2}{3}\left(\Gamma_{CO,a} + 3\Gamma_{CC,a}\right) \quad (5)$$

and

$$D_c = \frac{c^2}{4}\Gamma_{CC,c} + 0.005c^2\Gamma_{OO,c}. \quad (6)$$

Expressions (5), (6) allow estimating contributions of specific jumps to diffusion coefficients. Approximating the temperature dependence of D_a and D_c according to the Arrhenius equation by least squares method by points with a step of 50 K, we obtain final expressions for diffusion coefficients within the interstitial mechanism:

$$\begin{aligned} D_a &= 4.6 \cdot 10^{-7}\exp\left(-\frac{1.20}{k_BT}\right)m^2/s, \\ D_c &= 9.0 \cdot 10^{-8}\exp\left(-\frac{1.01}{k_BT}\right)m^2/s. \end{aligned} \quad (7)$$

In Fig. 5 it is evident that the theoretical values of temperature-dependent diffusion coefficient slightly exceed the experimental values from work [28], where diffusion coefficients were equal to the following expressions:

$$\begin{aligned} D_a &= 6.4 \cdot 10^{-6}\exp\left(-\frac{1.49}{k_BT}\right)m^2/s, \\ D_c &= 4.7 \cdot 10^{-7}\exp\left(-\frac{1.16}{k_BT}\right)m^2/s. \end{aligned} \quad (8)$$

Comparing expressions (7) and (8), it is clear that the calculation underestimates the activation energy by approximately 0.15–0.30 eV, and the pre-exponential factor by (0.38–5.94) · 10^{-6} m^2/s. In Fig. 5, it is seen, that the anisotropy of Fe diffusion in α-Ti has the correct character ($D_c > D_a$), however, the ratio D_c/D_a is underestimated, although it has the same order. As shown in work [48], calculation of migration barriers using the generalized gradient approximation in PBE form leads to their underestimation by approximately 0.1 eV on average. Additionally, Fe impurity contributes to the weakening of the nearest the Ti–Ti bonds. It can be seen from change in electron localization function (ELF) [49] when titanium is substituted with iron, shown in Fig. 6. The electron localization in the three-center interaction attractor region decreases from 0.8 to 0.6 near the Fe atom, indicating a decrease in covalent and increase in metallic contribution to chemical bonding. The weakening of bonds in α-Ti can also be indirectly seen from the phase diagram of the system Ti–Fe, presented in work [50]. Adding Fe to α-Ti

Table 3. Migration energies calculated within the eight-frequency model

Jump	A	a'	b'	c'	B	a	b	c
Present results	0.89	0.27	0.10	1.15	0.60	0.07	0.29	0.61
Theory [27]	0.71	–	0.13	–	0.68	0.09	0.30	0.56

reduces the melting temperature, which from the interatomic interaction point of view corresponds to an increase in metallic contribution. When calculating migration barriers, this can lead to overestimated displacements of Ti atoms nearest to Fe, which, in turn, lowers the energy migration barriers. Overall, the order of the ratio of diffusion coefficient to pre-exponential factor at T = 1000 K is 10^{-7}–10^{-6}, while the experimental value equals 10^{-8}–10^{-6} [28]. Note that the difference between theoretical and experimental diffusion coefficient values by one to two orders of magnitude is considered satisfactory, as the experimental results themselves have similar scatter. The approximate estimation of this ratio (10^{-4}) in work [27] is significantly overestimated compared to the experiment.

3.3. Vacancy Mechanism of Diffusion

Let's briefly discuss the results obtained for the vacancy mechanism of iron diffusion in titanium. Since the substitution of titanium with iron is the dominant defect, and in [27] only the exponential part of the diffusion coefficient was calculated at a temperature of 1000 K, its estimation within the vacancy mechanism framework is necessary to establish the most preferred mechanism. The obtained migration energy values are shown in Table 3. The vacancy formation energy in pure titanium equals 2.00 eV, which agrees well with the theoretical values of 2.05 eV [27] and 2.08 eV [51], but significantly exceeds the experimental values 1.27–1.55 eV [52,53]. Note that overestimation of vacancy formation energies in metals and alloys is a known issue. Taking into account the temperature contribution to vacancy formation energy allows reducing theoretical values by several tenths of an electron-volt.

Interaction with an iron atom, as mentioned above, weakens Ti-Ti bonding, which leads to a decrease in the formation energy of titanium vacancies. Thus, the formation energy of Ti vacancy in the same atomic layer with orientation (0001), where the iron impurity is located, is 1.62 eV, while vacancy

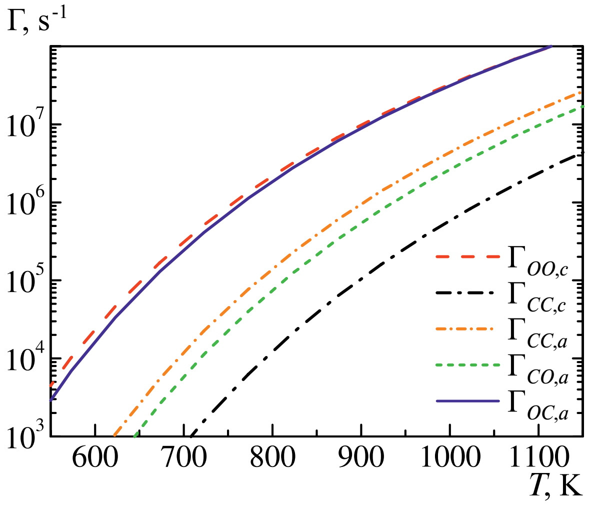

Fig. 4. Temperature dependence of jump rates Γ

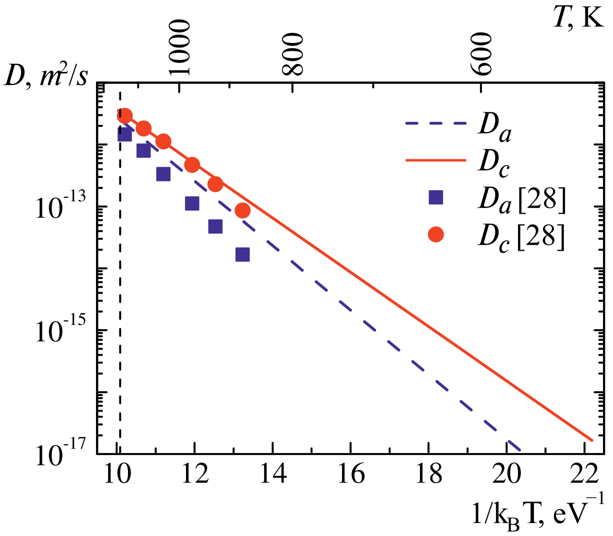

Fig. 5. Temperature-dependent diffusion coefficient of Fe in α-Ti compared with experimental data from [28]. The values obtained in this work are shown by lines, experimental data by symbols. The vertical dashed line corresponds to the phase transition temperature α ↔ β

formation in the adjacent atomic layer near the impurity requires

1.43 eV. Different values suggest that expressions for and should be multiplied by different vacancy concentrations. From an energy point of view, the decrease in vacancy formation energy near the iron impurity is due to the vacancy-impurity interaction energy, which is 0.38 eV and 0.57 eV when both defects are located in the same layer or in adjacent layers, which agrees with the value of 0.50 eV [54] obtained by the Faulkner method.

Within the eight-frequency model, the following expressions were obtained for iron diffusion coefficients along the axes *a* and *c*:

$$\begin{aligned} D_a &= 1.4 \cdot 10^{-7} \exp\left(-\frac{2.24}{k_B T}\right) m^2 / s, \\ D_c &= 4.9 \cdot 10^{-7} \exp\left(-\frac{2.32}{k_B T}\right) m^2 / s. \end{aligned} \tag{9}$$

From formulas (9), it follows that the theoretical activation energies in this case significantly exceed the experimental values of 1.16–1.49 eV [28]. The latter indicates that within the vacancy mechanism, high energies are required for elementary jumps between substitution positions. The ratio of the diffusion coefficient to the pre- exponential factor at 1000 K is 10^{-12} (the value 10^{-13} was obtained in work [27]), while within the interstitial mechanism, the value 10^{-7} (in the basal plane) and 10^{-6} (along *c*-axis) was obtained. Thus, despite the fact that the formation of substitution impurity in the case of Fe is more preferable than an interstitial defect, the dominant mechanism is its diffusion through interstitial sites in α-Ti. It should be noted that the temperature effect assessment in [27] on the difference between the formation energies of interstitial and substitution defects showed that it decreases by almost 0.3 eV at 1000 K. In the present work, the difference between these defects at 0 K is only 0.17 eV, and with increasing temperature, the interstitial defect may become dominant. In conclusion, we should also note that in the calculations, the iron concentration was about 1 at.%, while in the experiment it cannot exceed approximately 0.06 at.%. Increasing the number of atoms in the cell leads to significant computational costs and does not affect the obtained migration energy values. Moreover, even in the present model, diffusing atoms do not interact with each other. Therefore, the concentration effect will not affect the values of activation energy and pre-exponential factor.

4. CONCLUSION

The diffusion of iron in α-Ti has been studied using the projector augmented wave method within the interstitial and vacancy mechanisms, and the temperature-dependent diffusion coefficient has been evaluated. The energies of Fe atom incorporation into various interstitial sites were calculated, and it was established that two positions are dynamically stable: octahedral and crowdion. The latter is located between titanium atoms in adjacent basal planes. The formation of a crowdion is energetically preferable (0.76 eV), while the formation of a substitutional defect of titanium with iron requires 0.17 eV less energy, which is consistent with earlier theoretical results. The calculation of iron atom migration energy showed that the lowest barriers correspond to jumps between crowdions in the basal plane (0.41–0.42 eV) and between octahedral positions

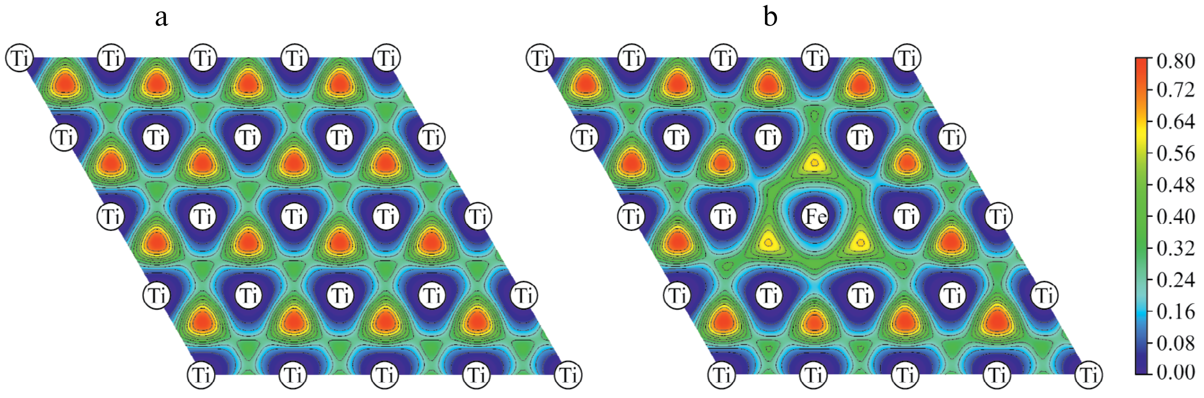

Fig. 6. Electron localization function in pure α-Ti (a) and in the presence of Fe atom (b). The distribution in the (0001) plane is shown. Isolines are drawn in the range from 0 to 0.80 with a step of 0.07

along the *c*-axis (0.55 eV). Analytical expressions for the temperature-dependent diffusion coefficient of iron in α-Ti were obtained within the interstitial mechanism. Numerical evaluation of diffusion coefficients showed that diffusion along the c-axis proceeds faster (activation energy equals 1.01 eV) than in the perpendicular direction (1.20 eV). The theoretical values of the anisotropy parameter D_c/D_a and the diffusion coefficients along two crystallographic directions are in satisfactory agreement with experiment [28], according to which the activation energies are 1.16 and 1.49 eV for diffusion along the *c*-axis and in the perpendicular direction, respectively. At the same time, iron diffusion via the vacancy mechanism requires higher activation energy (2.24–2.32 eV) and proceeds several orders of magnitude slower than interstitial diffusion. Thus, the present research allows us to conclude that for iron in α-Ti, the interstitial diffusion mechanism is preferred.

FUNDING

This work was financially supported by the Russian Science Foundation (project No. 24-23-00097). Numerical calculations were performed on the SKIF Cyberia supercomputer at Tomsk State University.

REFERENCES

1. C. Leyens and M. Peters, Titanium and Titanium Alloys: Fundamentals and Applications, Wiley-VCH Verlag GmbH & Co. KGaA, Weinheim (2003).

2. M. J. Donachie, Jr. Titanium. A Technical Guide (2nd ed.), ASM International, Materials Park, Ohio (2000).

3. M. M. Stupel, M. Bamberger, and M. Ron, J. Less-Common Met. 123, 1 (1986).

4. T. Heumann, Diffusion in Metallen: Grundlagen, Theorie, Vorgänge in Reinmetallen und Legierungen, Springer-Verlag, Berlin (1992).

5. H. Mehrer, Diffusion in Solids: Fundamentals, Methods, Materials, Diffusion-Controlled Processes, Springer, Berlin (2007).

6. Z. Li and W. Gao, in Intermetallics Research Progress, ed. by Y. N. Berdovsky, Nova Sci. Publ., New York (2008), p. 1.

7. D. P. Broom, Hydrogen Storage Materials: The Characterisation of Their Storage Properties, Springer, London (2011).

8. P. Hohenberg and W. Kohn, Phys. Rev. 136, B864 (1964).

9. M. J. Gillan, J. Phys. C: Solid State Phys. 20, 3621 (1987).

10. D. Connétable, Int. J. Hydrogen Energy 44, 32307 (2019).

11. M. G. Shelyapina, Hydrogen 3, 285 (2022).

12. 12. S. E. Kulkova, A. V. Bakulin, and L. S. Chumakova, Phys. Mesomech. 25, 424 (2022).

13. K. Klyukin, M. G. Shelyapina, and D. Fruchart, J. Alloys Compd. 644, 371 (2015).

14. H. H. Wu, P. Wisesa, and D. R. Trinkle, Phys. Rev. B 94, 014307 (2016).

15. A. V. Bakulin, S. S. Kulkov, and S. E. Kulkova, J. Exp. Theor. Phys. 130, 579 (2020).

16. E. Epifano and G. Hug, Comput. Mater. Sci. 174, 109475 (2020).

17. D. Connétable, A. Prillieux, C. Thenot et al., J. Phys.: Condens. Matter 32, 175702 (2020).

18. L. J. Zhang, T. I. Spiridonova, S. E Kulkova et al., Comput. Mater. Sci. 128, 236 (2017).

19. Y. Hu, L. Suo, Q. Long et al., Vacuum 209, 111739 (2023).

20. N. Zou, H.J. Lu, and X.G. Lu, J. Alloys Compd. 803, 684 (2019).

21. G. M. Hood and R. J. Schultz, Philos. Mag. 26, 329 (1972).

22. H. Nakajima and M. Koiwa, ISIJ Int. 31, 757 (1991).

23. L. Scotti and A. Mottura, J. Chem. Phys. 142, 204308 (2015).

24. W. W. Xu, S. L. Shang, B. C. Zhou et al., Phys. Chem. Chem. Phys. 18, 16870 (2016).

25. R. C. Pasianot, R. A. Pérez, V. P. Ramunni et al., J. Nucl. Mater. 392, 100 (2009).

26. R. C. Pasianot and R. A. Pérez, J. Nucl. Mater. 434, 158 (2013).

27. L. J. Zhang, Z. Y. Chen, Q. M. Hu et al., J. Alloys Compd. 740, 156 (2018).

28. H. Nakajima, M. Koiwa, and S. Ono, Scr. Metall. 17, 1431 (1983).

29. H. Nakajima, M. Koiwa, Y. Minonishi et al., Trans. Jpn. Inst. Met. 24, 655 (1983).

30. H. Nakajima and M. Koiwa, in Titanium, Science and Technology, ed. by G. Lütjering, U. Zwicker, and W. Bunk, Deutsche Gesellschaft für Metallkunde e. V., Oberursel (1984), Vol. 3, p. 1759.

31. P. E. Blöchl, Phys. Rev. B 50, 17953 (1994).

32. G. Kresse and D. Joubert, Phys. Rev. B 59, 1758 (1999).

33. J. P. Perdew, K. Burke, and M. Ernzerhof, Phys. Rev. Lett. 77, 3865 (1996).

34. R. M. Wood, Proc. Phys. Soc. 80, 783 (1962).

35. G. Henkelman, B. P. Uberuaga, and H. Jónsson, J. Chem. Phys. 113, 9901 (2000).

36. U. Landman and M. F. Shlesinger, Phys. Rev. B 19, 6207 (1979).

37. U. Landman and M. F. Shlesinger, Phys. Rev. B 19, 6220 (1979).

38. A. V. Bakulin, L. S. Chumakova, and S. E. Kulkova, J. Exp. Theor. Phys. 133, 169 (2021).

39. A. V. Bakulin, L. S. Chumakova, and S. E. Kulkova, Intermetallics 146, 107587 (2022).

40. S. Ganeshan, L. G. Hector Jr., and Z. K. Liu, Acta Mater. 59, 3214 (2011).

41. P. B. Ghate, Phys. Rev. 133, A1167 (1964).

42. A. Y. Lozovoi, A. Alavi, and M. W. Finnis, Phys. Rev. Lett. 85, 610 (2000).

43. S. S. Kulkov, A. V. Bakulin, and S. E. Kulkova, Int. J. Hydrogen Energy 43, 43 (2018).

44. T. A. Manz and N. G. Limas, RSC Adv. 6, 47771 (2016).

45. T. A. Manz, RSC Adv. 7, 45552 (2017).

46. R. Dronskowski and P. E. Blöchl, J. Phys. Chem. 97, 8617 (1993).

47. R. Nelson, C. Ertural, J. George et al., J. Comput. Chem. 41, 1931 (2020).

48. H. Wu, T. Mayeshiba, and D. Morgan, Sci. Data 3, 160054 (2016).

49. B. Silvi and A. Savin, Nature 371, 683 (1994).

50. G. Cacciamani, J. De Keyzer, R. Ferro et al., Intermetallics 14, 1312 (2006).

51. B. Medasani, M. Haranczyk, A. Canning et al., Comput. Mater. Sci. 101, 96 (2015).

52. V. O. Shestopal, Sov. Phys. Solid State 7, 2798 (1966).

53. E. Hashimoto, E. A. Smirnov, and T. Kino, J. Phys. F: Met. Phys. 14, L215 (1984).

54. N. Chen, Z. Yu, Acta Metall. Sin. 30, A112 (1994).

JOURNAL OF EXPERIMENTAL AND THEORETICAL PHYSICS, 2024, Vol. 165, No. 6, pp. 829–836

SOLIDS AND LIQUIDS

FEATURES OF POLARIZED LUMINESCENCE OF AN INHOMOGENEOUS ENSEMBLE OF LOCALIZED EXCITONS

© 2024 **L. V. Kotova*, V. P. Kochereshko**

Ioffe Institute, 194021, St. Petersburg, Russia

**e-mail: kotova@mail.ioffe.ru*

Received February 02, 2024
Revised February 12, 2024
Accepted February 15, 2024

Abstract. The paper considers the features of polarized luminescence induced by a magnetic field in an ensemble of localized excitons. It was found that: 1) in an inhomogeneous ensemble, the splitting of photoluminescence bands in a magnetic field in the right and left circular polarizations may exceed the value of the Zeeman splitting of individual excitons in the ensemble by orders of magnitude; 2) the lower photoluminescence band in terms of energy may have a lower intensity than the upper one, at first glance contradicting the Boltzmann energy distribution; 3) the sign of the circular polarization of photoluminescence may vary along the contour of the radiation band. It is shown that in an inhomogeneous ensemble, all these features are explained by the pendence of the exciton g-factor on its localization energy.

Keywords: *polarized photoluminescence; quantum inhomogeneous ensemble; localized excitons*

DOI: 10.31857/S004445102406e087

1. INTRODUCTION

Magnetic circular polarization of luminescence (MCPL) is an effective method for studying the spin orientation of excitons and carriers in crystals, which is related to the thermal redistribution of carriers and excitons between Zeeman sublevels in a magnetic field. This method was successfully used by Thomas and Hopfield to study bound excitons [1]. Using this method, the fine structure of acceptor impurities was investigated and the acceptor concentration profile was measured [2] in quantum wells. This method also proved to be very effective for studying spin dynamics of charge carriers and excitons [3–5] in nanostructures.

As is known, in a magnetic field, all states split according to the projection of the magnetic moment on the magnetic field direction. Under non-resonant unpolarized optical excitation, these states are populated according to the Boltzmann distribution. The population ratio of these states is determined by the Zeeman splitting value and the temperature factor. As a result, photoluminescence (PL) becomes circularly polarized. The degree of polarization of this radiation is determined by the population of Zeeman sublevels and a coefficient that accounts for the absence of complete thermodynamic equilibrium.

In strong magnetic fields, the degree of polarization ceases to depend on the magnetic field and is completely determined by the ratio of lifetime to spin relaxation time. In weak magnetic fields, the degree of polarization is proportional to the magnetic field magnitude. This dependence is often used to determine the g-factor and the ratio of lifetime to spin relaxation time. This model describes experimental results well in many cases [5]. However, in some cases, experimental results do not fit into such a simple scheme (see, for example, works [6–8]).

As a rule, emission spectra show not individual objects, but entire ensembles of such objects. This situation occurs during exciton localization on deep levels in bulk crystals [9] or on composition fluctuations in solid solutions [10], on quantum well thickness fluctuations or quantum wire cross-sectional area, on superlattice interfaces [13], as well as during dimensional quantization of excitons in quantum dots [14–16] or colloidal nanocrystals [17–19], taking into account the variation in their sizes and shapes. Their emission lines under real conditions almost always experience inhomogeneous broadening associated with fluctuations in resonant energies, center concentration, spatial position, or variation in other parameters that determine the energy and width of individual emission lines.

In ensembles of localized states, the MCPL signal can take various forms. Sometimes "inverse population" [20] of Zeeman sublevels is observed, sometimes — non-monotonic dependence of polarization degree [21] on magnetic field, and sometimes — dependence of the exciton g-factor on magnetic field, even with sign reversal. In some cases, giant splitting of emission bands in two polarizations is observed [21,22], while in other cases, conversely, there is no Zeeman splitting despite significant circular polarization of emission [23].

To explain such diversity of MCPL manifestations, various models were proposed, mainly based on the dependence of exciton and carrier capture rate on the distribution of localizing centers [5, 19, 21, 24]. However, some MCPL manifestations cannot be explained within these models, for example, the giant splitting of PL band maxima in two circular polarizations [22].

In quantum dots, unlike, for example, localized excitons on quantum well width fluctuations, there is no exciton migration between dots. This greatly simplifies the analysis of MCPL spectra, as it does not require introducing a poorly known additional parameter related to exciton migration.

The magnitude of level splitting in magnetic field is determined by g-factor. Quantization of excitons and carriers in nanostructures can lead to changes in their g-factors. For electrons, this change is due to spin-orbital interaction, as was first shown in [25] and confirmed by numerous experiments [26]. The hole g-factor is also sensitive to the shape of the quantization potential, as shown in [27, 28]. For excitons [29, 30], an additional contribution to the g-factor appears, caused by the motion of the exciton center of mass.

This paper discusses a model describing some unusual features of MCPL spectra caused by inhomogeneous emission line widths. The considered model takes into account the dispersion of g-factors of holes, electrons, and excitons in an ensemble of quantum dots of different sizes.

This model does not negate the possible dependence of lifetime, capture probability, and spin relaxation time on exciton localization energy. However, it explains some observed features of emission spectra under conditions of inhomogeneous line broadening. Obviously, the model can be useful not only for describing MCPL in quantum dot ensembles but also for describing polarized PL of impurity centers and excitons under conditions of inhomogeneous broadening of their emission bands.

2. RESULTS

As is known, in a magnetic field, all states split according to the projection of the magnetic moment on the direction of the magnetic field. Under non-resonant, unpolarized optical excitation, these states are populated according to the Boltzmann distribution. The population ratio of these levels is determined by the magnitude of Zeeman splitting ΔE and the temperature factor kT. or a two-level system under equilibrium conditions, this ratio of sublevel populations is described by the relation

$$n_2 n_1 = \exp\left(-\frac{\Delta E}{kT}\right), \tag{1}$$

where n_1 and n_2 are exciton concentrations at the sublevels, $\Delta E(B) = \mu g B$ is the magnitude of Zeeman splitting between sublevels, k is the Boltzmann constant, g is the g-factor, B is the magnetic field, μ is the Bohr magneton.

Radiation from these states has right σ^+ or left σ^- circular polarization depending on the sign of the angular momentum projection on the field direction. The emission line intensities are proportional to the level populations. The degree of polarization equals

$$P_{circ} = \frac{I_{\sigma^+} - I_{\sigma^-}}{I_{\sigma^+} + I_{\sigma^-}}, \tag{2}$$

where$I_{\sigma+}$ and $I_{\sigma-}$ are radiation intensities in right and left circular polarizations.

The splitting of emission lines equals the magnitude of Zeeman splitting of levels ΔE, and the intensity ratio is determined by the Boltzmann factor. In cases where the emission line width is greater than the magnitude of Zeeman splitting and exchange interaction in the exciton, the degree of polarization at PL line maxima equals

$$P_{circ} = \tau_0\tau_0 + \tau_s\Delta E 2kT, \tag{3}$$

where τ_0 is the lifetime, τ_s is the spin relaxation time, $\tau_0 / (\tau_0 + \tau_s)$ is a factor accounting for the fact that complete equilibrium is not reached at finite lifetime.

2.1 Polarized luminescence of an inhomogeneous ensemble

In polarized luminescence experiments, inhomogeneous ensembles of states usually participate. This especially applies to excitons in an ensemble of quantum dots, where there is a large spread of excitonic resonance energies. In this case, polarized luminescence acquires certain features.

For example, let's consider an ensemble of quantum dots. We assume that the excitonic luminescence lines from each single dot have δ-shaped form

$$L(E, E') \propto n(E)\delta(E - E'), \tag{4}$$

where E is the energy of excitonic resonance in a single quantum dot, n(E) is the population of this dot, $L(E)$ is the PL line shape in a single dot.

In an ensemble of quantum dots, there can be dots of different sizes. The size dispersion of E dots leads to a spread in energies of exciton resonances. We assume that the distribution of resonant energies in the ensemble has a Gaussian form:

$$G(E) \propto \exp\left(-\frac{E - E_0}{w}\right)^2, \tag{5}$$

where E_0 the most probable exciton energy in the ensemble, and is the width of this distribution.

Then the luminescence band shape of the quantum dot ensemble represents a convolution of δ-shaped luminescence lines from each quantum dot and the Gaussian distribution:

$$I(E') = \int_{-\infty}^{\infty} G(E) L(E, E') dE. \tag{6}$$

As a result, we obtain

$$I(E') \propto \exp\left(-\frac{E' - E_0}{w}\right)^2 n(E'). \tag{7}$$

In a magnetic field, states split in energy according to the projection of the magnetic moment on the magnetic field direction. The energies of these states in a magnetic field have the form

$$E' \to E' \pm 12\mu B g_{eff}(E'). \tag{8}$$

Here we assume that the effective g-factor g_{eff} depends only on the exciton energy in the quantum dot and does not depend on the dot shape. The dependence of the g-factor on the dot shape will be discussed in section 3.

Split levels will be populated according to the Boltzmann distribution. As a result, for the emission line of the quantum dot ensemble in a magnetic field, we obtain

$$I^{\pm}(E') \propto \exp\left\{\left(-\frac{E' - E_0}{w}\right)^2 \pm \frac{\Delta E(E')}{2kT}\right\}. \tag{9}$$

In a magnetic field, the PL band splits into two, $I^+(E')$ and $I^-(E')$, manifesting in two circular polarizations, σ^+ and σ^-, at a given magnetic field direction.

For simplification of formulas, let's assume $E_0 = 0$. The position of emission band maxima is determined from the solution of the equation

$$\left[E' \pm \mu B g_{eff}(E')\right] \times$$

$$\times \left[1 \pm \mu B d g_{eff}(E') d E'\right] n$$

$$n w^2 2kT \mu B d g_{eff}(E') dE' = 0. \tag{10}$$

This equation may have several roots. Consequently, the band shape will differ from Gaussian and may have several maxima.

The bands intersect when $I^+ = I^-$, i.e., when the Zeeman splitting value $\Delta E(E')$ in the exponential power of equation (9) becomes zero. At these points, the polarization $P_{circ}(E')$ changes sign.

Let's consider three possible cases of the exciton g-factor dependence on the exciton quantization energy.

2.2 The value of *g*-factor in the ensemble does not depend on energy

Let g_{eff} not depend on energy E':

$$g_{eff} = g_0.$$

Then

1. The maxima of emission bands in two circular polarizations are located at energies $E^{\pm}_{max} = \pm \mu g_0 B / 2$.

2. The ratio of these band amplitudes equals

$$e^{\frac{\mu B}{kT} g_{eff}}.$$

3. The more intense emission band is lower in energy than the less intense one. This is consistent with the Boltzmann distribution of excitons across sublevels.

4. The half-width of both bands is equal to $2w\sqrt{\ln 2}$.

5. The bands intersect at point $E' = w^2 / 2kT$.

Since $w \gg kT$, the intersection point is far from the band maxima.

6. The degree of polarization does not change sign along the emission band contour.

The spectral dependence of emission intensity in two circular polarizations is shown in Fig. 1. In this case, the choice of values E_0 does not play a role, only the ratios of values $\mu g B / w$ and kT / w are important. The calculation parameters are as follows:

$$w = E_0, \quad 10\mu g B = kT, \quad B = 5T.$$

Since the choice of does not affect anything, in Fig. 1 let's assume $E_0 = 1.0$.

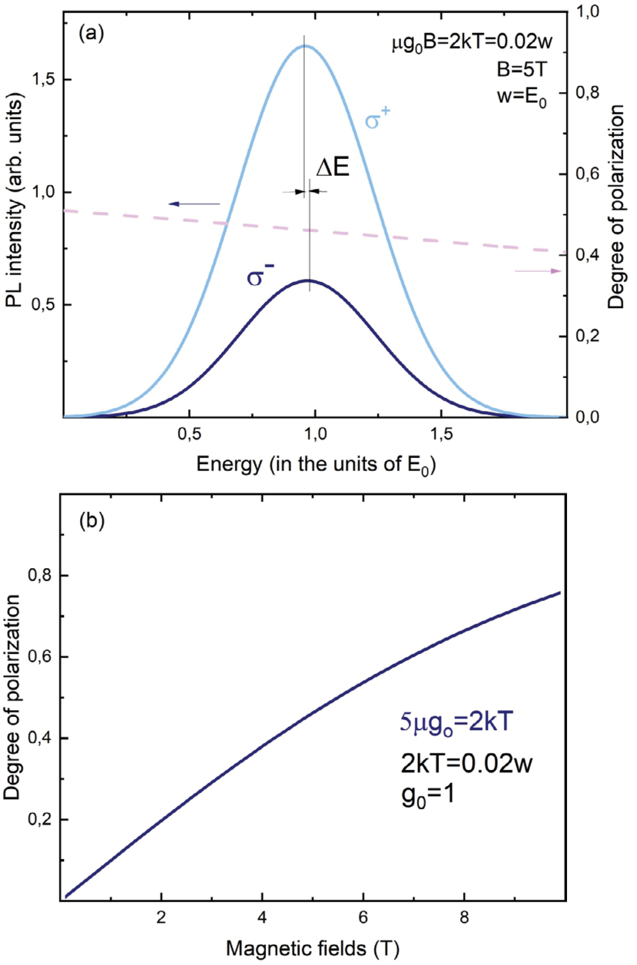

Fig. 1. *a* – Emission spectrum of quantum dot ensemble in two circular polarizations, σ_+ and σ_-, in a fixed magnetic field as a function of exciton quantization energy in the dot (in units of *w* in equation (5)) assuming that the *g*-factor does not depend on exciton quantization energy (solid lines). Calculation parameters: $w = E_0$, $\mu g B = kT$, $B = 5$ T. Degree of circular polarization induced by magnetic field as a function of exciton quantization energy (dashed line). *b* – Spectrum-integrated dependence of polarization degree on magnetic field

2.3 The value of the *g*-factor depends linearly on energy

Let's assume that g_{eff} depends linearly on energy, i.e.,

$$g_{eff}(E') = g_0 + \tilde{g}E'.$$

Let's estimate the value

$$\mu B d\tilde{g}_{eff}(E')dE'.$$

In the region of 10 T

$$\mu B d g_{eff}(E')dE' \approx 0.053 \cdot 10\tilde{g}.$$

We assume μB ≪ *w*. For non-magnetic materials, it is reasonable to assume that g_{eff} can vary no more than from -10 to 10 across the emission band width. Then

$$\mu B d g_{eff}(E')dE'n1$$

and in expression (10) this term can be neglected compared to unity. From this we obtain the following.

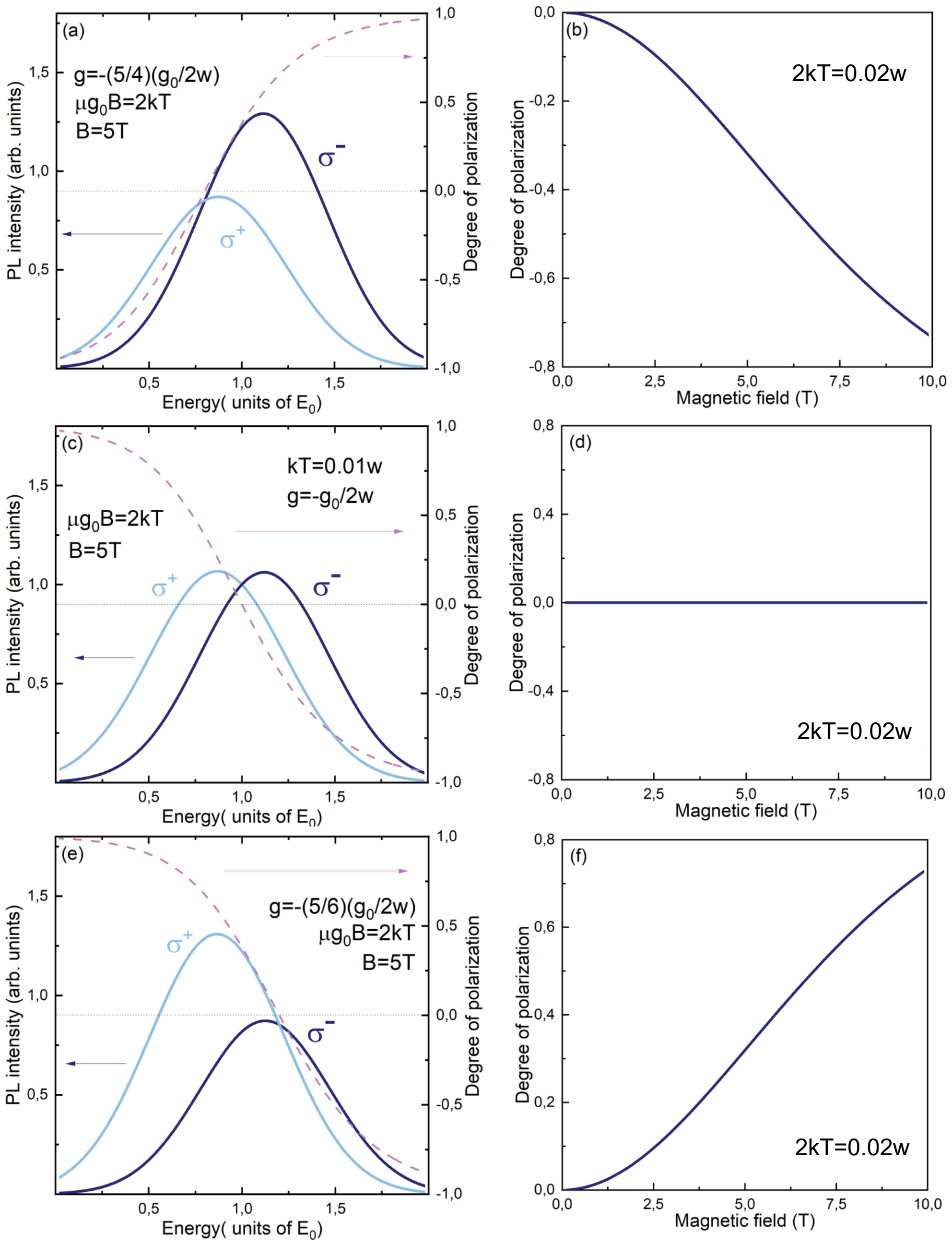

Fig. 2. Emission spectra of quantum dot ensemble in two circular polarizations at fixed magnetic field as a function of exciton quantization energy (in units of w in equation (5)) assuming that g-factor depends linearly on exciton quantization energy (solid lines). Degree of circular polarization induced by magnetic field as a function of exciton quantization energy (dashed lines). Calculation parameters: $\mu g_0 B = 2k$T = 0.02w, g = −54g$_0$2w (*a*), g = −g$_0$2w (*c*), g = −56g$_0$2w (*e*). *b*, *d*, *f* – Corresponding spectrum-integrated dependencies of polarization degree on magnetic field

1. The emission band maxima in two circular polarizations are at energies

$$E^{\pm}_{\max} = \frac{\mu B\left(\mu B g_0 g \pm \tilde{g}_0 \pm \dfrac{w^2}{2kT}\tilde{g}\right)}{(1 \pm \mu B\tilde{g})^2}. \qquad (11)$$

Note that the ratio $w^2 g / kT$ can reach values ~ 10^2–10^3. Consequently, approximately $E^{\pm}_{\max} \approx \pm\mu B \dfrac{w^2}{2kT} g$. In this case, the splitting of emission bands of the quantum dot ensemble can be very large compared to the Zeeman splitting of exciton emission lines in a single quantum dot.

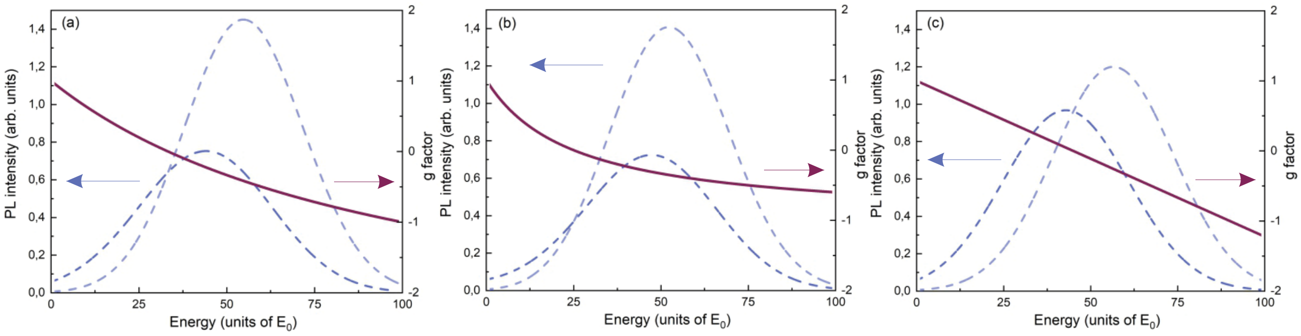

Fig. 3. Emission spectra in two circular polarizations σ_+ and σ_- (dashed curves). Calculated dependencies of g-factor on exciton quantization energy in localizing potential (13) (solid curves) for different cases: $b(E')$ is independent of quantization energy, pendent of quantization energy, $b(E') = 0.5E_0$, $R(E') = 0.25E'$ (*a*); $R(E')$ is independent of quantization energy, $b(E') = 0.5E'$, $R(E') = 0.25E_0$ (b); $b(E')$ and $R(E')$ is independent of quantization energy, $b(E') = 0.45E_0$, $R(E') = 0.45E_0$ (*c*)

2. The ratio of emission line amplitudes is about $(\mu Bgw / kT)^2$.

3. The amplitudes of these lines are

$$I^{\pm}_{\max} \approx \exp\left\{-\frac{\left(E^{\pm}_{\max}\right)^2 n \dfrac{\mu Bw^2 g_{eff}(E^{\pm}_{\max})}{2kT}}{w^2}\right\}. \qquad (12)$$

It can be seen that the ratio of band amplitudes depends on the sign of g-factor at the band maximum energy.

2.4. Realistic dependence of *g*-factor on energy

Let's assume that g_{eff} determined by the formula

$$g_{eff}(E) = g_0 + aE'b(E') + R(E'). \qquad (13)$$

Here E' is the exciton quantization energy in the localizing potential, g_0, a, b and R are certain parameters depending on E'.

Similar dependence for g-factor was obtained for excitons localized in quantum dots and for excitons in quantum wells [29, 33].

Depending on the values of $g_0, a, b, (E')$ and $R(E')$ all three cases described above are possible: g-factor changes sign at energy below emission band maximum, at maximum energy, and above maximum energy. This leads to emission spectra similar to those shown in Fig. 3.

Here, three cases are possible.

1. g-factor changes sign at energies below emission band maximum in zero magnetic field. In this case, the low-energy emission band has lower intensity than the high-energy one (Fig.2*a, b*).

2. g-factor changes sign at the energy of PL band maximum in zero magnetic field. Emission bands in both polarizations have equal amplitude (Fig. 2*c, d*).

3. g-factor changes sign at energies above the emission band maximum in zero magnetic field. The low-energy emission band is more intense than the high-energy one (Fig. 2 *e*, *f*).

Thus, we obtain the following.

1. The widths $\Delta_\pm$ of these two emission bands are equal

$$\Delta_\pm \approx 2w\sqrt{\ln 2}. \qquad (14)$$

The less intense band is slightly wider than the more intense one. The difference in band widths is less than 10%.

2. The intersection of bands and, consequently, the nullification of emission polarization degree occurs at the energy when $g_{eff}(E') = g_0 + gE' = 0$.

3. The polarization degree along the emission band contour changes sign at the energy value when $g_{eff}(E')$ changes sign.

The spectral dependence of emission intensity in two circular polarizations is shown in Fig. 2.

Obviously, qualitatively similar dependencies are obtained for any monotonic dependence of the g-factor on exciton energy.

3. DISCUSSION

If g-factor does not change sign, the polarization degree remains of the same sign for all energies. If g-factor changes sign at some energy, the PL polarization degree also changes sign along the PL band contour. The energy at which polarization changes sign corresponds to the energy at which g-factor becomes zero.

In this case, the splitting of emission band maxima is described by formula (10) and can be comparable to the width of the bands themselves, as if the effective exciton g-factor had a giant value $g_{\mathrm{eff}} \sim 100$. This appears very unusual for non-magnetic materials. This result is determined by the dispersion of g-factors and the magnitude of inhomogeneous broadening (formula (10)). In this case, the ratio of band intensities according to formula (12) depends on the sign of the g-factor.

The dependence of polarization degree $P_{circ}(B)$ on magnetic field also appears unusual. In the classical case (3), this dependence is linear with magnetic field in small magnetic fields:

$$P_{circ}(B) \propto \mu g B / 2kT.$$

However, in an inhomogeneous ensemble, we obtain a quadratic dependence of the integral polarization degree in small fields:

$$P_{circ}(B) \propto (\mu \tilde{g} \omega B / 2kT)^2.$$

The presented analysis was conducted for equilibrium PL, when thermodynamic equilibrium is established at Zeeman sublevels. Deviation from equilibrium distribution is accounted for in formula (3) using the depolarizing factor

$$\frac{\tau_0}{\tau_0 + \tau_s}. \tag{15}$$

Thus, we effectively assume that the spin relaxation time τ_s is much shorter than the lifetime τ_0. In a real situation, complete equilibrium may not be achieved. The population ratio of Zeeman sublevels in the non-equilibrium case is

$$\frac{n_1}{n_2} = \frac{\exp\left(-\dfrac{\Delta E}{2kT}\right) + \dfrac{\tau_s}{\tau_0}\mathrm{ch}\left(\dfrac{\Delta E}{2kT}\right)}{\exp\left(\dfrac{\Delta E}{2kT}\right) + \dfrac{\tau_s}{\tau_0}\mathrm{ch}\left(\dfrac{\Delta E}{2kT}\right)}. \tag{16}$$

Obviously, equation (16) transforms into equation (1) $\tau_s \leqslant \tau_0$. However, accounting for non- equilibrium does not qualitatively change the spectral dependencies (Fig. 2). In the limiting case of absent spin relaxation, $\tau_s \geqslant \tau_0$, the difference between emission spectra in two polarizations disappears.

Thus, the main factor affecting the unusual behavior of magnetic-induced polarized luminescence of quantum dot ensemble is the dependence of exciton g-factor on the size dispersion of quantum dots.

The dependence of hole g-factor on quantum well thickness was experimentally observed in quantum wells based on GaAs [34, 35] and InAs [33].

For electrons, the g-factor also depends on quantization energy [36,37]. These dependencies will either enhance or weaken each other. But typically, the electron g-factor is smaller than the hole g-factor, thus its contribution is small.

In practice, the g-factor value is experimentally determined from the splitting of emission band maxima in magnetic field, and the level population is determined from the ratio of band intensities in two circular polarizations. As seen from the presented work, this can give highly incorrect results.

4. CONCLUSION

In this work, using the example of a quantum dot ensemble, magnetic field-induced polarized luminescence of localized excitons was studied. The following was discovered.

1. The splitting of the luminescence band maxima of the ensemble exceeds the Zeeman splitting of each individual exciton by several orders of magnitude.

2. The low-energy luminescence band has a lower intensity than the high-energy one. This seemingly contradicts the Boltzmann distribution of excitons across Zeeman sublevels.

3. The effects described in points 1 and 2 only occur when the exciton factor depends on the localization energy and changes sign at a certain energy.

4. If the sign change of the g-factor occurs at energies above the emission band maximum, i.e., for small-sized points, then the intensity ratio of the bands becomes consistent with the Boltzmann distribution.

The results of this work are not limited to just inhomogeneous quantum dot ensembles. Emission lines of excitons and impurity centers in crystals are always inhomogeneously broadened. The only question is the ratio between homogeneous and inhomogeneous emission line widths.

The sign change of the *g*-factor in quantum dot ensembles can significantly affect mode-locking effects, spin echo, and spin coherence in quantum dot ensembles [38].

ACKNOWLEDGMENTS

The authors thank D. S. Smirnov and T. S. Shamirzaev for helpful discussions.

REFERENCES

1. D.G. Thomas and J.J. Hopfield, Bound Exciton Complexes, Phys. Rev. Lett. 7, 316 (1961).

2. V.P. Kochereshko, I.N. Uraltsev, Polarized Magnetoluminescence Study of Confinement Effects on Shallow Acceptors in: «Semiconductors and Insulators: Optical and Spectroscopic Research». Nova Science Publishing, Inc., (1992).

3. T.S. Shamirzaev, J. Rautert, D.R. Yakovlev et al., Spin dynamics and magnetic field induced polarization of excitons in ultrathin GaAs/AlAs quantum wells with indirect band gap and type-II band alignment, Phys. Rev. B 96, 035302 (2017).

4. T.S. Shamirzaev, J. Rautert, D.R. Yakovlev et al., Exciton recombination and spin relaxation in strong magnetic fields in ultrathin (In, Al)As/AlAs quantum wells with indirect band gap and type-I band alignment, Phys. Rev. B 104, 045305 (2021).

5. 5. E.L. Ivchenko, Magnetic circular polarization of exciton photoluminescence, Phys. Solid State 60, 1514 (2018).

6. D. R. Yakovlev, A. V. Platonov, E. L. Ivchenko et al., Hidden In-Plane Anisotropy of Interfaces in Zn(Mn)Se/BeTe Quantum Wells with a Type-II Band Alignment, Phys. Rev. Lett. 88, 2574011 (2002).

7. D. Andronikov, V. Kochereshko, A. Platonov et al., Singlet and triplet trion states in high magnetic fields: Photoluminescence and reflectivity spectra of modulation-doped CdTe/Cd0.7Mg0.3Te quantum wells, Phys. Rev. B 72, 165339 (2005).

8. I.N.Uraltsev, V.P.Kochereshko, V.S.Vikhnin et al., Polarized luminescence study of shallow acceptors in short-period superlattices, Materials Science Forum 65&66, 111 (1990), Proc. 4 Int.Conf. Shallow Impurities in Semiconductors, London (1990).

9. H.P. Gislason, B. Monemar, P.J. Bean et al., Photoluminescence studies of the 1.911-eV Cu-related complex in GaP, Phys. Rev. B 26, 827 (1982).

10. S. Pemogorov, A. Reznitsky, S. Verbin, V. Lysenko, Exciton mobility edge in CdS1−xSex solid solutions, Solid State Commun. 47, 5 (1983).

11. D. Gammon, E.S. Snow, B.V. Shanabrook et al., Fine Structure Splitting in the Optical Spectra of Single GaAs Quantum Dots, Phys. Rev. Lett. 76, 3005 (1996).

12. T.S. Shamirzaev, A.V. Nenashev, A.K. Gutakovskii et al., Atomic and energy structure of InAs/AlAs quantum dots, Phys. Rev. B 78, 085323 (2008).

13. J. Debus, T.S. Shamirzaev, D. Dunker et al., Spin-flip Raman scattering of the Gamma-X mixed exciton in indirect band gap (In,Al)As/AlAs quantum dots, Phys. Rev. B 90, 125431 (2014).

14. S.V. Gupalov, E.L. Ivchenko, A.V. Kavokin, Fine structure of localized excitonic levels in quantum wells, JETP 113, 703 (1998).

15. K.J. Moore, G. Duggan, P. Dawson et al., Short-period GaAs-AlAs superlattices: Optical properties and electronic structure, Phys. Rev. B 38, 5535 (1988).

16. R. Heitz, M. Grundmann, N.N. Ledentsov et al., Multiphonon-relaxation processes in self-organized InAs/GaAs quantum dots, Appl. Phys. Lett. 68, 361 (1996).

17. Feng Liu, L. Biadala, A.V. Rodina et al., Spin dynamics of negatively charged excitons in CdSe/CdS colloidal nanocrystals, Phys. Rev. B 88, 035302 (2013).

18. B. Siebers, L. Biadala, D.R. Yakovlev et al., Exciton spin dynamics and photoluminescence polarization of CdSe/CdS dot-in-rod nanocrystals in high magnetic fields, Phys. Rev. B 91, 155304 (2015).

19. G. Qiang, A. A. Golovatenko, E. V. Shornikova et al., Polarized emission of CdSe nanocrystals in magnetic field: the role of phonon-assisted recombination of the dark exciton, Nanoscale 13, 790 (2021).

20. V.P.Kochereshko, A.V.Platonov, G.V.Mikhailov et al. Temporal Dynamics of Exciton-Trion System, International Journal of Nanoscience 2 (6), 453 (2003).

21. G.V. Astakhov, A.A. Kiselev, V.P. Kochereshko et al., Radiative recombination of electrons and holes localized at GaAs/AlGaAs heterointerface under magnetic fields Semiconductors Sci&Tech. 14, 110 (1999).

22. L. Kotova, T. Shamirzaev, V. Kochereshko, Polarized photoluminescence and g-factor in an ensemble of quantum dots in magnetic fields, arXiv:2310.02082 (2023).

23. Ya.V. Terent'ev, S.N. Danilov, J. Loher et al., Magneto-Photoluminescence of InAs/InGaAs/InAlAs quantum well structures , Applied Physics Letters 104 (10), 101111 (2014).

24. Moskalenko, E. S. and Larsson, L. A. and Larsson, M. and Holtz et al., Comparative magneto-photoluminescence study of ensembles and of individual InAs quantum dots, Nano letters 9, 353 (2009).

25. L.M. Roth, B. Lax, and S. Zwerdling, Theory of optical magneto-absorption effects in semiconductors, Phys. Rev. 114, 90 (1959).

26. I.A. Yugova, A. Greilich, D.R. Yakovlev et al., Universal behavior of the electron g factor in GaAsAlxGa1−xAs quantum wells, Phys. Rev. B 75, 245302 (2007).

27. M.A. Semina, A.A. Golovatenko and A.V. Rodina, Influence of the spin-orbit split-off valence band on the hole g factor in semiconductor nanocrystals, Phys. Rev. B 104, 205423 (2021).

28. M.A. Semina and R.A. Suris, Holes localized in nanostructures in an external magnetic field: g-factor and mixing of states, Semiconductors 49, 797 (2015).

29. L.C. Smith, J.J. Davies, D. Wolverson et al., Motion-dependent magnetic properties of excitons in CdTe, Phys. Rev. B 78, 085204 (2008).

30. L.C. Smith, J.J. Davies, D. Wolverson et al., Wave-vector dependence of magnetic properties of excitons in ZnTe, Phys. Rev. B 83, 155206 (2011).

31. Th. Wimbauer, K. Oettinger, Al.L. Efros et al., Zeeman splitting of the excitonic recombination in InxGa1−xAs/GaAs single quantum wells, Phys. Rev. B 50, 8889 (1994).

32. D. Csontosov′a and P. Klenovsk′y, Theory of magneto-optical properties of neutral and charged excitons in GaAs/AlGaAs quantum dots, Phys. Rev. B 102, 125412 (2020).

33. P. S. Grigoryev, O. A. Yugov, S. A. Eliseev et al., Inversion of Zeeman splitting of exciton states in InGaAs quantum wells, Phys. Rev. B 93, 205425 (2016).

34. J.J. Davies, L. C. Smith, D. Wolverson et al., Motion-enhanced magnetic moments of excitons in ZnSe, Phys. Rev. B 81, 085208 (2010).

35. V.P.Kochereshko, A.V.Platonov, R.T.Cox et al., Increasing of the exciton-polariton Zeeman splitting due to its motion, Physica Status Solidi(C)11, 3928 (2005).

36. N. J. Traynor, R. J. Warburton, M. J. Snelling et al., Highly nonlinear Zeeman splitting of excitons in semiconductor quantum wells, Phys. Rev. B 55, 15701 (1997).

37. E.L. Ivchenko, A.A. Kiselev, Electronic g-factor in quantum wells and superlattices, FTP 26 (3), 1471 (1992).

38. A. Greilich, D.R. Yakovlev, A. Shabaev et al., Mode Locking of Electron Spin Coherences in Singly Charged Quantum Dots, SCIENCE 313, 341 (2006).

JOURNAL OF EXPERIMENTAL AND THEORETICAL PHYSICS, 2024, Vol. 165, No. 6, pp. 838–843

ORDER, DISORDER, AND PHASE TRANSITION IN CONDENSED MEDIA

THE INFLUENCE OF IRRADIATION OF XE IONS WITH ENERGY 167 MEV ON SUPERCONDUCTING PROPERTIES OF 2G HTS WIRES

© 2024 P. N. Degtyarenko[a, b]*, V. A. Skuratov[c], A. L. Vasiliev[d,e], A. V. Ovcharov[d]***,
A. M. Petrszhik[b,f]****, V. K. Semina[c], S. Y. Gavrilkin[g]*****, M. S. Novikov[c]******,
A. Y. Malyavina[h]*******, V. A. Amelichev[b], A.Y. Tsvetkov[g]**

[a] *Joint Institute for high temperature of RAS 125412, Moscow, Russia*
[b] *S-innovations LLC 117246, Moscow, Russia*
[c] *Joint institute for nuclear research 141989, Dubna, Moscow region, Russia*
[d] *National research center "Kurchatov institute" 123182, Moscow, Russia*
[e] *National Research University MPTI141701, Dolgoprudny, Moscow region, Russia*
[f] *Kotel'nikov Institute of Radio Engineering and Electronics of RAS, 125009, Moscow, Russia*
[g] *Lebedev Physical Institute of Russian Academy of Science, 119991, Moscow, Russia*
[h] *National Research Nuclear University MEPhI, 115409, Moscow, Russia*

* *e-mail: degtyarenkopn@gmail.com*
** *e-mail: skuratov@jinr.ru*
*** *e-mail: ovcharov.91@gmail.com*
**** *e-mail: a.petrzhik@s-innovations.ru*
***** *e-mail: gavrs@sci.lebedev.ru*
*******e-mail: msnovikov@jinr.ru*
********e-mail: ayu.malyavina@gmail.com*

Received September 14, 2023
Revised January 25, 2024
Accepted January 26, 2024

Abstract. Systematic studies of 2G HTS wires irradiated by high-energy 167 MeV Xe ions and fluences up to $1 \cdot 10^{12}$ cm^{-2} have been carried out. The optimal fluence value (the number of particles passing through 1 cm^2 of the sample surface) for obtaining the maximum critical current at different temperatures and external magnetic fields has been determined. An increase in the external magnetic field leads to a shift of the critical current peak towards higher fluences in the whole temperature range. The results of microstructural investigations by transmission electron microscopy and X-ray diffraction methods are given. It is shown that because of irradiation ion tracks with a diameter of about 5-8 nm are formed, acting as effective pinning centers. X-ray diffraction analysis indicates a decrease in texture sharpness under the influence of irradiation.

Keywords: *high temperature superconductor, critical current, irradiation, fluence, critical temperature, microstructure of HTS, ion tracks, morphology of HTS*

DOI: 10.31857/S004445102406e099

1. INTRODUCTION

Second-generation high temperature superconductor wire (2G HTS) is a film of HTS with a thickness typically of a few micrometers [1]. The superconductor $ReBa_2Cu_3O_{7-\delta}$ (where Re is a rare earth element) is deposited on a flexible metal substrate coated with buffer layers. The formation of buffer layer texture, necessary for oriented growth of the HTS film, is achieved either through the use of a RABiTS (Rolling Assisted Biaxially Textured Substrate) textured substrate or through IBAD (Ion Beam Assisted Deposition) technology. The HTS layer is covered with protective and shunting layers on top. The vast majority of modern applications of HTS wire involve their operation in strong external magnetic fields, which significantly reduce the superconducting capabilities of the tapes [2]. The deterioration of HTS superconducting properties in the presence of magnetic fields is caused by the drift of Abrikosov magnetic vortices, which requires the creation of artificial pinning centers to prevent such vortices [3]. For this purpose, defects that locally suppress superconductivity are deliberately introduced into the superconductor [4]. When the non-superconducting core of a vortex encounters such a defect, the vortex becomes pinned. Various approaches to creating artificial pinning centers are known, involving the use of different types of defects [5–8]. One of the most studied methods is the introduction of non-superconducting phase nano-inclusions with perovskite structure in the form of so-called nanocolumns $BaZrO_3$ [9] or $BaSnO_3$. This work examines the features and prospects of radiation pinning application with emphasis on flux optimization for various external conditions of temperature and magnetic field. The samples used were 4 mm wide sections of industrial 2G HTS wire manufactured by S-Innovations [11] with a silver protective layer. The irradiation technique is described in detail in works [12, 13], which also address the determination of optimal irradiation energy for tapes manufactured by Superpower.

2. SAMPLES AND EXPERIMENTAL METHODOLOGY

Square-shaped samples 3 mm × 3 mm were cut from industrial 2G HTS wire with a width of 4 mm. The tape manufactured by S-Innovations consisted of a flexible substrate (Hastelloy), buffer layers, a superconducting layer YBa2Cu3O7 with a thickness of about 2 μm and an upper protective Ag layer with a thickness of about 0.5 μm. The manufacturing technology is detailed in [1, 11].

The samples were irradiated with ions ^{132}Xe with energy of 167 MeV. The fluence value varied from $3 \cdot 10^{10}$ to $1 \cdot 10^{12}$ cm^{-2}. Irradiation with Xe ion flux of about $2 \cdot 10^8$ $cm^{-2} \cdot s^{-1}$ was carried out at room temperature using the IC-100 cyclotron at the Laboratory of Nuclear Reactions, JINR.

X-ray structural analysis was performed using a Rigaku SmartLab diffractometer with a rotating copper anode. All measurements were carried out in parallel beam geometry with Ge(220)×2 monochromator (wavelength $\lambda Cu_{K\alpha 1} = 1.541$ Å).

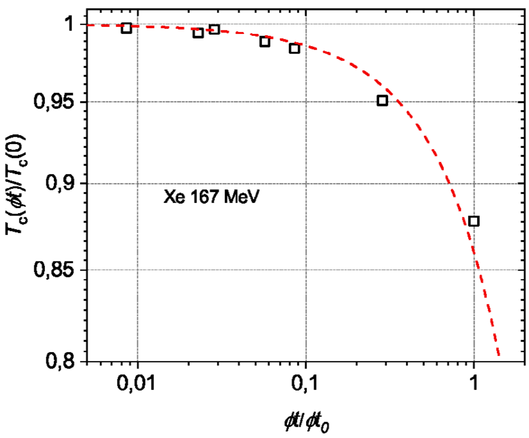

Fig. 1. Dependence of the normalized critical temperature of the superconducting transition of 2G HTS samples versus the normalized fluence value of Xe ions with energy of 167 MeV. Points – experimental data, dashed curve – dependence $T_c \approx T_{c0}(1 - k(\varphi t))$, $k \approx 0.14 \cdot 10^{12}$, where, T_{c0} – critical temperature of non-irradiated sample

Phase analysis and out-of-plane film orientation analysis were performed using 2Theta/Omega scanning. Omega scanning (so-called "rocking curves") was measured for (005) reflections of phase $YBa_2Cu_3O_7$ in the rolling direction (RD) and transverse direction (TD). Analysis of rocking curve widths allowed evaluation of the HTS film texture sharpness out of the substrate plane. Determination of the superconducting film texture sharpness in the substrate plane was performed using Phi- scanning for the (103) reflection of phase $YBa_2Cu_3O_7$ (2Theta = 32.5°, sample tilt angle Chi=45.3°). For each sample, preliminary spatial alignment was performed (maximizing reflection position for YBCO (005) reflection). The measurements and subsequent processing of results (determining FWHM parameter for rocking curves and Phi-scans) were carried out using standard software packages SmartLab Guidance and Integral Intensity Calculation.

Microstructural studies were carried out using a Tecnai Osiris transmission/scanning electron microscope at an accelerating voltage of 200 kV. Cross-sectional and planar sections for the studies were prepared using focused ion beam Ga^+ on focused ion beam scanning electron microscope Helios Nanolab 600.

3. RESULTS AND DISCUSSION

The dependence of the normalized value of the critical temperature of the superconducting transition, shown in Fig. 1, demonstrates a monotonic decrease T_c with increasing fluence. The dependence of the critical temperature on the irradiation dose is noted $T_c \approx T_{cO}(1 - k(\varphi t))$, $k \approx 0.14 \cdot 10^{12}$, where T_{cO} – critical temperature of non-irradiated sample. The decrease in T_c begins at fluence $8 \cdot 10^{10}\,\text{cm}^{-2}$ and at fluence $1 \cdot 10^{12}\,\text{cm}^{-2}$ decreases by 4 percent to 84.5 K (see table). Such behavior is associated with the formation of ion tracks, which cause deterioration in the sharpness of sample texture. At the same time, the created ion tracks are effective pinning centers for the vortex structure, which leads to an increase in the current-carrying capacity of the samples.

Fig. 2a shows the experimental dependencies of normalized (to non-irradiated sample under conditions of 77 K, 0T) critical current values on the normalized Xe ion fluence at temperatures of 77, 65, and 20 K in a field of 1 T. The nature of dependencies for the presented temperatures is similar, with curve maxima corresponding to the optimal fluence for the given field of about $2 \cdot 10^{11}\,\text{cm}^{-2}$.

At $T = 20$ K (see Fig. 2 b) in a field of 1 T, the critical current peak is in the fluence region , and with increasing field noticeably shifts and at 8 T corresponds to the fluence region $3 \cdot 10^{11}\,\text{cm}^{-2}$, and with increasing field noticeably shifts and at 8 T corresponds to the fluence $5 \cdot 10^{11}\,\text{cm}^{-2}$. The observed behavior of the critical current is associated with an increase in the concentration of ion tracks acting as effective pinning centers. Thus, irradiation leads to the formation of a higher density of ion tracks with length of the order of HTS film depth (the Bragg range of such ions is several μm). With increasing fluence, the number of formed ion tracks increases, and the distance between them becomes comparable to 2λ (λ – penetration depth). It is at this distance that the maximum increase in collective pinning force occurs, i.e., the peak effect in critical current. According to work [15], for non-irradiated samples $YBa_2Cu_3O_7$ penetration depth at T = 0 K is 150 nm. According to our data for the sample irradiated with Xe ions with fluence $3 \cdot 10^{11}\,\text{cm}^{-2}$, the penetration depth is 30 nm. The estimation was made from the relation for the second Fig. 4. critical field ($H_{c2} = \Phi_O/(\pi\lambda^2)$), which value was obtained from experimental data by plotting the superconducting transition temperature versus external magnetic field. The sample exhibits elastic inter-vortex interaction state, which contributes to maximum increase in current- carrying capacity. For clarity, the table shows maximum critical current values I_c , obtained for three characteristic external conditions: at $B = 0$, $T = 77$ K fluence $1{\cdot}10^{11}\,\text{cm}^{-2}$ gives $I_c = 274$ A, at $B = 2$T, $T = 50$ K, optimum shifts to fluence $2 \cdot 10^{11}\,\text{cm}^{-2}$ (735 A), and at $B = 8$ T, $T = 20$ K, – up to $5 \cdot 10^{11}\,\text{cm}^{-2}$ (critical current 921 A). The table shows that at high fluences, the critical current I_c at 77 K in self-field and critical temperature begin to decrease significantly due to superconductor structure degradation.

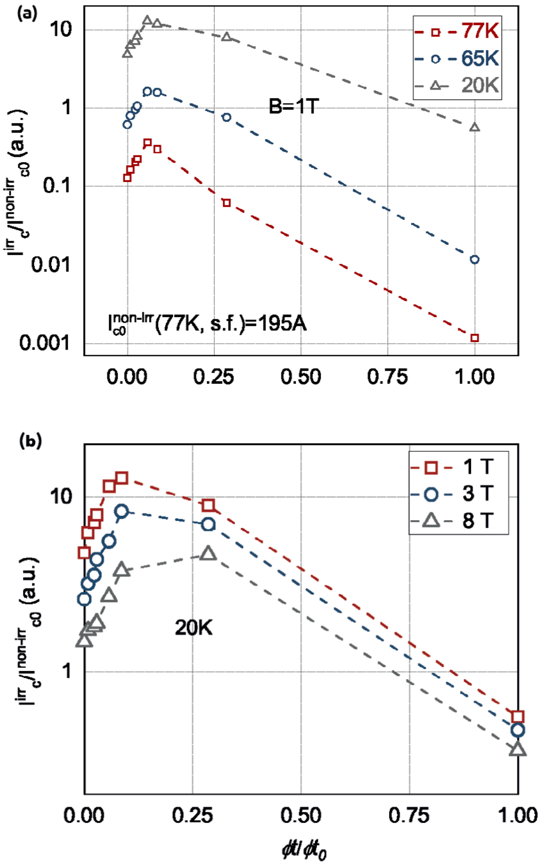

Fig. 2. Dependencies of the normalized critical current of 2G HTS wire samples on the normalized value of Xe ion fluence with energy of 167 MeV: a – in a field of 1 T and at temperatures of 77, 65 K and 20 K; b - in fields of 1, 3 and 8 T and temperature of 20 K

Figure 3 shows microstructure images of the sample irradiated with Xe ions with fluence cm $3 \cdot 10^{11}\,\text{cm}^{-2}$, at different magnifications. The full-size cross-section image (Fig. 3*a*) clearly shows high film uniformity without any defects. In the magnified

Table 1: Parameters of non-irradiated and Xe ion-irradiated samples with different fluences. XRD RD and XRD TD are the rocking curve half-widths (005) YBCO along and across the tape, respectively. The XRD Phi column corresponds to the YBCO (103) reflection during Phi scanning. Maximum values are highlighted in bold with underline for various external condition

Fluence, cm^{-2}	I_c, A (4 mm, $B = 0$, 77 K),	I_c, A (4 mm, $B = 2$ T, 50 K)	I_c, A (4 mm, $B = 8$ T, 20 K)	T_c, K	XRD RD FWHM, deg.	XRD TD FWHM, deg.	XRD Phi FWHM, deg.
0	195	207	291	88	1.129	1.350	2.86
3×10^{10}	195	257	336	88	1.144	1.887	3.39
8×10^{10}	233	368	400	87.8	1.163	2.33	3.81
1×10^{11}	**274**	455	496	87.7	1.175	2.413	4.53
2×10^{11}	270	**735**	734	87.4	1.227	5.346	5.03
3×10^{11}	198.5	635	725	87	1.179	3.079	4.39
5×10^{11}	171	644	**921**	86.5	1.192	4.359	5.29
1×10^{12}	63	397	906	84.5	1.268	5.294	5.89

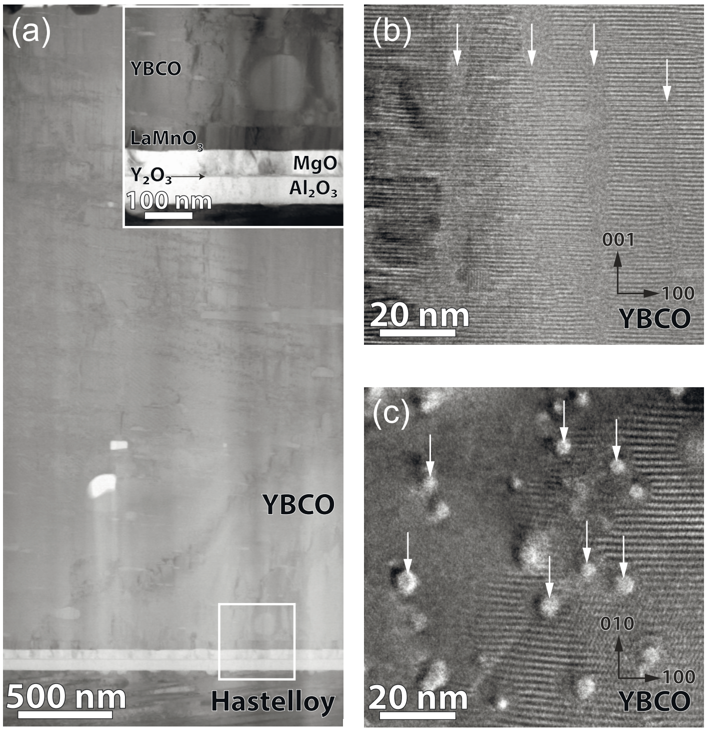

Fig. 3. Bright-field scanning transmission electron microscope (STEM) images of HTS wire full-size cross-section (a); inset shows magnified image of substrate/buffer layers/HTS interface. Transmission electron microscope (TEM) images of cross-sectional (b) and planar (c) sections of HTS layer. White arrows in the images indicate defects forming in the HTS matrix after Xe ion irradiation

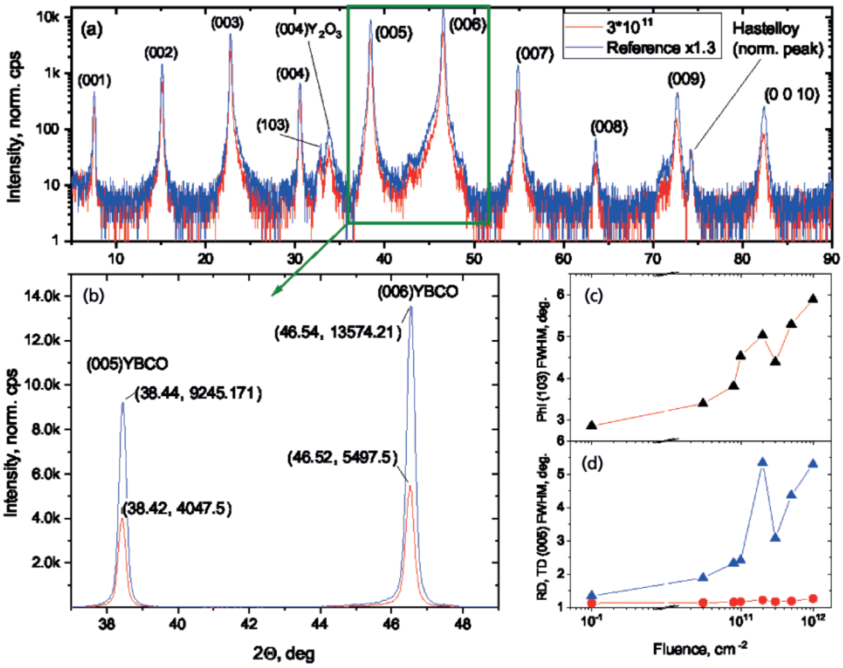

Fig. 4. a – X-ray diffraction patterns taken in symmetric Theta/2Theta mode for initial (non- irradiated) and Xe ion-irradiated samples with fluence of $3 \cdot 10^{11}$cm^{-2} . "Norm. peak" is the substrate reflection used for intensity normalization. b - Magnified area of figure a, which shows in detail the significant change in intensity of YBCO (005) and (006) reflections before and after irradiation. c - Average FWHM values of YBCO (103) reflection during Phi-scanning depending on fluence value. d - FWHM of rocking curve (005)YBCO in parallel (RD) and perpendicular (TD) directions to the tape depending on fluence value

TEM image of the cross-section of HTS film, ion tracks can be noticed, appearing as amorphous vertical nanocolumns with diameter of about 6 nm (Fig. 3b). For better track visualization, TEM images of the planar section of HTS layer were obtained, which clearly show rounded amorphous regions (Fig. 3c). It should be noted that there is a small variation in track diameters and their partial overlap.

Figure 4 shows diffraction patterns taken in symmetric mode on a Rigaku Smart Lab diffractometer. In Fig. 4*a* it is evident that the peak positions of the initial and irradiated samples (as an example, the diffraction pattern is shown for a sample irradiated with Xe ions with a fluence of $3 \cdot 10^{11}$ cm^{-2}) are practically indistinguishable, meaning that the crystal lattice parameter c does not change under irradiation. However, the peak widths increase significantly, indicating a decrease in texture sharpness, see the approximated area in Fig. 4*b*. Comparison of diffraction peak widths and their amplitudes is correct considering the same sample thickness and performed normalization by the substrate (Hastelloy) reflection amplitude. The deterioration of texture sharpness with increasing fluence is also confirmed by the Phi-scan (103) YBCO (see Fig. 4*c*). Notable is the different character of peak width increase in rocking curves (005)YBCO in parallel (RD) and perpendicular (TD) directions to the tape depending on the fluence value: in the non-irradiated sample, the rocking curves in two perpendicular directions (RD and TD) have approximately the same width, while in irradiated samples, there is a definite broadening in the TD direction. Such behavior confirms that an amorphous structure of regular tracks with a slight inclination relative to the crystallographic plane *ab* is realized in the sample.

4 CONCLUSION

Thus, systematic studies of electrophysical parameters and microstructure of samples before and after irradiation with Xe ions with previously determined [12] energy of 167 MeV and fluences up to $1 \cdot 10^{12}$ cm^{-2} have been conducted. The optimal fluence values at which peak of critical current values are observed for various external conditions have been established. It has been found that with increasing fluence, the critical current peak shifts towards stronger magnetic fields. Based on microstructural studies, it was revealed that ion tracks with a diameter of about 6 nm are formed as a result of irradiation. The formed tracks are effective pinning centers, which is confirmed by the analysis of hysteresis magnetization curves of irradiated samples and the results of their morphology studies. A decrease in texture sharpness is observed with increasing fluence. The obtained results are planned to be used for calculating the necessary tape winding speeds directly through the ion beam, which will allow creating 2G HTS wires with increased current-carrying capacity due to the conducted radiation pinning.

FUNDING

The work was carried out with the support of the Ariadna MSTE collaboration under the applied materials science research program. X-ray phase analysis was conducted by

A.M.P. with financial support from the Russian Science Foundation (project No. 23-49-10006). Magnetic measurements were performed at the Shared Research Facility of the Lebedev Physical Institute RAS. Electron microscopy studies were carried out using the equipment of the Resource center of probe and electron microscopy (Kurchatov complex of NBICS-natural-like technologies, NRC “Kurchatov institute“) and analysis of the obtained results were carried out with financial support from the Ministry of Science and Higher Education (State Assignment of JIHT RAS No. 075-01129-23-00).

REFERENCES

1. Markelov, A.; Valikov, A.; Chepikov, V.; Petrzhik, A.; Massalimov, B.; Degtyarenko, P.; Uzkih, R.; Soldatenko, A.; Molodyk, A.; Sim, K.; Hwang, S. 2G HTS Wire with Enhanced Engineering Current Density Attained through the Deposition of HTS Layer with Increased Thickness. Progress in Superconductivity and Cryogenics 2019, 21 (4), 29–33. https://doi.org/10.9714/PSAC.2019.21.4.029.

2. Malozemoff, A. P. Second-Generation High-Temperature Superconductor Wires for the Electric Power Grid. Annu. Rev. Mater. Res. 2012, 42 (1), 373–397. https://doi.org/10.1146/annurev-matsci-100511-100240.

3. Abrikosov, A. A. The Magnetic Properties of Superconducting Alloys. Journal of Physics and Chemistry of Solids 1957, 2 (3), 199–208. https://doi.org/10.1016/0022-3697(57)90083-5.

4. Blatter, G.; Feigel’man, M. V.; Geshkenbein, V. B.; Larkin, A. I.; Vinokur, V. M. Vortices in High-Temperature Superconductors. Rev. Mod. Phys. 1994, 66 (4), 1125–1388. https://doi.org/10.1103/RevModPhys.66.1125.

5. Selvamanickam, V.; Carota, G.; Funk, M.; Vo, N.; Haldar, P. High-Current Y-Ba-Cu-0 Coated Conductor Using Metal Organic Chemical-Vapor Deposition and Ion-Beam-Assisted Deposition. IEEE TRANSACTIONSON APPLIED SUPERCONDUCTIVITY 2001, 11 (I), 3379–3381. https://doi.org/10.1109/77.919787.

6. Catana, A.; Broom, R. F.; Bednorz, J. G.; Mannhart, J.; Schlom, D. G. Identification of Epitaxial Y2O3 Inclusions in Sputtered YBa2Cu3O7 Films: Impact on Film Growth. Appl. Phys. Lett. 1992, 60 (8), 1016–1018. https://doi.org/10.1063/1.106507.

7. MacManus-Driscoll, J. L.; Foltyn, S. R.; Jia, Q. X.; Wang, H.; Serquis, A.; Maiorov, B.; Civale, L.; Lin, Y.; Hawley, M. E.; Maley, M. P.; Peterson, D. E. Systematic Enhancement of In-Field Critical Current Density with Rare-Earth Ion Size Variance in Superconducting Rare-Earth Barium Cuprate Films. Applied Physics Letters 2004, 84 (26), 5329–5331. https://doi.org/10.1063/1.1766394.

8. Strickland, N. M.; Wimbush, S. C.; Kennedy, J. V.; Ridgway, M. C.; Talantsev, E. F.; Long, N. J. Effective Low-Temperature Flux Pinning by Au Ion Irradiation in HTS Coated Conductors. IEEE Trans. Appl. Supercond. 2015, 25 (3), 1–5. https://doi.org/10.1109/TASC.2014.2366079.

9. Erb, A.; Walker, E.; Flükiger, R. The Use of BaZrO3 Crucibles in Crystal Growth of the High-Tc Superconductors Progress in Crystal Growth as Well as in Sample Quality. Physica C: Superconductivity 1996, 258 (1–2), 9–20. https://doi.org/10.1016/0921-4534(95)00807-1.

10. Varanasi, C. V.; Barnes, P. N.; Burke, J.; Brunke, L.; Maartense, I.; Haugan, T. J.; Stinzianni, E. A.; Dunn, K. A.; Haldar, P. Flux Pinning Enhancement in YBa2Cu3O7−x Films with BaSnO3 Nanoparticles. Supercond. Sci. Technol. 2006, 19 (10), L37–L41. https://doi.org/10.1088/0953-2048/19/10/L01.

11. Molodyk, A.; Samoilenkov, S.; Markelov, A.; Degtyarenko, P.; Lee, S.; Petrykin, V.; Gaifullin, M.; Mankevich, A.; Vavilov, A.; Sorbom, B.; Cheng, J.; Garberg, S.; Kesler, L.; Hartwig, Z.; Gavrilkin, S.; Tsvetkov, A.; Okada, T.; Awaji, S.; Abraimov, D.; Francis, A.; Bradford, G.; Larbalestier, D.; Senatore, C.; Bonura, M.; Pantoja, A. E.; Wimbush, S. C.; Strickland, N. M.; Vasiliev, A. Development and Large Volume Production of Extremely High Current Density YBa2Cu3O7 Superconducting Wires for Fusion. Sci Rep 2021, 11 (1), 2084. https://doi.org/10.1038/s41598-021-81559-z.

12. Suvorova, E. I.; Degtyarenko, P. N.; Karateev, I. A.; Ovcharov, A. V.; Vasiliev, A. L.; Skuratov, V. A.; Buffat, P. A. Energy Dependent Structure of Xe Ion Tracks in YBCO and the Effect on the Superconductive Properties in Magnetic Fields. Journal of Applied Physics 2019, 126 (14), 145106. https://doi.org/10.1063/1.5120894.

13. Suvorova, E. I.; Degtyarenko, I. A.; Ovcharov, A. V.; Vasiliev, Influence of the Structure of Ion Tracks in YBCO on the Superconducting Properties of Composite Wires. Journal of Surface investigation 2022, 16 (1), 112-117. https://doi.org/10.1134/S1027451022010360.

14. Bean, C. P. Magnetization of Hard Superconductors. Phys. Rev. Lett. 1962, 8 (6), 250–253. https://doi.org/10.1103/PhysRevLett.8.250.

15. Larbalestier, D.; Gurevich, A.; Feldmann, D. M.; Polyanskii, A. High-Tc Superconducting Materials for Electric Power Applications. MATERIALS FOR SUSTAINABLE ENERGY 2010, 414. https://doi.org/10.1038/35104654.

JOURNAL OF EXPERIMENTAL AND THEORETICAL PHYSICS, 2024, Vol. 165, No. 6, pp. 845–850

ELECTRONIC PROPERTIES OF SOLID

QUANTUM TRANSPORT THROUGH THE GRAPHENE-SILICENE NANORIBBONS JUNCTION

© 2024 M. Najarsadeghi, A. A. Fouladi*, A. Z. Rostami, A. Pahlavan

Department of Physics, Sari Branch, Islamic Azad University 4818168984 Sari, Iran
** e-mail: a.ahmadifouladi@iausari.ac.ir*

Received October 06, 2022
Revised December 15, 2023
Accepted December 17, 2023

Abstract. In this paper, the quantum transport through armchair graphene-silicene nanoribbons junction has been investigated by using non-equilibrium Green's function method and tight binding approximation in Landauer-Büttiker formalism. The results demonstrate that this junction exhibits metallic behavior in the absence of intrinsic spin-orbit interaction and by increasing the size of the intrinsic spin-orbit interaction, the transition from conductor to semiconductor for the system occurs. Moreover, the electron transport characteristics of the system can be controlled by changing the size of the length and width of the junction and the strength of GNR-SiNR coupling. These results can be useful for designing nanoelectronic devices.

DOI: 10.31857/S004445102406e105

1. INTRODUCTION

Two-dimensional hexagonal structures such as graphene and silicene have attracted a great deal of attention due to their unique electronic properties as well as their many applications in the manufacture of nanoelectronic devices [1–13]. Silicene, which is a monolayer, honeycomb structure of silicon atoms, has been successfully synthesized and many studies have been done on its electronic properties in recent years [14, 15]. Unlike graphene, silicene has no plate structure and has a buckled structure [16]. This feature of silicene is useful for adjusting the band gap, because of an external electric field effect transistors [17, 18]. Also, the spin-orbit interaction in silicene, unlike graphene, is large, which can be used to make spintronic devices [19].Another useful feature of Silicene is its good compatibility with today's silicon-based electronics technology. Silicene nanoribbons, like graphene nanoribbons, can be divided into zigzag edges and armchair edges depending on the type of edge. The results show that the armchair silicene nanoribbons are the same as armchair graphene nanoribbons with width $N_W = 3$ m + 2 (m is an integer) are conductive and the rest are semiconductors [20]. Recent investigations have shown that hybrid nanostructures such as graphene-silicene heterostructures reveal greater physical properties than similar single graphene or silicene nanoribbons [21–26].

In this paper, electron transport through the arm-chair graphene-silicene nanoribbons junction (GNR-SiNR junction) has been studied numerically by using non-equilibrium Green's function and tight-binding approximation in Landauer-Büttiker formalism. The design model of this junction is shown in Fig. 1. In particular, the effect of the power of the intrinsic spin-orbit interaction, the strength of GNR-SiNR coupling, the length and width of the junction on the transmission probability function, and the electric current have been investigated.

2. METHODOLOGY

In this article, we characterize our method based on the GNR-SiNR junction consisting of armchair graphene/silicene nanoribbon as a central region (CR) contacted to two semi-infinite armchair GNR and SiNR electrodes, as shown in Fig. 1. To study the quantum transport properties of the GNR-SiNR

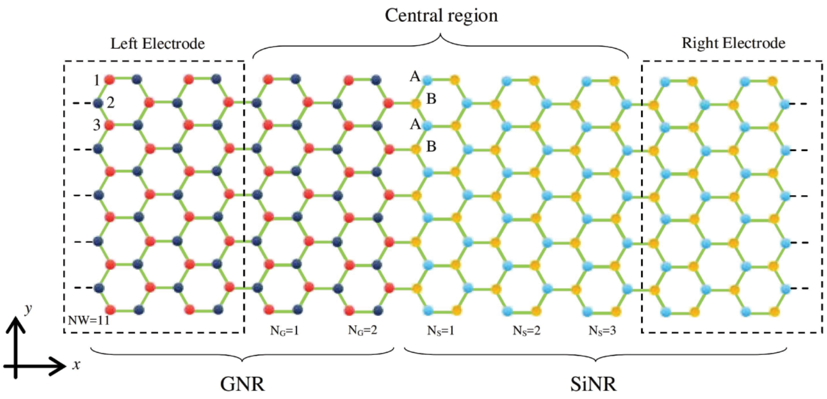

Fig. 1. Graphene nanoribbons (GNR), silicene- nanoribbons junction design. The left semi-infinite electrode is a graphene nanoribbons and the right semi-infinite electrode is a silicene nanoribbons that are connected to the central region

junction, we de-compose the total Hamiltonian of the system as

$$H = H_{CR} + H_R + H_L + H_C, \qquad (1)$$

where $H_{CR} = H_{GNR} + H_{SiNR} + H_{GS}$ describes the Hamiltonian of the central region, $H_R(H_L)$ is the Hamiltonian of the right SiNR (left GNR) elecrode, and HC is the Hamiltonian for the coupling between CR and electrodes. Using the tight-binding model with nearest-neighbor hopping approximation, the Hamiltonians HGNR, HSiNR, and HC can be expressed as follows:

$$H_{GRN} = \varepsilon\sum_{i,\sigma} c^{\dagger}_{i,\sigma}c_{i,\sigma} = -t_G \sum_{i,j,\sigma} (c^{\dagger}_{i,\sigma}c_{i,\sigma} + H.c), \qquad (2)$$

$$\begin{aligned} H_{GRN} &= -t_S \sum_{(ij)\alpha} c^{\dagger}_{j,\alpha} + \\ &+ i\frac{\lambda_{SO}}{3\sqrt{3}} \sum_{((ij))\alpha\beta} \eta_{ij} c^{\dagger}_{j,\alpha}\sigma^2_{\alpha\beta}c_{j\beta} - \\ &- i\frac{2}{3}\lambda_R \sum_{((ij))\alpha\beta} \xi_{ij} c^{\dagger}_{j,\alpha}(\sigma \times d^0_{ij})^z_{\alpha\beta}c_{j\beta}, \end{aligned} \qquad (3)$$

$$H_{GS} = -\sum_{i,j,\sigma} t_{GS(i,j,\sigma)}(c^{\dagger}_{i,\sigma}c_{i,\sigma} + H.c), \qquad (4)$$

$$H_C = \sum_{i,j,\sigma} t_{c(i,j,\sigma)}(c^{\dagger}_{i,\sigma}d_{i,\sigma} + H.c), \qquad (5)$$

$c^{\dagger}_{i,\sigma}$, and $c_{i,\sigma}$ ($d^{\dagger}_{i,\sigma}$, and $d_{i,\sigma}$) are the creation and annihilation operators of a π-electron at the ith site of the GNR-SiNR (electrodes), respectively. i and j stand for the nearest-neighbor pairs in the GNR and SiNR lattices. ε is the on-site energy. The hopping integral between the nearest-neighbor GNR(SiNR) lattice is $t_G = 2.7$ eV ($t_S = 1.6$ eV [27]). $\langle ij\rangle$ and $\langle\langle ij\rangle\rangle$ stand for the nearest-neighbor and next nearest-neighbor pairs in the SiNR lattice, respectively. The effective intrinsic spin-orbit interaction (SOI) parameter and the intrinsic Rashba SOI parameter are λ_{SO} and λ_R, respectively. $\vec{\sigma} = (\sigma_x, \sigma_y, \sigma_x)$ is the Pauli matrix with $\eta_{ij} = -1$ ($\eta_{ij} = +1$) if the next-nearest neighbor hopping is clockwise (anticlockwise) with respect to the positive z-axis, and $\xi_{ij} = +1$ ($\xi_{ij} = -1$) for A(B) site. $\vec{d}^0_{ij} = \frac{\vec{d}_{ij}}{|\vec{d}_{ij}|}$ is the unit vector parallel to the vector $\vec{d_{ij}}$ connecting the two sites i and j in the same sublattice. HGR is the Hamiltonian for the coupling between GNR-SiNR in the central region and tGS is the coupling strength between the GNR and SiNR. Also, $t_c = t_G$ ($t_c = t_S$) is the coupling strength between left GNR (right SiNR) electrode and GNR (SiNR) in the central region. The Green's function of the system is expressed as

$$G(E) = [(E + i\eta)I - H_{GS} - \Sigma_{L,\sigma} - \Sigma_{R,\sigma}]^{-1}, \qquad (6)$$

where I represents the identity matrix and $\eta \to 0^+$, E is the energy of the injecting electron. Σ_L and Σ_R are the self-energy matrices due to the connection of right and left electrodes to the central region, respectively, that can be calculated numerically by the recursive method described by Sancho and coworkers [28]. The surface Green's function of the right and left electrodes are calculated as

$$9^L_{0,0} = [(E + i0^+)I - H_{0,0} - H^\dagger_{-1.0}T]^{-1}, \quad (7)$$

$$9^R_{N+1,N+1} = [(E + i0^+)I - H_{N+1,N+1} - H^\dagger_{N+1,N+2}T]^{-1}, \quad (8)$$

where $H_{0,0}(H_{\mathrm{N+1,N+1}})$ and $H_{-1,0}(H_{\mathrm{N+1,N+2}})$ are the Hamiltonian of a unit-cell and the coupling matrix between two unit cells in the left (right) electrode, respectively. Here T and $\tilde{T}$ are the transfer matrices, which can be computed from the Hamiltonian matrix elements via an iterative procedure as [28]

$$T = t_0 + \tilde{t}_0 t_1 + \tilde{t}_0 \tilde{t}_1 t_2 + \ldots + \tilde{t}_0 \tilde{t}_1 \tilde{t}_2 \ldots t_{\mathrm{m}}, \quad (9)$$

$$\tilde{T} = \tilde{t}_0 + t_0 \tilde{t}_1 + t_0 t_1 \tilde{t}_2 + \ldots + t_0 t_1 t_2 \ldots \tilde{t}_{\mathrm{m}}, \quad (10)$$

where t_i and $\tilde{t}_i$ with $1 \leqslant \mathrm{i} \leqslant m$ are defined by recursion formulas

$$t_{\mathrm{i}} = (I - t_{\mathrm{i}-1}\tilde{t}_{\mathrm{i}-1} - \tilde{t}_{\mathrm{i}-1}t_{\mathrm{i}-1})^{-1} t^2_{\mathrm{i}-1}, \quad (11)$$

$$\tilde{t}_{\mathrm{i}} = (I - t_{\mathrm{i}-1}\tilde{t}_{\mathrm{i}-1} - \tilde{t}_{\mathrm{i}-1}t_{\mathrm{i}-1})^{-1} \tilde{t}^2_{\mathrm{i}-1}. \quad (12)$$

The following conditions are applied to calculate $\tilde{t}_i$ and t_i in Eq. (8) for the left electrode

$$\tilde{t}_0 = [(E + i0^+)I - H_{0,0}]^{-1} H^\dagger_{-1,0}, \quad (13)$$

$$t_0 = [(E + i0^+)I - H_{0,0}]^{-1} H_{-1,0}, \quad (14)$$

and for the right electrode in Eq. (9)

$$\tilde{t}_0 = [(E + i0^+)I - H_{\mathrm{N+1,N+1}}]^{-1} H^\dagger_{\mathrm{N+1,N+2}}, \quad (15)$$

$$t_0 = [(E + i0^+)I - H_{\mathrm{N+1,N+1}}]^{-1} H_{\mathrm{N+1,N+2}}. \quad (16)$$

The iteration is repeated until $\tilde{t}_m, t_m \leqslant \delta$ with δ arbitrarily small. Finally, we can calculate the self-energies of the two left and right electrodes by

$$\Sigma_L = H^\dagger_{0,1} g^L_{0,0} H_{0,1}, \quad (17)$$

$$\Sigma_R = H_{N,N+1} g^R_{N+1,N+1} H^\dagger_{N,N} \quad (18)$$

The energy-dependent transmission function in terms of the Green's function of the central region and the coupling of it with two left and right electrodes can be written as

$$T(E) = Tr(\Gamma_L(E)\, G^r(E) \Gamma_R(E) G^a(E)). \quad (19)$$

Where Gr (Ga) is the retarded (advanced) Green's function, and $\Gamma_{L(R)} = i(\Sigma_{L(R)} - \Sigma^\dagger_{L(R)})$ is the coupling matrix. The electric current can be calculated by the Landauer-Büttiker formula [29]:

$$I(V) = \frac{e}{h} \int_{-\infty}^{+\infty} T(E)[f_L - f_R]\, dE. \quad (20)$$

where $f_{L(R)} = f(E - \mu_{L(R)})$ is the Fermi–Dirac distribution functions in the left (right) electrode with chemical potential $\mu_{L(R)} = E_F \pm \frac{eV}{2}$ and Fermi energy E_F.

3. RESULTS AND DISCUSSION

In this section, we represent the results of the numerical calculations of the quantum transport of the GNR-SiNR system. The Fermi energy and tempera-ture are chosen $E_F = 0$, $T = 4K$ respectively. Also, the intrinsic Rashba SOI parameter is $\lambda_R = 0.7$ meV [27]. The intrinsic and intrinsic Rashba spin-orbit interactions in graphene is omitted since it is negligible compared to the one in silicene [30, 31].

3.1. The effects of spin-orbit interaction

Figures 2*a*, *b* illustrate the diagram of electron transmission probability in terms of energy and electric current in terms of bias voltage, respectively, for different values of λ_{SO} with $N_W = 11$, $N_S = 5$, $N_G = 5$. As it is shown in Fig. 2*a*, the transmission probability diagram has oscillating behavior; whereas for a junction that all its parts are composed of graphene or silicene nanoribbons, the transmission function has a step form. This is due to the effect of quantum interference, which occurs due to the scattering of electron waves at the junction of graphene and silicene nanoribbons due to the mismatch of transmission modes in these locations. In the transmission probability diagram, the resonant peaks are symmetrically located around the Dirac point ($E = 0$). In the absence of intrinsic spin-orbit interaction ($\lambda_{SO} = 0$), the probability of transmission at the Dirac point has a non-zero value, which indicates that the system is conductive. By increasing the value of λ_{SO}, it is observed that the probability of

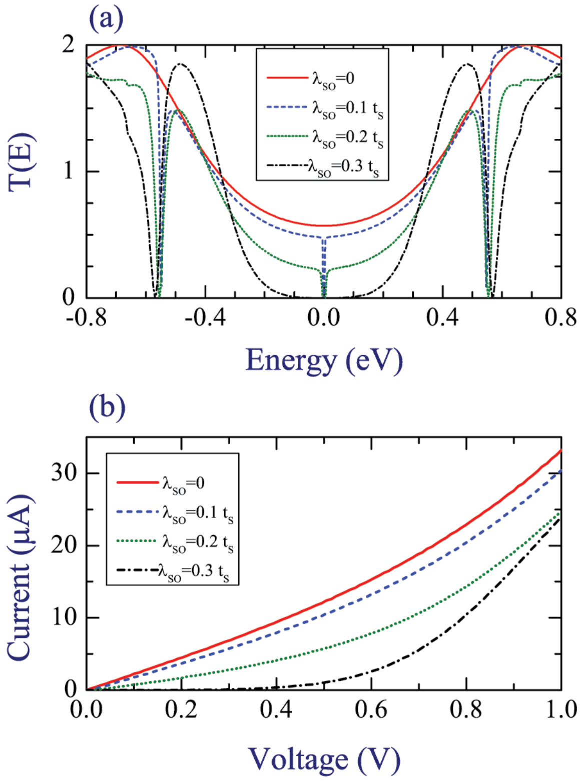

Fig. 2. a — Transmission function as a function of energy. b — The current-voltage characteristic for different values of λ_{SO} with $N_W = 11$, $N_S = 5$, $N_G = 5$

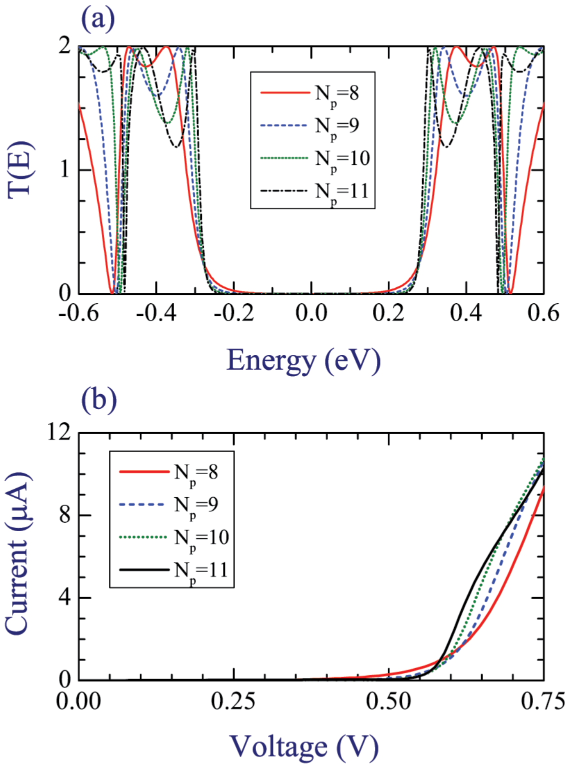

Fig. 3. a — Transmission function as a function energy. b — The current-voltage characteristic for different NS values with $N_W = 11$, $N_G = 5$, $\lambda_{SO} = 0.2t_s$

transmission at the Dirac point decreases and $\lambda_{SO} = 0.3t_s$ reaches zero and the gap in transmission function (the zero range of the transmission function around the Dirac point) appears. Thus, by increasing the λ_{SO} value, we see the transition from conductive to semiconductor for the system. Also, for $\lambda_{SO} \neq 0$ the probability of transmission in the energy range ±0.5 eV < E < ±0.5 eV has a valley, which is called the anti-resonance state and is due to the destructive interference between the propagated states along the nanoribbons for the presence of spin-orbit interaction. As λ_{SO} increases, the amplitude of these anti-resonance modes increases. The important point is that for a system in which all parts (electrodes and central region) are composed of graphene nanoribbons, the transmission probability diagram has no gaps and the system is conductive. It also remains conductive for a system in which all parts are made of silicene nanoribbons, even in the presence of an intrinsic spin-orbit interaction. Therefore, by connecting graphene and silicene nanoribbons, a junction can be designed that has the property of switching from conductive to the semiconductor. We now interpret the current-voltage characteristic in Fig. 2*b*. For λ_{SO}, there is no threshold voltage to turn on the current because of the lack of a gap in the transmission probability diagram. As λ_{SO} increases, the size of the current decreases due to a decrease in the probability of transmission near the Dirac point (−0.3 eV < E < 0.3 eV). As the λ_{SO} increases due to the appearance of the emission function gap, the magnitude of the threshold voltage to turn on the current also increases.

3.2. The study of geometric factors

Figure 3 investigates the effect of nanoribbon lengthon the electron transport properties for $N_W = 11$, $\lambda_{SO} = 0.2t_s$ values. In this case, we consider the length of the graphene nanoribbons to be constant($N_G = 5$) and the length of the silicene nanoribbons(N_S) to be variable. As it is shown in Fig. 3*a*, the nearest resonance peaks to the Dirac point move towards the Dirac point with the increase of N_S and the width of these peaks also decreases. However, the magnitude of the probability of transmission near the Dirac point (−0.27 eV < E < 0.27 eV) decreases with increasing length. As a result of the gap, the probability of transmission increases with

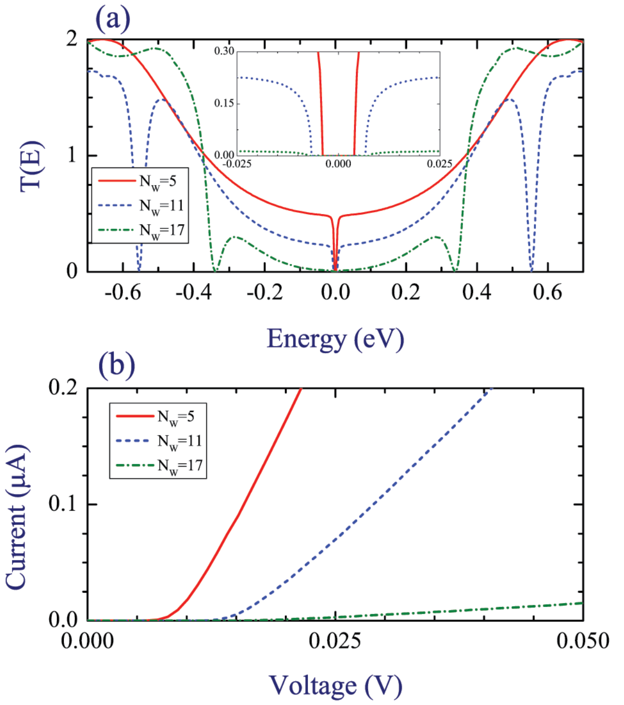

Fig. 4. a — Transmission function as a function energy. b — The current-voltage characteristic for different *NW* values with $N_G = 5$, $N_S = 5$, $\lambda_{SO} = 0.2t_s$

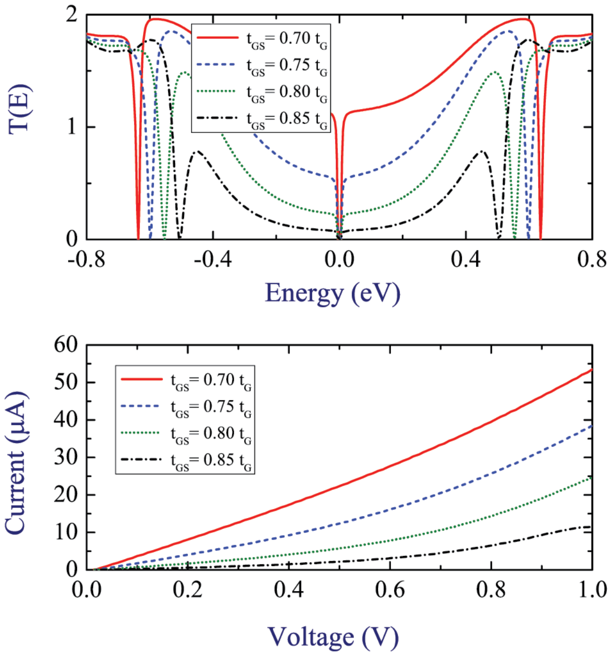

Fig. 5. a — Transmission function as a function energy. b — The current-voltage characteristic for different t_{GS} values with NW = 0, $N_G = 5$, $N_S = 5$, $\lambda_{SO} = 0.2t_s$

the increase of N_S. The effect of this gap increase is reflected in the diagram in a way that the threshold voltage increases with increasing N_S (see Fig. 3*a*). In Fig. 4, we investigated the effect of nanoribbon's width (N_W) size on the system's electronic transport for $N_W = 11$, $N_S = 5$, $\lambda_{SO} = 0.2t_s$ values. Figure 4*a* represents the diagram of the energy transmission probability in terms of energy for different widths of the junction. As it is observed, as the width of the junction increases, the magnitude of the transmission probability decreases around the Dirac point (−0.35 eV < E < 0.35 eV), and the magnitude of the transmission probability gap increases (internal figure of Fig. 4*a*). Also, the transmission function valleys approach the Dirac point by increasing the width of the nanoribbons. In Fig. 4*b*, the effect of nanoribbon's width size on current-voltage characteristics is plotted. It is observed that with increasing the width of the nanoribbons, the threshold voltage increases, also the current size decreases. Therefore, by changing the geometry (length and width) of the nanoribbons, the electron transport characteristics of the system can be controlled.

3.3. The effect of the strength of GNR-SiNR coupling

Figure 5 investigates the effect of the strength of GNR-SiNR coupling (tGS) on the electron transport properties of the system for $N_W = 0$, $N_G = 5$, $N_S = 5$, $\lambda_{SO} = 0.2t_s$. With the increase of tGS, the antiresonance dips become wider and smaller and approach zero energy (see Fig. 5*a*). Also the antiresonance dip at the zero energy becomes smaller. As a result, the current decreases with the increase of t_{GS} as seen in Fig. 5*b*. This result shows how we can control the quantum transport of the system by changing the strength of GNR-SiNR coupling.

4. CONCLUSION

In this paper, the electron transport through the graphene-silicene nanoribbons junction is investigated using the non-equilibrium Green's function method and tight-binding approximation in the Landauer-Büttiker formalism. The results show that the electron transport characteristics of the junction are very sensitive to the power of the intrinsic spin-orbit interaction quantity as well as the geometry (length and width) of the junction. In the presence of an intrinsic spin-orbit interaction quantity, the transmission function gap is created and the conductor to the semiconductor transition occurs. As the transmission function gap increases, the threshold voltage magnitude in the current-voltage characteristic increases. As the length of the junction increases, the width of the nearest resonant peaks to the Dirac point decreases and they move towards the Dirac point. The transmission probability gap also increases with increasing length, resulting in an increase in the threshold voltage magnitude. As the width of the nanoribbons increases, the magnitude of the transmission probability around the Dirac point decreases, the gap size of the transmission probability increases, and the valleys of the transmission function approach the Dirac point. Consequently, the magnitude of the electric current decreases, and the magnitude of the threshold voltage increases. These results can be used to control electron transport in nanoelectronic devices.

REFERENCES

1. M. Brzezinska, Y. Guan, O. V. Yazyev, S. Sachdev, and A. Kruchkov, Engineering Syk Interactions in Disordered Graphene Flakes Under Realistic Experimental Conditions, Phys. Rev. Lett. 131, 036503 (2023), doi:10.1103/PhysRevLett.131.036503.

2. Y.-Z. Chou and S. Das Sarma, Kondo Lattice Model in Magic-Angle Twisted Bilayer Graphene, Phys. Rev. Lett. 131, 026501 (2023), doi:10.1103/PhysRevLett.131.026501.

3. S. Jois, J. L. Lado, G. Gu, Q. Li, and J. U. Lee, Andreev Reflection and Klein Tunneling in High-Temperature Superconductorgraphene Junctions, Phys. Rev. Lett. 130, 156201 (2023), doi:10.1103/PhysRevLett.130.156201.

4. C. Lu, Y. Gao, X. Cao, Y. Ren, Z. Han, Y. Cai, and Z. Wen, Linear and Nonlinear Edge and Corner States in Graphenelike Moire Lattices, Phys. Rev. B 108, 014310 (2023), doi:10.1103/PhysRevB.108.014310.

5. G. Yu, Y. Wang, M. I. Katsnelson, and S. Yuan, Origin of the Magic Angle in Twisted Bilayer Graphene From Hybridization of Valence and Conduction Bands, Phys. Rev. B 108, 045138 (2023), doi:10.1103/PhysRevB.108.045138.

6. M. Najarsadeghi, A. Ahmadi Fouladi, A. Z. Rostami, and A. Pahlavan, Tunnel Magnetoresistance of Trilayer Graphene-Based Spin Valve, Phys. E 144, 115422 (2022), doi:10.1016/j.physe.2022.115422.

7. A. A. Fouladi, Spin-Dependent Transport Properties of Aa-Stacked Bilayer Graphene Nanoribbon, Phys. E 102, 117 (2018), doi:10.1016/j.physe.2018.05.002.

8. A. A. Fouladi, Effect of Uniaxial Strain on the Tunnel Magnetoresistance of T-Shaped Graphene Nanoribbon Based Spinvalve, Superlattices and Microstructures 95, 108 (2016), doi:10.1016/j.spmi.2016.04.043.

9. A. A. Fouladi and S. Ketabi, Electronic Properties of Z-Shaped Graphene Nanoribbon Under Uniaxial Strain, Phys. E 74, 475 (2015), doi:10.1016/j.physe.2015.08.018.

10. G. Le Lay, Silicene Transistors, Nature Nanotech. 10, 202 (2015), doi:10.1038/nnano.2015.10.

11. H. Emami-Nejad, A. mir, Z. Lorestaniweiss, A. Farmani, and R. Talebzadeh, First Designing of a Silicene-Based Optical Mosfet With Outstanding Performance, Sci. Rep. 13, 6563 (2023), doi:10.1038/s41598-023-33620-2.

12. A. A. Fouladi, Electronic Transport Properties of T-Shaped Silicene Nanoribbons, Phys. E 91, 101 (2017), doi:10.1016/j.physe.2016.10.040.

13. A. A. Fouladi, Quantum Transport Through a Z-Shaped Silicene Nanoribbon, Chinese Phys. B 26, 047304 (2017), doi:10.1088/1674-1056/26/4/047304.

14. B. Lalmi, H. Oughaddou, H. Enriquez, A. Kara, S. Vizzini, B. Ealet, and B. Aufray, Epitaxial Growth of a Silicene Sheet, Appl. Phys. Lett. 97, 223109 (2010), doi:10.1063/1.3524215.

15. C. Grazianetti, E. Cinquanta, and A. Molle, Two-Dimensional Silicon: The Advent of Silicene, 2D Materials 3, 012001 (2016), doi:10.1088/2053-1583/3/1/012001.

16. P. Vogt, P. Padova, C. Quaresima, J. Avila, E. Frantzeskakis, M. Asensio, A. Resta, B. Ealet, and G. Le Lay, Silicene: Compelling Experimental Evidence for Graphenelike Two-Dimensional Silicon, Phys. Rev. Lett. 108, 155501 (2012), doi:10.1103/PhysRevLett.108.155501.

17. M. Ezawa, A Topological Insulator and Helical Zero Mode in Silicene Under an Inhomogeneous Electric Field, New J. Phys. 14, 033003 (2012), doi:10.1088/1367-2630/14/3/033003.

18. N. Drummond, V. Zolyomi, and V. Falko, Electrically Tunable Band Gap in Silicene, Phys. Rev. B 85, doi:10.1103/PhysRevB.85.075423.

19. Z. Zhu, Y. Cheng, U. Schwingenschlogl, Giant Spin-Orbit-Induced Spin Splitting in Two-Dimensional Transition-Metal Dichalcogenide Semiconductors, Phys. Rev. B 84, 153402 (2011), doi:10.1103/PhysRevB.84.153402.

20. Y. Ding and J. Ni, Electronic Structures of Silicon Nanoribbons, Applied Phys. Lett. 95, 083115 (2009), doi:10.1063/1.3211968.

21. B. Kiraly, A. J. Mannix, M. C. Hersam, and N. P. Guisinger, Graphene-silicon Heterostructures at the Two-Dimensional Limit, Chemistry of Materials 27, 6085 (2015), doi:10.1021/acs.chemmater.5b02602.

22. L. Meng, Y. Wang, L. Li, and H.-J. Gao, FAbrication of Graphene-silicon Layered Heterostructures by Carbon Penetration of Silicon Film, Nanotechnology 28, 084003 (2017), doi:10.1088/1361-6528/aa53cf.

23. G. Li, L. Zhang, W. Xu, J. Pan, S. Song, Y. Zhang, H. Zhou, Y. Wang, L. Bao, Y.-Y. Zhang, S. Du, M. Ouyang, S. T. Pantelides, and H.-J. Gao, Stable Silicene in Graphene/silicene Van Der Waals Heterostructures, Advanced Materials 30, 1804650 (2018), doi:10.1002/adma.201804650.

24. B. Liu, J. A. Baimova, C. D. Reddy, S. V. Dmitriev, W. K. Law, X. Q. Feng, and K. Zhou, Interface Thermal Conductance and Rectification in Hybrid Graphene/silicene Monolayer, Carbon 79, 236 (2014), doi:10.1016/j.carbon.2014.07.064.

25. H. Pourmirzaagha and S. Rouhi, Molecular Dynamic Simulations of the Heat Transfer in Double-Layered Graphene/Silicene Nanosheets, Phys. B 666, 415079 (2023), doi:10.1016/j.physb.2023.415079.

26. J. Zhou, H. Li, H.-K. Tang, L. Shao, K. Han, and X. Shen, Phonon Thermal Transport in Silicene/graphene Heterobilayer Nanostructures: Effect of Interlayer Interactions, ACS Omega 7, 5844 (2022), doi:10.1021/acsomega.1c05932.

27. C.-C. Liu, H. Jiang, and Y. Yao, Low-Energy Effective Hamiltonian Involving Spin-Orbit Coupling in Silicene and Two-Dimensional Germanium and Tin, Phys. Rev. B 84, 195430 (2011), doi:10.1103/PhysRevB.84.195430.

28. M. P. L. Sancho, J. M. L. Sancho, J. M. L. Sancho, and J. Rubio, Highly Convergent Schemes for the Calculation of Bulk and Surface Green Functions, J. Phys. F: Metal Physics 15, 851 (1985), doi:10.1088/0305-4608/15/4/009.

29. S. Datta, Electronic Transport in Mesoscopic Systems, Cambridge University Press, Cambridge (1995).

30. J. C. Boettger and S. B. Trickey, First-Principles Calculation of the Spin-Orbit Splitting in Graphene, Phys. Rev. B 75, 121402 (2007), doi:10.1103/PhysRevB.75.121402.

31. H. Min, J. E. Hill, N. A. Sinitsyn, B. R. Sahu, L. Kleinman, and A. H. Mac-Donald, Intrinsic and Rashba Spin-Orbit Interactions in Graphene Sheets, Phys. Rev. B 74, 165310 (2006), doi:10.1103/PhysRevB.74.165310.

JOURNAL OF EXPERIMENTAL AND THEORETICAL PHYSICS, 2024, Vol. 165, No. 6, pp. 852–858

ELECTRONIC PROPERTIES OF SOLID

CAPTURE OF ELECTRONS AND HOLES ON MERCURY VACANCIES VIA SINGLE OPTICAL PHONON EMISSION DURING SHOCKLEY–READ–HALL RECOMBINATION IN A NARROW GAP HGCDTE

© 2024 D. V. Kozlov[a, b]**, V. V. Rumyantsev**[a, b]**, A. A. Yantser**[a, b*]**, S. V. Morozov**[a, b]**,**
V. I. Gavrilenko[a, b]

[a] *Institute for Physics of Microstructures, Russian Academy of Sciences;*
603087, Nizhniy Novgorod, Russia
[b] *Lobachevsky Nizhny Novgorod State University*
603950, Nizhny Novgorod, Russia
** e-mail: yantser@ipmras.ru*

Received November 06, 2023
Revised January 16, 2024
Accepted January 18, 2024

Abstract. The aim of the present work is to calculate the recombination time of Shockley–Read–Hall (SRH) process with the capture of charge carriers on mercury vacancy states in HgCdTe ternary alloys with a bandgap of about 40 meV. In the considered case the capture of both electron and hole is possible due to the emission of a single optical phonon. It is found that at T = 4.2 K and T = 77 K the SRH recombination determines the total lifetime of carriers in the p-type material with recombination centers density more than ~$2{\cdot}10^{15}$ cm^{-3}, which makes it possible to control the lifetime of carriers by changing the concentration of mercury vacancies.

Keywords: *HgCdTe, Shockley-Read-Hall recombination, mercury vacancy*

DOI: 10.31857/S004445102406e117

1. INTRODUCTION

For several decades, HgCdTe has remained one of the primary materials for infrared radiation detection [1]. The range of available wavelengths for commercial interband photodetectors based on HgCdTe extends from the near-IR range to approximately 25 μm, which is due to the wide possibilities for varying the bandgap of the solid solution. Since HgTe has virtually zero bandgap, working wavelengths beyond 25 μm are theoretically achievable in detectors based on HgCdTe solutions with high Hg content. However, several obstacles arise on the path to the far-IR range. Besides technological challenges, such as composition fluctuations or p-type doping problems for photodiodes, there are fundamental limitations on the material's detection capability related to carrier lifetime. As the bandgap decreases, the acceleration of non-radiative recombination processes leads to a reduction in carrier lifetime and corresponding decrease in sensitivity. Although this topic has been intensively studied for several decades, some quantitative uncertainties still remain, particularly regarding Auger recombination [2]. Another type of non-radiative processes – Shockley–Read–Hall (SRH) recombination is associated with defect/impurity centers that are always present in HgCdTe at least due to mercury vacancies. In HgCdTe, vacancy formation is essentially inevitable due to weak bonding Hg–Te, while their energy spectrum is still subject to debate [3–5]. Increasing mercury vacancy concentration through post-growth annealing is often used to convert HgCdTe films conductivity type from n-type to p-type. Carrier lifetimes during conversion typically decrease significantly [6], presumably because the emerging mercury vacancies serve as additional recombination centers. On the other hand, short carrier lifetimes enable the creation of high-speed IR detectors, including heterodyne type. Heterodyne receivers and mixers in the long-wavelength part of the mid-IR range may be of interest for spectroscopy in astrophysics. In particular, studying emission spectra of cosmic objects, such as nebulae, at hydrogen characteristic lines (28.221 μm, 17.035 μm, 12.279 μm, 9.665 μm, 8.026 μm) allows visualization of heating and cooling of such objects, shock waves and collisions, and other effects [7].

Mercury vacancy is a double or two-charge acceptor. Such an acceptor can exist in three charge states: neutral A_2^0-center with two holes bound to it, singly ionized A_2^{-1}-center with one hole bound to it, and finally, fully ionized A_2^{-2}-center. Due to numerous studies, the spread of ionization energies known from literature for A_2^0 -center and A_2^{-1}-center is quite large. However, the existence of states located at 15–20 meV from the valence band edge has been reliably established [8–11]. Note that the difficulty in unambiguous determination of ionization energy in this case is also related to the fact that it overlaps with the energy of optical phonons, which in the solid solution are represented by HgTe-like and CdTe-like modes with energies from 15 to 17.5 meV and from 16 to 20 meV respectively. Thus, if the band gap in the material is from 30 to 40 meV (with Cd fraction in solid solution 18.8 %), one can expect that the discrete defect level appears near the middle of the band gap. During SRH recombination through mercury vacancies, the following recombination channels are possible:

- Through neutral vacancies (A_2^0-center). An electron is captured at the neutral center, forming A_2^{-1} -center. Then a hole is captured at this center (process 1: $A_2^0 + e = A_2^{-1}$, $A_2^{-1} + h = A_2^0$).
- Through A_2^{-1} -center. Either a hole is captured at the $A_2^{-}1$ -center forming a neutral vacancy, and then an electron is captured at it (process 2: $A_2^{-1} + h = A_2^0$, $A_2^0 + e = A_2^{-1}$). Or an electron is captured at the A_2^{-1} -center forming A_2^{-2} -center, and then a hole is captured at this center (process 3: $A_2^{-1} + e = A_2^{-2}$, $A_2^{-2} + h = A_2^{-1}$).
- Through A_2^{-2} -center. A hole is captured at the fully ionized vacancy forming A_2^{-1} -center, then an electron is captured at this center (process 4: $A_2^{-2} + h = A_2^{-1}$, $A_2^{-1} + e = A_2^{-2}$).

Non-radiative capture of both holes and electrons occurs with the emission of optical and acoustic phonons. In all such processes, the law of energy conservation must be satisfied: the difference between the energy of the continuum state and the energy of the impurity-defect center state must be equal to the phonon energy. In this work, we focus on examining SRH recombination processes in a material with a bandgap from 35 to 40 meV. The wavelength range corresponding to these energies (from 30 to 35 μm) appears to be the next natural "frontier" for advancing HgCdTe-based detectors into the long-wavelength region. As a recombination center, we will consider the A_2^{-1} -center with an ionization energy of 20 meV, previously discovered in a series of studies on HgCdTe epitaxial layers grown by MBE method [12,13]. Thus, in the considered case, the capture of both holes and electrons into the state can occur with the emission of a single optical phonon. Comparison of calculation results with characteristic times for other recombination processes (Auger recombination and radiative recombination) shows that the considered type of SRH recombination can be the dominant channel for relaxation of non-equilibrium carrier concentration both at liquid helium temperature and at liquid nitrogen temperature.

2. CALCULATION METHOD

Below, we will calculate the capture times of holes to the states of the A_2^{-2}-center and electron capture times to the A_2^{-1}-center with emission of single optical phonons (processes 3,4). In the first case, the carrier must lose energy equal to the ionization energy of the A_2^{-1}-center (E_2), in the second case, the energy transferred to the phonon by the electron equals $E_g - E_2$, where E_g is the band gap width. As previously noted, the binding energy of the A_2^{-1}-center in narrow-band (up to 50 meV) HgCdTe layers is about 20 meV, and the band gap width changes rapidly depending on the composition of the solid solution. In the case of optical phonon emission, we will use Fermi's golden rule to calculate the intensity of carrier transitions from the valence band and conduction band to the ground state of the A_2^{-1}-center of the mercury vacancy. Due to lattice vibrations, a correction to the crystal potential (δV), is introduced, which can be decomposed into two components: electrostatic macrofield ($\delta\bar{V}$) and deformation field ($\delta\tilde{V}$): $\delta V = \delta\tilde{V} + \delta\bar{V}$ [14].The macrofield appears only in polar semiconductors, as polarization occurs due to the displacement of lattice atoms. In polar semiconductors, carriers interact with the macrofield much stronger than with the deformation potential [14], therefore in further calculations only scattering on the macrofield (PO-mechanism) will be considered.

As known from [14], the probability of transverse optical phonon emission in this case equals zero. When considering the probability of longitudinal phonon emission per unit time in the case of a hole transition from the valence band or an electron from the conduction band to the ground state of the acceptor A_2^{-1}-center, it takes the form [14]

$$W_{if} = \int \left(\frac{16\pi^3 a^3}{\mu\omega_{LO}(q)} \right) \frac{e^2\gamma^2}{q^2} \,|\langle \Psi_{cont} \,|\, e^{iqr} \,|\, \Psi_0 \rangle|^2 \times$$
$$\times (N_\Phi(q) + 1)\delta(\varepsilon_{cont} - n\omega_{LO}(q) - \varepsilon_0) d^3q, \quad (1)$$

where i and f are the initial and final states respectively, $N_\Phi(q)$ are the occupation numbers of phonon states, $\mu = m_{Hg}m_{Te} / (m_{Hg} + m_{Te})$ — reduced mass of atoms in the elementary cell (tellurium and mercury atoms), q is the phonon wave vector, ω_{LO}), is the frequency of the longitudinal optical phonon (HgTe-like or CdTe-like), is the lattice constant of the solid solution $Hg_{1-x}Cd_xTe$, $\Psi_{cont,0}$, $\varepsilon_{cont,0}$ are the wave functions and energies of continuous spectrum states and the ground localized acceptor leve (A_2^{-2}-center of mercury vacancy). According to [14], the coefficient value for longitudinal optical phonons is presented as

$$\gamma = \sqrt{\frac{1}{4\pi}\left(\frac{1}{\kappa_\infty} - \frac{1}{\kappa_0}\right)\frac{\mu}{a^3}}\omega_{LO}(0), \quad (2)$$

where $\kappa_{\infty,0}$ — high-frequency and static dielectric permittivities of the HgCdTe solid solution respectively, $\omega_{LO}(0)$ is the frequency of the longitudinal optical phonon at $q = 0$. Values for HgTe and CdTe from [15] were used to obtain dielectric permittivity values for the solid solution by linear interpolation. According to [16], $\omega_{LO}(0) = 4.85 \cdot 10^{12}$ Hz and $4.24 \cdot 10^{12}$ Hz for CdTe-like and HgTe-like phonons respectively. The energies and envelope wave functions of holes were obtained by solving the Schrödinger equation, which included the Kane Hamiltonian, acceptor ion potential, and central cell potential describing the chemical shift. This method is described in detail in [13]. The wave functions of continuous spectrum hole states were calculated beyond the Born approximation taking into account the impurity center potential [13], and the electron wave functions in the conduction band were chosen as plane waves.

Integrating expression (1) over the states of the continuous spectrum in the valence band/conduction band, taking into account the distribution function of holes/electrons, one can obtain the capture frequency of a particle (inverse capture time) from the continuous spectrum:

$$\frac{1}{\tau} = \sum_{cont} W_{cont \to f} f_{p,n}. \quad (3)$$

Paper [17] shows that the lifetime of piezo-acoustic electron scattering in the conduction band in HgCdTe layers is a fraction of picoseconds. Therefore, the distribution functions $f_{p,n}$ can be considered quasi-equilibrium:

$$f_{p,n} = \frac{1}{1 + \exp\left(\frac{\varepsilon_{cont} - F_{p,n}}{T}\right)}, \quad (4)$$

where $F_{p,n}$ is the quasi-Fermi level for holes and electrons respectively ε_{cont} is the particle energy in the continuum of the conduction band or valence band.

The position of the quasi-Fermi level for holes is determined depending on the concentration of holes in the valence band and temperature according to expression [18]

$$p = \frac{2}{(2\pi)^3}\int \left(1 + \exp\frac{-E_V + \frac{n^2k^2}{2m_{hh}} + F_p}{T} \right)^{-1} d^3k +$$

$$+ \frac{2}{(2\pi)^3}\int \left(1 + \exp\frac{-E_V + \frac{n^2k^2}{2m_{lh}} + F_p}{T} \right)^{-1} d^3k. \quad (5)$$

Here m_{hh} and m_{lh} are the effective masses of heavy and light holes in HgCdTe solid solution respectively, E_V is the energy of the valence band ceiling, T is temperature in energy units. Note that the mass of light holes is an order of magnitude less than the mass of heavy holes, therefore the second term in expression (2) is much smaller than the first and can be neglected. The calculated position of the

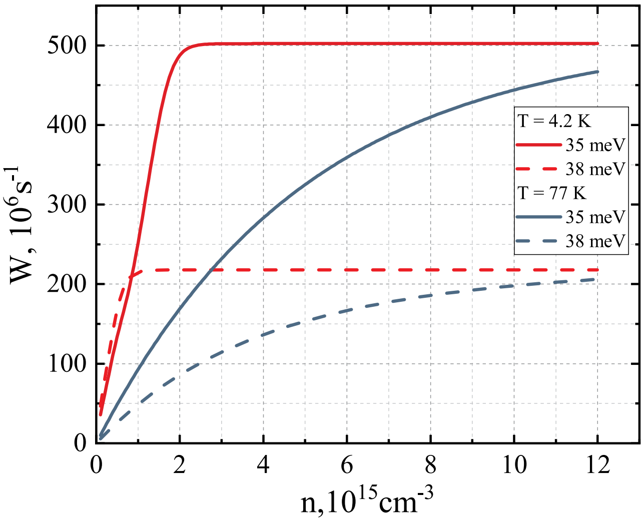

Fig. 1. Calculated frequencies of electron transitions from the conduction band to A_2^{-1}-center depending on their concentration at different values of HgCdTe bandgap The calculation was performed for concentration range from 10^{13} cm^{-3} to $1.2 \cdot 10^{16}$ cm^{-3}.

Fermi level was used in calculating the frequency of hole capture from the valence band according to expression (3).

The position of the quasi-Fermi level for electrons is determined depending on the concentration of electrons in the conduction band according to expression [18]

$$n = \frac{2}{(2\pi)^3}\int\left(1+\exp\frac{E_c+\dfrac{n^2k^2}{2m_e}-F_e}{T}\right)^{-1}d^3k. \quad (6)$$

Here m_e is the effective mass of electrons in the solid solution E_c is the energy of the conduction band bottom of HgCdTe.

For analyzing the obtained results in relation to real structures produced by MBE method [19], besides the carrier lifetime in the considered SRH process, it is necessary to determine the characteristic times of other processes: interband recombination during radiative transitions, as well as Auger processes. The radiative and Auger recombination times in this work were calculated using widely cited approximate analytical formulas, presented, for example, in works [2,20]. The expression for Auger recombination time includes, besides material constants, the threshold energy (E_{th}) of various Auger processes and parameter $|F1F2|^2$. In this work, the threshold energies were calculated not approximately (analytically), but numerically based on the energy spectrum obtained in the Burt-Foreman model with Kane Hamiltonian 8 × 8 [21, 21]. $F1$ and $F2$ represent the overlap integrals of wave functions in different states occupied by electrons during the Auger process. Analytical expression for $F1$ and $F2$ can be found in the classical work of Beattie and Landsberg [23], however, in the vast majority of works, the value $|F1F2|^2$ is considered as a fitting parameter [24]. Typically, in most publications $|F1F2| \sim 0.2$, however, in recent works, values around 0.05 are encountered. To account for data from various publications in analyzing the results of this work, below are provided Auger recombination times for $|F1F2|^2$ values across the entire range from 0.05 to 0.2.

3. RESULTS AND DISCUSSION

The frequencies of electron capture from the conduction band to A_2^{-1}-centers with emission of single optical phonons were calculated. Note that unlike the process of hole capture at acceptor levels, electron capture can only occur directly to the main acceptor level, since there are no intermediate levels between the conduction band and the main acceptor state. The calculation of electron capture frequency from the conduction band was performed for the main level of A_2^{-1}-center, located 20 meV above the valence band edge. Since the optical phonon energies range from 15 to 17.5 meV for HgTe-like phonon and from 18 to 20 meV for CdTe-like phonon, electron transitions to the ground state of A_2^{-1}-center will occur if the bandgap E_g is within the range of 35 to 40 meV.

Fig. 1 shows the calculated transition frequencies from the conduction band to the A_2^{-1}-center depending on the electron concentration in the band at different values of E_g and temperature T. It can be seen that with an increase in concentration from 10^{13} cm^{-3} there is a linear growth in transition intensity, which reaches saturation above a certain carrier concentration in the conduction band. This is due to the fact that transitions to acceptor states are possible only for carriers having kinetic energy within a certain range. For a band gap of 38 meV, it is no more than 20–18 = 2 meV (the difference between the maximum energy of the optical phonon and the energy gap between the conduction band edge and the acceptor level), and for a band gap of 35 meV, no more than 20–15 = 5 meV. With increasing concentration, the transition frequency initially grows due to the increase in the number of particles emitting phonons, and then, when the Fermi level becomes higher than the band edge by more than 2 (5) meV and the number of particles participating in transitions becomes constant, the growth of transition frequency stops. At liquid nitrogen temperature, the dependence of transition frequency on carrier concentration in the band is smoother due to the smearing of the electron distribution function in the conduction band at elevated temperatures. It can be seen that the optical phonon emission time during electron capture at the A_2^{-1}-center for sufficiently high carrier concentration in the band is on the order of ns.

The frequencies of hole transitions from the valence band with optical phonon emission to the ground state of the A_2^{-2} mercury vacancy center were also calculated. It was found that the time of such transition for the solid solution with 18.8% cadmium content and bandgap of 36 meV (where the ionization energy of the A_2^{-2}-center is 18 meV) is 3 ps. Thus, the electron capture time for the A_2^{-1} mercury vacancy center was three orders of magnitude longer than the hole capture time. Therefore, it can be expected that the SRH recombination time is determined by electron transitions. In this case, the SRH recombination time can be calculated using the following formula (see Appendix)

$$\tau_{SRH} = \tau_{ph}\left(\frac{n}{N_{A_2^{-1}}}\right). \tag{7}$$

Here τ_{SRH} is the relaxation time of electrons in the conduction band, τ_{ph} is the phonon emission time during capture at one center, $N_{A_2^{-1}}$ concentration of A_2^{-1}-centers, n – electron concentration. Thus, to calculate the SRH recombination time in narrow-gap HgCdTe layers, it is necessary to know not only the phonon emission time but also the number of carrier capture centers, i.e., the number of A_2^{-1}-centers. The number of such centers is the sum of the equilibrium number of A_2^{-1}-centers. The number of such centers is the sum of the equilibrium number of A_2^{-1}-centers ($N^P_{A_2^{-1}}$) and the number of centers generated by excitation radiation ($N^G_{A_2^{-1}}$):

$$N_{A_2^{-1}} = N^P_{A_2^{-1}} + N^G_{A_2^{-1}}.$$

Considering that the process of hole capture at mercury vacancies is three orders of magnitude faster than electron capture at such centers, it can be assumed that when considering electron relaxation processes, the stationary distribution of holes across states has already been established.

Let's consider the following cases.

3.1. Material of *n* type

In this case, at low temperature, all mercury vacancies are in the charge state A_2^{-2} (acceptor centers are free of holes). A_2^{-1}-centers arise due to the capture of holes generated by exciting radiation ($N_{A_2^{-1}} = N^G_{A_2^{-1}}$). Their concentration equals the concentration of non-equilibrium holes (Δp), if the number of such holes does not exceed the number of mercury vacancies; otherwise, the holes will completely fill A_2^{-2}-centers (forming A_2^{-1}-centers), and the remaining particles will fill the emerging A_2^{-1}-centers, forming neutral mercury vacancies. Thus, in the case of HgCdTe — n-type material — the relation $N_{A_2^{-1}} \le \Delta p$. is valid. Since during optical excitation, the number of non-equilibrium holes equals the number of non-equilibrium electrons (Δn) for the SRH recombination time from relation (7) we have

$$\tau_{SRH} \ge \tau_{ph}\left(\frac{n}{\Delta n}\right). \tag{8}$$

The equality in relation (8) is realized when the number of mercury vacancies exceeds the number of generated holes, i.e., in the case of low excitation intensity. In *n*-type material, the lifetime of non-equilibrium carriers in the SRH recombination process depends on their concentration, even when the latter is less than the dark concentration of electrons. This can lead to substantially non-exponential relaxation dynamics of excess carrier concentration, which complicates the analysis of experimental curves. Since the number of A_2^{-1}-centers is less than the total number of mercury vacancies, the following relation can be used to estimate the minimum SRH recombination time from expression (7):

$$\tau_{SRH} \ge \tau_{ph}\left(\frac{n}{N_{A_2}}\right). \tag{9}$$

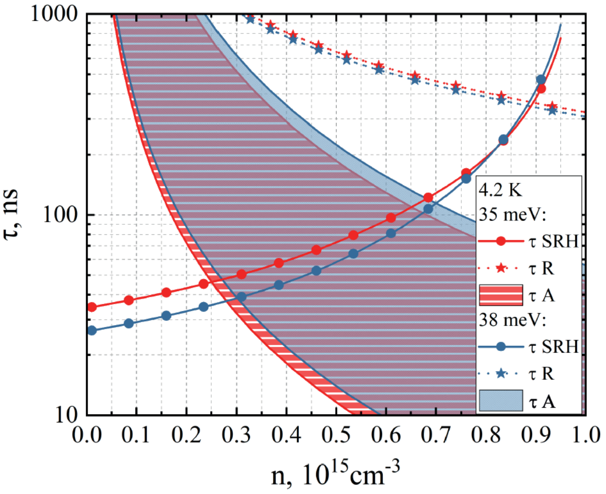

Fig. 2. Calculated for $T = 4.2$ K recombination times in p-type HgCdTe depending on the concentration of free electrons in the conduction band. The concentration of compensating donors equals 10^{15} cm^{-3}

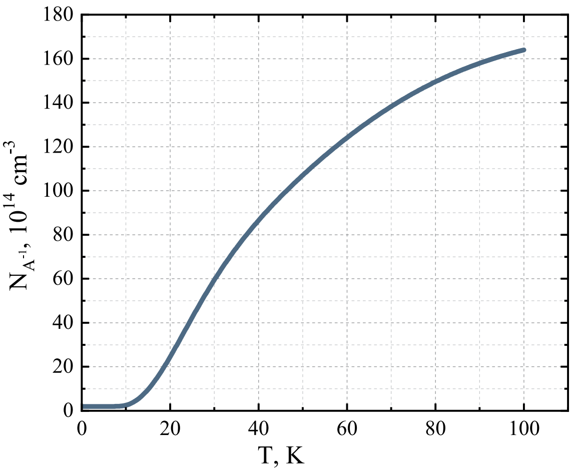

Fig. 3. Temperature dependence of the equilibrium concentration of A_2^{-1}-centers of mercury vacancies in the HgCdTe layer with Cd fraction in solution $x = 17.7$ %. The concentration of compensating donors is $N_D = 2 \cdot 10^{14}$ cm^{-3}, mercury vacancy concentration $N_A = 2.5 \cdot 10^{16}$ cm^{-3}

The equality in expression (9) is realized when the number of holes arising during pumping equals the number of double acceptors. At $T = 4.2$ K, the estimation of SRH recombination time from (9) for HgCdTe with a band gap of 35 meV gives a value of about 170 ns for an equilibrium electron concentration of $2 \cdot 10^{14}$ cm^{-3} and mercury vacancy concentration of $2 \cdot 10^{13}$ cm^{-3}, which satisfactorily agrees with experimental data [25]. At $T = 77$ K, the estimated SRH recombination times exceed 500 ns and thus do not contribute significantly to the total recombination time, since Auger recombination times are considerably shorter.

3.2. p-type material at T = 4,2 K

The equilibrium number of A_2^{-1}-centers at low temperature is determined by the degree of compensation: the number of such centers equals the number of compensating donors (N_D). Under illumination, as previously noted, the generated holes transition to A_2^{-1}-centers within about 3 ps, converting them into neutral A_2^{0}-centers. Then the number of A_2^{-1}-centers under illumination:

$$N_{A_2^{-1}} = N_d - \Delta p \qquad (10)$$

Then, considering that $\Delta p = \Delta n$ and the concentration of equilibrium electrons at low temperature is negligibly small, expression (7) in this case takes the form

$$\tau_{SRH} = \tau_{ph}\left(\frac{\Delta n}{N_d - \Delta n}\right). \qquad (11)$$

Figure 2 shows the graphs of carrier lifetime dependencies for three recombination processes (SRH recombination (τ_{SRH}) calculated from (10), radiative recombination (τ_R) and Auger recombination (τ_A)) on the concentration of free electrons in the conduction band at (10), on the concentration of free electrons in the conduction band at $T = 4.2$ K. Calculations were performed for HgCdTe p-type layer, corresponding to $E_g = 35$ meV and Eg = 38 meV. The concentration of compensating donors N_D is chosen to be 10^{15} cm^{-3}.

Mercury vacancy concentration is assumed to be $N_A > N_D$. For Auger recombination time τ_A the range of values is shown, corresponding to the variation of the fitting parameter $|F1F2|$ within the range from 0.05 to 0.2, similar to work [2]. Considering that the total relaxation time τ is defined as

$$\tau^{-1} = \tau_R^{-1} + \tau_{SRH}^{-1} + \tau_A^{-1}, \qquad (12)$$

it corresponds to the shortest recombination time. Figure 2 shows that SRH recombination time will have a noticeable effect on in p-type material at free electron concentration (sum of equilibrium and non-equilibrium concentration) in the conduction band up to values of about $2 \cdot 10^{14}$ cm^{-3} or about

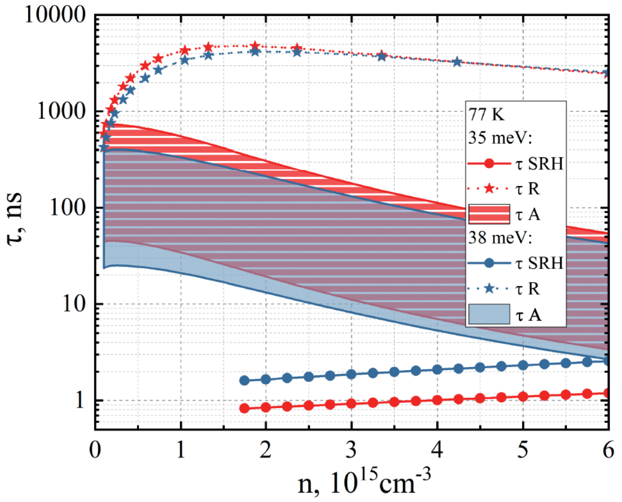

Fig. 4. Calculated for T = 77 K recombination times in HgCdTe p-type depending on the concentration of free electrons in the conduction band. The concentration of compensating donors is $N_D = 2 \cdot 10^{14}$ cm^{-3}, mercury vacancy concentration $N_A = 2.5 \cdot 10^{16}$ cm^{-3}

$6 \cdot 10^{14}$ cm^{-3} depending on the value of $|F1F2|^2$. At higher concentrations of non-equilibrium electrons, the total recombination time is controlled by Auger processes.

3.3 Material of p-type at T = 77 K

Fig. 3 shows the temperature dependence of the equilibrium concentration of A_2^{-1}-centers in the HgCdTe layer with Cd fraction in solution x = 17.7 %. The dependence was calculated using the method presented in work [26]. Mercury vacancy concentration $N_A = 2.5 \cdot 10^{16}$ cm^{-3} was chosen at the level of maximum achievable for low-temperature annealing of HgCdTe [27]. At T = 77 K the equilibrium concentration of free electrons in the conduction band was $1.75 \cdot 10^{15}$ cm^{-3}, which corresponds to typical “dark” concentration in epitaxial films grown by MBE method [19].

In Fig. 3, it can be seen that the concentration be noted that the band gap in the film with $N_{A_2^{-1}}$ at T = 77 K is $1.4 \cdot 10^{16}$ cm^{-3}. It should be noted that the band gap in the film with x = 17.7 % at T = 77 K is about 38 meV.

Fig. 4 shows a graph of carrier lifetime dependence for three recombination processes in HgCdTe p-type material with E_g = 35 meV and E_g = 38 meV. It can be seen that the SRH recombination time is on the order of several nanoseconds over a wide range of total electron concentrations in the conduction band and determines the overall lifetime. When the non-equilibrium electron concentration increases above $6 \cdot 10^{15}$ cm^{-3} , the expression for SRH recombination time without accounting for the change in mercury vacancy occupancy by non- equilibrium holes becomes inapplicable. Note that for concentrations near equilibrium, SRH recombination will remain the dominant process even with a tenfold decrease in mercury vacancy concentration. At the same time, it is known that during high-temperature annealing, it is possible to increase the vacancy concentration up to values of approximately $3 \cdot 10^{18}$ cm^{-3} [28], which theoretically allows reducing SRH recombination times to approximately 10 ps. The latter is of interest for heterodyne receivers, where ensuring effective mixing imposes rather strict requirements on mixer speed

4. CONCLUSION

In this work, electron and hole capture times for states of partially ionized mercury vacancy in HgCdTe solid solutions with a band gap of about 40 meV were calculated for different values of temperature and carrier concentration in bands. It is shown that electron transition times to vacancy states from the conduction band exceed the characteristic hole capture time by at least three orders of magnitude. Thus, the SRH recombination time is determined by the electron capture time to acceptor states. Comparison of rates of different recombination mechanisms shows that the SRH process determines the overall carrier lifetime in HgCdTe p-type with mercury vacancy concentration more than approximately $2 \cdot 10^{15}$ cm^{-3} both at liquid helium temperature and at liquid nitrogen temperature. The obtained results create prerequisites for controlling the photoresponse time in such materials, including in the sub-nanosecond range, by changing the concentration of mercury vacancies.

ACKNOWLEDGMENTS

The authors thank E.V. Andronov for help in developing the software used in this work.

FUNDING

This work was supported by grants from the Russian Science Foundation 22-12-00298 (calculation of electron and hole capture times for an isolated acceptor center) and the Russian Foundation for Basic Research 21-52-12020 (calculations of carrier lifetimes for various recombination processes).

APPENDIX

The number of electron captures by one acceptor center equals τ_{ph}^{-1}, then the change in the number of electrons (n) in the conduction band per unit time has the form

$$\frac{dn}{dt} = -\frac{1}{\tau_{ph}} N_{A_2^{-1}}, \tag{13}$$

here $N_{A_2^{-1}}$ — number of electron capture centers (A_2^{-1}-centers).

Formula (13) can be reduced to the form

$$\frac{dn}{dt} = -\frac{1}{\tau_{SRH}} n, \tag{14}$$

$$\frac{dn}{dt} = -\frac{N_{A_2^{-1}}}{n\tau_{ph}} n. \tag{15}$$

We obtain

$$\tau_{SRH} = \tau_{ph}\left(\frac{n}{N_{A_2^{-1}}}\right). \tag{16}$$

REFERENCES

1. W. Lei, J. Antoszewski, and L. Faraone, Appl. Phys. Rev. 2, 041303 (2015).
2. K. Jóźwikowski, M. Kopytko, and A. Rogalski, J. Appl. Phys. 112, 033718 (2012).
3. F. Gemain, I.C. Robin, M. De Vita et al., Appl. Phys. Lett. 98, 131901 (2011).
4. B. Li, Y. Gui, Z. Chen et al., Appl. Phys. Lett. 73, 1538 (1998).
5. T. Sasaki, N. Oda, M. Kawano et al., J. Crystal Growth. 117, 222 (1992).
6. V. V. Rumyantsev, M. A. Fadeev, S. V. Morozov et al., Semiconductors 50, 1679 (2016).
7. M. G. Wolfire and A. Konigl, The Astrophys. J. 383, 205 (1991).
8. K. D. Mynbaev, A. V. Shilyaev, N. L. Bazhenov et al., Semiconductors. 49, 367 (2015).
9. F. Gemain, I. C. Robin, S. Brochen et al., J. Electr. Materials. 41, 2867 (2012).
10. X. Zhang, J. Shao, L. Chen et al., J. Appl. Phys. 110, 043503 (2011).
11. X. Chen, M. Wang, L. Zhu et al., Appl. Phys. Lett. 123 (2023).
12. A. Ikonnikov, V. Rumyantsev, M. Sotnichuk et al., Semiconductor Science and Technology 38, 085003 (2023).
13. V. V. Rumyantsev, D. V. Kozlov, S. V. Morozov et al., Semiconductor Science and Technology 32, 095007 (2017).
14. V. F. Gantmakher, I. B. Levinson, Carrier Scattering in Metals and Semiconductors, Nauka, Moscow (1984).
15. O. Madelung, Semiconductors: Data Handbook, Springer-Verlag, New York (2003).
16. D. N. Talwar and M. Vandevyver, J. Appl. Phys. 56, 1601 (1984).
17. D. V. Kozlov, M. S. Zholudev, K. A. Mazhukina et al., Semiconductors Physics and Technology (2023).
18. V. L. Bonch-Bruevich, S. G. Kalashnikov, Physics of Semiconductors, Nauka, Moscow (1977).
19. S. Krishnamurthy, M. A. Berding, and Z. G. Yu, J. Electron. Materials 35, 1369 (2006).
20. E. G. Novik, A. Pfeuffer-Jeschke, T. Jungwirth et al., Phys. Rev. B 72, 035321 (2005).
21. S. V. Morozov, V. V. Rumyantsev, M. S. Zholudev et al., ACS Photonics 8, 3526 (2021).
22. A. R. Beattie and P. T. Landsberg, Proc. of the Royal Society A: Mathematical, Physical and Engineering Sciences 249, 16 (1959).
23. A. R. Beattie and P. T. Landsberg, Proc. of the Royal Society A: Mathematical, Physical and Engineering Sciences 249, 16 (1959).
24. N. L. Bazhenov, K. D. Mynbaev, G. G. Zegrya, Semiconductors Physics and Technology 49,444 (2015).
25. V. V. Rumyantsev, S. V. Morozov, A. V. Antonov et al., Semiconductor Science and Technology 28, 125007 (2013).
26. D. V. Kozlov, M. S. Zholudev, V. V. Rumyantsev et al., Semiconductors Physics and Technology 56, 465 (2022).
27. P. A. Bakhtin, S. A. Dvoretsky, V. S. Varavin et al., Semiconductors Physics and Technology 38, 1207 (2004).
28. D. Chandra, H. F. Schaake, J. H. Tregilgas et al., J. Electronic Materials 29, 729731 (2000).

JOURNAL OF EXPERIMENTAL AND THEORETICAL PHYSICS, 2024, Vol. 165, No. 6, pp. 860–867

STATISTICAL, NONLINEAR, AND SOFT MATTER PHYSICS

NONLINEAR OSCILLATIONS OF POORLY CONDUCTING LIQUID IN ALTERNATING ELECTRIC FIELD IN THE FRAMEWORK OF LOW-MODE APPROXIMATION

© 2024 O.O. Nekrasov*, N.N. Kartavykh**

Perm State University 614068, Perm, Russia
** e-mail: dakeln2@gmail.com*
*** e-mail: kartavykh@psu.ru*

Received January 30, 2023
Revised February 25, 2024
Accepted February 25, 2024

Abstract. Flat horizontal infinite layer of viscous incompressible poorly conducting liquid is investigated. The layer is placed in gravitational and electric field and heated from above. Eight-mode electroconvection model (extended Lorenz-model) is used to carry the problem out numerically. As a result of the linear stability analysis of the system, the critical wave number and critical electric Rayleigh number are obtained for different external electric field periods. In the case of nonlinear evolution of the system, bifurcation diagrams are obtained as dependences of the dimensionless heat flow on the amplitude of the oscillations of the external electric field. Various types of system response to the external impact are found: periodic, quasiperiodic and chaotic oscillations, as well as hysteretic transitions between them and quiescent state. The map of flow regimes is obtained.

Keywords: *electroconvection, low-mode model, electroconductive charge formation, oscillations, alternating electric field, hysteresis*

DOI: 10.31857/S004445102406e129

1. INTRODUCTION

Currently, the problem of controlling heat flux in continuous media, for example, in fluids, is relevant. The ability to control heat and mass transfer in fluids can be used in various technological applications: in designing effective heat removal systems or for process control in zero gravity [1–3].

The problem of thermogravitational mechanism of convection generation, when motion in non-uniformly heated fluid occurs due to buoyancy force, has been very well studied [4]. In this case, the fluid can possess a number of other physical properties, for example, it can be a carrier of free charge. In this case, there appears an additional way to control convective motion by affecting the fluid through the application of an external electric field [5, 6]. It is known that such influence can lead to changes in convection onset thresholds [6–9], to the generation of oscillatory [10] and chaotic [11] motion regimes.

This article examines the case of interaction between two convection mechanisms: thermogravitational and electroconductive [6, 9], associated with inhomogeneous conductivity distribution.

There are many approaches to studying the dynamics of nonlinear systems, most of which reduce to the application of numerical methods. The main difficulty is related to the absence of analytical solutions in the general form of the Navier–Stokes equations describing the behavior of viscous fluid.

In the mid-20th century, E. Lorenz demonstrated a new method of numerical modeling of the Navier-Stokes equations, based on studying the amplitudes of system field decomposition using a small set of trial functions [12]. In this convection model, the phase variables are time-dependent amplitudes of spatial trigonometric functions (modes), one for the velocity field and two for temperature.

This approach revealed new important patterns in the behavior of dynamical systems and led to the creation of a new branch of physics – the theory of dynamical chaos [13]. Despite the intensive use of numerical models and commercial computational packages, low-mode systems are still used to analyze the nonlinear evolution of flows in various fluids [14–17], including the initial stage of laminar-turbulent transition [14]. The use of low-mode models for theoretical description of convection in variable fields shows good agreement with experiments even for large supercriticalities [18,19].

In this work, a modified Lorenz model is used to analyze electrothermo-convective flows, based on the decomposition of hydrodynamic system fields into eight basis functions reflecting the symmetry of the problem [10, 20]. Within the framework of the proposed model, cases of instantaneous and finite-time charge relaxation have been studied for heating of weakly conducting fluid from below in a constant electric field [20], in the isothermal case and with strong heating from above in an alternating electric field [9]. This paper presents the results of studying the evolution of weakly conducting fluid flows arising in an alternating electric field with moderate heating from above. New sequences of transitions between regular and chaotic oscillatory flows have been discovered and analyzed.

2. PROBLEM STATEMENT

A flat infinite horizontal layer of viscous incompressible weakly conducting fluid of thickness h, placed between plates of a flat infinite horizontal capacitor, is considered. The fluid is subjected to an alternating electric field with intensity E, gravitational field g, and the capacitor plates are heated to a temperature difference Θ. The capacitor plates are perfectly heat and electrically conductive, with physical conditions on them expressed by the following relations:

$$\begin{aligned} z = 0 &: \hat{T} = \Theta, \Phi = \hat{U}\cos(\omega t), \\ z = h &: \hat{T} = 0, \Phi = 0, \end{aligned} \tag{1}$$

where z is the vertical coordinate, ω is the frequency of the external electric field, $\hat{U}$ is the amplitude of electric potential variation Φ.

A weakly conducting fluid is defined as having electrical conductivity $\sigma \sim 10^{-9}–10^{-11}\,\mathrm{Ohm}^{-1}\cdot\mathrm{m}^{-1}$, which allows using the electrohydrodynamic approximation: due to small currents, magnetic effects and Joule heating can be neglected [6, 7].The system of differential equations describing the system includes the Navier–Stokes equation, heat conduction equation, charge conservation law, Gauss's law, relation between electric field intensity and its potential, continuity equation [21]:

$$\begin{gathered} \rho\left(\frac{\partial \boldsymbol{v}}{\partial t} + (\boldsymbol{v}\cdot\nabla)\boldsymbol{v}\right) = -\nabla p + \rho\boldsymbol{g} + \eta\Delta\boldsymbol{v} + q\boldsymbol{E}, \\ \frac{\partial \hat{T}}{\partial t} + (\boldsymbol{v}\cdot\nabla)\hat{T} = \chi\Delta\hat{T}, \\ \frac{\partial q}{\partial t} + div(\sigma\boldsymbol{E}) + (\boldsymbol{v}\cdot\nabla)q = 0, \\ div\boldsymbol{E} = q/\varepsilon\varepsilon_0, \\ \boldsymbol{E} = -\nabla\Phi, \\ div\boldsymbol{v} = 0, \end{gathered} \tag{2}$$

where $\mathbf{v}, p, \hat{T}$ are velocity, pressure, and temperature fields respectively, η is fluid dynamic viscosity, χ is fluid density, q is fluid density, σ is fluid electrical conductivity, ε is dielectric permittivity, ε_0 is electric constant.

Linear dependencies of fluid density and electrical conductivity on temperature are considered:

$$\rho = \rho_0(1 - \beta_\theta\hat{T}), \quad \sigma = \sigma_0(1 + \beta_\sigma\hat{T}),$$

see [6,21], where ρ_0 and σ_0 are density and conductivity values at mean temperature, β_θ and β_σ are positive coefficients. Thus, thermogravitational and electroconductive mechanisms are the main causes of convection onset [9]. Due to small conductivity inhomogeneity (for weakly conducting fluid under moderate heating $\beta_\sigma\hat{T} \ll 1$), spatial inhomogeneity of the electric field and field changes caused by charge redistribution can be neglected, i.e., the induction-free approximation can be used [20].

System (2) is reduced to dimensionless form according to the following relations:

$$[t] = \frac{\rho_0 h^2}{\eta}, [\Phi] = \hat{U}, [v] = \frac{\chi}{\eta}, [r] = h,$$
$$[\hat{T}] = \Theta, E = \frac{\hat{U}}{h}, [p] = \frac{\eta\chi}{h^2}, [q] = \frac{\varepsilon\varepsilon_0\hat{U}}{h^2}, \tag{3}$$

and considering the Boussinesq approximation [4], it can be written as

$$\frac{\partial \mathbf{v}}{\partial t} + \frac{1}{\Pr}(\mathbf{v}\cdot\nabla)\mathbf{v} =$$
$$= -\nabla p + \Delta\mathbf{v} + Ra\hat{T}\mathbf{j} + Ra_\sigma q\cos(\omega t)\boldsymbol{j},$$
$$\Pr\frac{\partial \hat{T}}{\partial t} + (\mathbf{v}\cdot\nabla)\hat{T} = \Delta\hat{T}, \tag{4}$$
$$\Pr_e\frac{\partial q}{\partial t} + div(\sigma\mathbf{E}) + \frac{Pr_e}{Pr}(\mathbf{v}\cdot\nabla)q = 0,$$

where j is a unit vector codirectional with the vertical z-axis. System (4) contains the following dimensionless parameters:

$$Ra = \frac{\rho_0 g\beta_\theta\Theta h^3}{\chi\eta}$$

— Rayleigh number, characterizing the intensity of fluid heating,

$$Ra_\sigma = \frac{\varepsilon_0\varepsilon\hat{U}^2\beta_\sigma\Theta}{\chi\eta}$$

— electrical analog of the Rayleigh number, related to the amplitude of the external electric field,

$$Pr = \frac{\eta}{\chi\rho_0}$$

— Prandtl number, reflecting the ratio between viscous and heat-conductive energy transfer in the fluid,

$$\Pr_e = \frac{\varepsilon\varepsilon_0\eta}{h^2\sigma_0\rho_0}$$

— electrical analog of the Prandtl number, characterizing the ratio between viscous and electrical forces.

3. LOW-MODE MODEL

Let's represent the fields $v, \hat{T}$ and q in the form $v, \hat{T} = \hat{T}_0 + \theta$ and $q = q_0 + q'$, where v, θ and q' are deviations of values from their equilibrium values (hereafter primes will be omitted). Considering the absence of horizontal anisotropy, we can consider only two-dimensional perturbations in the vertical plane $x - z$, which actually arise at the threshold of convective stability. Let's introduce the stream function ψ, such that

$$v_x = -\partial\psi / \partial z, \quad v_z = \partial\psi / \partial x,$$

see [9], then the system of equations (4) can be rewritten as [20]

$$\frac{\partial}{\partial t}\Delta\psi + \frac{1}{\Pr}\left(\frac{\partial\psi}{\partial x}\frac{\partial}{\partial z}\Delta\psi - \frac{\partial\psi}{\partial z}\frac{\partial}{\partial x}\Delta\psi\right) = \Delta^2\psi +$$
$$+Ra\frac{\partial\theta}{\partial x} + Ra_\sigma\frac{\partial q}{\partial x}\cos(\omega t),$$
$$\Pr\frac{\partial\theta}{\partial t} + \frac{\partial\psi}{\partial x}\frac{\partial\theta}{\partial z} - \frac{\partial\psi}{\partial z}\frac{\partial\theta}{\partial x} = \Delta\theta + \frac{\partial\psi}{\partial x}, \tag{5}$$
$$\Pr_e\frac{\partial q}{\partial t} + \frac{\Pr_e}{\Pr}\left(\frac{\partial\psi}{\partial x}\frac{\partial q}{\partial z} - \frac{\partial\psi}{\partial z}\frac{\partial q}{\partial x}\right) +$$
$$+q + \frac{\partial\theta}{\partial z}\cos\omega t = 0,$$

with boundary conditions

$$z = 0\colon\ \psi = \psi'' = \theta = 0,$$
$$z = h\colon\ \psi = \psi'' = \theta = 0. \tag{6}$$

To find solutions of the system of equations (5) satisfying boundary conditions (6), the Galerkin method [4] is applied with approximation of fields ψ, θ and q by a minimal set of basis functions [9]:

$$\psi = \frac{\sqrt{2}(1+k^2)}{k}\times$$
$$\times(X(t)\sin\pi z + V(t)\sin 2\pi z)\sin\pi kx,$$

$$\Theta = \frac{\sqrt{2}}{\pi}(Y(t)\sin\pi z + W(t)\sin 2\pi z)\cos\pi kx +$$
$$+\frac{1}{\pi}Z(t)\sin 2\pi z, \tag{7}$$

$$q = (\sqrt{2}S(t)\cos\pi z + 2\sqrt{2}T(t)\cos 2\pi z)\cos\pi kx +$$

$$+U(t)\cos 2\pi z.$$

Here k is the wave number characterizing the periodicity of solutions horizontally, and coefficients X, V, Y, W, Z, S, T, U are amplitudes showing the contribution of spatial modes to the solution.

Expansions (7) contain terms of different parity in z, which is related to the presence of derivatives of different orders in in system (5). Amplitudes $X - U$ are determined using conditions expressing the orthogonality of the residual of system equations (5) with respect to each of the basis functions [4]. After time rescaling

$$t \to \frac{\mathrm{Pr}}{\pi^2(1+k^2)}t$$

we obtain a system of eight ordinary differential equations for the amplitudes of spatial harmonics (dot above variable denotes time derivative) [9,22]:

$$
\begin{gathered}
X = \mathrm{Pr}(-X + rY - eT\cos\omega t),\\
Y = -Y + X + XZ,\\
Z = -bZ - XY,\\
V = \mathrm{Pr}(-dV + (rW + eS\cos\omega t)/d), \qquad (8)\\
W = -dW + V,\\
S = -gS + XU - gY\cos\omega t,\\
T = -gT - gW\cos\omega t,\\
U = -gU - XS - 2gZ\cos\omega t.
\end{gathered}
$$

In system (8), the following notations are introduced:

$$
\begin{gathered}
r = \frac{Ra}{Ra_0}, e = \frac{Ra_\sigma}{Ra_{\sigma 0}},\\
Ra_0 = \frac{\pi^4(1+k^2)^3}{k^2}, Ra_{\sigma 0} = \frac{3\pi^4(1+k^2)^3}{8k^2}, \qquad (9)\\
d = \frac{4+k^2}{1+k^2}, b = \frac{4}{1+k^2}, g = \frac{\mathrm{Pr}}{\pi^2(1+k^2)\mathrm{Pr}_e},
\end{gathered}
$$

where r, e — are normalized thermal and electrical Rayleigh numbers, Ra_0 — is the critical Rayleigh number at which thermogravitational convection begins, $Ra_{\sigma 0}$ is the system parameter.

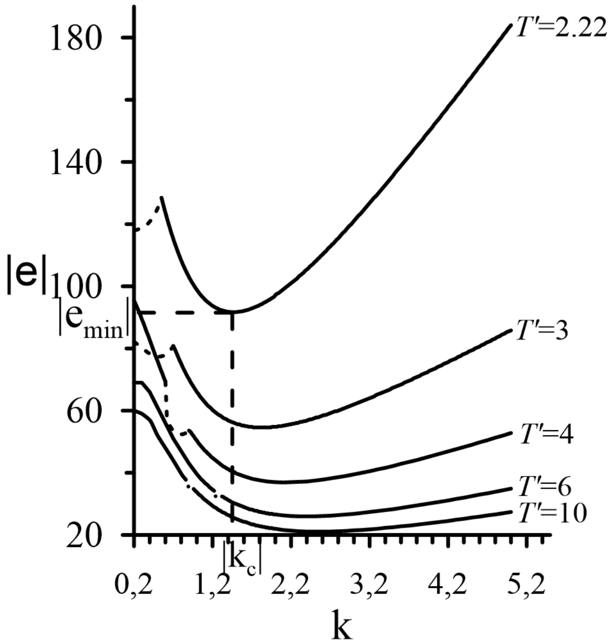

Fig. 1. Family of neutral curves in coordinates wave number k – modulus of electrical parameter $|e|$ at different periods T' of external electric field variation. Solid lines correspond to quasi-periodic regimes, dashed lines to synchronous ones [23]

4. LINEAR STABILITY ANALYSIS

The case of moderate heating from above is studied, where the normalized thermal Rayleigh number r takes a negative value of −1 [23]. As seen from relations (9), with heating from above, the normalized electric Rayleigh number is e also negative, but the study considered its absolute value. Other fluid parameters have values $Pr = 400, Pr_e = 30$. They correspond to weakly conducting fluids, electrical conductivity of which depends on temperature, for example, corn or transformer oil [24–26]. Real physical characteristics of the system correspond to a layer thickness of 1 cm, voltage difference of 1 kV, temperature difference: ~10°C.

As seen from system (8) with a set of dimensionless parameters (9), the wave number k, corresponding to the spatial horizontal scale of perturbations, remains undetermined. The standard approach for finding the value of this parameter is the analysis of linear perturbations of the system.

After linearization, system (8) can be represented in matrix form

$$\dot{\mathbf{x}}(t) = A(t)\mathbf{x}(t)$$

with a linear matrix dependent on time with period $T' = 2\pi / \omega$. Then for analysis of its linear stability, Floquet theory can be applied [27], which was used to obtain neutral curves of linear stability of the system for different periods of external electric field (Fig. 1) [23].

By determining the extremum point of the neutral curve, one can calculate the minimum modulus value of the dimensionless electric parameter at which convective fluid motion begins, as well as the corresponding critical wave number, for example, $|e_{min}|(T' = 2.22) = 91.7$ and $k_c(T' = 2.22) = 1.45$. Linear stability analysis of the system predicts the emergence of quasi-periodic oscillations in areas of global minimum of neutral curves Fig. 1. In areas of local minima of curves, oscillations are synchronous, corresponding areas are constructed with dashed lines.

5. NONLINEAR CONVECTION MODES

To describe the intensity of convective processes, the Nusselt number (Nu) was calculated, a parameter equal to the time-averaged heat flux per unit of horizontal boundary of the condenser [9]. The Nusselt number can be expressed through the amplitude Z of system (8):

$$Nu = 1 - \frac{2}{t_{end}} \int_0^{t_{end}} Z(t)dt, \qquad (10)$$

where t_{end} is chosen in such a way that it accommodates more than a hundred periods of system oscillations.

Wave numbers k were taken from the results of linear theory application ($k = k_c$, where k_c corresponds to the global minimum of the neutral curve for the selected period of external field). Geometric parameters b, g and d were determined based on the selected wave number. Values of other dimensionless parameters are given at the beginning of Section 4.

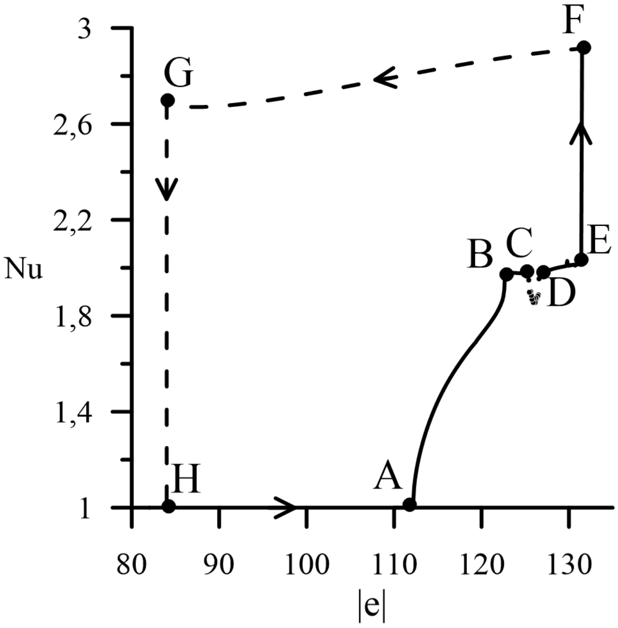

Fig. 2. Dependence of the Nusselt number Nu on the absolute value of the dimensionless electric parameter |e| at external field period $T' = 2$. Solid line – movement towards increasing |e|, dashed line – towards decreasing |e|

The study of electroconvection modes was conducted as follows: system (8) was numerically integrated using the fourth-order Runge-Kutta method at different values of dimensionless normalized electric Rayleigh number |e| and period of electric field variation T'. The |e| parameter continuation method was used: when calculating the Nusselt number for each value, distributions obtained at the previous step for were used as initial conditions |e|. This method allows continuous change of the control parameter, determining the boundaries of hysteresis transitions [28]. Thus, dependencies Nu (|e|) were determined for different periods of external electric field T', for each period the corresponding critical wave number value was taken.

During the study, several types of system evolution were identified for different periods of external field T'.

5.1. External field period $T' = 2$

The dependence of dimensionless heat flux Nu on parameter |e| for the given period of external field is presented in Fig. 2.

With increasing parameter |e| from initial conditions corresponding to small perturbations of mechanical equilibrium, convection emerges as quasi-periodic oscillations at point A Fig. 2

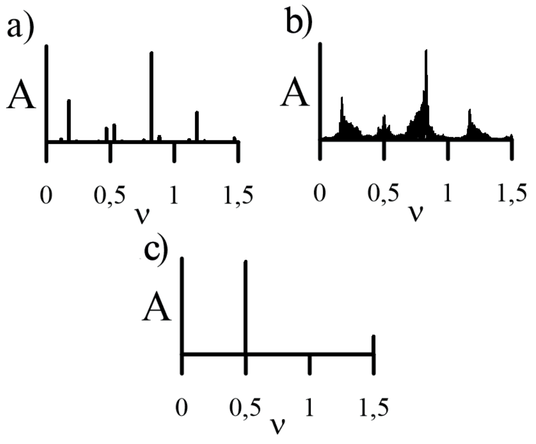

Fig. 3. Fourier spectra of amplitude oscillations X at forcing period for different values of $T' = 2$. Lower branch of Fig. 2: *a* — |e| = 120, quasiperiodic response; *b,* |e| = 126 chaotic oscillations. Upper branch of Fig. 2: *c*, |e| = 131 synchronous response

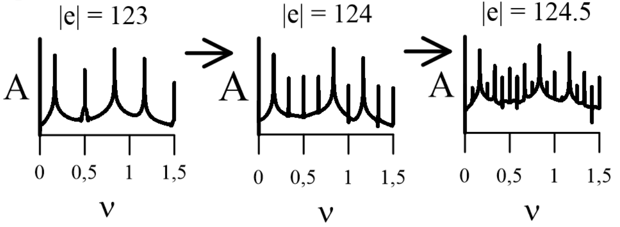

Fig. 4. Fourier spectra of amplitude oscillations X in logarithmic scale at forcing period $T' = 2$. Oscillations correspond to section BC of Fig. 2, where subharmonic cascade occurs

(|e| = 112.2) (the Fourier spectrum of amplitude oscillations contains two or more frequencies incommensurable with the external one (ν = 0.5, Fig. 3*a*)) .

With further increase of the parameter |e| quasiperiodic oscillations transition at point B Fig. 2 (|e| = 122.7) into a specific subharmonic oscillation regime: the Fourier spectrum contains the external frequency, as well as a frequency three times lower than the external one, and their linear combinations (Fig. 4).

In the BC section, a cascade of period-doubling bifurcations occurs (Fig. 4), transitioning into chaos at point C Fig. 2 (|e| = 124.7). Chaotic oscillations exist in the CD section of Fig. 2 and are characterized by a continuous Fourier spectrum (Fig. 3*b*). At point D Fig. 2 (|e| = 126.6) a regime emerges again, characterized by a frequency three times lower than the external field frequency.

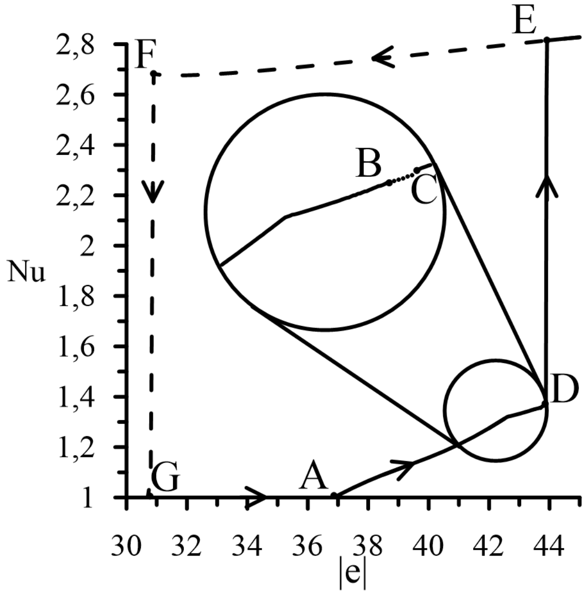

Fig. 5. Dependence of the Nusselt number Nu on the absolute value of the dimensionless electric parameter |e| at the external field period $T' = 4$. Solid line - movement towards increasing , dashed line — towards decreasing of |e|

With further increase of |e| the system oscillates in this way until point E Fig. 2 (|e| = 122.7), where heat flow sharply increases. At Nusselt numbers greater than 2.5, synchronous disturbances appear in the layer, whose Fourier spectra contain only frequencies that are multiples of the external one (Fig. 3*c*).

If, using the parameter continuation method, parameter |e| is sequentially decreased from values lying to the right of point F Fig. 2, then the system's transition from convective flow to mechanical equilibrium will occur differently, with a sharp decrease in the Nusselt number at point G Fig. 2 (|e| = 84). Thus, hysteresis is realized in the system (loop HAFG in Fig. 2), accompanied by heat flow jumps.

5.2 External field period $T' = 4$

The dependence of dimensionless heat flux on parameter |e| for the given external field period is shown in Fig. 5.

With increasing absolute value of parameter |e| convection occurs at point A Fig. 5 (|e| = 36.9) in the form of quasi-periodic oscillations. With further increase of |e| these oscillations transition to chaos through quasi-periodicity at point B Fig. 5 (|e| = 43.5). The transition to chaos through quasi-periodicity is

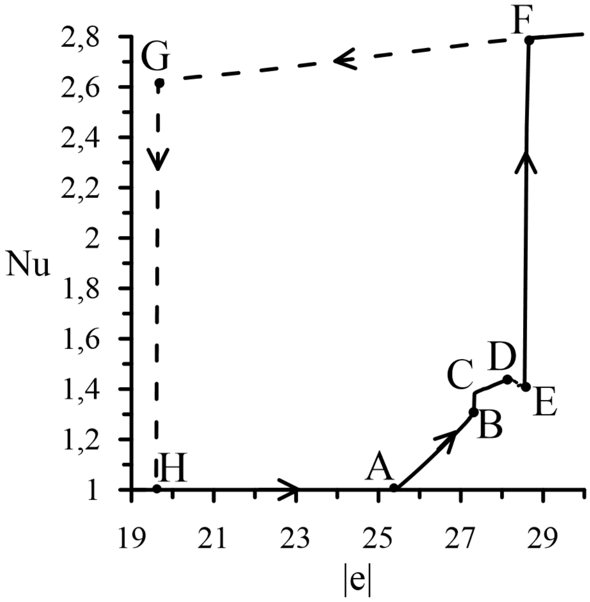

Fig. 6. Dependence of the Nusselt number Nu on the absolute value of the dimensionless electric parameter |e| at the external field period $T' = 6.2$. Solid line – movement towards increasing |e|, dashed line – towards decreasing |e|

accompanied by the appearance of an increasing number of linear frequency combinations incommensurable with the external one, until the spectrum becomes continuous. Chaos exists in section BC Fig. 5 (at point C (|e| = 43.78)). In section CD Fig. 5, a synchronization region is realized, where subharmonic oscillations are observed. Then, at point D Fig. 5 (|e| = 43.9) the heat flux experiences a sharp jump, and the system transitions to synchronous oscillations.

Similar to the previous case, hysteresis phenomenon is observed (loop ADEFG in Fig. 5): simultaneous coexistence of regimes with different Nusselt numbers. At Nu > 2.6 synchronous oscillations are realized (section EF in Fig. 5). When parameter |e| decreases at point F Fig. 5 (|e| = 30.9) the system transitions to equilibrium state.

5.3. External field period $T' = 6.2$

The dependence of dimensionless heat flux on parameter |e| for the given external field period is shown in Fig. 6.

Similar to all previous cases, convection occurs in the form of quasi-periodic oscillations at point A Fig. 6 (|e| = 25.4). With increasing parameter at point B Fig. 6 (|e| = 27.3) a reverse bifurcation occurs (Nusselt number sharply increases for a certain value |e|), and the system transitions at point C Fig. 6 to oscillations characterized by a frequency three times lower than the external field frequency. Then a period-doubling cascade occurs, leading to the appearance of chaos at point D Fig. 6 (|e| = 28.2) which exists up to point E in Fig. 6 (|e| = 28.6), where the system transitions to synchronous oscillations with a sharp increase in the Nusselt number.

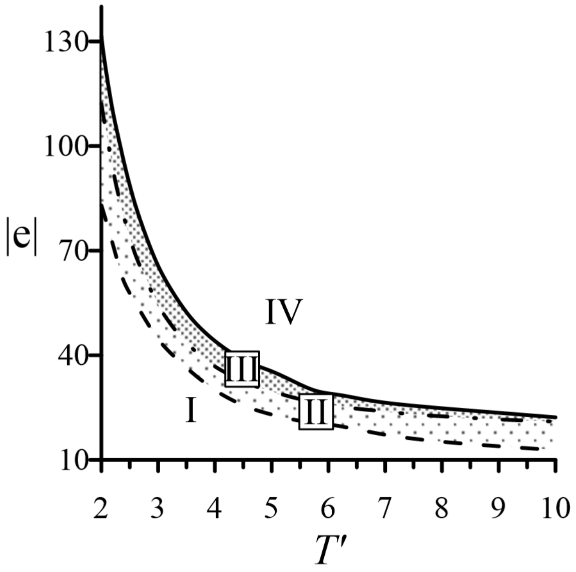

Fig. 7. Map of fluid motion regimes on the plane of external electric field period variation T' – absolute value of electric parameter |e|. I – region of no convection; II – region of coexistence of synchronous oscillations and no convection; III – region of coexistence of synchronous oscillations and various regimes: quasi-periodic oscillations, subharmonic oscillations, and chaos; IV – region of synchronous oscillations

At this period of the external field, a hysteresis phenomenon is also observed (loop AEFGH in Fig. 6). On the upper branch of this loop FG Fig. 6, synchronous oscillations occur, and when synchronous oscillations occur, and when parameter e decreases at point G in Fig. 6 (|e| = 19.6), convection sharply disappears in the system

Based on the study of Nusselt number dependencies on the dimensionless electric parameter for different periods of external electric field variation, a map of electroconvection regimes was constructed for the period range [2; 10] (Fig. 7).

For all considered periods of external field variation, instability occurs with an increase in the control parameter |e| from the equilibrium state through quasi-periodic oscillations (dash- dotted line in Fig. 7). With further increase in the electric Rayleigh number, low-intensity quasi-periodic oscillations can transform into subharmonic or chaotic regimes. With growth of the electroconvective parameter at the boundary marked by a solid line in Fig. 7, high-intensity synchronous oscillatory flows emerge. When decreasing the control parameter from regions of intense convection at the boundary marked by a dashed line in Fig. 7, transition to mechanical equilibrium of the fluid occurs.

CONCLUSION

The problem of electroconvection in a flat horizontal layer of viscous incompressible weakly conducting fluid placed in an alternating electric field and heated from above has been studied within the framework of a low-mode approximation. The case of moderate heating from above is considered.

As a result of studying linear perturbations under variable external influence, neutral curves depending on the electric field period were obtained, and corresponding critical wave numbers were determined.

In the nonlinear case, the evolution of the system under changes in amplitude and period of external electric field has been studied. Various types of system responses were discovered: quasi-periodic, subharmonic characterized by a frequency three times lower than the external forcing frequency, synchronous, and chaos. Different scenarios of transition to chaos were identified, through quasi-periodicity and through subharmonic cascade.

The phenomenon of hysteresis was discovered. Depending on initial conditions, oscillatory flows of weakly conducting fluid can have high or low intensity. The high-intensity regime corresponds to synchronous perturbations. For low-intensity oscillations, various system response modes are observed. Hysteresis transitions are accompanied by bifurcations. Linear theory predictions are confirmed in the nonlinear case.

FUNDING

This work was supported by the Russian Science Foundation (grant No. 23-21-00344, https://rscf.ru/project/23-21-00344/).

REFERENCES

1. V. S. Avduevskii, I. V. Barmin, S. D. Grishin et al., Cosmic Development Problems, Mashinostroenie, Moscow (1980).
2. V. I. Polezhaev, A. V. Bunet, N. A. Verezub el al., Mathematical Modelling of Convective Heat-masstransfer Based on the Navier-Stokes Equations, Nauka, Moscow (1987).
3. A. V. Getling, Rayleigh–Bénard Convection: Structures and Dynamics, Editorial URSS, Moscow (1999).
4. G. Z. Gershuni and E.M. Zhukhovitskii, Convective Stability of Incompressible Fluids, Nauka, Moscow (1976).
5. G. A. Ostroumov, Interaction of Electric and Hydrodynamic Fields. Physical Principles of Electrohydrodynamics, Nauka, Moscow (1979).
6. M. K. Bologa, F. P. Grosu and I. A. Kozhukhar', Electrical Convection and Heat Transfer, Sttintsa, Chisinau (1977).
7. B. L. Smorodin and M. G. Verlade, J. Electrostatics 48, 261 (2000).
8. V. A. Il'in, B. L. Smorodin, Technical Physics Letters 31, 57 (2005).
9. N. N. Kartavykh, B. L. Smorodin, V. A. Il'in, JETP 148, 178 (2015).
10. V. A. Il'in, B. L. Smorodin, Technical Physics Letters 33, 81 (2007).
11. B. L. Smorodin, A. V. Taraut, JETP, 180 (2014).
12. E. N. Lorenz, J. Atmosph. Sci. 20, 130 (1963).
13. P. Berge, I. Pomo, K. Bidal, Towards a Deterministic Approach to Turbulence, Mir, Moscow (1991).
14. N. B. Volkov, N. M. Zubarev, JETP 107, 1868 (1995).
15. J. Jawdat, Int. Commun. Heat Mass Transfer 37, 629 (2010).
16. D. Laroze, Commun. Nonlin. Sci. Numer. Simul. 18, 2436 (2013).
17. A. Srivastava and B. Bhadauria, J. Nanofluids 12, 904 (2023).
18. R. Finucane and R. Kelly, Int. J. Heat and Mass Transfer 19, 71 (1976).
19. G. Ahlers, P. C. Hohenbergm, and M. Luke, Phys. Rev. A 32, 3519 (1985).
20. V. A. Il'in, Technical Physics 83, 64 (2013).
21. L. D. Landau, E. M. Lifshitz, Theoretical Physics, vol. VI. Fluid Mechanics, Nauka, Moscow (1986).
22. B. Smorodin and N. Kartavykh, Micrograv. Sci. Technol. 32, 423 (2020).

23. O. O. Nekrasov and N. N. Kartavykh, Interfacial Phenomena and Heat Transfer 7, 217 (2019).

24. S. R. Kosvintsev, Perm University Herald, Physics 2, 128 (1994).

25. S. A. Zhdanov, S. R. Kosvintsev, I. Yu. Makarihin, JETP 117, 398 (2000).

26. S. R. Kosvintsev, B. L. Smorodin, S. A. Zhdanovet al., Proc. Int. Conf. Modern Problems of Electrophysics and Electrohydrodynamics of Liquids» (MPEEL), 79 (2000).

27. E. A. Coddington and N. Levinson, Theory of Ordinary Differential Equations, Foreign Languages Publishing House, Moscow (1958).

28. E. L. Tarunin, Computational Experiment in Free Convection Problems, Irkutsk University Publishing, Irkutsk (1990).

JOURNAL OF EXPERIMENTAL AND THEORETICAL PHYSICS, 2024, Vol. 165, No. 6, pp. 869–880

SUBTERAHERTZ DIELECTRIC AND PLASMA-DIELECTRIC CHERENKOV AMPLIFIERS ON RELATIVISTIC HIGH-CURRENT ELECTRON BEAMS

© 2024 A.V. Ershov *, I.N. Kartashov **, M.V. Kuzelev ***

**Faculty of Physics, Lomonosov Moscow State University 119991, Moscow, Russia*

**e-mail: ershov.av17@physics.msu.ru*
*** e-mail: igorkartashov@mail.ru*
**** e-mail: kuzelev@mail.ru*

Received November 28, 2023
Revised January 25, 2024
Accepted January 25, 2024

Abstract. Amplifiers with dielectric and plasma-dielectric filling, based on excitation of surface electromagnetic waves at dielectric boundary by relativistic electron beam, are considered. The focus is on the subterahertz operating frequency range. In linear approximation dispersion equation is obtained and areas of amplified frequencies and field structure are determined. Two limiting modes of Cherenkov beam instability depending on electron beam density are identified. The role of plasma near the dielectric boundary was evaluated. Efficiency of conversion of energy of directed motion of electron beam into energy of electromagnetic waves is determined on the basis of solution of shortened system of nonlinear equations. Schemes of radiation output from amplifier working area are proposed.

Keywords: *Plasma-dielectric waveguide, subterahertz radiation, relativistic electron beam, Cherenkov effect*

DOI: 10.31857/S004445102406e130

1. INTRODUCTION. PROBLEM STATEMENT

Intensive theoretical and experimental studies begun in the 1970s, aimed at obtaining powerful coherent electromagnetic radiation in the microwave range using high-current electron beams propagating in electrodynamic systems with plasma filling, have been undoubtedly successful. Currently, there are operating sub-gigawatt plasma sources of electromagnetic radiation in the centimeter wavelength range [1–3]. During their creation, a new direction of applied physics emerged – high-current relativistic plasma microwave electronics [4], which continues to actively develop today [5]. Therefore, it is completely natural to desire to "advance" the existing successes and achievements in the microwave field to a higher frequency region, for example, to the subterahertz or even terahertz ranges. The study of the possibility of advancing existing Cherenkov plasma sources of electromagnetic radiation into the subterahertz range is addressed in work [6].

This paper examines Cherenkov emitters on dense relativistic electron beams, using dielectric and plasma-dielectric waveguides as electrodynamic systems. The idea of using combined plasma-dielectric structures for wave deceleration in Cherenkov emitters was considered, for example, in works [7–9]. We will mainly consider the interaction of an electron beam with high modes of dielectric waveguides when they belong to the type of so-called spatially developed (multi-wave) electrodynamic systems [10], since the wavelengths of high (and therefore high-frequency) waveguide modes are small compared to its transverse dimension.

When the inequality $c/\sqrt{\varepsilon_d} < u$, is satisfied, where u is beam velocity, ε_d is dielectric permittivity, sufficient wave deceleration exists even without plasma. This case represents the main interest in the present work. If the opposite inequality $c/\sqrt{\varepsilon_d} > u$, is satisfied, then wave deceleration is provided only by plasma, which is less interesting for us here. We consider the case of simultaneous presence of both dielectric and plasma in the waveguide, if only because in strong high-frequency fields, breakdown develops on the dielectric surface, leading to plasma formation in waveguide regions adjacent to the dielectric [11,12]. Plasma significantly changes the electrodynamics of the dielectric waveguide, which should be taken into account within the framework of the problems outlined above. Essentially, this work is a continuation of our work [6], which addressed the problem of increasing the operating frequency of emitters using only high-density plasma without any dielectric inserts. Thus, in this work, we are trying to solve the same problem of frequency increase by using a different electrodynamic system[1].

Let's consider the interaction of a straight electron beam with a wave E-type of a circular cross-section waveguide with radially inhomogeneous isotropic medium filling with dielectric permittivity of the form

$$\varepsilon_{ij}(\omega,r) = \varepsilon(\omega,r)\delta_{ij}, \qquad i,j = r,\varphi,z, \tag{1}$$

where r,φ,z are cylindrical coordinates, and $\varepsilon(\omega,r)$ is some function of the radial coordinate r (and frequency ω). Let's direct the axis $0Z$ along the waveguide axis, coinciding with the beam direction, and define the azimuthally symmetric longitudinal component of the electric field intensity by the formula

$$E_z(t,z,r) = \frac{1}{2}[E(r)\exp(-i\omega t + ik_z z) + C.C.]. \tag{2}$$

From Maxwell's equations with the dielectric permittivity tensor (1) follows the equation for the complex amplitude $E(r)$ in formula (2)

$$\frac{1}{r}\frac{d}{dr}\left(r\frac{\varepsilon(\omega,r)}{\chi^2(\omega,r)}\frac{dE}{dr}\right) - \varepsilon(\omega,r)E = 0, \tag{3}$$

where $\chi^2(\omega,r) = k_z^2 - \varepsilon(\omega,r)\omega^2/c^2$.

We will consider two variants of waveguide medium filling. In the first variant

$$\varepsilon(\omega,r) = \begin{cases} \varepsilon_d, & 0 < r < r_0, \\ \varepsilon_p = 1 - \omega_p^2/\omega^2, & r_0 < r < R, \end{cases} \tag{4}$$

where ω_p is a constant electron Langmuir frequency. According to (4), in the inner region of the waveguide $r < r_0$ there is a dielectric with permittivity $\varepsilon_d > 1$, and in the outer region — cold collisionless electron plasma. This filling variant will be called the direct geometry case. In the second filling variant, called the inverse geometry case,

$$\varepsilon(\omega,r) = \begin{cases} \varepsilon_p = 1 - \omega_p^2/\omega^2, & 0 < r < r_0, \\ \varepsilon_d, & r_0 < r < R, \end{cases} \tag{5}$$

i.e., the inner region of the waveguide is filled with plasma.

As can be seen from formulas (1), (4), and (5), the plasma in the waveguide with a dielectric insert is unmagnetized. In the above-mentioned works [7–9], the opposite case was considered — fully magnetized plasma. Below it will be shown that the cases of plasma without external magnetic field and plasma in infinitely strong external magnetic field differ significantly from each other. The matter here is in the different set of eigenwaves of plasma-dielectric waveguides.

Directly from equation (3), the following boundary conditions at the interface between dielectric and plasma are obtained:

$$\{E\}_{r=r_0} = 0, \qquad \left\{\frac{\varepsilon(\omega,r)}{\chi^2(\omega,r)}\frac{dE}{dr}\right\}_{r=r_0} = 0. \tag{6}$$

Here and further, curly brackets denote the difference of expressions on both sides of the boundary, that is, for example, $\{E\}_{r=r_0} = E(r_0+0) - E(r_0-0)$. Another boundary condition $E(R) = 0$ is written at the perfectly conducting waveguide boundary.

As can be seen from (1), the medium in the waveguide is isotropic, which in relation to plasma means it is unmagnetized. However, in any of the known Cherenkov plasma emitters, there is necessarily some external magnetic field required for obtaining and transporting high-current relativistic electron beam. Plasma unmagnetization assumes the fulfillment of inequalities [14]

$$\Omega_e^2 \ll \omega^2, \; \Omega_e\omega_p^2 \ll \omega^3, \tag{7}$$

where Ω_e is the electron cyclotron frequency. In this work, we are only interested in the region of

---

[1] Wave amplification in dielectric waveguides without plasma in the low-frequency range was considered in work [13].

sufficiently high frequencies, therefore we consider inequalities (7) to be unconditionally fulfilled. The situation is different with the electron beam. The densities of electron beams used in plasma emitters are small compared to plasma densities. Therefore, assuming the inequalities are fulfilled [7, 14]

$$\Omega_e^2 \gg \omega_b^2\gamma^{-3}, |\,\delta k u\,|^2 \tag{8}$$

we consider the electron beam to be fully magnetized. Moreover, following experimental conditions, we use the model of an infinitely thin tubular electron beam. Here ω_b is the Langmuir frequency of beam electrons, $\gamma = (1 - u^2/c^2)^{-1/2}$, δ_b is the thickness of the tubular beam, and is δk is the spatial increment (gain coefficient) of resonant Cherenkov beam instability.

The current density of an infinitely thin tubular magnetized electron beam is defined by the formula

$$j_z(t,z,r) = \delta_b\delta(r - r_b) j_b(t,z;r_b), \tag{9}$$

where $j_b(t,z;r_b)$ — is a function that requires beam dynamics equations to find, and the parametric dependence on the tubular beam radius r_b indicates that the field (2) acts on the electrons of the thin beam precisely at point $r = r_b$. The presence of current with density (9) in the waveguide leads to the following jump in the azimuthal component of the magnetic field induction

$$\left\{B_\varphi(t,z,r)\right\}_{r=r_b} = \frac{4\pi}{c}\delta_b j_b(t,z;r_b). \tag{10}$$

The azimuthal component of the magnetic field induction is determined by a formula of type (2) with complex amplitude

$$B(r) = -i\varepsilon(\omega,r)\frac{\omega}{c\chi^2(\omega,r)}\frac{dE}{dr}. \tag{11}$$

Substituting the formula of type (2) with complex amplitude (11) into (10) and assuming that the electron beam passes through one of the plasma regions of the waveguide, we find the following boundary conditions for function $E(r)$ on the electron beam:

$$\{E\}_{r=r_b} = 0, \quad \left\{\frac{dE}{dr}\right\}_{r=r_b} = \delta_b\frac{\chi_p^2}{\varepsilon_p}\frac{4\pi i}{\omega}\left\langle j_b(r_b)\right\rangle, \tag{12}$$

where

$$\left\langle j_b(r_b)\right\rangle = \frac{\omega}{\pi}\int\limits_0^{2\pi/\omega} j_b(t,z;r_b)\exp\left(i\omega t - ik_z z\right)dt \tag{13}$$

is the space-time Fourier harmonic of the beam current density, and $\chi_p^2 = k_z^2 - \varepsilon_p\omega^2/c^2$. In (12), an obvious condition for the continuity of the function itself on the electron beam is added $E(r)$. In the linear approximation, to calculate function (13), one can use the known expression for electron beam conductivity obtained in the hydrodynamic model [7, 14], which gives

$$\frac{4\pi i}{\omega}\left\langle j_b(r_b)\right\rangle = -\frac{\omega_b^2\gamma^{-3}}{(\omega - k_z u)^2}E(r_b). \tag{14}$$

The procedure for calculating function (14) in nonlinear theory will be described below.

2. DISPERSION EQUATION OF LINEAR THEORY FOR THE CASE OF DIRECT GEOMETRY

Let us now proceed to consider the waveguide in the case of direct geometry (4). Since the beam passes through the plasma region of the waveguide, we assume that $r_0 < r_b < R$. Taking into account the boundary conditions $r = r_0$ and $r = R$, the solution of equation (3) in different regions of the waveguide can be written as

$$E(r) = \begin{cases} AI_0(\chi_d r), & r < r_0, \\ A\chi_p r_0[UI_0(\chi_p r) + VK_0(\chi_p r)], & r_0 < r < r_b, \\ BF_0(\chi_p r), & r_b < r < R, \end{cases} \tag{15}$$

where

$$\begin{gathered} V(\omega,k_z) = I_0(\chi_d r_0)I_1(\chi_p r_0) - \\ -\frac{\varepsilon_d\chi_p}{\varepsilon_p\chi_d}I_1(\chi_d r_0)I_0(\chi_p r_0), \\ U(\omega,k_z) = I_0(\chi_d r_0)K_1(\chi_p r_0) + \\ +\frac{\varepsilon_d\chi_p}{\varepsilon_p\chi_d}I_1(\chi_d r_0)K_0(\chi_p r_0), \\ F_0(\chi_p r) = K_0(\chi_p r) - I_0(\chi_p r)\frac{K_0(\chi_p R)}{I_0(\chi_p R)}, \end{gathered} \tag{16}$$

A and B constants, $I_0(x)$ and $K_0(x)$ are Infeld and MacDonald functions, and $\chi_d^2 = k_z^2 - \varepsilon_d\omega^2/c^2$. Substituting solutions (15) into the boundary conditions (12), we obtain the following relations:

$$A = B\frac{F_0(\chi_p r_b)}{\chi_p r_0 I_0(\chi_p r_b) D_0(\omega, k_z; r_b)}, \tag{17}$$

$$D_0(\omega, k_z; R)B =$$

$$= -D_0(\omega, k_z; r_b) I_0(\chi_p r_b)\delta_b r_b \frac{\chi_p^2}{\varepsilon_p}\frac{4\pi i}{\omega}\langle j_b(r_b)\rangle, \tag{18}$$

where

$$D_0(\omega, k_z; x) = U(\omega, k_z) + V(\omega, k_z)K_0(\chi_p x)/I_0(\chi_p x). \tag{19}$$

According to formula (15), relation (17) determines the field structure of the wave excited by the electron beam in the plasma-dielectric waveguide. The main one is certainly relation (18), which can be interpreted as the excitation equation of the waveguide by the beam (see below).

It is easy to see that equation

$$D_0(\omega, k_z; R) = 0 \tag{20}$$

is the dispersion equation determining the frequencies of the natural waves of the plasma-dielectric waveguide without the beam. Indeed, in the absence of a beam (for example, at $\delta_b = 0$) equation (18) has a non-trivial solution $B \neq 0$ only at $D_0(\omega, k_z; R) = 0$.

In the linear approximation, using formulas (14) and (15), from (18) we obtain the following dispersion equation for determining complex spectra of a plasma-dielectric waveguide with a thin tubular straight electron beam in the case of direct geometry:

$$D_0(\omega, k_z; R) - \frac{\delta_b r_b}{R^2} W_0(\omega, k_z)\frac{\omega_b^2\gamma^{-3}}{(\omega - k_z u)^2} = 0, \tag{21}$$

where

$$W_0(\omega, k_z) = R^2\frac{\chi_p^2}{\varepsilon_p} D_0(\omega, k_z; r_b) I_0(\chi_p r_b) F_0(\chi_p r_b). \tag{22}$$

If the wavelengths excited by the electron beam are small compared to the waveguide radius ($c/\omega \ll R$), which is exactly the case for high modes, then the dispersion equation (20) significantly simplifies. Indeed, in (19), we obtain the following dispersion equation:

$$D_0(\omega, k_z; \infty) = U(\omega, k_z) = 0. \tag{23}$$

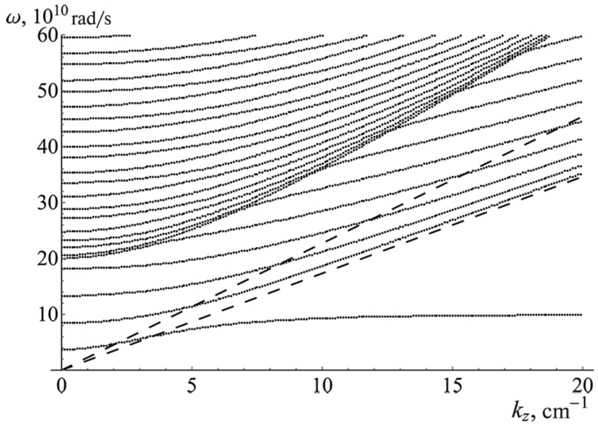

Fig. 1. Characteristic dispersion curves of the plasma-dielectric waveguide and lines (lower dashed line) $\omega = k_z c/\sqrt{\varepsilon_d}$ and (upper dashed line) $\omega = k_z u$

3. WAVE AMPLIFICATION IN A PLASMA-DIELECTRIC WAVEGUIDE IN THE REGIME OF SINGLE-PARTICLE CHERENKOV EFFECT. CASE OF DIRECT GEOMETRY

Let us investigate spatial wave amplification in a plasma-dielectric waveguide with a beam in the case of direct geometry, for which we will solve equation (21) with respect to the complex wave number $k_z(\omega)$ at real frequency ω. Assuming, as is usually done in Cherenkov interaction of beams with waves of any nature [7]

$$k_z = k_{z\omega} + \delta k, \qquad |\delta k| \ll k_{z\omega}, \tag{24}$$

where $k_{z\omega} = \omega/u$, we transform equation (21) into a cubic equation for the complex amplification coefficient δk

$$\left(D_0(\omega, k_{z\omega}; R) + \frac{\partial D_0(\omega, k_{z\omega}; R)}{\partial k_{z\omega}}\delta k\right)\delta k^2 =$$

$$= \frac{\delta_b r_b}{R^2}\left(W_0(\omega, k_{z\omega}) + \frac{\partial W_0(\omega, k_{z\omega})}{\partial k_{z\omega}}\delta k\right)\frac{\omega_b^2\gamma^{-3}}{u^2}. \tag{25}$$

Let the condition of single-particle Cherenkov resonance be satisfied (i.e., the wave is in Cherenkov resonance with the electron), and therefore

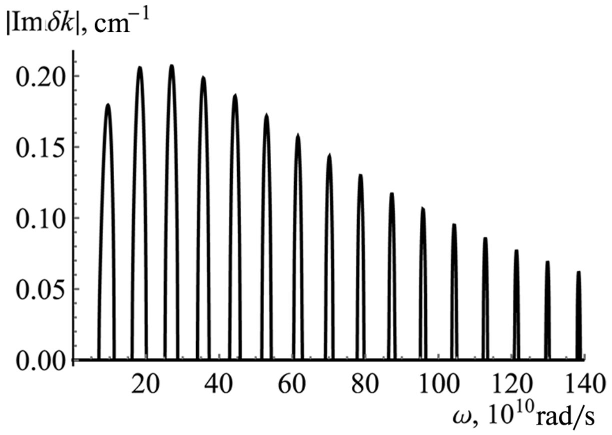

Fig. 2. Gain coefficient dependence on frequency in a dielectric waveguide without plasma

$$D_0(\omega, k_{z\omega}; R) = 0, \tag{26}$$

and the beam density is so low that the second term in brackets on the right side of the dispersion equation (25) can be neglected. Then, for the complex amplification coefficient at the frequency of single-particle Cherenkov resonance, we obtain the following expression:

$$\delta k(\omega_0) = \frac{1 - i\sqrt{3}}{2}\frac{\omega_0}{u}\left|\frac{\delta_b r_b}{R^2}\frac{\omega_b^2\gamma^{-3}}{\omega_0^2}\times \right.$$
$$\left. \times W_0(\omega_0, k_0)\left(k_0\frac{\partial D_0(\omega_0, k_0; R)}{\partial k_0}\right)^{-1}\right|^{1/3}, \tag{27}$$

where ω_0 is the solution of equation (26), and $k_0 = \omega_0 / u$. The amplification coefficient (27) has the structure typical for any single-particle Cherenkov effect. The condition for applicability of solution (27), i.e., the condition for single-particle amplification is the inequality

$$\left|\frac{1}{W_0(\omega_0, k_0)}\frac{\partial W_0(\omega_0, k_0)}{\partial k_0}\delta k(\omega_0)\right| n1. \tag{28}$$

To determine the resonant frequencies ω_0 one should solve equation (26) with respect to frequency *w*. The frequencies ω_0 are most clearly represented on the dispersion diagram (Fig. 1), which shows the dispersion curves — solutions of the dispersion equation (20), the line $\omega = k_z c / \sqrt{\varepsilon_d}$ (lower dashed line) and the line $\omega = k_z u$ (upper dashed line). Frequencies ω_0 are given by the intersection points of dispersion curves with the line $\omega = k_z u$. The calculation was performed for a system with the following parameters: $\omega_p = 2\cdot 10^{11}$ rad/s, $r_0 = 1$ cm, $R = 3$ cm, $\varepsilon_d = 3$, $u = 2.27 \cdot 10^{10}$ cm/s. The figure shows resonances only with the six lowest modes (although resonance exists at arbitrarily high modes), the first of which is plasma mode.

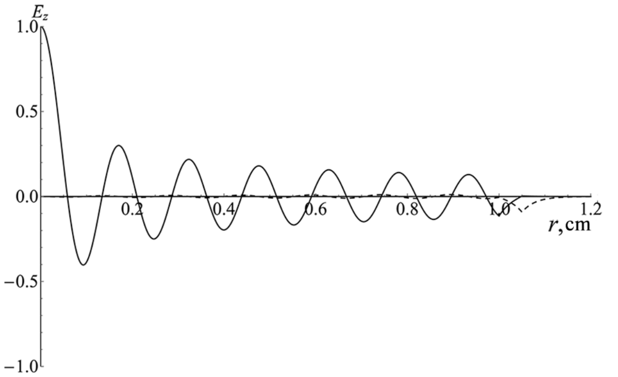

Fig. 3. Longitudinal component of the electric field mode $E_{0.13}$ during its resonant excitation by electron beam: Re*Ez* solid line, Im*Ez* dashed line

Let's pay attention to the lowest dispersion curve in Fig. 1 — it corresponds to the surface plasma wave[2]. As we can see, the cutoff frequency of this wave is not zero, which is characteristic only for a waveguide with plasma filling in the external region [15], which is exactly the case in direct geometry. Therefore, the Cherenkov resonance of the electron beam with such a surface plasma wave always exists, which must be taken into account when developing Cherenkov dielectric amplifiers with an internal dielectric insert. Indeed, with high power of the amplified signal, the plasma arising from breakdown fundamentally changes the electrodynamic properties of the system — instability appears on the low-frequency surface plasma wave, which can suppress amplification in the high-frequency region.

4. REGIME OF COLLECTIVE CHERENKOV EFFECT

In principle, equation (21) also describes the collective Cherenkov effect [7,16]. To understand this issue, equation (21) should be written in such a way as to explicitly highlight the dispersion function of the waveguide without beam (it has already been highlighted) and the dispersion function of the beam's Langmuir waves, which can be done easily

---

[2] The term "surface wave" refers only to the frequency range $\omega < k_z c$.

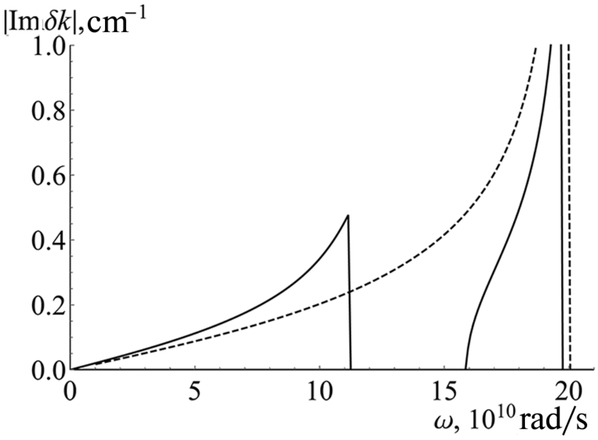

Fig. 4. Gain coefficients versus frequency: homogeneous plasma filling – dashed line; plasma-dielectric filling – solid line

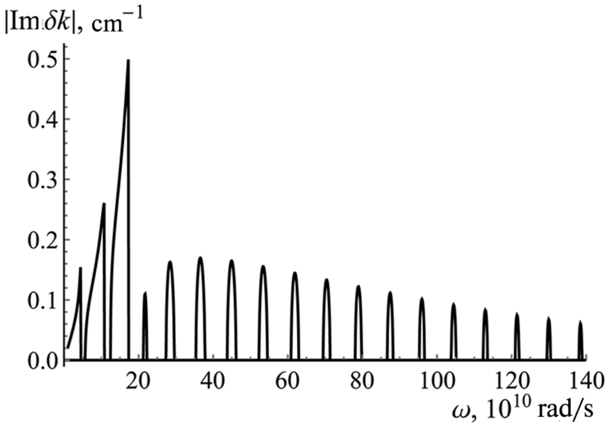

Fig. 5. Dependence of gain coefficient on frequency in plasma-dielectric waveguide.

using expressions (19) and (22). As a result, equation (21) transforms to the form

$$D_0(\omega,k_z;R)D_b(\omega,k_z) = \delta_b r_b \frac{\chi_p^2}{\varepsilon_p}\omega_b^2\gamma^{-3}\theta(\omega,k_z), \quad (29)$$

where

$$D_b(\omega,k_z) = (\omega - k_z u)^2 - \Omega_b^2(\omega,k_z)/\varepsilon_p \quad (30)$$

is the aforementioned dispersion function of the beam's Langmuir waves, where

$$\begin{aligned}\Omega_b^2(\omega,k_z) &= \delta_b r_b \chi_p^2 \omega_b^2 \gamma^{-3} I_0^2(\chi_p r_b) \times \\ &\times \left(\frac{K_0(\chi_p r_b)}{I_0(\chi_p r_b)} - \frac{K_0(\chi_p R)}{I_0(\chi_p R)}\right), \\ \theta(\omega,k_z) &= V(\omega,k_z) I_0^2(\chi_p r_b) \times \\ &\times \left(\frac{K_0(\chi_p r_b)}{I_0(\chi_p r_b)} - \frac{K_0(\chi_p R)}{I_0(\chi_p R)}\right)^2.\end{aligned} \quad (31)$$

The dispersion equation determining the frequencies of Langmuir waves (charge density waves) of a thin tubular magnetized electron beam in a plasma waveguide without a dielectric cylinder is$D_b(\omega,k_z) = 0$. The left side of the dispersion equation (29) is written in the "canonical" form of coupled waves equation — waves of the dielectric cylinder in plasma and waves of the tubular beam in plasma. The wave coupling coefficient is contained in the value $\theta(\omega,k_z)$.

When the inequality $\Omega_b^2 \ll \omega^2 \sim |k_z u|^2$ is satisfied, the spectrum of the slow charge density wave of the beam can be determined by the formula[3]

$$k_z^b(\omega) = k_{z\omega}\left(1 + \frac{\Omega_b(\omega,k_{z\omega})}{\omega\sqrt{\varepsilon_p}}\right). \quad (32)$$

The resonance frequency ω_0^b of one of the waves of the plasma-dielectric waveguide and the slow beam wave is determined from the equation $D_0\left(\omega,k_z^b(\omega);R\right) = 0$. At the resonance frequency, the solution of equation (29) is sought in the form

$$k_z(\omega_0^b) = k_0^b + \delta k, \quad (33)$$

where $k_0^b = k_z^b(\omega_0^b)$. Substituting (33) into equation (29), we find the following expression for the resonant gain coefficient in the regime of collective Cherenkov effect:

$$\delta k(\omega_0^b) = -i\left|\frac{1}{2}\delta_b r_b \frac{\chi_p^2}{\varepsilon_p}\frac{\omega_b^2\gamma^{-3}}{u\Omega_b(\omega_0^b,k_0^b)} \times \theta(\omega_0^b,k_0^b)\left(\frac{\partial U(\omega_0^b,k_0^b)}{\partial k_0^b}\right)^{-1}\right|^{1/2}. \quad (34)$$

The condition for the applicability of solution (34), i.e., the condition for collective amplification, is the inequality[4]

$$|\,\delta k(\omega_0^b)u\,| = \;\Omega_b(\omega_0^b,k_0^b). \quad (35)$$

---

[4] We do not explicitly present inequalities (28) and (35) here due to their complexity. The fulfillment of these inequalities was verified by us during numerical calculations. At those densities and radii of the electron beam that were taken during numerical calculations, the weak inequality (28) was usually satisfied.

5. WAVE GAIN COEFFICIENTS BY ELECTRON BEAM FOR THE CASE OF DIRECT GEOMETRY OF PLASMA-DIELECTRIC WAVEGUIDE

Let us now consider the results of calculating wave gain coefficients in a waveguide with the following parameters: waveguide radius $R = 3$ cm, dielectric cylinder radius $r_0 = 1$ cm, dielectric permittivity $\varepsilon_d = 3$. Let's take the following beam parameters: velocity $u = 2.27 \cdot 10^{10}$ cm/s, Langmuir frequency $\omega_b = 2.5 \cdot 10^{10}$ rad/s, average radius $r_b = 1.05$ cm, thickness $\delta_b = 0.1$ cm (the current of such beam is about 1 kA). For the case when there is no plasma in the waveguide, the frequency dependence of the gain coefficient is shown in Fig. 2.

A large number of gain zones can be seen, each corresponding to Cherenkov interaction of the beam with one of the waveguide modes — from mode E_{01} to mode $E_{0,16}$. Higher gain zones, which, if not accounting for frequency dispersion of permittivity ε_d, are infinitely many, are located in the higher frequency region. The gain zones are quite narrow, although even at frequency: 10^{12} rad/s, their width is several units at 10^{10} rad/s. Moreover, the gain coefficients are quite large. Thus, at frequency: 10^{12} rad/s, the gain coefficient is about 0.1 cm^{-1}, which provides power amplification by 1000 times with an amplifier length of 35 cm.

It should be noted that the results shown in Fig. 2 were obtained for the case when the inner boundary of the electron beam $r_b - \delta_b / 2$ coincides with the dielectric boundary r_0. When the beam moves away from the dielectric boundary, due to strong wave field attenuation in the vacuum region, the gain coefficient drops sharply. This circumstance constitutes one of the main difficulties for using already implemented Cherenkov microwave emitters in higher frequency ranges. Fig. 3 shows the real and imaginary parts of the longitudinal component of the electric field mode $E_{0,13}$ at the point of maximum gain coefficient ($\omega = 112.85 \cdot 10^{10}$ rad/s, $k_z = (50.46 - 0.08i)$ cm^{-1}). It is evident that there is virtually no field in the vacuum region of the waveguide, and at $r = r_b$ the field is not large.

Let us now turn to the case when plasma is present in the waveguide region $r \in (r_0, R)$ The presence of plasma, as noted above, significantly changes the electrodynamics of the waveguide and considerably complicates the overall picture of wave amplification. To better understand this, let's consider special cases of independent interest. Let's assume that in the waveguide region $r \in (0, r_0)$ instead of a dielectric, there is the same plasma as in $r \in (r_0, R)$. The dispersion equation for this case is obtained by replacing ε_d with ε_p. It can be shown that this equation reduces to $D_b(\omega, k_z) = 0$ (see formula (30)), which is convenient to rewrite as follows:

$$1 - \frac{\omega_p^2}{\omega^2} - \frac{\Omega_b^2(\omega, k_z)}{(\omega - k_z u)^2} = 0. \tag{36}$$

If we replace $\Omega_b^2(\omega, k_z)$ with $\omega_b^2 \gamma^{-3}$, we obtain the dispersion equation describing the interaction of an unbounded electron beam with an unbounded isotropic plasma [14]. From it, for the complex wave number we have

$$k_z = \frac{\omega}{u} - i \frac{\omega}{u} \sqrt{\frac{\omega_b^2 \gamma^{-3}}{\omega_p^2 - \omega^2}}. \tag{37}$$

At $\omega < \omega_p$ formula (37) describes the spatial amplification of the longitudinal field during beam self-modulation in a medium with negative dielectric permittivity [17]. At $\omega = \omega_p$ the amplification coefficient (37) becomes infinite, which is due to the zero group velocity of the Langmuir wave in cold plasma (oscillation accumulation effect). Similar processes occur in the waveguide as well. Indeed, at $\omega < \omega_p$ the dielectric permittivity of the plasma is negative, and the longitudinal Langmuir wave with frequency $\omega(k_z) = \omega_p$ exists in the waveguide with homogeneous isotropic plasma. Figure 4 shows the modulus of the imaginary part of the wave number obtained by numerical solution of equation (36) at $\omega_p = 20 \cdot 10^{10}$ rad/s (dashed line).

Now let the plasma be present only in the region $r \in (r_0, R)$, while the rest of the waveguide is filled with a dielectric with permittivity $\varepsilon_d < c^2 / u^2$ (one can even set $\varepsilon_d = 1$). In this case, Cherenkov resonance of the beam with electromagnetic waveguide modes is impossible. However, in addition to the potential Langmuir wave $\omega = \omega_p$ due to the presence of plasma boundary $r = r_0$ a non-potential surface wave appears in the waveguide. In the shortwavelength limit, the surface wave frequency approaches$\omega_p / \sqrt{\varepsilon_d + 1}$,

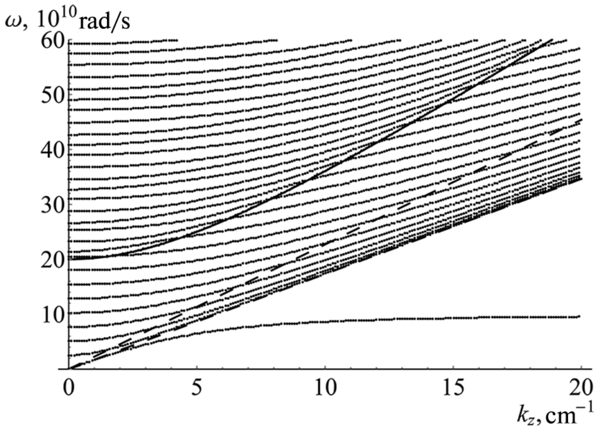

Fig. 6. Characteristic dispersion curves of the plasma-dielectric waveguide in the case of inverse geometry and lines $\omega = k_z c / \sqrt{\varepsilon_d}$ (lower dashed line) and $\omega = k_z u$ (upper dashed line)

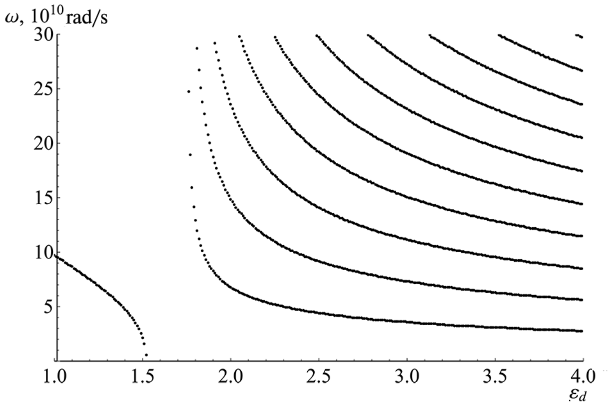

Fig. 7. Cherenkov resonances depending on the dielectric permittivity

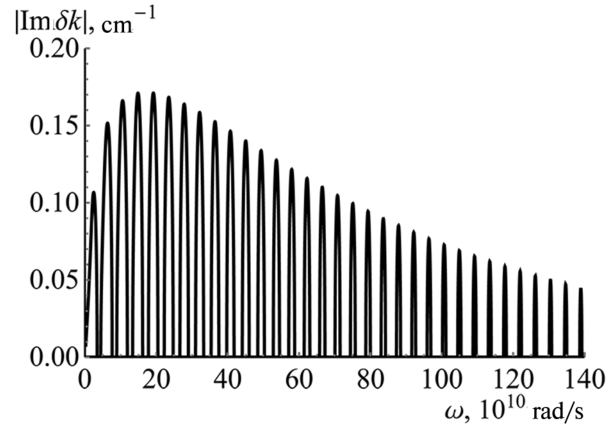

Fig. 8. Dependence of gain coefficient on frequency in a dielectric waveguide without plasma, inverse geometry

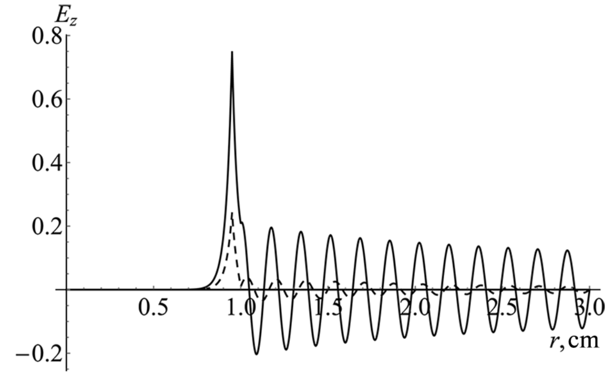

Fig. 9. Longitudinal component of electric field strength of mode $E_{0,24}$ during its resonant excitation by electron beam in inverse geometry: $\Re E_z$ − solid line, $\Im E_z$ − dashed line $\omega = 100.8 \times 10^{10}$ rad/s, $k_z = (44.9 - 0.07i)$ cm^{-1}

and at $k_z = 0$ there is a certain non-zero cutoff frequency (see the lower dispersion curve in Fig. 1). Therefore, there are two Cherenkov resonances — with bulk Langmuir and surface Langmuir waves. Consequently, two frequency regions of amplification appear. The gain coefficient for this case is shown by solid lines in Fig. 4.

Now let, as in the case of Fig. 2, $\varepsilon_d = 3$, but there is also plasma with Langmuir frequency $20 \cdot 10^{10}$ rad/s. In this case, resonances with surface plasma wave, bulk Langmuir wave, and electromagnetic modes become possible. The gain coefficient for this case is shown in Fig. 5, which is essentially a combination of Fig. 2 and 4.

One might assume that the presence of plasma in a dielectric waveguide with dielectric in region $r < r_0$ is a negative factor for solving the problem of increasing the frequency of amplified waves. Indeed, in the presence of plasma in the frequency region below the plasma frequency, the wave gain coefficients are high. The lower the wave frequency, the worse it radiates through the amplifier output boundary. Therefore, parasitic self-excitation of the amplifier in the low-frequency region is possible, which leads to beam “deterioration” and reduction in Cherenkov radiation efficiency in the high-frequency region[5]. One can, of course, take another approach: use such dense plasma that Cherenkov radiation of the surface plasma wave would occur in the sub-terahertz region. Then there would be no need for a dielectric insert in the waveguide. This approach has both advantages and disadvantages [6].

---

[5] As for the amplification coefficients in the high-frequency region, as can be seen from Fig. 2 and Fig. 3, plasma practically does not affect them.

6. THE CASE OF INVERSE GEOMETRY OF THE PLASMA-DIELECTRIC WAVEGUIDE

Let us now consider the inverse geometry of system (5). Assuming $r_b < r_0$ and taking into account the boundary conditions $r = r_0$ and $r = R$, the solution of equation (3) in different regions of the waveguide can be written as

$$E(r) = \begin{cases} AI_0(\chi_p r), & r < r_b, \\ B\chi_p r_0[UI_0(\chi_p r) + VK_0(\chi_p r)], & r_b < r < r_0, \\ BF_0(\chi_d r), & r_0 < r < R, \end{cases} \tag{38}$$

where

$$\begin{gathered} F_0(\chi_d r) = K_0(\chi_d r) - I_0(\chi_d r)\frac{K_0(\chi_d R)}{I_0(\chi_d R)}, \\ F_1(\chi_d r) = K_1(\chi_d r) + I_1(\chi_d r)\frac{K_0(\chi_d R)}{I_0(\chi_d R)}, \\ U(\omega,k_z) = F_0(\chi_d r_0)K_1(\chi_p r_0) - \\ -\frac{\varepsilon_d\chi_p}{\varepsilon_p\chi_d}F_1(\chi_d r_0)K_0(\chi_p r_0), \\ V(\omega,k_z) = F_0(\chi_d r_0)I_1(\chi_p r_0) + \\ +\frac{\varepsilon_d\chi_p}{\varepsilon_p\chi_d}F_1(\chi_d r_0)I_0(\chi_p r_0). \end{gathered} \tag{39}$$

Substituting solutions (38) into boundary conditions (12), we obtain the following relations:

$$B = A\times$$

$$\times\frac{I_0(\chi_p r_b)}{\chi_p r_0[U(\omega,k_z)I_0(\chi_p r_b) + V(\omega,k_z)K_0(\chi_p r_b)]}, \tag{40}$$

$$\begin{gathered} D_0(\omega,k_z)A = -[U(\omega,k_z)I_0(\chi_p r_b) + \\ +V(\omega,k_z)K_0(\chi_p r_b)]\times \\ \times\delta_b r_b\frac{\chi_p^2}{\varepsilon_p}\frac{4\pi i}{\omega}\langle j_b(r_b)\rangle, \end{gathered} \tag{41}$$

where

$$D_0(\omega,k_z) = V(\omega,k_z) \tag{42}$$

is the dispersion equation determining the frequencies of natural waves of the plasma-dielectric waveguide without beam in the case of inverse geometry.

In the linear approximation, using formulas (14) and (38), from (42) we obtain the following dispersion equation for determining the complex spectra of a plasma-dielectric waveguide with a thin tubular straight electron beam:

$$D_0(\omega,k_z) - \frac{\delta_b r_b}{R^2}W(\omega,k_z)\frac{\omega_b^2\gamma^{-3}}{(\omega - k_z u)^2} = 0, \tag{43}$$

where

$$W(\omega,k_z) = R^2\frac{\chi_p^2}{\varepsilon_p}\times$$

$$\times[U(\omega,k_z)I_0(\chi_p r_b) + V(\omega,k_z)K_0(\chi_p r_b)]\times$$

$$\mathit{times}I_0(\chi_p r_b). \tag{44}$$

Equation (43) does not differ in form from the dispersion equation (21), therefore we omit its approximate analytical consideration here, and we will consider numerical solutions a little later.

An essential feature of inverse geometry is associated with the surface plasma wave. In the case of plasma localized in the inner region of the waveguide $r < r_0$ the cutoff frequency of the surface plasma wave equals zero. Using formulas (39) and (42), it is easy to show that in the long-wavelength limit, the frequency of the surface plasma wave is determined by the formula

$$\omega = \frac{k_z c}{\sqrt{\varepsilon_d}}\left(1 + \frac{I_1(\omega_p r_0 / c)}{I_0(\omega_p r_0 / c)}\frac{\omega_p r_0}{c}\ln\frac{R}{r_0}\right)^{-1/2}. \tag{45}$$

Considering that in the long-wavelength limit the phase velocity of the surface plasma wave is maximal, from (45) we see that at $u > c / \sqrt{\varepsilon_d}$ the surface plasma wave cannot be excited. In principle, it can be excited, but only when the inverse inequality is satisfied $u < c / \sqrt{\varepsilon_d}$, when Cherenkov resonance of the beam and electromagnetic waves is absent. For this work, the case $u < c / \sqrt{\varepsilon_d}$, i.e., weak deceleration of electromagnetic waves, is of no interest (unlike work [6], in which there is no deceleration of electromagnetic waves at all).

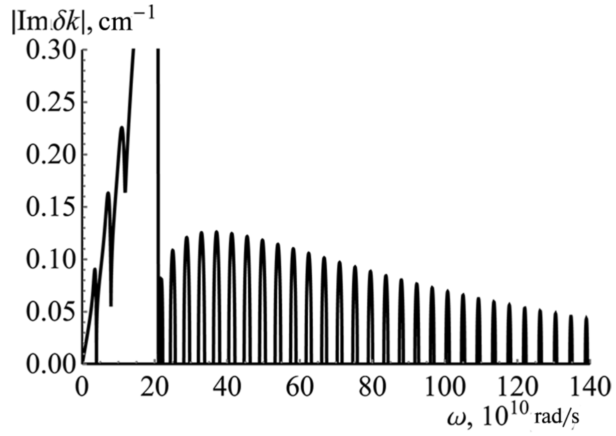

Fig. 10. Dependence of gain coefficient on frequency in plasma-dielectric waveguide, inverse geometry

The surface plasma wave in this case is not excited since because $\varepsilon_d = 3 > c^2 / u^2 \approx 1.73$. Resonances possible at different dielectric permittivities, for electron beam with velocity $u = 2.27 \cdot 10^{10}$ cm/s are shown in Fig.7.

Let's now consider wave amplification in a system with inverse filling[6]. Let the parameters of plasma-dielectric waveguide and electron beam be the same as in the case discussed in Fig. 2–5, only interchange plasma and dielectric, and set beam radius to $r_b = 0.95$ cm. The calculation results are presented in Fig. 8,9 and 10, which are analogous to Fig. 2, 3 and 5 respectively.

Notable is the similarity between Fig. 5 and 10. It was previously stated that when $u > c / \sqrt{\varepsilon_d}$, which is the case in Fig. 5 and 10, excitation of surface plasma wave is impossible in a system with inverse geometry[7]. However, resonant excitation of bulk Langmuir wave occurs for any geometry. This resonance appears as the highest maximum both in Fig. 5 and Fig. 10. Regarding the maxima in the region $\omega < \omega_p$, in case of Fig. 5 one of them is related to resonance on surface plasma wave, while in Fig. 10 all maxima are caused by resonances with electromagnetic waves (see Fig. 6). The main features of inverse geometry are more frequent placement of amplification zones and smaller width of each zone. The latter, in our opinion, is a serious disadvantage of the system with inverse geometry.

7. NONLINEAR THEORY OF CHERENKOV WAVE AMPLIFICATION IN PLASMA-DIELECTRIC WAVEGUIDE IN CASE OF DIRECT GEOMETRY

Let us now turn to the nonlinear theory. We will limit ourselves to the case of geometry with internal localization of the dielectric insert. The nonlinear theory of Cherenkov plasma-dielectric amplifiers can be based on equation (18), which, taking into account (15), can be written as

$$D_0(\omega,k_z;R)E(r_b) = -D_0(\omega,k_z;r_b)I_0(\chi_p r_b)\times$$

$$\times F_0(\chi_p r_b)\delta_b r_b \frac{\chi_p^2}{\varepsilon_p}\frac{4\pi i}{\omega}\langle j_b(r_b)\rangle. \qquad (46)$$

Here $E(r_b)$ is the field amplitude (2) at the electron beam passage location. If the field were represented not in the form of (2), but in the form

$$E_z(t,z,r) = \frac{1}{2}[E(z,r)\exp(-i\omega t + ik_{z\omega}z) + \mathrm{C.C.}], \qquad (47)$$

then in the linear approximation it would be $E(z,r) = E(r)\exp(i\delta kz)$, and in the dispersion equation, the wave number would be replaced by $k_{z\omega} + \delta k$ (see (24)). In the nonlinear case, formula (14) for the beam current density is not valid, but equation (46) is still relevant if rewritten in the following operator form:

$$D_0(\omega,\hat{k}_z;R)E(z,r_b) =$$

$$= -W_0(\omega,\hat{k}_z;r_b)\frac{\delta_b r_b}{R^2}\frac{4\pi i}{\omega}\langle j_b(z;r_b)\rangle, \qquad (48)$$

where the wave number k_z is replaced by the wave number operator $\hat{k}_z = k_{z\omega} - id / dz$.

To calculate the nonlinear beam current density, we use the method of integration over initial data in the boundary value problem formulation [18]. Omitting the standard derivation procedure, which can be found, for example, in [6], we present only the final formula for the beam current density

$$\langle j_b(z;r_b)\rangle = en_{0b}u\frac{\omega}{\pi}\int\limits_0^{2\pi/\omega} \exp\big(i\omega\tau(z,\tau_0)\big)dt_0, \qquad (49)$$

---

[6] Equation (42) has a degenerate solution χ_p=0, shown in Fig. 6 by a solid line. As can be seen from formulas (38), the solution χ_p=0 corresponds to zero electromagnetic field.

[7] Mathematically, this is described by the multiplier $\varepsilon^{-1}{}_{\mathrm{p}}$ in expressions (22) and (44) and is related to the fact that in any geometry, the beam passes through the plasma volume.

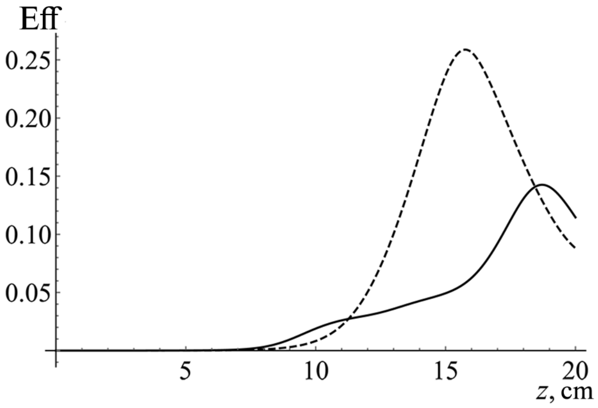

Fig. 11. Amplification efficiencies of high-frequency electromagnetic wave at frequency ω = 50.6 · 10^{10} rad/s (dashed line), ω = 100.9 · 10^{10} rad/s (solid line)

where n_{0b} is the unperturbed electron beam density. Function $\tau(z,\tau_0)$ is the local time at which the beam electron, which entered the waveguide cross-section $z = 0$ at moment τ_0, reaches cross-section z. This function is determined from the following equations of motion:

$$\begin{gathered}\frac{d\tau}{dz} = \frac{V}{u^2},\\ \frac{dV}{dz} = -\frac{e}{mu\gamma^3}\left(1 + 2\frac{u^2}{c^2}\gamma^2\frac{V}{u}\right)^{3/2} \times \\ \times\frac{1}{2}[E(z,r_b)\exp\left(-i\omega\tau(z,\tau_0)\right) + c.c.],\end{gathered} \tag{50}$$

and $V = V(z,\tau_0)$ — is the perturbation of the electron beam velocity. The boundary conditions for equations (50) are

$$\tau(z = 0) = \tau_0, \qquad V(z = 0) = 0. \tag{51}$$

In addition to the electron beam entry conditions (51), the system with the wave excitation condition at the amplifier input

$$E(z = 0, r_b) = E_0. \tag{52}$$

If the electron beam was pre-modulated before injection into the waveguide, then conditions (50) should be set as

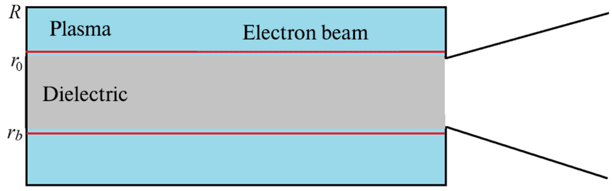

Fig. 12. Diagram of amplifier with plasma-dielectric waveguide in direct geometry

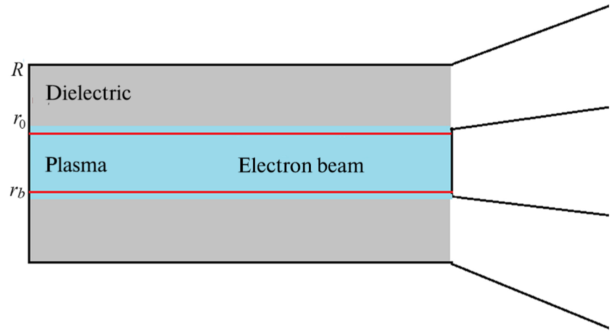

Fig. 13. Diagram of amplifier with plasma-dielectric waveguide in inverse geometry

$$\begin{gathered}\tau(z = 0) = \tau_0 + \alpha\sin(\tau_0 + p_0),\\ V(z = 0) = \beta\sin(\tau_0 + q_0),\end{gathered} \tag{53}$$

where α, β, p_0, q_0 sets the velocity modulation depth.

The pseudodifferential equation (48) is not suitable for computer modeling purposes; it should be properly simplified. Due to inequality (24), the dispersion operator $D_0(\omega, \hat{k}_z; R)$ and the right-hand side of equation (48) can be expanded in id/dz, which leads to the following equation::

$$\begin{gathered}\left(D_0 - i\frac{\partial D_0}{\partial k_{z\omega}}\frac{d}{dz}\right)E(z,r_b) = \\ = -\frac{\delta_b r_b}{R^2}\frac{4\pi i}{\omega}\left(W_0 - i\frac{\partial W_0}{\partial k_{z\omega}}\frac{d}{dz}\right)\langle j_b(z;r_b)\rangle,\end{gathered} \tag{54}$$

where D_0 — function (19) at $k_z = k_{z\omega}$ and $x = R$, and W_0 — function (22) at $k_z = k_{z\omega}$. Equation (54) and equations (50) form a closed nonlinear system of equations for the Cherenkov plasma-dielectric amplifier. The efficiency of electromagnetic wave amplification by electron beam can be determined by the obvious formula

$$\text{Eff} = \frac{\gamma - \langle\gamma(z,\tau_0)\rangle}{\gamma - 1}, \tag{55}$$

where angle brackets denote averaging over all electrons entering the cross-section $z = 0$ during the period $2\pi/\omega$. Value (55) depends on coordinate, which allows determining the optimal amplifier length in terms of achieving maximum efficiency and output radiation power.

In the linear approximation, the dispersion equation (25) can be obtained from equations (54) and (50). Earlier, when presenting the linear theory, we proceeded not from solutions of the approximate equation (25), but from solutions of the exact dispersion equation (19), which is not accidental. The fact is that in the case of a high-density electron beam, the solutions of equations (19) and (25) differ, sometimes significantly, although they qualitatively coincide. Therefore, we always precede the solution of the nonlinear problem with linear analysis. Nonlinear solutions can be considered quantitatively reliable only in cases where the solutions of dispersion equations (19) and (25) are close. We will dedicate a separate work to the systematic analysis of nonlinear amplification modes. Here, we present some particular results characterizing possible values of amplification efficiencies and powers of amplified signals.

In Fig. 11 for a system with parameters $\omega_p = 20 \cdot 10^{10}$ rad/s, $r_0 = 1$ cm, $R = 3$ cm, $\varepsilon_d = 3$, $u = 2.27 \cdot 10^{10}$ cm/s, $\omega_b = 2.5 \cdot 10^{10}$ rad/s, the gain efficiencies at the frequencies of the eighth and fourteenth resonances are shown. The maximum efficiency of 15 to 25 percent is achieved at a length of 15–25 cm, after which it begins to decrease. As we can see, the gain efficiencies are quite high, and the optimal amplifier lengths are quite acceptable from an experimental point of view.

One of the important problems in developing Cherenkov amplifiers on high-current electron beams is the problem of radiation output through the output boundary of the beam-wave interaction region. The matching of the interaction region with the radiating device should be as good as possible. The electromagnetic field structure of high modes in the considered plasma-dielectric waveguides (see Fig. 3 and 9) suggests possible schemes of radiating devices. In the case of a waveguide in direct geometry, a conventional horn with a radius smaller than the waveguide radius can be used (Fig. 12). The walls of the waveguide and horn should be at the potential of the high-current accelerator anode. In this case, the surface connecting the waveguide to the horn simultaneously serves as a collector for the electron beam.

In the case of a waveguide in inverse geometry, a coaxial horn can be used (Fig. 13), such as those used in operating amplifiers on cable plasma waves [1–3]. The electron beam collector is the inner part of the coaxial. To equalize potentials, a jumper between the inner and outer parts of the coaxial horn is used, which makes the scheme less convenient compared to the direct geometry scheme.

8. CONCLUSION

In conclusion, let us formulate some findings from this work.

1. The use of waveguides with dielectric inserts allows the implementation of powerful single-mode (single-frequency) amplifiers with an operating frequency of about 10^{12} rad/s and even higher (wavelength: ~ 0.2 cm and even less). The efficiency of amplification at a length of ~ 20 cm can reach 15%. For an electron beam with a current of 1 kA and electron energy of 270 keV, this means an output power of about 40 MW.

2. The presence of plasma in waveguides with dielectric inserts should be considered undesirable. On one hand, in the sub-terahertz frequency range, the gain coefficient practically does not depend on the presence or absence of plasma. On the other hand, in the low-frequency region, due to the excitation of potential bulk Langmuir waves with high gain coefficient, low-frequency self-excitation of the emitter is possible, which will lead to suppression of gain in the sub-terahertz region.

3. The characteristic dependences of gain coefficients on frequency indicate the possibility of creating broadband amplifiers, including noise amplifiers, based on waveguides with dielectric inserts. Indeed, as can be seen from Fig. 2 and 8, the gain coefficient consists of a set of relatively narrow lines of approximately equal magnitude over a wide frequency range. There are reasons to believe that with an increase in the electron beam current, these individual lines broaden and merge into a single wide region of electromagnetic wave amplification.

4. The case of direct geometry of a waveguide with a dielectric insert is preferable compared to the case of inverse geometry due to the greater width of amplification zones.

REFERENCES

1. P.S. Strelkov, I.E. Ivanov, E.D. Dias Mikhailova and D.V. Shumeiko, Plas. Phys. Rep. 47 (3), 269-278 (2021)
2. A.B. Buleyko, A.V. Ponomarev, O.T. Loza, D.K. Ulyanov and S.E. Andreev, Phys. Plasmas 28, 023303 (2021)
3. D.K. Ul’yanov, R.V. Baranov, O.T. Loza et al, Tech. Phys. 58, 1503-1506 (2013)
4. M.V. Kuzelev, A.A. Rukhadze and P.S. Strelkov, Plasma relativistic microwave electronics, M: LENAND (2018) [in russian]
5. P.S. Strelkov, Phys. Usp. 62, 465-486 (2019)
6. I.N. Kartashov and M.V. Kuzelev, J. Exp. Theor. Phys. 134 (2), 235-248 (2022)
7. M.V. Kuzelev and A.A. Rukhadze, Electrodynamics of high density electron beam in plasma, M: LENAND (2018) [in russian]
8. M.A. Krasil'nikov, M.V. Kuzelev, V.A. Panin and D.S. Filipychev, Plas. Phys. Rep. 19, 554 (1993)
9. A.S. Shlapakovski, E. Schamiloglu, Plas. Phys. Rep. 30 (7), 587-594 (2004)
10. S.P. Bugaev, V.I. Kanavets and V.I. Koshelev, Soviet J. Comm. Tech. Electr. 34 (4), 119 (1989)
11. G.P. Kuz'min, I.M. Minaev and A.A. Rukhadze, Plas. Phys. Rep. 36 (12), 1082-1084 (2010)
12. T.V. Bazhenova, I.A. Znamenskaya, I.V. Mursenkova and A.E. Lutsky, High Temp. 45 (4), 523-530 (2007)
13. A.S. Shlapakovskii, Tech. Phys. Lett. 25 (4), 267-270 (1999)
14. A.F. Alexandrov, L.S. Bogdankevich and A.A. Rukhadze, Principles of Plasma Electrodynamics, Heidelberg: Springer Verlag (1984)
15. M.V. Kuzelev, Wave phenomena in dispersive media, M: URSS (2018) [in russian]
16. M.V. Kuzelev and A.A. Rukhadze, Soviet Phys. Usp. 30 (6), 507-524 (1987)
17. V.V. Bogdanov, M.V. Kuzelev and A.A. Rukhadze, Plas. Phys. Rep. 10, 319 (1984)
18. Yu.V. Bobylev and M.V. Kuzelev, Nonlinear phenomena during electromagnetic interaction of electron beam with plasma, M: FIZMATLIT (2009) [in russian]

JOURNAL OF EXPERIMENTAL AND THEORETICAL PHYSICS, 2024, Vol. 165, No. 6, pp. 882–886

STATISTICAL, NONLINEAR, AND SOFT MATTER PHYSICS

MODEL OF SOLITON TURBULENCE OF HIGH-FREQUENCY FLUCTUATIONS IN PARTIALLY MAGNETIZED PLASMA

© 2024 **I. Kh. Kovaleva, A. T. Kovalev***

Sadovsky Institute of Geosphere Dynamics of the Russian Academy of Sciences 119334, Moscow, Russia

** e-mail: akoval@idg.chph.ras.ru*

Received December 09, 2023
Revised January 21, 2024
Accepted January 24, 2024

Abstract. A theoretical consideration of high-frequency microfluctuations formed by electron current across the magnetic field has been conducted. The Ginzburg–Landau equation with a nonlocal term was obtained to describe the dynamics of electron-cyclotron drift fluctuations. The thresholds for transition to turbulent regime and the boundaries within which soliton turbulence regime can be realized were determined, depending on the parameters of this equation.

Keywords: *Plasma-dielectric waveguide, subterahertz radiation, relativistic electron beam, Cherenkov effect*

DOI: 10.31857/S004445102406e142

1. INTRODUCTION

Numerous active space experiments involving releases of high-velocity or explosion-generated plasma clouds have shown that at the plasma cloud front, a region forms with significant electron heating, increased ionization rate, and anomalous transport, where transverse electron transport greatly exceeds the level of classical and Bohm diffusion. This phenomenon in space plasma physics is known as CIV – Critical Ionization Velocity phenomenon (see review [1]). Active ionospheric experiments often focused primarily on studying this phenomenon. Experimental data were interpreted within this framework, for example, in the CRIT II experiment [2, 3]. At the time, several participants of the active space experiment CRIT II saw an analogy between these processes in space and laboratory plasma of magnetrons and Hall thrusters, and attempted to investigate this phenomenon in more detail under laboratory conditions [4,5]. It seems reasonable to use the extensive experimental material and theoretical developments made in the study of anomalous transport, heating, and ionization in laboratory plasma of magnetrons and Hall thrusters as applied to space plasma.

Generally, to explain electron transfer in these problems, one of the following hypotheses is invoked: electron-cyclotron drift waves, Simon-Howe instability, lower-hybrid, modified two-stream, or ion-acoustic instability. The main factors exciting instability are considered to be gradients of density, magnetic field, temperature, drift motion, and dissipation. Typically, theoretical considerations draw a clear line between fluid treatment of low-frequency long-wave perturbations and kinetic treatment of short-wave perturbations. In kinetic considerations, plasma is usually non-dissipative. In many cases, attempts are made to account for nonlinear effects. Including particle-in-cell methods that yielded electron-cyclotron wave structures. Several examples of nonlinear numerical models and calculations can be found in works [6–8]. Some authors associate anomalous transport with the existence of nonlinear structures (for example, [9]).

In ionospheric experiments, the electron concentration in plasma formations has the same orders of magnitude (10^{10}–10^{10} cm^{-3}). With this, the electric and magnetic fields are smaller by 2–3 orders (≈ 0.5 Gs and V/m respectively). Such small magnetic field values in the ionosphere (compared to laboratory ones) lead to a significant frequency shift in some of these instabilities. As a result, electron-cyclotron drift (ECD) turbulence appears to be the most preferable explanation for high-frequency turbulence in ionospheric experiments. There is no noticeable deviation of the electron distribution function from Maxwellian, due to significantly lower electric field values. The directional drift velocity of electrons is much less than the electron thermal velocity. The problem parameters go beyond the kinetic consideration conducted in work [10]. This suggests the possibility of fluid treatment of high-frequency turbulence with consideration of dissipation. Furthermore, the geometry of expanding plasma, in which the ion Larmor radius is comparable to the plasma front width, while the electron Larmor radius is much smaller, allows, unlike [11], the use of partially magnetized plasma models for constructing nonlinear structures.

In this work, an attempt is made to construct a model of small-scale, fast-moving high-frequency nonlinear wave structures of electrons forming in plasma in the presence of electron drift due to an electric field perpendicular to the magnetic field (in $E \times B$-plasma). Unlike reproducible laboratory plasma conditions, when considering the dynamics of plasma formations in ionospheric conditions, the main issues become plasma parameters corresponding to various modes of small-scale turbulence, conditions and time parameters of its development, and the effects produced by this turbulence. Therefore, to describe turbulence based on the system of fluid equations and Maxwell's equations using the small parameter expansion method, a one-dimensional complex Ginzburg-Landau equation (CGL) with an additional nonlocal (integral) nonlinear term was obtained as the simplest model of ECD turbulence near its threshold. The boundaries of transition to turbulence were investigated. A region of plasma parameters corresponding to soliton turbulence was obtained, which, according to the authors, is associated with the anomalous transport regime.

2. BASICS OF THE MODEL

For high-frequency small-scale fluctuations, plasma can be considered partially magnetized, as the fluctuation scales are much smaller than the ion Larmor radius. For laboratory plasma, several authors associate the growth of instability with non-Maxwellian electron velocity distribution; however, in the present work, a simpler model of distribution distortion is adopted in the form of adding drift velocity to the Maxwellian distribution. The factors determining the growth of instability and its nonlinear stabilization are taken to be the plasma density gradient and electron collisions and diffusion.

In our consideration, we used a system of fluid equations for electron motion in the plane perpendicular to the magnetic field. Temperature changes at the scale of small-scale high- frequency turbulence are not taken into account, and the gyroviscosity tensor (inapplicable at such scales) is not considered. At the same time, it seems necessary to take into account electromagnetic corrections, since at electron temperatures of $T_e \geqslant 1$ eV observed in experiments, purely electrostatic waves do not exist.

The system of equations assumes oscillatory motion of electrons only against the background of stationary ions. Additional consideration of ion motion leads to accounting for the ponderomotive force, which introduces a correction to the nonlinear term. Electron drift occurs along the x axis with velocity u_d. The magnetic field is directed along the z axis. A wave perturbation propagating along the drift direction (axis x) perpendicular to the magnetic field is sought. The system of equations includes

1. electron motion equations along the axes x and y:

$$m_e n_e \frac{dV_e}{dt} = en_e\left(E + \frac{1}{c}H\right) - \nabla p_e; \tag{1}$$

continuity and Poisson equations

$$\begin{gathered} \frac{\partial n_e}{\partial t} + \nabla(n_e V_e) = -eD\nabla^2 n_e, \\ \frac{\partial E_x}{\partial x} = n_{i0} - n_e; \end{gathered} \tag{2}$$

2. two Maxwell equations introducing electromagnetic corrections:

$$\begin{gathered} \operatorname{rot} \quad H = \frac{4\pi}{c} j, \\ \operatorname{rot} \quad E = -\frac{1}{c}\frac{\partial H}{\partial t}. \end{gathered} \tag{3}$$

In quasi-one-dimensional consideration, all quantities depend only on the coordinate x and time t taking into account changes in electron velocities along the axes x and y, magnetic field components H_z and electric field E_x and E_y. Additionally, non-uniformity along the axis x of electron gas density is assumed

$$\gamma_n = \frac{\partial \ln(n_e(x))}{\partial x}.$$

The modeling is based on expansion in a small parameter of the system of equations in dimensionless form. Variables are normalized to corresponding constants: time t to inverse plasma frequency ω_{pe}^{-1}, spatial coordinate – to Debye radius r_D, velocities — to electron thermal velocity. The Krylov–Bogolyubov–Mitropolsky expansion method [12, 13] allows obtaining the dispersion equation and Ginzburg-Landau equation for the amplitude of the electric field wave perturbation.

In paper [14], when considering two-fluid plasma in the 5-moment approximation, it was found that the ECR dispersion relation has two asymptotic solutions. One of them is similar to the ion-sound mode, while the other agrees with the dispersion relation obtained in our expansion. This mode is defined in this work as a relation for Doppler-shifted "hybrid" waves. The authors suggest that the waves arise at the intersection of these two branches of the dispersion curve, forming the resulting nonlinear response. The system of equations used in the present work is supplemented so that the dispersion relation obtained in this work includes two corrections. One is determined by accounting for electromagnetic perturbations (two Maxwell equations). The other correction is introduced as a dissipative term to account for the role of dissipation in the formation of nonlinear wave structure. This dissipative term is similar to the term in equation (25) of paper [15] – the continuity equation. This is a diffusion term $D\nabla_{\perp}^2 n$, where the diffusion coefficient $D = \nu\rho_e$ depends on the electron Larmor radius ρ_e and their collision frequency ν with both ions and the neutral component. The focus on diffusion when considering plasma formation dynamics is also related to the fact that in paper [9], when analyzing numerical simulation results, diffusion leading to the smearing of resonances is assigned the main role in forming the frequency spectrum.

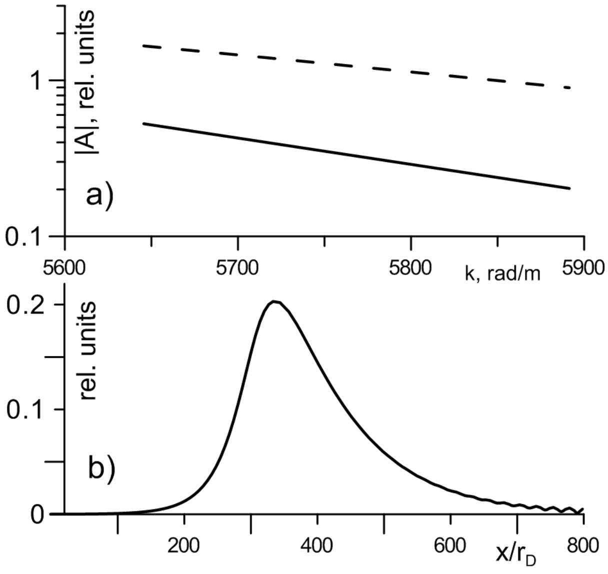

Fig. 1. *a* — Amplitude of the exact solution (solid line) and analytical estimate (dashed line). *b* — Example of soliton shape lence.

The real frequency in dimensionless variables is found from equation (4):

$$\mathrm{Disp} = -(\omega - ku_d)^2 + k^2 + 1 +$$
$$+ \frac{\omega_{ce}^2 / \omega_{pe}^2}{1 + (V_{Te}^2 / c^2)/k^2} + \Delta D' = 0. \quad (4)$$

The imaginary frequency component λ determines the correction

$$\Delta(D') = 3\lambda^2 + 2\lambda D' k^2,$$

associated with the diffusion coefficient D' (in dimensionless form).

The resulting equation can be considered as a nonlinear Schrödinger equation or complex Ginzburg–Landau equation with additional terms with coefficients $c_{1'}$, $c_{2'}$, the second of which represents the coefficient of the nonlocal integral term:

$$iA_t + PA_{xx} + Q|A|^2 A = i\delta' A + i\beta' A_{xx} +$$
$$+ i\varepsilon' |A|^2 A - c_{1'}A_x - c_{2'}A\int_{-\infty}^{x} e^{\gamma(x'-x)} |A|^2 dx'. \quad (5)$$

The reduction A_{xx} corresponds to $\partial^2 A / \partial x^2$; A_t corresponds to $\partial A / \partial t$ and so on. The coefficient P equals

$$P = \frac{1}{2}\frac{\partial V_g}{\partial k}.$$

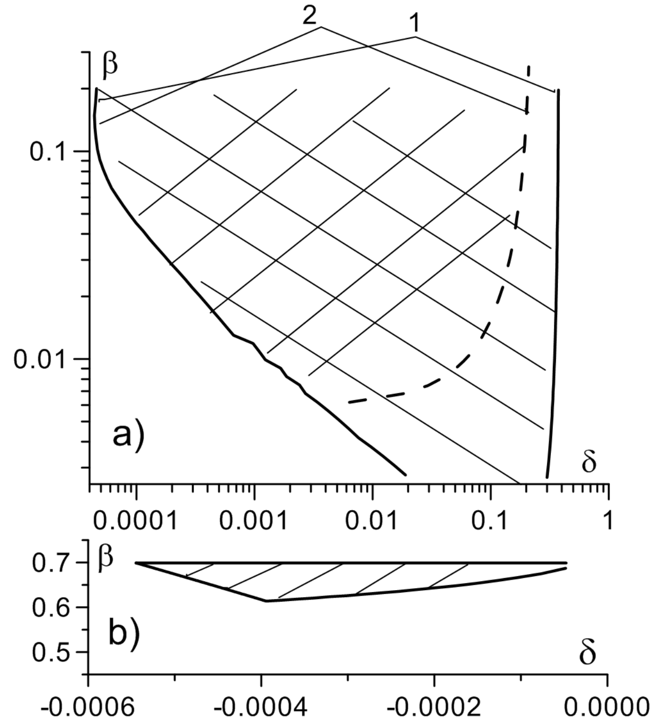

Fig. 2. Boundaries of parameter regions where soliton turbulence is realized: *a* – at plasma concentration 5×10¹¹ cm⁻³ and two drift velocity values; *b* – at plasma concentration 5×10⁹ cm⁻³:

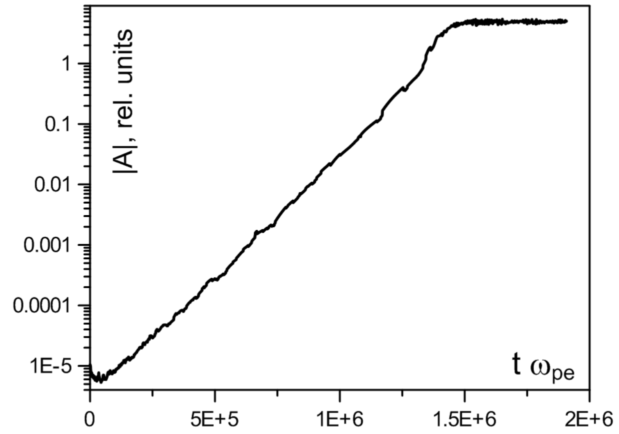

Fig. 3. Time dependence of average oscillation amplitude |A|

The coefficient δ' is determined by the difference of terms proportional to the density gradient and electron collision frequency; coefficients β' and ε' are determined by the diffusion coefficient; coefficient c_1 is determined by the electron collision frequency. All these coefficients depend on the wave vector. The exact form of the expressions defining the coefficients is not provided since some of them are quite cumbersome. Further consideration is conducted only for wave vector values corresponding to the anomalous dispersion of the equation.

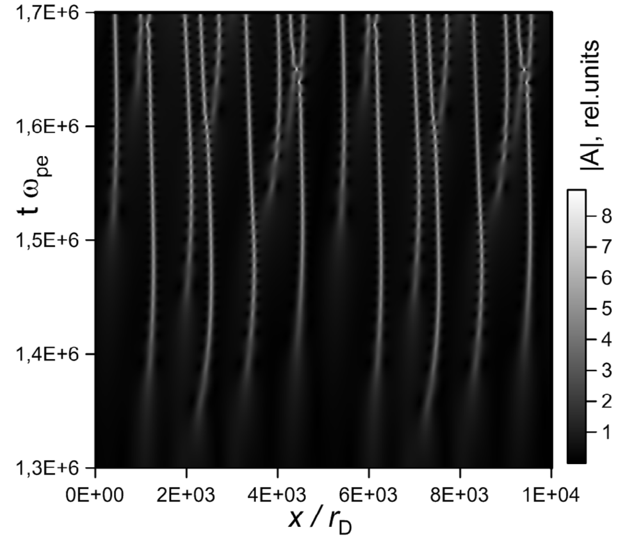

Fig. 4. Numerical solution of system (6)

An equation of this type is the simplest equation describing the system near the turbulence threshold. For the wave vector region corresponding to anomalous dispersion, the equation describes the subcritical bifurcation area, where above a certain plasma density gradient threshold, the fluctuation regime changes abruptly, and turbulence emerges (see [16] and literature cited therein). In the area near the bifurcation threshold, the formation of soliton turbulence is possible.

The analysis of CGL regimes is typically carried out for the equation form normalized so that

$$P = \pm\frac{1}{2}, \quad Q = \pm 1.$$

Under standard normalization transformation, the equation is reduced to a form depending on fewer parameters:

$$iA_t + A_{xx} + |A|^2 A = i\delta A + i\beta A_{xx} +$$

$$+i\varepsilon |A|^2 A - c_1 A_x - c_2 A \int_{-\infty}^{x} e^{\gamma(x'-x)} |A|^2 \, dx'. \quad (6)$$

In this form, the main factors affecting the solution become δ and β. Many authors have studied the equation in this form. The stabilizing role of nonlocal (integral) terms of various types in CGL has been analyzed in recent years in works [19–21]. Additional dissipative and nonlocal terms in our derived equation suggest the possibility of soliton turbulence formation. To estimate the amplitudes of emerging solitons, works [22,23] were used with a somewhat different integral term $A\int_{-\infty}^{x}|A|^2dx$ in the auto-soliton generation mode [24,25]. The exact semi-analytical solution was obtained using the method proposed in work [26]. Comparing it with the analytical estimate shows that such an estimate gives several times overestimated soliton amplitudes and does not account for their shape distortion. However, these solutions allow estimating the range of plasma parameters where stable solitons exist (soliton stability was evaluated using the method described in works (27, 28), and estimating their amplitudes and wave vectors. The stable soliton regime is only realized for fluctuations with wave vectors $k > k_s$, where $k_s^2 \sim \delta/\beta$. Thus, this solution applies only to short-wave turbulence.

Comparison of analytically estimated amplitudes and amplitudes of the exact solution is shown in Fig. 1*a*. The solid line represents exact solution amplitudes, the dashed line represents analytical estimate. Fig. 1*b* shows an example of soliton shape. The exponential in the integrand of the integral included in equation (6) leads to soliton shape distortion and frequency shifts.

The stability limits determine the lower boundary of soliton wave vectors in Fig. 1*a*. The asymmetric shape of solitons (see Fig.1*b*) is determined by the density gradient value.

Fig. 2 shows the regions of soliton turbulence existence depending on two defining parameters δ and β. In Fig. 2*a* these regions are shown for plasma typical for magnetrons, with large magnetic and electric fields and high ionization level. In this case, the plasma has the following parameters: $n_e = 5\cdot 10^{11}$ cm^{-3}; $u_d / v_{Te} = 0.02$ (shaded area within boundaries 1) and $u_d / v_{Te} = 2.0$ (shaded area within boundaries 2). To the right of this region, chaotic turbulence forms. The main conclusion that can be drawn from this graph: soliton turbulence occurs only with small deviations of from zero, and with increasing electric field, the region of soliton turbulence implementation decreases and partially transitions into chaotic. Figure δ shows the region of soliton turbulence realized under parameters corresponding to space experiment conditions. In this case $n_e = 5\cdot 10^{9}$ cm^{-3}, $u_d / v_{Te} = 0.002$. Under these conditions, soliton turbulence is realized at $\delta < 0$. Under these conditions, soliton turbulence is realized at. Solitons have negative group velocity.

3. NUMERICAL CALCULATIONS

To confirm the possibility of forming a sequence of solitons in the system described by the above equation, numerical calculation was performed to reach stable solutions from initial chaotic perturbation of small amplitude at system parameter values corresponding to the region of stable solitons, in particular, at point $\delta = 0.0773$, $\beta = 0.0176$, lying in the region of soliton turbulence on the plane of Fig. 2*a*. Equation (6) was solved on a segment of length $L / r_D = 10^4$ Equation (6) was solved on a segment of length $-0.765\cdot 10^{-2}$.For the approximation of spatial derivatives, a compact differencing scheme was used (see, for example, [29]) with periodic boundary conditions. A small initial perturbation was set as random oscillations with frequencies within the Nyquist frequency. For time integration, a 6th order Runge–Kutta method was used. Figure 3 shows the time dependence of the average oscillation amplitude on the considered segment. During the shown time $t\omega_{pe} \approx 10^6$ the amplitude of forming solitons stabilizes. The dependence $|A(x,t)|$ obtained from solving system (6) is shown in Fig. 4. Formation of soliton structures with limited amplitude is observed.

4. CONCLUSION

Thus, the paper shows the possibility of formation of small-scale wave structures of ECD. This consideration allows finding the parameter region where soliton turbulence and associated anomalous plasma transport are formed. Obtaining these criteria for soliton turbulence can help both in numerical modeling of collisionless plasma expansion in the ionosphere and in analyzing experimental data on such expansion.

FUNDING

The work was carried out within the State Assignment No. 122032900184-8.

REFERENCES

1. N. Brenning, Space Sci. Rev. 59, 209 (1992).
2. C. M. Swenson, M. C. Kelley, F. Primdahl et al., Geophys. Res. Lett. 17, 2337 (1990).
3. O. Bolin, N. Brenning, C.M. Swenson et al., J. Geophys. Res. A 101, 19729 (1996).

4. N. Brenning, R.L. Merlino, D. Lundin et al., Phys. Rev. Lett. 103, 225003 (2009).

5. N. Brenning and D. Lundin, Phys. Plasmas 19, 093505 (2012).

6. O. Koshkarov, A. Smolyakov, Y. Raitses et al., Phys. Rev. Lett. 122, 185001 (2019).

7. K. Hara and S. Tsikata, Phys. Rev.E 102, 023202 (2020).

8. A. Smolyakov, T. Zintel, L. Kedel et al., Plasma Physics 46, 408 (2020).

9. S. Janhunen, A. Smolyakov, O. Chapurin et al., Phys. Plasmas 25, 011608 (2018).

10. A. Ducrocq, J. C. Adam, A. Heron et al., Phys. Plasmas 13, 102111 (2006).

11. S. I. Popel, S. V. Vladimirov, and V.N. Tsytovich, Phys. Rep. 259, 327 (1995).

12. T. Kakutani and N. Sugimoto, Phys. Fluids 17, 1617 (1974).

13. A. Nayfeh, Introduction to Perturbation Methods, Mir, Moscow (1984).

14. L. Wang, A. Hakim, B. Srinivasan et al., arXiv: 2107. 09874v2 [physics.plasm-ph] (2022).

15. A. Smolyakov, O. Chapurin, W. Frias et al., Plasma Phys. Control. Fusion 59, 014041 (2017).

16. I. S. Aranson and L. Kramer, Rev. Mod. Phys. 74, 99 (2002).

17. V. E. Zakharov, A. N. Pushkarev, V. F. Shvets et al., JETP Letters 48, 79 (1988).

18. A. I. Dyachenko, V. E. Zakharov, A. N. Pushkarev et al., JETP 96, 2026 (1989).

19. M. Golles, S. Darmanyan, F. Lederer et al., Opt. Lett. 25, 293 (2000).

20. A. Picozzi and J. Garnier, Phys. Rev.Lett. 107, 233901 (2011).

21. S. Wabnitz, Opt. Lett. 20, 1979 (1995).

22. V.S. Grigoryan and T. S. Muradyan, J. Opt. Soc. Amer. B 8, 1757 (1991).

23. S. K. Turitsyn, Phys. Rev. E 54, R3125 (1996).

24. B. S. Kerner, V. V. Osipov, Phys. Usp. 154, 201 (1989).

25. B. S. Kerner, V. V. Osipov, Phys. Usp. 160, 2 (1990).

26. J. M. Soto-Crespo, N. Akhmediev, and K. S. Chiang, Phys. Lett. A 291, 115 (2001).

27. N. Akhmediev and J. M. Soto-Crespo, Phys. Lett. A 317, 287 (2003).

28. N. Akhmediev, A. Ankiewicz, Dissipative Solitons, Fizmatlit, Moscow (2008).

29. S. K. Lele, J. Comput. Phys. 103, 16 (1992).

JOURNAL OF EXPERIMENTAL AND THEORETICAL PHYSICS, 2024, Vol. 165, No. 6, pp. 888–899

STUDY OF DENSE LEAD PLASMA

© 2024 E. M. Apfelbaum, A. M. Kondratyev, A. D. Rakhel*

Joint Institute for High Temperatures of the Russian Academy of Sciences 125412, Moscow, Russia

**e-mail: rakhel@oivtran.ru*

Received January 12, 2024
Revised January 30, 2024
Accepted January 30, 2024

Abstract. The thermodynamic functions and electrical resistivity of dense lead plasma were assessed at specific volumes ranging from 5 to 20 times greater than the standard value, under pressures between 0.4 and 4.0 hPa, and with specific internal energies 3 to 18 times higher than the energy required for sublimation. The recorded dependencies were later evaluated against those estimated through a classical plasma chemical model. This research aimed to uncover the effects of non-ideality on the thermodynamic characteristics and resistivity behavior of plasma. A significant finding was that the Grüneisen coefficient for this plasma varied between 0.2 and 0.4 across the entire range of states examined. Findings from the research showed that the chemical model did not accurately reflect the energy expenditure for plasma ionization and atom excitation, underestimating it by close to a factor of two, while also overestimating the temperature by a similar proportion. The inquiry additionally disclosed that in the whole spectrum of plasma states being analyzed, "pressure ionization" was a key element, and that resistivity lessened with a decrease in specific volume along isotherms.

Keywords: *strongly coupled plasma, Grüneisen coefficient, ionization state, the caloric properties, the sound speed, the virial theorem*

DOI: 10.31857/S004445102406e154

1. INTRODUCTION

The study of dense plasma with an ionization degree of order unity encounters serious difficulties from both theoretical and experimental perspectives. Theoretical problems are associated with the fact that for such a system, the interaction parameter, i.e., the ratio of Coulomb interaction energy between plasma particles to their kinetic energy, takes values of order unity. In this case, the application of perturbation theory using ideal gas as an unperturbed system is fairly difficult.

Experimental difficulties in studying dense plasma with developed ionization are associated with high temperatures and pressures at which such plasma can exist and which are unattainable in static experiments for the vast majority of elements in the periodic system. Various dynamic experimental methods are used to study such plasma [1–4]. However, for these experiments, questions remain open about the homogeneity of the obtained plasma and the reliable estimation of measurement uncertainties [5]. Comparison of the specific resistance values of aluminum plasma measured in experiments [4] with the results of a more accurate technique [6] showed that measurement errors [4] are 20–30% (see Fig. 7 of work [6]). The error of experiment [2] is of the same order of magnitude, as follows from the comparison presented in Fig. 5 of work [7]. Such large measurement uncertainties did not allow identifying the characteristic properties of non-ideal plasma associated with strong interaction between particles.

To study the properties of metals in liquid state and supercritical fluid state, a dynamic experimental method was developed [8], which allows measurements with accuracy not worse than 3–5 % (depending on the measured value). Using this method, measurements of thermodynamic functions and specific electrical resistance of lead [9], as well as lead-bismuth eutectic [10] were conducted for a wide range of states on the *VP*

(V — specific volume, P — pressure). Based on the obtained data, caloric equations of state (EOS) of these fluids were constructed and critical points of liquid-gas transition and metal-nonmetal transition were estimated [10]. A significant feature of such EOS is that its accuracy depends only on the error of experimental data, based on which two characteristic functions are determined: the dependence of the Grüneisen coefficient and the cold component of internal energy on specific volume. Since in each individual experiment [9, 10] the dependence of specific internal energy of the sample on specific volume and pressure is measured along some line on the *VP*-plane (which extends from the normal state), rather than at a single point on the shock adiabat or unloading isentrope, as is the case in shock-wave experiments [11], this allows for sufficiently accurate analysis of isochore behavior in the *PE -plane* (E – specific internal energy). Based on such analysis, a general pattern was established: within measurement error, these isochores are straight lines. This fact made it possible to establish the form of function *P(V, E)*, i.e., the caloric EOS, based on general thermodynamic relations [12], and also to measure with necessary accuracy the dependencies of the Grüneisen coefficient and cold component of internal energy on relative volume [9,10]. This eliminates the need to make assumptions about the form of these dependencies [11].

Measurement errors [9, 10] for the range of specific volumes close to the normal value, for which accurate literature data is available, were reliably estimated and proved to be no worse than 3 %. However, for the region of states $P > 0.3$ hPa, $V > 4V_0$ (V_0 – normal value of specific volume of the studied metal) there is no literature data. To estimate the systematic error of experiments in this region of states, a method was developed for direct measurement of shock wave velocities excited in the sample during the dynamic experiment. Since the shock adiabat of the studied metal can be determined using a pre-constructed caloric EOS, and the accuracy of the latter, as noted above, depends only on the accuracy of experimental data, then by comparing the measured shock wave velocities with values calculated using EOS, it is possible to estimate the systematic measurement error at large values of sample specific volume and pressure. Such work was performed in experiments with lead [13], and measurement errors were estimated for the volume range $V/V_0 = 2 - 7$ and pressure range $P = 0.4 - 3.4$ hPa. In this work, experimental data on the properties of dense lead plasma for the region of states $V/V_0 = 6 - 20$, $P = 0.4 - 4$ hPa are presented.

To interpret the results of these experiments, a chemical plasma model (CPM) [14,15] was used. In this model, plasma is considered as an equilibrium mixture of neutral atoms, positive ions with charges $ze = 1–4$ (e — elementary charge, z — ionization degree) and electrons. The free energy of plasma is represented as the sum of the free energy of an ideal gas of such particles and three terms that describe three types of interactions between them: interaction between charged particles, between charged particles and atoms, and interaction between atoms. Note that ions in this model are considered as point-like classical particles, and the contribution to free energy from interactions between ions, as well as between ions and free electrons, is described using an analytical dependence [16]. Charge-atom and atom-atom interactions are described considering only pair interactions, i.e., up to the second term of the virial expansion. Minimization of free energy with respect to the numbers of particles of all types allows determining the plasma composition (at given values of temperature, volume, and total number of atoms). After calculating the plasma composition, its thermodynamic functions can be determined, which are obtained by differentiating free energy as a function of specific volume and temperature. The resistivity of plasma was calculated within the relaxation time approximation [14]. Since the CPM used here has already been described in detail [14,15], we will not discuss it here. We only note that, strictly speaking, this model can be applied to describe relatively low-density plasma, when it is possible to determine with sufficient accuracy such composite particles as molecules, isolated atoms, or ions. However, despite the limited range of applicability, chemical plasma models allow obtaining qualitatively correct results even for the region of states where the interaction parameter is not small [17, 18].

In this work, measurements of thermodynamic functions and specific resistance of lead were carried out for the region of states where specific volume, temperature, and pressure exceed the values at the critical point of the liquid-gas phase transition. As known, the states of matter where temperature and pressure exceed critical values is called a supercritical

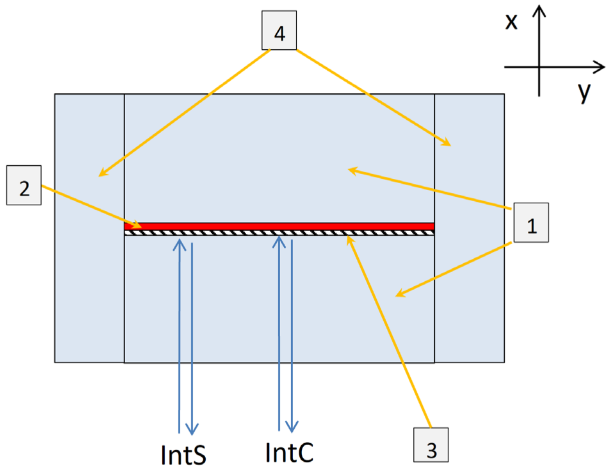

Fig. 1. Cross-sectional diagram of the experimental assembly by a plane perpendicular to the electric current direction: window material plates (*1*); sample (*2*); side plates of technical glass (*4*). The direction of the two laser interferometer beams (IntC, IntS) is shown, as well as the dielectric mirror (*3*) from which the interferometer beams are reflected (mirror is applied to the plate surface)

fluid. In this work, consequently, we will deal with gaseous supercritical fluid. Such fluid, as will be shown below, has relatively low resistivity: its values are only 2–6 times higher than the specific resistivity of liquid lead in metallic state near the Mott-Ioffe-Regel limit [9]. Thus, there is good reason to call such supercritical fluid a dense plasma. The main goal of this work was to discover characteristic features of dense plasma (in thermodynamic functions and specific resistance behavior) related to strong interaction between particles.

In case of classical plasma, where electron degeneracy and quantum scattering effects are insignificant, the interaction parameter is usually taken as the ratio of potential energy of electrostatic repulsion between neighboring ions located at average distance from each other (without considering correlations) to their average kinetic energy. If we denote the average number of ions per unit volume as n_j, then the average distance between them will be of order $n_i^{-1/3}$, and their average kinetic energy, according to equipartition law, will be of order of temperature. For the coupling parameter, which we will denote by Γ, we get the expression

$$\Gamma = \frac{z^2 e^2}{kT} n_i^{1/3}, \tag{1}$$

where T is temperature, k is Boltzmann constant. For lead plasma studied in this work, $nj = (1 - 8) \cdot 10^{21}$ cm^{-3}, $T = 10 - 40$ kK, $z = 1 - 2$, $\Gamma = 0.5 - 5$. In this case, the ionic component of plasma is not degenerate, and the degeneracy parameter of the electronic component $\vartheta = kT / \varepsilon_F$ takes values $\vartheta = 1 - 10$, where ε_F is Fermi energy, which is determined according to formula

$$\varepsilon_F = \frac{n^2}{2m}\left(3\pi^2 n_e\right)^{2/3}, \tag{2}$$

where m is electron mass, n_e is average number of electrons per unit volume.

2. DESCRIPTION OF THE EXPERIMENTAL TECHNIQUE

For measurements, the experimental technique developed in works [9,10] was used. Let us note only some changes that were introduced during the execution of this work. After the systematic error of such measurements was evaluated at large values of specific volume of the sample [13], it became possible to study the properties of metals in gaseous state. Lead was chosen as the sample material for studying dense plasma because samples of required thickness and quality for our experiments (foil strips) could be manufactured in the laboratory. In this case, the foils had to be made sufficiently thin (9–15 μm). This is necessary to maintain uniform heating of the sample and its one-dimensional thermal expansion even at large volume values. This requires meeting two conditions: the sample thickness should be small compared to its width and length (which were about 10 mm for these experiments), and the substance velocity should be small compared to the speed of sound. Since the measurement time for such experiments is about 1 μs and is actually determined by the geometric dimensions of the window plates, obtaining large thickness increments of the sample during this time, at relatively low velocities, imposes an upper limit on its initial thickness. Lead was also chosen because experimental data on the properties in the liquid state had been previously obtained [9, 13], and this allowed for a more accurate assessment of the errors in the present measurements.

To control the one-dimensionality of the sample's thermal expansion at high volume values, two interferometers were used simultaneously

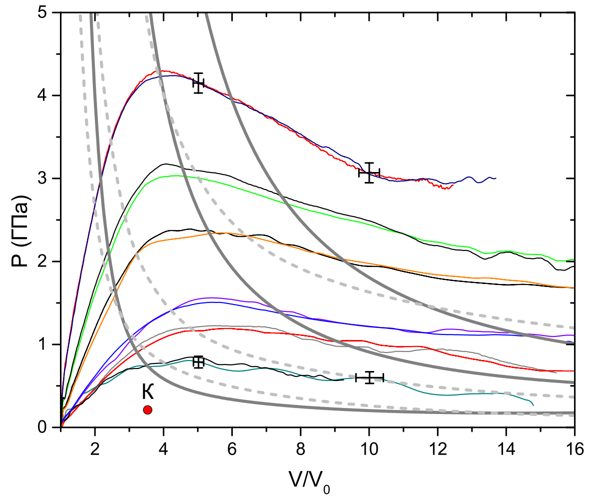

Fig. 2. State region on the *VP*-plane, for which measurements of thermodynamic functions and specific resistance of lead fluid were performed. The family of lines emerging from the normal state represents quasistatic processes under which measurements were conducted. The critical point (*K*) and isentropes (three thick solid gray lines) were obtained using EOS from work [13]. Dashed gray lines are isotherms T = 20, 30, 50 kK, EOS from work [11]. Crosses show measurement uncertainties

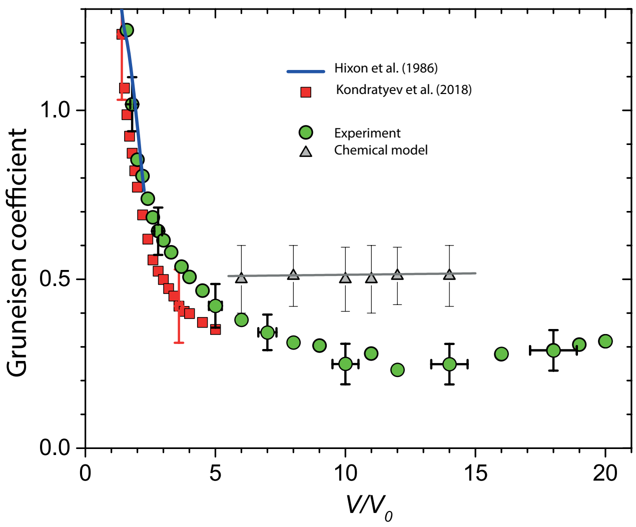

Fig. 3. Grüneisen coefficient of lead fluid as a function of relative volume. The experimental data obtained in this work (green circles) are compared with measurement results from works [9] (red squares) and [19] (blue line), as well as with calculations using SHM (gray triangles and the straight line approximating these values). For experiments, crosses indicate measurement errors, and for the model - the range of Grüneisen coefficient variation for a specific relative volume value

in the present experiments. The cross-sectional diagram of the sample and the interferometer arrangement are shown in Fig. 1. The beam of one interferometer (IntC) was reflected from the central part of the sample surface, while the spot of the second interferometer (IntS) was shifted sideways by 2–3 In these experiments, two window plates with dimensions of $5 \times 10 \times 10$ mm^3 were used. The glued experimental assembly, consisting of two window plates, sample, and side plates of technical glass, represented a rectangular parallelepiped with two edges having a length of about 10 mm, and the third one (which is parallel to the axis in Fig. 1) – 16 mm. In all experiments, the width and length of the sample were equal to the width and length of the 10 mm, window plates, respectively. Such assembly allowed maintaining practically one-dimensional deformation of the window material plates during time $t \leq 2D / c_l$, where D — is the plate thickness, and c_l — is the longitudinal sound velocity in the window material. The present experiments showed that the relative difference between the sample surface displacements easured by the two interferometers did not exceed 2% up to the maximum sample volume values.

The region of states on the *VP*-plane, for which measurements of thermodynamic functions and resistivity of supercritical lead fluid were performed, is shown in Fig. 2. Previously, it was discovered that when liquid lead is heated under pressure of 0.5-4 hPa, it undergoes a metal-nonmetal transition near the relative volume value $V/V_0 \approx 4$, which practically coincides with the critical volume value of the liquid-gas transition [10, 13]. This critical point is marked in Fig. 2. As shown in the figure, for supercritical volume values, measurements were conducted at supercritical pressures and, consequently, at supercritical temperatures. It is also evident that the state region studied in this work is significantly expanded compared to work [9], which obtained data for the volume interval $V/V_0 \leqslant 5$. To characterize in more detail the quasi-static processes under which measurements were conducted in present experiments, Fig. 2 shows three isentropes, obtained using EOS from work [13]. For this EOS, characteristic functions were determined based on the entire set of experimental data for lead, including data from this work. Fig. 2 also shows three isotherms of the interpolation EOS [11]. As shown in the figure, in the region of supercritical volumes for experiments with pressure

$P < 1$ hPa, these processes are close to isothermal, and for experiments with pressure $P > 1$ hPa — to isobaric.

3. MEASUREMENT RESULTS

Figure 3 shows the measurement results obtained in this work for the dependence of the Grüneisen coefficient on relative volume. These results are compared with experimental data from works [9] and [19], as well as with results obtained by the CPM. The Grüneisen coefficient, which we denote as Υ, is defined by the formula

$$\gamma = \left(\frac{\partial PV}{\partial E}\right)_V. \tag{3}$$

The value of the Grüneisen coefficient for a certain specific volume was determined by the method of least squares of the data points *PV, E*, obtained for this volume in all experiments of the present work. It was verified that specifically linear approximation (rather than a higher-degree polynomial) is the most accurate.

From Figure 3, it follows that in the volume range $V/V_0 = 6 - 14$ our model predicts an almost constant value of the Grüneisen coefficient, being close to the value 2/3, which this coefficient takes for a monatomic ideal gas of constant composition. However, the values calculated using chemical model (which were determined for the same ranges of energy and pressure values as in the experiment) in the interval $V/V_0 = 10 - 14$ are almost twice the measured values. As seen in Figure 3, the difference between calculated and measured values is minimal at volumes $V/V_0 = 5 - 6$, for which our chemical model is, strictly speaking, not applicable.

The decrease in the Grüneisen coefficient to values less than 2/3 can be explained by the presence of strong interaction between charged plasma particles and ionization (composition change). Let us show that for plasma with strong Coulomb interaction, the inequality $\gamma < 2/3$ must be satisfied. For simplicity, we will assume that the plasma is fully ionized. Using the expression for the free energy of weakly non-ideal classical plasma [20], we find

$$\gamma = \frac{2}{3} - \frac{\sqrt{2\pi}}{9}\Gamma^{3/2}, \tag{4}$$

from which it follows that in this case, the inequality $\gamma < 2/3$ is indeed satisfied. This formula is derived for weakly non-ideal plasma ($\Gamma \leqslant 1$), but if we use it to estimate the Grüneisen coefficient at values $\Gamma \approx 1$, we obtain values $\gamma \approx 0.3$. Therefore, we can expect that strong electrostatic interaction between plasma particles leads to a decrease in the Grüneisen coefficient to the observed values.

Let us now show that for plasma in which ionization occurs, the Grüneisen coefficient also becomes less than 2/3. For simplicity, let's consider ideal plasma at temperatures where only single ionization of atoms occurs. In this case, the formulas for pressure and specific internal energy of plasma will take a relatively simple form:

$$PV = \frac{R}{A}\left[1 + \alpha(T)\right]T, \tag{5}$$

$$E = \frac{3}{2}PV + \frac{N_A}{A}I_1\alpha(T), \tag{6}$$

where R is the gas constant, A is the molar mass of gas, N_A is Avogadro's number, I_1 is the first ionization potential, α — the degree of gas ionization. The degree of ionization is determined according to the relation $\alpha = n_e/n_n$, where n_n is the total number of atoms per unit volume (i.e., the sum of ionized and neutral atoms). Substituting expressions (5), (6) into formula (3), for the Grüneisen coefficient we obtain

$$\gamma = \left[\frac{3}{2} + \frac{\frac{I_1}{k}\left(\frac{\partial \alpha}{\partial T}\right)_V}{\left(\frac{\partial \alpha}{\partial T}\right)_V + \alpha + 1}\right]^{-1}. \tag{7}$$

Since the degree of ionization increases with temperature at constant volume, the second term in brackets is always positive, and consequently, $\Upsilon < 2/3$. It should be noted that in deriving formula (7), we neglected the energy contribution from atomic excitations, assuming that ionization occurs from the ground state of the atom. However, if such contribution is considered, it is obvious in advance that it will also lead to a decrease in the Grüneisen coefficient.

Thus, the fact that our measured values of the Grüneisen coefficient are significantly lower than may indicate both strong interaction between lead

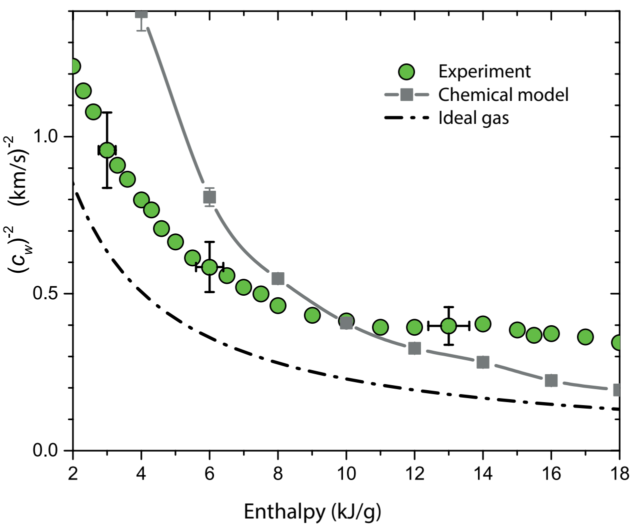

Fig. 4. Isenthalpic compressibility of supercritical lead fluid as a function of specific enthalpy. Green circles – experiment, solid gray line with markers – CPM, dash-dotted black line – dependence calculated for ideal gas. For experiments, crosses indicate measurement errors, and for the model – the range of isenthalpic compressibility variation at a certain enthalpy value

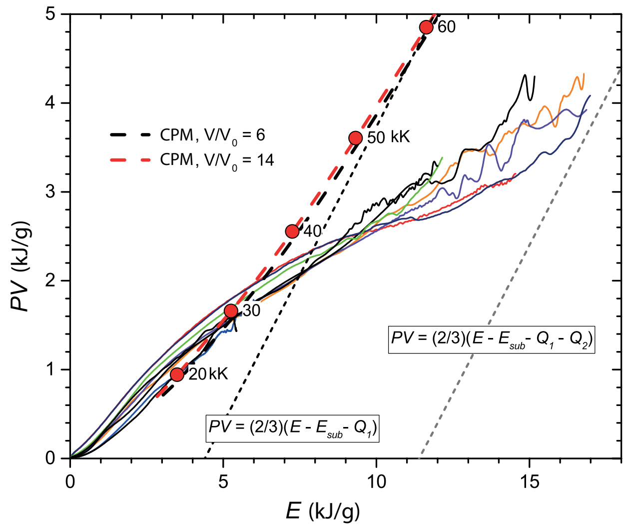

Fig. 5. Measured dependencies of PV on E (thin solid lines starting from the origin) are compared with dependencies calculated using CPM for two isochores (thick black and red dashed lines), red circles indicate calculated temperature values (in kK) on the isochore $V/V_0 = 14$. Thin dashed lines show dependencies for singly ($\alpha = 1$) and doubly ($\alpha = 2$) ionized ideal lead gas of constant composition

plasma particles and the process of developed ionization. Since accurate calculation of the ionization degree of such plasma requires correct description of the particle interaction influence on ionization potential reduction, shifts in atomic electron levels, and electron transition probabilities between atoms, this problem cannot be solved within the CPM framework. The interpretation of the dense plasma Grüneisen coefficient behavior observed here, which follows from very general considerations, will be given in the next section.

Let us consider another thermodynamic quantity that is directly determined from the results of present experiments and characterizes mechanical properties of plasma. This refers to the partial derivative of density with respect to pressure at constant enthalpy: $(\partial\rho/\partial P)_W$, where $\rho = V^{-1}$ is density, and the letter W will denote specific enthalpy. This derivative, which we will call isenthalpic compressibility, is conveniently expressed through the isenthalpic sound velocity c_w, which we define according to the formula

$$c_w{}^2 = \left(\frac{\partial P}{\partial \rho}\right)_W. \tag{8}$$

The usual sound velocity c_s (isentropic) is related to c_w by the relation

$$c_s = (\gamma + 1)^{1/2} c_w. \tag{9}$$

Figure 4 shows the dependence of isenthalpic compressibility of supercritical lead fluid on specific enthalpy. As seen in Fig. 4, within measurement uncertainty, this quantity is a function of a single variable – enthalpy and, consequently, practically does not depend on pressure. The values calculated using CPM also fall well on a single line. However, the compressibility values obtained using the model differ significantly from measurement results: at low enthalpy values, these values are almost twice higher than measured values, and at enthalpy values of 16–18 kJ/g, they are almost twice lower. Note that in the range $W > 14$ kJ/g, the calculated compressibility values are close to those for ideal gas (where gas enthalpy is measured from the normal state of solid body).

The fact that CPM predicts significantly higher compressibility at low enthalpy values, which correspond to low specific volumes for these experiments, can be explained by the fact that in this model, ions are point-like and repulsion associated with their finite size is absent. Note that the enthalpy value of 5 kJ/g was achieved in these experiments at volumes $V/V_0 = 4–8$. The relatively low values of isenthalpic compressibility predicted by CPM at high enthalpy values are explained by

Table 1. Measured values in this work of pressure P (hPa), specific internal energy E (kJ/g) and specific resistance σ^{-1} (μΩ•m) of supercritical lead fluid on isochores $V/V_0 = 5, 6, 8, 10, 12, 14, 18$

V/V_0	P	E	σ^{-1}	V/V_0	P	E	σ^{-1}
5	4.16	5.44	15.43	10	3.05	11.55	15.01
5	4.16	5.42	15.38	10	3.07	11.37	15.07
5	3.00	3.84	20.56	10	2.44	7.23	19.06
5	2.32	3.33	23.50	10	1.98	6.13	21.61
5	2.45	3.18	24.28	10	1.98	6.00	22.29
5	2.39	3.34	23.47	10	1.98	6.01	22.31
5	2.37	3.20	23.92	10	1.93	5.88	21.82
5	1.49	2.48	32.15	10	1.93	5.69	23.19
5	1.38	2.54	31.04	10	1.22	3.98	37.67
5	2.36	3.28	23.78	10	1.21	3.96	37.06
5	1.16	2.06	33.78	10	1.03	3.40	50.37
5	1.08	2.08	37.22	10	0.91	3.04	58.98
5	1.21	2.16	36.17	10	0.96	3.26	52.91
5	1.25	2.15	35.95	10	1.00	3.24	50.47
5	0.79	1.84	44.66	10	0.60	2.33	97.96
5	0.84	1.90	41.71	12	2.97	14.22	15.02
5	0.82	1.70	42.32	12	2.92	13.95	15.06
6	3.94	6.65	15.40	12	2.23	8.48	18.63
6	3.98	6.59	15.36	12	1.83	7.12	20.79
6	2.91	4.61	20.43	12	1.85	6.98	21.49
6	2.34	4.00	23.72	12	1.85	6.93	21.25
6	2.36	3.83	24.79	12	1.79	6.81	21.10
6	2.34	3.96	23.85	12	1.79	6.45	22.34
6	2.32	3.85	23.89	12	1.12	4.42	35.55
6	2.28	3.87	24.18	12	1.14	4.38	36.34
6	1.49	2.86	35.40	12	0.92	3.69	51.47
6	1.40	2.90	34.35	12	0.80	3.18	62.81
6	1.19	2.40	41.20	12	0.94	3.38	57.21
6	1.09	2.38	44.45	12	0.79	3.51	51.29
6	1.22	2.51	42.25	12	0.39	2.41	114.37
6	1.21	2.49	41.59	14	2.17	9.91	18.55
6	0.68	2.02	56.85	14	2.13	9.75	18.47
6	0.76	2.07	53.91	14	1.78	8.08	20.21
	0.75	1.86	56.64	14	1.75	7.95	20.81
8	3.54	8.99	15.18	14	1.74	7.84	21.03
8	3.50	8.88	15.22	14	1.72	7.73	20.54
8	2.65	5.97	19.65	14	1.73	7.15	21.95
8	2.15	5.12	22.77	14	1.11	4.81	34.51
8	2.13	4.97	23.53	14	1.13	4.73	35.60
8	2.13	5.04	23.39	14	0.74	3.99	50.57
8	2.17	4.90	22.83	14	0.67	3.27	65.90
8	2.10	4.86	23.31	14	0.79	3.48	59.63
8	1.33	3.47	37.17	14	0.40	2.48	129.89
8	1.32	3.49	36.78	18	2.14	12.16	18.45
8	1.11	2.97	48.15	18	1.67	10.02	19.56
8	0.98	2.78	53.68	18	1.60	9.90	20.12
8	1.07	2.96	49.35	18	1.64	9.67	20.00
8	1.16	2.99	46.80	18	1.67	9.39	20.28
8	0.63	2.21	78.17	18	1.02	5.49	32.82
8	0.63	2.29	75.48	18	1.06	5.29	34.74
8	0.70	2.06	82.64	18	0.55	4.36	50.63

the fact that, as will be shown below, this model overestimates plasma temperature by almost a factor of two.

For a more detailed comparison of measurement results with CPM predictions, Fig. 5 shows the dependencies of PV on specific internal energy E. To avoid cluttering the figure, results are shown for a small group of experiments in which maximum values of specific volume and internal energy were achieved. In Fig. 5, it can be seen that significant deviation of calculated dependencies from measured ones begins at energy values of 6–7 kJ/g. At higher energy values, the calculated dependencies become close to the dependency for singly ionized ideal gas. For reference, the specific ionization energy values for single, double, and triple ionization of ideal lead gas atoms are: Q_1 = 3.44 kJ/g, Q_2 = 6.97 kJ/g and Q_3 = 14.8 kJ/g [21]. Using the sublimation energy value for lead E_{sub} = 0.942 kJ/g [22], for internal energy of singly ionized ideal lead gas at temperature

$T = 10 - 30$ kK, we obtain energy values of $E = 6 - 8$ kJ/g. This estimate shows that calculated dependencies begin to deviate from measured ones when double ionization of atoms begins, and it might seem that the ionization degree predicted by the model does not exceed one. However, this is not the case.

The degree of ionization as a function of plasma specific internal energy, calculated using CPM for isochores $V/V_0 = 6$, $V/V_0 = 14$, is shown in Fig. 6. It can be seen that it increases monotonically and reaches a value of 1.9. The figure also shows the dependence of the value $E-(3/2)PV$ on plasma internal energy values. For classical plasma, this value equals the energy that goes into ionization, since the value $(3/2)PV$ is the average kinetic energy of a classical particle system. As follows from Fig. 6, in the energy range $E-(3/2)PV$ kJ/g, the calculated values of are about 5 kJ/g, which is two times less than the measured values. Thus, CPM predicts almost two times lower energy expenditure for plasma ionization compared to the values obtained in the experiment. This implies that the plasma temperature values predicted by this model may be significantly overestimated.

For detecting plasma non-ideality effects, studying the behavior of electrical conductivity is very important [17,18]. Fig. 7 shows the measured dependence of lead fluid's resistivity on specific internal energy in this work. Also presented are the resistivity dependencies on isochores obtained from these experimental data. The figure clearly shows the characteristic behavior of isochores near the metal-nonmetal transition [10]. This transition manifests in that near the volume value $V/V_0 = 2.7$ the temperature coefficient of resistance changes sign from positive to negative and the metal transitions into a strongly correlated metallic state. When specific volume becomes larger than value $V/V_0 \approx 4$, this coefficient, being negative, begins to rapidly increase in absolute magnitude with volume increase. The critical density estimation for metal-nonmetal transition in supercritical lead fluid was made based on analysis of the "cold curve", i.e., temperature-independent part of internal energy [10]. As follows from Fig. 7, in plasma state ($V/V_0 > 4$) the resistivity on isochores monotonically decreases with energy increase. It is noteworthy that the dependencies calculated using CPM in the energy interval $E < 5$ kJ/g practically merge into one line, which is not observed experimentally. Also note that at energy values $E > 10$ kJ/g, the slopes of measured isochores are significantly less than those demonstrated by the model. Experimental isochores of resistivity in this energy interval become almost horizontal. With increasing relative volume, agreement between measured dependencies and calculated ones improves. Note that calculation of lead plasma resistivity for volumes $V/V_0 = 10 - 20$ on isotherm $T = 20$ kK [23] gives resistivityvalues in the interval 50–100 μOhm, which agree with our calculation results.

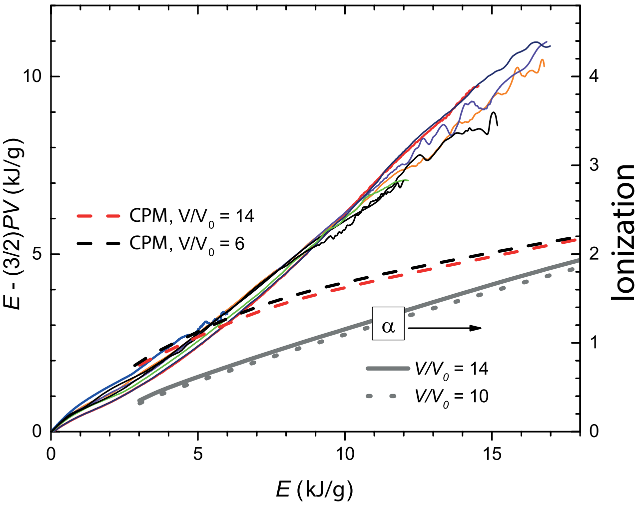

Fig. 6. The measured dependencies of the value $E-(3/2)PV$ on specific internal energy (thin lines originating from the origin) are compared with dependencies calculated using CPM for two isochores (two thick dashed lines). The plasma ionization degree dependencies calculated using CPM for two isochores are shown by gray solid and gray dotted lines

The results of our measurements of pressure, specific internal energy, and resistivity of supercritical lead fluid for a family of seven isochores are presented in Table 1.

4. DISCUSSION OF THE OBTAINED RESULTS

As follows from Fig. 5, our chemical model predicts rather high plasma temperature values. Due to such high temperatures, a question arises about the estimation of measurement errors in the present study related to energy losses through thermal radiation. For lead plasma with density of 0.5–2.0 g/cm^3 at temperature of 1-5 eV, the mean free path of photons (Rosseland averaged) is ~ 10^{-6} cm [24, 25], which is much smaller than the plasma

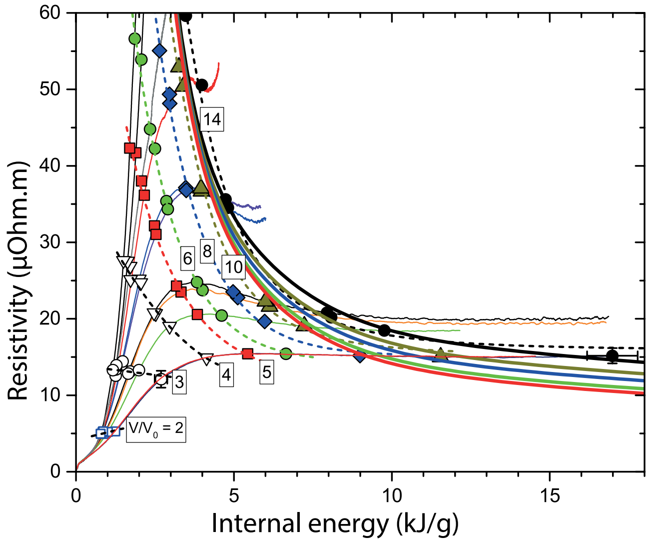

Fig. 7. Specific resistance of lead as a function of specific internal energy. Thin solid lines emerging from the normal state are dependencies measured in experiments of this work (marked with the same colors as these experiment lines in Fig. 2), symbols are specific resistance values on isochores obtained in these experiments, thin dotted lines are approximations of these isochores, thick solid lines are isochores V/V_0 = 5, 6, 8, 10, 14, calculated using CPM (marked with the same colors as corresponding experimental isochores)

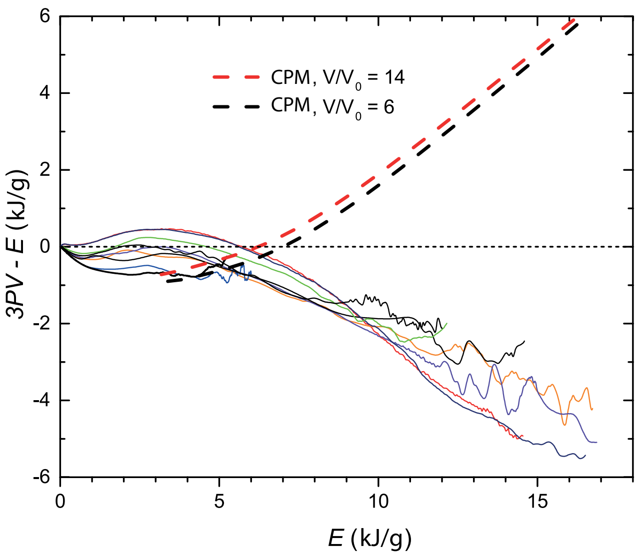

Fig. 8. Change in the average kinetic energy of lead fluid relative to the normal state as a function of internal energy. Thin solid lines originating from the origin are dependencies measured in present experiments, two thick dashed lines are dependencies calculated using CPM for two isochores

sample thickness in our experiments. This implies that this plasma is opaque and thermal radiation emerges from a thin layer near the sample surface. If we estimate the radiation losses from above, assuming that the sample temperature increases as predicted by the model, and its surface radiates as a black body, and all radiation energy is lost by the sample, it turns out that even for experiments with maximum pressure values, these losses do not exceed 10 % of the sample energy up to the energy value of 10 kJ/g. However, as seen in Fig. 6, at this energy value, the difference between measured and calculated values of PV reaches 50% and, consequently, this difference cannot be explained by energy losses through thermal radiation.

It should also be noted that the present experiments were conducted with samples whose initial thickness varied by almost 3 times in different experiments, and sapphire and silica glass were used as window materials, whose optical properties differ significantly from each other, and therefore energy losses due to radiation in different experiments, if they were noticeable, would have been different. However, the data obtained in various experiments are in good agreement with each other. Furthermore, measurements of sample volume and pressure, whose accuracy is not affected by thermal radiation, demonstrate rather smooth and monotonic pressure-volume dependencies, which approach practically constant pressure values at large sample volumes. If thermal radiation losses were significant, then due to the sharp dependence of thermal radiation intensity on temperature, one could expect a more or less sharp decrease in pressure in the sample.

Thus, our CPM predicts significantly lower energy expenditure for ionization and excitation of atoms than the values obtained in the experiment. This suggests that the model overestimates plasma temperature (for given values of V and E). As shown in Fig. 5, at an energy value of 12 kJ/g, the calculated values of PV are approximately 1.7 times higher than the measured ones. If we assume that the kinetic energy of plasma particles, which is proportional to $(1 + \alpha)\ T$, is overestimated by the same factor, and considering that the ionization degree in our model is practically independent of density and increases almost linearly with temperature (see Fig. 6), then instead of the temperature value of 60 kK predicted by the model, we get 40 kK. If we reduce the plasma temperature values by 1.7 times (relative to the values given by the model), then the maximum energy losses due to radiation will not exceed up to the 5% maximum measured energy values. Certainly, this temperature estimate cannot claim high accuracy, but it agrees with the results of present experiments, which showed no significant energy losses.

There is another experimental confirmation of the correctness of this conclusion. As follows from Fig. 4, in the enthalpy range of $W > 8$ kJ/g (which corresponds to the energy range of $E > 6$ kJ/g), the dependence of isenthalpic compressibility on specific enthalpy becomes very flat. On the other hand, radiation energy losses cannot affect this dependence since they do not influence density and pressure measurements, and compressibility is practically independent of enthalpy. Since the calculated compressibility values for this enthalpy range become almost twice lower than the measured ones, this definitely indicates that the model gives overestimated temperature values by approximately two times. Note that the temperature values obtained using the interpolation EOS [11] also turn out to be overestimated.

Due to such a significant difference between experimental results and XMP predictions, let's try to interpret these results based on general considerations that are not tied to any particular model. For this, we will use the virial theorem, which establishes the relationship between the average kinetic energy of a system of particles interacting according to Coulomb's law, with internal energy and pressure [20]:

$$K = 3PV - E, \tag{10}$$

where K is the average kinetic energy of the system. Note that this theorem is valid for both classical and quantum particle systems. For a classical particle system $K = (3/2)NkT$ (N is the number of particles in the system). Substituting this expression into (10) and differentiating it with respect to E at fixed volume and number of particles N, we obtain

$$\gamma = \frac{1}{3} + \frac{k}{2c_v}, \tag{11}$$

where c_v is the heat capacity per particle. From this, it follows that for classical plasma of constant composition, the following inequalities hold $1/3 < \gamma \leqslant 2/3$. We emphasize that this result is no longer restricted by the assumption of weak coupling that was used in deriving formula (4).

Let's consider the case when the number of particles in the system changes due to ionization. We will examine plasma consisting of atoms, ions, and free electrons at temperatures where only single ionization of atoms occurs. The kinetic energy of such a particle system consists not only of the kinetic energy of "classical particles" listed above but also of “quantum” particles of bound electrons in atoms. Differentiating relation (10) with respect to energy at fixed volume, we obtain

$$(\partial K / \partial E)_V = 3\gamma - 1. \tag{12}$$

Consider that the increment of kinetic energy is related not only to the increase in kinetic energy of “classical” particles but also to the change in kinetic energy of electrons transitioning from bound states to free motion states. For the subsystem of bound electrons, since they do not contribute to pressure, the virial theorem takes the form

$$K_b = -E_b, \tag{13}$$

where index “b” indicates that the value refers to bound electrons. Consequently, when an electron leaves an atom and becomes free, its kinetic energy decreases by the binding energy value (ionization potential). Obviously, the excitation of bound electrons also leads to a decrease in the system's kinetic energy. Therefore, the total kinetic energy increment equals

$$dK = d\left(\frac{3}{2}NkT\right) - I_1 dN_e - dE_{exc}, \tag{14}$$

where the last term is the contribution from excited states. Using the relation $N = N_\text{n} + N_\text{e}$, where N_n is the total number of atoms, after simple transformations we obtain

$$\left(\frac{\partial K}{\partial E}\right)_V = \frac{N_n}{C_V}\left[\frac{3}{2}k(1+\alpha)\right] - \\ -\frac{N_n}{C_V}\left(I_1 - \frac{3}{2}kT\right)\left(\frac{\partial \alpha}{\partial T}\right)_V - \frac{1}{C_V}\left(\frac{\partial E_{exc}}{\partial T}\right)_V, \tag{15}$$

where $CV = (\partial E/\partial T)_\text{V}$ — the plasma heat capacity, and the degree of ionization is $\alpha = Ne/Nn$. From relation (15), it follows that the derivative $(\partial E/\partial T)_\text{V}$ can become zero and even negative, if the second and third terms combined are greater than the first term.

According to relation (12), the sign of the derivative $(\partial E/\partial T)_\text{V}$ is determined only by the value of the Grüneisen coefficient. Consequently, the fact that the Grüneisen coefficient values become less than indicates a significant influence of ionization processes and excitation of bound electrons on the thermodynamic properties of plasma. The study of this issue for dense plasma is complicated by difficulties in separating electrons into free and bound ones, as well as accounting for the influence of interactions between plasma particles on their energy spectrum [26].

In this regard, it is interesting to compare the measured dependencies of plasma kinetic energy on the internal energy value with the predictions of CPM. In formula (10), energy is measured from the state where all particles of the system are removed to infinity (and are at rest there). In the experiment, energy is measured from the normal state of a solid. To express kinetic energy through measurable quantities, note that relation (10) should also hold for the state $T = 0$, $P = 0$, for which it takes the form

$$K_0 = -E_0, \tag{16}$$

where the index “0” denotes the state at $T = 0$, $P = 0$. Subtracting equation (16) from (10), we get

$$K - K_0 = 3PV - \left(E - E_0\right). \tag{17}$$

If we neglect the difference between the energy in the normal state and in the state $T = 0$, $P = 0$, then the value $E - E_0$ in the right part of (17) will represent the energy measured in the experiment; below we will continue to denote it with the letter E.

Fig. 8 shows a comparison of measured and calculated using CPM dependencies of K–K_0 on energy E, counted from the normal state. The fact that the kinetic energy of the system remains practically unchanged in the interval $E \leqslant 6$ kJ/g means that the increase in kinetic energy of atoms and free electrons is compensated by the decrease in kinetic energy of bound electrons, which transition to excited bound states or free motion states. The decrease in kinetic energy with increasing internal energy in the interval $E > 6$ kJ/g indicates that here the contribution from ionization and excitation of bound electrons dominates. The large difference between calculated and measured values of plasma kinetic energy indicates that the energy costs for plasma ionization and bound electron excitation in our CPM are greatly underestimated. Therefore, it can be stated that the reason for the discrepancy between model and experimental results lies in insufficiently accurate description of bound states. This fact partly confirms the conclusion about the inadequacy of classical description of non-degenerate dense plasma [27].

Note that the values of the Grüneisen coefficient for metals and silicates at pressures of 10-100 hPa and temperatures $T \leqslant 50$ kK were estimated in shock compression experiments of porous samples [28]. For metals, values of $\gamma = 0.6$–0.7 were obtained, while for silicates, the Grüneisen coefficient turned to zero and even became negative. This anomaly was interpreted by the authors as a consequence of the transition of matter to an amorphous state and partial dissociation of molecules SiO_2. Such behavior may also be related to diffuse structural transformations in the liquid state [29].

In conclusion, let's consider the behavior of the resistivity of lead plasma. As is known, one of the theoretically predicted effects of plasma non-ideality is the reduction of ionization potentials. Generally, this effect leads to an increase in the degree of ionization, and with it, the electrical conductivity of plasma, and such an increase in the degree of ionization with increasing density is sometimes called pressure ionization. This effect manifests in the fact that on isotherms, the resistivity decreases with decreasing specific volume. Theoretical models predict the presence of maxima on isotherms of resistivity [14, 23, 30], which separate the region of strongly non-ideal plasma from weakly non-ideal. According to work [23], for lead, the maxima on isotherms of resistivity $T = 10$ kK, $T = 20$ kK are in the volume interval $V/V_0 = 10$–20. The results of our experiments show that in the entire studied region of states for lead plasma, the inequality $(\partial\sigma^{-1}/\partial V)_T > 0$ holds, where σ^{-1} – resistivity (σ – electrical conductivity). Let's briefly explain where this statement comes from.

First of all, note that as seen in Fig. 2, in the volume interval $V/V_0 = 4$–6 for all presented experiments, the pressure reached its maximum, i.e., in this interval, the heating was close to isobaric and, consequently, the temperature increased with volume increase. In Fig. 7, it can be seen that in this volume interval, the resistivity either increases or remains constant with increasing energy. But since the total derivative of resistivity with respect to volume for some quasi-static process on the *VT*-plane can be represented as

$$\frac{d\sigma^{-1}}{dV} = \left(\frac{\partial\sigma^{-1}}{\partial T}\right)_V \frac{dT}{dV} + \left(\frac{\partial\sigma^{-1}}{\partial V}\right)_T,$$

and the derivative $(\partial\sigma^{-1}/\partial V)_T < 0$ (as seen in Fig. 7), it follows that $(\partial\sigma^{-1}/\partial V)_T > 0$. For experiments with pressure of 1–2 hPa (see Fig. 2), for which the sample heating process in the volume interval $V/V_0 = 8$–16 was close to isobaric, and the resistivity practically did not change (see Fig. 7), we come to the same conclusion. It can be shown that this is valid for the entire studied region of plasma states, but we won't dwell on this here. Thus, for dense lead plasma studied in this work, “pressure ionization“ plays a significant role.

5. CONCLUSION

Experimental data on thermodynamic properties and resistivity of dense lead plasma were obtained for a wide range of states on the *VP*-plane. The measurement results were compared with predictions of the chemical model of classical plasma. It was shown that the chemical model underestimates the energy costs for plasma ionization and atom excitation by almost two times. Considerations are provided explaining that the reason for this lies in insufficiently accurate description of bound states. It was shown that measurements of caloric properties of dense plasma together with the use of the virial theorem allows to determine how correctly the theory describes the system's energy division into kinetic and potential. It was also shown that for the dense lead plasma studied here, the "pressure ionization" effect plays a significant role – along isotherms, the resistivity decreases with decreasing specific volume.

ACKNOWLEDGMENTS

The authors express sincere gratitude to A. S. Shumikhin, who read the manuscript and made several valuable comments.

REFERENCES

1. A. W. DeSilva and A. D. Rakhel, Contrib. Plasma Phys. 45, 236 (2005).
2. A. W. DeSilva and G. B. Vunni, Phys. Rev. E 83, 037402 (2011).
3. J. Clérouin, P. Noiret, P. Blottiau et al., Phys. Plasmas 19, 082702 (2012).
4. P. Renaudin, C. Blancard, J. Clérouin et al., Phys. Rev. Lett. 91, 075002 (2003).
5. A. W. DeSilva and A. D. Rakhel, Int. J. Thermophys. 26, 1137 (2005).
6. J. Clérouin, P. Noiret, V.N. Korobenko, and A. D. Rakhel, Phys. Rev. B 78, 224203 (2008).
7. V. N. Korobenko and A. D. Rakhel, Phys. Rev. B 88, 134203 (2013).
8. V. N. Korobenko and A. D. Rakhel, Phys. Rev. B 75, 064208 (2007).
9. A. M. Kondratyev, V. N. Korobenko, A. D. Rakhel, J. Exp. Theor. Phys. 127, 1074–1086 (2018)..
10. A. M. Kondratyev, V.N. Korobenko, and A. D. Rakhel, J. Phys.: Condens. Matter 19, 195601 (2022).
11. L. V. Altshuler, A. V. Bushman, M. V. Zhernokletov et al., JETP 78, 741 (1980) [L. V. Al'tshuler, A. V, Bushman, M. V. Zhernokletov et al., Sov. Phys. JETP 51, 373 (1980)].
12. A. D. Rakhel, J. Phys.: Condens. Matter 30, 295602 (2018).
13. A. M. Kondratyev and A.D. Rakhel, Phys. Rev. B 107, 195134 (2023).
14. E. M. Apfelbaum, Contrib. Plasma Phys. 59, e201800148 (2019).
15. E. M. Apfelbaum, Contrib. Plasma Phys. 61, e202100063 (2021).
16. A. Yu. Potekhin, G. Chabrier, A. I. Chugunov, E. DeWitt, and F. J. Rogers, Phys. Rev. E 80, 047401 (2009).
17. A. L. Khomkin, A. S. Shumikhin, Phys.-Usp. 64, 1125 (1921) [A. L. Khomkin, A. S. Shumikhin, UFN 191, 1187 (2021)].
18. V.K. Gryaznov, I. L. Iosilevskiy, and V.E. Fortov, Thermodynamic Properties of Shock- Compressed Plasmas Based on a Chemical Picture, in HighPressure Shock Compression of Solids VII: Shock Waves and Extreme States of Matter, Springer, New York (2004), p. 437.
19. R.S. Hixson, M. A. Winkler, and J.W. Shaner, Physica B+ C 139-140, 893 (1986).
20. L. D. Landau, E. M. Lifshitz, Theoretical Phy sics: Vol. V. Statistical Physics. Part I. 5th ed. Fizmatlit, Moscow (2002).
21. Tables of Physical Values. Reference Book, ed. by I. K. Kikoin. Atomizdat, Moscow (1976).
22. L. V. Gurvich, I. V. Veits, V. A. Medvedev et al., Thermodynamic Properties of Individual Substances. Reference Edition in 4 volumes. Nauka, Moscow (1979).

23. A. L. Khomkin and A. S. Shumikhin, High Temp. High Press. 49, 143 (2020).

24. A. F. Nikiforov, V. G. Novikov, V. B. Uvarov, Quantum-Statistical Models of High- Temperature Plasma and Methods for Calculating Rosseland Mean Free Paths and Equations of State, Fizmatlit, Moscow (2000).

25. G. D. Tsakiris and K. Eidmann, J. Quant. Spectr. Rad. Transfer. 38, 353 (1987).

26. G. E. Norman, A. N. Starostin, TVT 8, 381 (1970) [G. E. Norman, A. N. Starostin, Teplofiz. Vys. Temp. 6, 410 (1968)]

27. G. E. Norman, A. N. Starostin, TVT 6, 410 (1968).

28. A. B. Medvedev, R. F. Trunin, UFN 182, 829 (2012).

29. V. V. Brazhkin, UFN 182, 847 (2012).

30. R. Redmer, Phys. Rep. 282, 35 (1997).